SIMULATING COSMIC REIONISATION

SIMULATING COSMIC REIONISATION

Proefschrift

ter verkrijging van
de graad van Doctor aan de Universiteit Leiden,
op gezag van de Rector Magnificus prof. mr. P. F. van der Heijden,
volgens besluit van het College voor Promoties
te verdedigen op woensdag 30 september 2009
klokke 13.45 uur

door

Andreas Heinz Pawlik

geboren te Finsterwalde
in 1978

Promotiecommissie

Promotor:	Prof. Dr. H. Röttgering	
Co-promotor:	Dr. J. Schaye	
Overige leden:	Prof. Dr. V. Icke	
	Prof. Dr. K. Kuijken	
	Dr. V. Springel	(MPA Garching)
	Prof. Dr. S. Zaroubi	(Universiteit Groningen)

Because something is happening here.
But you don't know what it is.
Do you, Mr Jones?
BALLAD OF A THIN MAN

Section of the East Side Gallery, Berlin, December 2007. The East Side Gallery is a memorial for freedom that consists of about 100 paintings by international artists on part of the Berlin wall between Ostbahnhof and Oberbaumbrücke along the river Spree. Photo taken by the author. Digitalization: Machteld Dekens. Cover design: Thomas Wilhelmi.

Contents

Zwei Dinge erfüllen das Gemüt mit
Bewunderung und Ehrfucht, der
bestirnte Himmel über mir und das
moralische Gesetz in mir.

Kant, Kritik der praktischen Vernunft

CHAPTER 1

Introduction

1.1 THE EPOCH OF REIONISATION

The first stars and galaxies formed a few hundred million years after the Big Bang, when the Universe was only a small fraction of its present age. Their radiation is thought to have transformed the previously cold and neutral hydrogen that filled intergalactic space into the hot and ionised cosmic plasma that is observed today. This milestone in the history of the Universe is called the epoch of reionisation.

When did reionisation occur? Was it a simple instantaneous event, or a complex transition of extended duration? Were the first stars in the first galaxies sufficiently powerful to reionise the Universe, or was an additional source of ionising radiation at play? Much about the cosmic reionisation transition is still unknown.

Theoretical studies of the epoch of reionisation are currently particularly timely because of the wealth of observational data of unparallelled quality that will soon be provided by a new generation of observatories. Radio interferometers like LOFAR[1], MWA[2] and SKA[3] will open a previously unexplored observational window by surveying the Universe at very low frequencies with unprecedented high resolution and sensitivity. The infrared space-based observatory JWST[4] and the optical ground-based adaptive optics telescope ELT[5] will even enable the direct imaging of the sources responsible for the reionisation process.

Radiative transfer simulations coupled to hydrodynamical simulations of the early Universe are one of the most promising techniques to study reionisation. Simulating reionisation is a challenging task that requires the radiation-hydrodynamical modelling of large representative volumes of the Universe at very high resolution. The main goal of this thesis is to present a radiative transfer method for use in this computationally demanding regime. To accomplish this goal, we will analyse the challenges posed by the desire to include the transfer of radiation in cosmological simulations of reionisation and show how they can be overcome.

The organisation of this chapter is as follows. In Sec. 1.2 we give a brief overview of the history of our Universe, sketch the physics behind the formation and evolution of the first stars and discuss some of the key aspects of the transition from the neutral to the ionised Universe they trigger. In Sec. 1.3 we review current observational constraints on the epoch of reionisation

---

[1] http://www.lofar.org

[2] http://www.haystack.mit.edu/ast/arrays/mwa/

[3] http://www.skatelescope.org

[4] http://www.jwst.nasa.gov/

[5] http://www.eso.org/sci/facilities/eelt/

and in Sec. 1.4 we discuss the main challenges encountered in simulating this important epoch. In Sec. 1.5 we present an outline of this thesis by summarising the content of its chapters, which concludes this chapter.

1.2 THE FIRST STARS AND THE REIONISATION OF THE UNIVERSE

The theory of hierarchical structure formation constitutes one of the pillars of modern Big Bang cosmology. According to this theory, matter assembles to form increasingly larger structures, or *halos*, through the gravitational amplification of tiny primordial density fluctuations. The dilute cosmic gas accreted by these halos soon condensed to form the first generation of stars and galaxies. Their radiation photo-ionised and photo-heated the previously predominantly neutral intergalactic gas, causing a global phase transition that is referred to as reionisation.

In this section we give a brief overview of some of the most important physical processes behind reionisation. This overview is not intended to be exhaustive. Rather, we focus our discussion on a few key issues that are of direct relevance to the work presented in this thesis. The reader is referred to the excellent reviews by, e.g., Barkana & Loeb (2001), Ciardi & Ferrara (2005), Furlanetto, Oh, & Briggs (2006), and Fan, Carilli,& Keating (2006) and to the textbooks by, e.g., Peacock (1999), Kolb & Turner (1990), Peebles (1993) and Padmanabhan (1993) for more information.

1.2.1 The expanding Universe

The history of the expanding Universe (see, e.g., Kolb & Turner 1990) starts with its birth in the Big Bang about 13.7 billion years ago. Back then it was so dense and so hot that frequent collisions, for instance between protons, electrons and photons, prevented elements from being formed. It was only about 380000 yr after the Big Bang, corresponding to a redshift $z \approx 1100$, that the adiabatic expansion of space had cooled the hot primordial plasma down to temperatures $T \approx 3000$ K that allowed the formation of neutral atoms. This key event in the history of the Universe is known as cosmological recombination.

Cosmological recombination (see Sunyaev & Chluba 2008 for a recent review) freed most of the photons that were previously trapped by Thompson scattering off free electrons. Today, these photons - witnesses of the infancy of the Universe - constitute the Cosmic Microwave Background (CMB) radiation and offer a direct view on the conditions in the Universe at the time of their last scattering (for a review see, e.g., Hu & Dodelson 2002). Together with observations of redshift $z \sim 0.5$ Type Ia supernova explosions that indicate a late-time acceleration in the expansion of space (Riess et al. 1998; Perlmutter et al. 1999) and observations of the large-scale structure of the Universe (e.g., Percival et al. 2007), the CMB observations (e.g., Komatsu et al. 2009) support a concordance cosmological model that specifies the composition of the expanding Universe and provides the current framework for investigations into its evolution.

At present, about 74% of the energy content of the Universe is assumed to be in the form of an elusive fluid dubbed dark (or vacuum) energy (for a review, see, e.g., Carroll, Press, & Turner 1992; Frieman, Turner, & Huterer 2008), which drives the observed late-time accelerated expansion of space. The matter in the Universe, which accounts for about 26% of its present energy density, is mostly (about 83% of the total matter mass) in the form of a cold and dark, weakly interacting, non-baryonic substrate (for a review see, e.g., Bertone, Hooper, & Silk 2004; Bergström 2000). The existence of this dark matter component is firmly established through observations of its gravitational interaction with ordinary (baryonic and leptonic) matter (e.g., Clowe et al. 2006; for a review see, e.g., Trimble 1987).

Ordinary matter, which may be detected through its emission/absorption of radiation across the electromagnetic spectrum, accounts for only about 17% of the total matter mass. Most of this matter is in the form of gas (e.g., Fukugita, Hogan, & Peebles 1998). Its initial (primordial) composition is well-constrained by Big Bang nucleosynthesis (e.g., Tytler et al. 2000; Kolb & Turner 1990). Just after recombination, about 75% of its mass consisted of neutral hydrogen and about 25% consisted of neutral helium. It contained trace amounts of free electrons, hydrogen and helium ions, deuterium and molecular hydrogen (as well as trace amounts of other light elements, like lithium and beryllium). The last component of the Universe, radiation (CMB photons, neutrinos and other light relativistic relics), presently contributes only an insignificant amount of less than 0.1% to the total energy budget (e.g., Fukugita & Peebles 2004).

The expansion of the Universe, i.e. the observation that the physical separation between idealised observers at rest increases with time t in proportion to the expansion factor $a(t) = [1+z(t)]^{-1}$, is characterised by the Hubble parameter $H \equiv \dot{a}/a$, where the dot indicates the time derivative. From dimensional analysis one may expect that the Hubble parameter is closely related to age of the Universe, $t \sim H^{-1}$. With this notation, the composition of the Universe is conveniently specified in terms of the set of cosmological parameters $\Omega_\Lambda \equiv \bar{\rho}_{\Lambda,0}/\rho_{\rm c}$, $\Omega_{\rm m} \equiv \bar{\rho}_{\rm m,0}/\rho_{\rm c}$ and $\Omega_{\rm r} \equiv \bar{\rho}_{\rm r,0}/\rho_{\rm c}$, where $\bar{\rho}_{\Lambda,0}, \bar{\rho}_{\rm m,0}$ and $\bar{\rho}_{\rm r,0}$ are, respectively, the present mean densities of dark energy, total (dark + ordinary) matter and radiation, $\rho_{\rm c} \equiv 3H_0^2/(8\pi G)$ is the critical density, G is the gravitational constant, c is the speed of light and $H_0 = 100h$ km s^{-1} Mpc^{-1} is the Hubble constant, i.e. the present value of the Hubble parameter. The value of h is confirmed to be about 0.7 by several independent measurements (e.g., Riess et al. 2009; for a review see, e.g., Jackson 2007).

Dilution due to the expansion of space implies that the density of matter evolves according to $\bar{\rho}_{\rm m}(a) = m\bar{n}_{\rm m}(a) = a^{-3}\bar{\rho}_{\rm m,0}$, where $\bar{n}_{\rm m}$ is the mean number density of particles of mass m. The energy density of radiation evolves both because of dilution and because of the stretching of the wavelength λ_0 with the expanding space, yielding $\bar{\rho}_{\rm r}(a) = \bar{n}_{\rm r}(a)h_{\rm P}c/(a\lambda_0) = a^{-4}\bar{\rho}_{\rm r,0}$, where $\bar{n}_{\rm r,0}$ is the mean number density of the massless relativistic particles and $h_{\rm P}$ is Planck's constant. The energy density of the vacuum simply remains constant, $\bar{\rho}_\Lambda(a) = \bar{\rho}_{\Lambda,0}$.

The mathematical description of the expansion of the concordance Universe is provided by Einstein's theory of General Relativity and (curved) space-time (e.g., Wald 1984; Nabler 1989). A central role in this theory is played by Einstein's field equation, which relates the geometry and energy content of the Universe. Employing the postulated (and observationally supported) homogeneity and isotropy of space as well as the scalings of the (energy) densities of dark energy, matter and radiation that we have derived above, Einstein's field equation transforms into $H^2(a) = H_0^2(\Omega_{\rm r}a^{-4} + \Omega_{\rm m}a^{-3} + \Omega_\Lambda)$, a relation known as the Friedmann equation. Note that we assumed that space is flat, which is, both on theoretical and observational grounds, the preferred geometry of the Universe in the concordance model, and which manifests itself in the relation $\Omega_{\rm r} + \Omega_{\rm m} + \Omega_\Lambda = 1$. Hence, $\Omega_\Lambda \approx 0.74$, $\Omega_{\rm m} \approx 0.26$ and $\Omega_{\rm r} \sim 10^{-4}$ are, respectively, identical to the fractional contributions of dark energy, matter and radiation to the total energy content of the Universe given above.

The Friedmann equation encapsulates the dependence of the expansion of space on the composition of the Universe. At present, the expansion rate is dominated by the densities of dark energy and matter. The different redshift dependencies of the densities of dark energy, matter and radiation imply, however, that this was not always the case. Indeed, the expansion of space was dominated by the radiation density for redshifts $z \gtrsim z_{\rm eq}$, where $z_{\rm eq} = (\Omega_{\rm m}/\Omega_{\rm r}) - 1 \sim 5 \times 10^3$ marks the redshift at which the radiation density becomes equal to the matter density. The expansion was dominated by the matter density for redshifts $z_\Lambda < z < z_{\rm eq}$, where $z_\Lambda = (\Omega_\Lambda/\Omega_{\rm m})^{1/3} - 1 \approx 0.3$ marks the redshift at which matter density becomes equal to the dark energy density. The history of the expanding Universe may thus be divided into an early radiation-dominated epoch, an intermediate matter-dominated epoch and the current epoch of dark energy domination.

1.2.2 The formation of galaxies

The galaxies observed today evolved from tiny fluctuations in the matter distribution through gravitational amplification. The characteristic time-scale associated with galaxy formation is therefore given by the free-fall time $\sim (G\rho_{\rm m})^{-1/2}$, where $\rho_{\rm m}$ is the local density of matter (dark + ordinary).

Linear theory

The initial growth of matter fluctuations due to gravitational instability in the expanding Universe is well described by linear theory (for reviews see, e.g., Peebles 1980; Peacock 1999; Padmanabhan 1993; Loeb 2006). It crucially depends on the size of the fluctuation wavelength λ with respect to the size of the causally connected Universe, whose boundaries are marked by the (particle) horizon (e.g., Kolb & Turner 1990). The (proper) radius $\lambda_{\rm H}$ of the horizon is given by the physical distance light could have travelled since the Big Bang, i.e. $\lambda_{\rm H}(t) \sim ct \sim cH^{-1}$.

Linear theory describes the growth of fluctuations in terms of the density contrast $\delta(\mathbf{r}) \equiv \rho_{\rm m}(\mathbf{r})/\bar{\rho}_{\rm m} - 1$, where $\mathbf{r}$ is the spatial coordinate. Fluctuations grow at different rates during different epochs of the expansion history of the Universe. We will briefly review the growth of fluctuations in the different regimes to facilitate the understanding of the fluctuation power spectrum that we present further below.

Linear fluctuations on super-horizon scales grow in proportion to the square of the expansion factor, $\delta \propto a^2$, during radiation-domination and in proportion to the expansion factor, $\delta \propto a$, during matter-domination. A super-horizon fluctuation will eventually enter the horizon (at $\lambda_{\rm H} \sim \lambda$) and become a sub-horizon fluctuation. If the fluctuation enters the horizon during the radiation-dominated era, then its gravitational growth is suppressed by the rapid expansion of space caused by the high (with respect to the matter density) radiation density (Meszaros 1974).

Sub-horizon fluctuations in the weakly interacting dark matter may continue to grow, in proportion to the expansion factor, $\delta \propto a$, once the Universe enters the matter-dominated era. On the other hand, sub-horizon fluctuations in ordinary matter may only continue to grow (in proportion to the expansion factor) after recombination. Before recombination, frequent scatterings of photons off free electrons smooth the fluctuations in the free electron density and, through electromagnetic coupling of electrons and protons, in the proton density.

Fluctuations that enter the horizon during the matter-dominated era evolve in a slightly different manner. Fluctuations in dark matter that enter the horizon during matter-domination simply continue their super-horizon growth, $\delta \propto a$. Fluctuations in ordinary matter that enter the horizon during matter-domination but before recombination are washed out by the radiation pressure mediated by photon-electron scattering. These fluctuations may only grow (in proportion to the expansion factor) after recombination. Finally, fluctuations in ordinary matter that enter the horizon after recombination are not affected by radiation pressure and continue to grow in proportion to the expansion factor, $\delta \propto a$.

Jeans mass

Thermal gas pressure prevents the growth of sub-horizon fluctuations in ordinary matter if the sound-crossing time $\lambda/c_{\rm s}$ becomes smaller than the gravitational free-fall time, i.e. if $\lambda \leq \lambda_{\rm J} \equiv c_{\rm s}\pi^{1/2}(G\rho_{\rm m})^{-1/2}$, where $c_{\rm s}$ is the sound speed (and the additional factor $\pi^{1/2}$ results from a detailed linear theory analysis of the fluctuation growth). The sound speed $c_{\rm s}^2 = \gamma k_{\rm B}T/(\mu m_{\rm H})$, where μ is the mean gas particle mass in units of the hydrogen mass $m_{\rm H}$ and γ is the ratio of specific heats, which for an ideal, mono-atomic gas is 5/3. The Jeans scale $\lambda_{\rm J}$ defines the Jeans mass $M_{\rm J} \equiv (4\pi/3)\rho_{\rm m}(\lambda_{\rm J}/2)^3$. Introducing the overdensity $\Delta \equiv \rho_{\rm m}/\bar{\rho}_{\rm m}$, the total (dark matter + gas) Jeans mass reads

$$M_{\rm J} \approx 6 \times 10^7\ {\rm M}_\odot\ \Delta^{-1/2} \left(\frac{T}{10^3\ {\rm K}}\right)^{3/2} \left(\frac{1+z}{10}\right)^{-3/2} \left(\frac{\mu}{1.22}\right)^{-3/2} \left(\frac{\Omega_{\rm m}h^2}{0.13}\right)^{-1/2}. \tag{1.1}$$

In fluctuations with masses greater than the Jeans mass, gravity cannot be supported by the gas pressure gradient, enabling the fluctuation to grow.

The temperature of the cosmic gas remains coupled to the temperature of the cosmic microwave background due to scattering off residual free electrons down to redshifts $1 + z_{\rm dec} \approx 160(\Omega_{\rm b}h^2/0.022)^{2/5}$ (e.g., Peebles 1993; Barkana & Loeb 2001), i.e. down to redshifts well after recombination. At present ($z = 0$), the distribution of energies of CMB photons is observed to be very close to that of photons emitted by a black body of temperature $T_{\rm CMB,0} = 2.73$ K (Fixsen et al. 1996). The temperature $T_{\rm bb}$ of a black body is related to the energy density $c^2\rho_{\rm bb}$ of the black-body radiation it emits through $aT_{\rm bb}^4 = c^2\rho_{\rm bb}$, where $a = 4\sigma_{\rm SB}/c$ is the radiation constant and $\sigma_{\rm SB}$ is the Stefan-Boltzmann constant. For $z > z_{\rm dec}$, the gas temperature therefore evolves according to $T = T_{\rm CMB} = T_{\rm CMB,0}(1 + z)$ and as a result, the Jeans mass becomes independent of redshift. At the mean density ($\Delta = 1$), $M_{\rm J} \approx 2.4 \times 10^5(\mu/1.22)^{-3/2}(\Omega_{\rm m}h^2/0.2)^{-1/2}$.

For redshifts $z < z_{\rm dec}$, the fraction of residual free electrons becomes so small that photon-electron scattering becomes improbable and the gas thermally decouples from the CMB. In the absence of other heating or cooling mechanisms, the gas then cools adiabatically, $T \propto (1 + z)^2$. The cosmological Jeans mass, i.e. the Jeans mass at density $\rho_{\rm m} = \bar{\rho}_{\rm m}$, then becomes

$$M_{\rm J} \approx 4 \times 10^3\ {\rm M}_\odot \left(\frac{1+z}{10}\right)^{3/2} \left(\frac{\mu}{1.22}\right)^{-3/2} \left(\frac{\Omega_{\rm m}h^2}{0.13}\right)^{-1/2} \left(\frac{\Omega_{\rm b}h^2}{0.022}\right)^{-3/5}. \tag{1.2}$$

Nonlinear collapse

Once $\delta \sim 1$, linear theory breaks down. An analytical approximation to the nonlinear growth of top-hat (i.e. spherical and homogeneous) sub-horizon fluctuations is provided by the spherical collapse model (Gunn & Gott 1972; for a textbook treatment see, e.g., Padmanabhan 1993). Near the linear regime, a fluctuation still grows approximately linearly with the expansion factor ($\delta \propto a$, assuming that the fluctuation becomes nonlinear well after recombination) while expanding with the Universe. Due to the pull-back from its self-gravity, the fluctuation then turns around, decoupling its dynamics from that of the expanding background. The fluctuation eventually becomes highly nonlinear and collapses to form a halo of density $\rho_{\rm coll}$.

The halo properties follow from the virial theorem, which relates the halo potential and kinetic energies. Accordingly, $v_{\rm vir}^2 \sim GM_{\rm vir}/r_{\rm vir}$, where $v_{\rm vir}$ is the halo velocity dispersion,

$M_{\rm vir}$ is the halo mass and $r_{\rm vir}$ is the halo radius. The latter two are related through $M_{\rm vir} = 4\pi/3\bar{\rho}_{\rm m}\Delta_{\rm coll} r_{\rm vir}^3$, where $\Delta_{\rm coll} \equiv \rho_{\rm coll}/\bar{\rho}_{\rm m}$ is the halo overdensity. Spherical collapse theory predicts a halo overdensity $\Delta_{\rm coll} \approx 180$ independent of halo mass and nearly independent of redshift. The collapse shock-heats the gas in the halo to temperatures $T_{\rm vir} \equiv \mu m_{\rm H} v_{\rm vir}^2/(3k_{\rm B})$. The virial mass is related to the viral temperature through

$$M_{\rm vir} \approx 2 \times 10^6 \,{\rm M}_\odot \left(\frac{T_{\rm vir}}{10^3\,{\rm K}}\right)^{3/2} \left(\frac{1+z}{10}\right)^{-3/2} \left(\frac{\mu}{1.22}\right)^{-3/2} \left(\frac{\Delta_{\rm coll}}{180}\right)^{-1/2} \left(\frac{\Omega_{\rm m}h^2}{0.13}\right)^{-1/2} \qquad (1.3)$$

The fact that this is of the same order as the Jeans mass (Eq. 1.1), evaluated at the collapse overdensity, is not surprising, since both the virial and the Jeans mass are derived assuming similar balances between gravitational and thermal energy.

Hierarchical formation of galaxies in the concordance cosmology

The density fluctuations are thought to be seeded by the blow-up of quantum fluctuations during inflation, a theoretized brief (10^{-43} s $\lesssim t \lesssim 10^{-30}$ s) phase of accelerated expansion shortly after the Big-Bang (Guth 1981; for textbook treatments see, e.g., Linde 1990; Liddle & Lyth 2000). While our description so far considered fluctuations in real space $\mathbf{r}$, a description of fluctuations in Fourier space $\mathbf{k}$ is often more convenient mathematically (e.g., Barkana & Loeb 2001). Accordingly, a real space fluctuation $\delta(\mathbf{r})$ of wavelength λ is replaced by the corresponding Fourier space fluctuation $\delta(\mathbf{k})$ of wave number $k = |\mathbf{k}| = 2\pi/\lambda$. Standard models of inflation predict a Gaussian field of isotropic, scale-dependent random fluctuations, which are independent (in Fourier space) of each other. Their statistical properties are fully characterised by the scale-dependent variance, or power $P(k)$ at wave number k.

Standard inflationary theory predicts a primordial power spectrum $P(k) = k^{n_{\rm s}}$ with $n_{\rm s} \approx 1$. The scale-dependence of the (linearly evolving) fluctuation spectrum is modified due to the subsequent linear growth of fluctuations. The suppression of fluctuation growth during radiation-domination leads to a turn-over in the power spectrum at a comoving[6] scale of the order of the horizon at matter-radiation equality, $\lambda_{\rm H,com}(z_{\rm eq}) \sim a_{\rm eq}^{-1} c H^{-1}(z_{\rm eq}) \sim 100$ Mpc comoving, and implies a small-scale asymptotic scaling $P(k) \propto k^{n_{\rm s}-4}$. At comoving scales larger than $\lambda_{\rm H,com}(z_{\rm eq})$, the power spectrum preserves its primordial shape.

The overall amplitude of the (linearly evolved) power spectrum, which is commonly expressed in terms of the rms density variation σ_8 (extrapolated to redshift $z = 0$ using linear theory and averaged using a top-hat filter of radius 8 h^{-1} Mpc), is not predicted by inflation and needs to be observationally determined. According to recent observational estimates, e.g. based on the analysis of CMB fluctuations (Komatsu et al. 2009), $\sigma_8 \approx 0.8$. Note that the shape of the power spectrum is also modified due to the nonlinear growth of fluctuations (e.g., Peacock & Dodds 1996).

The primordial shape of the power spectrum, together with its subsequent linear evolution, implies a fluctuation variance that increases with decreasing mass of the fluctuation. This mass-dependence is at the basis of the current paradigm of structure formation, the hierarchical formation of galaxies (White & Rees 1978; Blumenthal et al. 1984; White & Frenk 1991; for a review see, e.g., Baugh 2006). The lower the mass of a fluctuation, the larger its variance and the earlier (on average) it collapses. This bottom-up growth successfully explains for instance

---

[6] Comoving scales $\lambda_{\rm com}$ are related (by definition) to physical scales λ through $\lambda = a\lambda_{\rm com}$, where a is the expansion factor.

why galaxy-size halos are already observed at redshifts $z \lesssim 10$, while cluster-size halos, i.e. halos hosting hundreds of galaxies, do not assemble until much later, $z \lesssim 1$.

The mass-function of halos, i.e. the abundance of halos of a given mass, generally must be obtained using numerical simulations of the nonlinear structure formation process (see Sec. 1.4). Analytical approximate models help, however, to gain insight into the physical process at work. An excellent approximation to the mass function in numerical simulations is obtained from excursion set theory (Press & Schechter 1974; Bond et al. 1991; Sheth, Mo, & Tormen 2001; Maggiore & Riotto 2009), which combines the statistical description of the growth of fluctuations with the spherical (or its variant, the ellipsoidal) collapse model. The mass-function may be compared with observations by modelling the observed stellar luminosity distribution of (clusters of) galaxies as a function of halo mass. The stellar luminosities of galaxies depend on their star formation histories. The physics of star formation will be the subject of the next section.

1.2.3 The first stars

Stars form due to the gravitational collapse of gas in dark matter halos. The ability of a halo to contain gas is determined by the balance between the attractive gravitational forces and the repulsive pressure forces exerted on the gas. Only halos whose gravitational binding energy $\sim k_{\mathrm{B}}T_{\mathrm{vir}}$ per particle exceeds the gas thermal energy $\sim k_{\mathrm{B}}T$ may therefore retain accreted gas (e.g., Barkana & Loeb 1999). To form stars, the halo gas must efficiently cool (i.e. on cooling time scales smaller than the free-fall time; Rees & Ostriker 1977; Silk 1977) and reduce its thermal pressure to collapse to higher densities.

The ability of gas to cool efficiently depends on its density, temperature and composition. At temperatures $T < 10^4$ K, primordial gas cools mostly through radiative de-excitation of collisionally excited molecular hydrogen (e.g., Bromm, Coppi, & Larson 2002; Abel, Bryan, & Norman 2002). Cooling times smaller than the free fall time require gas temperatures $T \gtrsim 10^3$ K and molecular hydrogen fractions of $n_{\mathrm{H_2}}/n_{\mathrm{H}} \gtrsim 10^{-4}$ (e.g., Bromm & Larson 2004). Both these criteria are satisfied in halos with virial temperatures $T_{\mathrm{vir}} \sim 10^3$ K (Haiman, Thoul, & Loeb 1996; Tegmark et al. 1997; Yoshida et al. 2003). These *mini-halos*, which are expected to form as early as $z \gtrsim 10$ (see, e.g., the review by Barkana & Loeb 2001) and hence have masses $M_{\mathrm{vir}} \sim 10^6$ $\mathrm{M_\odot}$ (Eq. 1.3), constitute the first sites of star formation in the hierarchically evolving concordance Universe. Note that their mass is significantly larger than the cosmological Jeans mass (Eq. 1.2), which determines the ability of fluctuations to grow.

The details of stellar formation and evolution are not very relevant for the work presented in this thesis. We will therefore content ourselves with a brief presentation of (some) key aspects. Our discussions will be largely based on the recent reviews by Bromm & Larson (2004) and Ciardi & Ferrara 2005, to which the reader is referred for further details.

The birth of the first stars

Detailed three-dimensional simulations (Bromm, Coppi, & Larson 2002; Abel, Bryan, & Norman 2002) show that the gravitationally collapsing gas settles into a quasi-static configuration once it reaches temperatures $T \sim 200$ K and hydrogen number densities $n_{\mathrm{H}} \sim 10^4$ cm^{-3}. These characteristic values for the temperature and density are set by the physics of molecular hydrogen cooling (e.g., Bromm & Larson 2004). Below $T \lesssim 200$ K, molecular hydrogen cannot cool because of the lack of excitable transitions with correspondingly low energies. Above densities

$n_{\rm H} \gtrsim 10^4~{\rm cm}^{-3}$, collisional excitations and de-excitations become so frequent that the population of the energy states of molecular hydrogen reaches its thermal equilibrium value, rendering radiative cooling inefficient. The gas only continues to collapse once the accumulated gas mass becomes larger than the Jeans mass, $M_{\rm J} \sim 700~{\rm M}_\odot (T/200~{\rm K})^{3/2} (n_{\rm H}/10^4~{\rm cm}^{-3})^{-1/2}$ (Bromm & Larson 2004). The collapse then proceeds to densities $n_{\rm H} \sim 10^{22}~{\rm cm}^{-3}$ at which the gas becomes optically thick to its cooling radiation and forms a hydrostatical proto-stellar core of mass $\sim 5 \times 10^{-3}~{\rm M}_\odot$ (e.g., Omukai & Nishi 1998).

The final stellar mass will be determined by the physics of accretion. Dimensional analysis (Bromm & Larson 2004) suggests that the accretion rate is given by the ratio of Jeans mass and free-fall time, $\dot{M}_{\rm acc} \sim c_{\rm s}^3/G \propto T^{3/2}$. While the initial mass of the accreting proto-stellar core is comparable to the mass of proto-stellar cores in present-day star formation, a comparison of the temperatures of present-day star-forming regions ($T \sim 10$ K) and those in primordial ones ($T \sim 200$ K) indicates that primordial proto-stellar clumps may accrete gas at rates that are about two orders of magnitude higher than the rates at which present-day proto-stellar clumps accrete their gas. Although dimensional arguments certainly oversimplify the description of the accretion problem, it is thus generally expected that the first stars are typically much more massive ($\sim 100~{\rm M}_\odot$) than their present-day analogues ($\sim 1~{\rm M}_\odot$).

Life and death of the first stars

Being formed out of primordial gas, the first stars are metal-free. The nuclear fusion that powers the luminosities of stars must then proceed via proton-proton burning. Consequently, the first stars are much hotter than their present-day counterparts whose finite metallicity enables nuclear fusion to proceed via the more efficient CNO cycle. In fact, the first stars are found to resemble black-body emitters with black-body temperatures $T_{\rm bb} \approx 10^5$ K. As a result, the rate of emission of hydrogen (and helium) ionising photons by primordial stars may exceed that by present-day metal-enriched stars by more than an order of magnitude (e.g., Bromm, Kudritzki, & Loeb 2001; Schaerer 2002). The large masses of the first stars imply short stellar life-times. The final fates of the first stars depend on the precise values of their masses (e.g., Heger & Woosley 2002; for a review see Woosley, Heger, & Weaver 2002).

Stars with masses $10~{\rm M}_\odot \lesssim M \lesssim 30~{\rm M}_\odot$ built up iron cores with masses in excess of the Chandrasekhar mass and hence collapse and explode as supernovae (SNe), enriching their surroundings with the products of their stellar nucleosynthesis. Stars with masses $30~{\rm M}_\odot \lesssim M \lesssim 140~{\rm M}_\odot$ and masses $M > 260~{\rm M}_\odot$, on the other hand, collapse into black holes that lock up most of the stellar material. The stellar black holes may provide the seeds for the massive ($10^5 - 10^9~{\rm M}_\odot$) black holes observed as high-redshift quasars and at the centres of todays galaxies (e.g., Madau & Rees 2001; Volonteri & Rees 2005; Booth & Schaye 2009; Milosavljević et al. 2009). The death of stars in the mass-range $40~{\rm M}_\odot \lesssim M \lesssim 100~{\rm M}_\odot$ is expected to be accompanied by a burst of gamma-rays. High-redshift gamma-ray burst are indeed observed and provide important observational probes of the epoch of reionisation (e.g., Ciardi & Loeb 2000; Salvaterra et al. 2009). For stars in the mass range $140~{\rm M}_\odot \lesssim M \lesssim 260~{\rm M}_\odot$ no black hole is expected to form. These stars are instead disrupted in pair-instability SNe which leave no stellar remnants behind.

1.2.4 The transition to the ionised Universe

The first stars (and quasars) transformed the highly neutral post-recombination gas into a highly ionised plasma within only a few hundred million years (e.g., Sec. 1.1; Barkana & Loeb

2001). It is straightforward to see why the mere conversion of only trace amounts of gas into stars or black holes could have caused such a dramatic effect (Loeb & Barkana 2001): nuclear fusion releases $\sim 7 \times 10^6$ eV per hydrogen atom, and thin-disc accretion onto Schwarzschild black holes releases 10 times more energy. The ionisation of hydrogen requires, however, only 13.6 eV. It is therefore sufficient to convert a small fraction, i.e. $\sim 10^{-5}$, of the total baryonic mass into stars or black holes in order to reionise the Universe, at least if recombinations are unimportant.

Because of the spatially clustered distribution of stars and galaxies, the reionisation process is expected to have occurred in a highly inhomogeneous manner. The neutral gas in and around the overdense regions that host the first star-forming halos is generally ionised first. The low-density gas far away from the these first sites of star formation, on the other hand, only becomes reionised once the stellar ionising radiation is channelled into the large-scale underdense voids (Ciardi, Stoehr, & White 2003). Consequently, reionisation starts from the inside-out (e.g., Lee et al. 2008). The ionised regions powered by individual star-forming halos would then grow until they overlap. Thereafter, the reionisation process would reverse to proceed from the outside in, with ionising radiation slowly carving its way from the highly ionised voids into remaining dense pockets of neutral gas (Miralda-Escudé, Haehnelt, & Rees 2000).

Reionisation is therefore a (geometrically) highly complex process whose detailed understanding requires the use of radiative transfer simulations (Sec. 1.4). These simulations are, however, computationally extremely demanding. As an alternative, (semi-) analytical models (e.g., Madau, Haardt, & Rees 1999; Valageas & Silk 1999; Chiu & Ostriker 2000; Furlanetto, Zaldarriaga, & Hernquist 2004; Benson et al. 2006; Choudhury, Haehnelt, & Regan 2009; for a review on the semi-analytical treatment of galaxy formation see Baugh 2006) that go beyond the type of order of magnitude estimates presented in the beginning of this section may be employed. Two parameters crucially determine the predictions of such models: the average fraction $f_{\rm esc}$ of ionising photons that escape star-forming galaxies to ionise the intergalactic medium and the average recombination rate of the intergalactic gas, $\langle \alpha_{\rm rec}(T) n_{\rm e} n_{\rm HII} \rangle$, where $\alpha_{\rm rec}$ is the recombination rate coefficient (e.g., Osterbrock 1989), $n_{\rm e}$ is the electron number density and $n_{\rm HII}$ is the number density of ionised hydrogen. Note that the average recombination rate is proportional to the average of the square of the gas density if the gas is highly ionised and hence is highly sensitive to density fluctuations (Sec. 1.2.5). The fact that the values of both the escape fraction (e.g., Wise & Cen 2009; Gnedin, Kravtsov, & Chen 2008; Inoue, Iwata, & Deharveng 2006; Razoumov & Sommer-Larsen 2006) and the average recombination rate (e.g., Madau, Haardt, & Rees 1999; Pawlik, Schaye, & van Scherpenzeel 2009) are highly uncertain, currently presents one of the most severe obstacles for a quantitative modelling of the reionisation epoch.

1.2.5 Feedback from star formation

The first stars affect the properties of the surrounding intergalactic gas through the emission of radiation and the ejection of mass and metals, which may change the initial conditions for the formation of subsequent generations of stars and galaxies. This *feedback* from star formation on star formation may be both positive, i.e. it may facilitate the formation of subsequent stellar populations and/or the reionisation of the cosmic gas, and negative, i.e. it may impede subsequent star formation and/or reionisation. Stellar feedback may be broadly classified as thermal, radiative, mechanical and chemical. In this section we will present an outline of these four types of feedback. Detailed discussions may be found in the extensive reviews by, e.g., Barkana & Loeb 2001, Ciardi & Ferrara (2005) and Ciardi (2008).

The ionising radiation emitted by the first stars (and quasars) photo-heats the intergalactic gas to temperatures $T \sim 10^4$ K (e.g., Miralda-Escudé & Rees 1994; Hui & Haiman 2003; Tittley & Meiksin 2007), raising the cosmological Jeans mass (Eq. 1.1 with $\Delta = 1$) to values $\sim 10^9$ $\mathrm{M}_{\odot}$ (Eq. 1.1 with $\Delta = 1$). This *Jeans filtering* (Shapiro, Giroux, & Babul 1994; Gnedin & Hui 1998; Okamoto, Gao, & Theuns 2008) prevents the further assembly of gas in halos with virial temperatures $T_{\mathrm{vir}} \lesssim 10^4$ K, corresponding to virial masses $M_{\mathrm{vir}} \lesssim 10^8$ $\mathrm{M}_{\odot}$ (Eq. 1.3). Photo-heating furthermore evaporates gas that already assembled in halos of such low masses, significantly reducing the halo gas fractions (e.g., Thoul & Weinberg 1996; Barkana & Loeb 1999; Kitayama & Ikeuchi 2000; Shapiro, Iliev, & Raga 2004; Dijkstra et al. 2004; Susa & Umemura 2004; Iliev, Shapiro, & Raga 2005; Pawlik & Schaye 2009). Both effects lead to a strong suppression of star formation and hence provide a negative feedback on reionisation.

Photo-ionisation heating provides, however, also a positive feedback on reionisation, because the suppression of small-scale gas density fluctuations due to Jeans filtering reduces the average recombination rate of the intergalactic gas (e.g, Haiman, Abel, & Madau 2001; Wise & Abel 2005; Pawlik, Schaye, & van Scherpenzeel 2009). Less photons are then required to keep the intergalactic gas ionised, which facilitates the reionisation of the Universe. In Chapter 2 we will demonstrate that this positive feedback is, in fact, very strong. The evaluation of the net thermal feedback from photo-heating will require the use of radiation-hydrodynamical simulations.

In addition to copious amounts of ionising radiation, the first stars emit radiation in the Lyman-Werner absorption band of molecular hydrogen, characterised by frequencies 11.2 eV $\lesssim h_{\mathrm{P}}\nu \lesssim 13.6$ eV. This soft ultra-violet (UV), non-ionising radiation may propagate un-absorbed by neutral hydrogen and dissociate the molecular hydrogen in nearby star-forming regions. Because molecular hydrogen is the main coolant in halos with virial temperatures $T_{\mathrm{vir}} \sim 10^3$ K, which present the first sites of star formation in the hierarchical Universe, the presence of a photo-dissociating background is expected to substantially suppress early star formation (Haiman, Rees, & Loeb 1997). The efficient formation of stars may only continue with the (hierarchical) build-up of halos with virial temperatures $T_{\mathrm{vir}} \gtrsim 10^4$ K, in which the gas cools through the emission of de-excitation radiation from collisionally excited atomic hydrogen (e.g., Barkana & Loeb 2001).

Ionising radiation may, on the other hand, increase the ability of primordial gas of temperatures $T \sim 10^3$ K to cool. This is because the formation of molecular hydrogen is catalyzed by free electrons, whose abundance is increased by the presence of an ionising background. If the ionising spectrum is sufficiently hard (e.g. X-rays), then ionising photons may penetrate into the dense star-forming regions and counteract the photo-dissociations by soft UV photons. Stellar photons may therefore provide a positive feedback on star formation in halos with virial temperatures $T_{\mathrm{vir}} \sim 10^3$ K (e.g., Haiman, Rees, & Loeb 1996; Ricotti, Gnedin, & Shull 2002; Glover & Brand 2003; Machacek, Bryan, & Abel 2003). Note, however, that photo-ionisation reduces the ability of primordial gas to cool radiatively in halos with virial temperatures $T_{\mathrm{vir}} \gtrsim 10^4$ K (Efstathiou 1992; Wiersma, Schaye, & Smith 2009), because it reduces the abundance of neutral hydrogen, their main coolant.

SN explosions of massive stars typically inject a few solar masses of gas with velocity of $\sim 10^4$ km s^{-1}, corresponding to a kinetic energy of $\sim 10^{51}$ erg. The ejected material sweeps up and shock-heats the surrounding gas, entraining outflows sufficiently powerful to, at least temporarily, substantially reduce the gas fractions for low-mass halos (e.g., Yepes et al. 1997; Tassis et al. 2003; Scannapieco et al. 2006; Dalla Vecchia & Schaye 2008; Whalen et al. 2008). Since this leads to a suppression of the star formation rate, the mechanical feedback from SN explosions, like photo-evaporation, provides a negative feedback on reionisation. As shown in Pawlik & Schaye (2009) and in Chapter 3 of this thesis, the negative feedback from SN explosions may, moreover, be amplified by the presence of a photo-evaporating UV background.

SN explosions (in particular, pair-instability SN explosions) also provide a chemical feedback on the subsequent star formation process by enriching the intergalactic gas with the metals synthesised in the first stars. It is well-known that gravitationally collapsing metal-enriched gas clouds may cool more efficiently than their metal-free counterparts and hence become more easily unstable to fragmentation into low-mass proto-stellar clumps (e.g., Bromm et al. 2001). In fact, enrichment to metalicities as low as $Z \sim 10^{-4}\ Z_{\odot}$, where $Z_{\odot}$ is the solar metalicity, may be sufficient to trigger the transition from the high-redshift ($z \sim 10$) massive (~ 100 $\mathrm{M}_{\odot}$, see Sec. 1.2.3) star formation mode to the more standard low-mass (~ 1 $\mathrm{M}_{\odot}$) star formation mode observed today (e.g., Bromm et al. 2001; Schneider et al. 2002).

Thermal, radiative, mechanical and chemical stellar feedbacks will likely occur simultaneously and give rise to complicated non-linear interactions between very different physical processes (we already mentioned the interplay between SN mechanical feedback and photo-heating). Different feedback processes are, moreover, expected to affect the properties of the cosmic gas over very different scales. Radiative transfer effects like self-shielding will play a critical role in determining the efficiencies of the radiative/thermal feedbacks. Because of these complexities, investigations of stellar feedback generally require the use of numerical simulations (Sec. 1.4).

1.3 OBSERVING THE EPOCH OF REIONISATION

The epoch of reionisation is one of the last missing links in the story of the formation and evolution of galaxies. Evidence for reionisation is circumstantial - reionisation has, to date, not been directly observed. The detection and analysis of reionisation signatures in the highly ionised, post-reionisation Universe already provide, however, many interesting constraints on the duration and character of this important epoch. We summarise some of these constraints here and briefly discuss the prospective of direct observations of reionisation. The reader is referred to the recent reviews by Fan, Carilli,& Keating (2006) and Furlanetto, Oh, & Briggs (2006) for more information.

Observations of the absorption of light from quasars by intervening gas put strong constraints on the ionisation state of the Universe. Residual neutral hydrogen imprints a forest of Ly-α absorption lines in the spectra of background quasars (see Rauch 1998 for a review). The fraction of light transmitted by the intergalactic gas rapidly decreases with increasing redshift until, at redshift $z \gtrsim 6$, complete absorption troughs appear. The first clear-cut detection of such Gunn-Peterson troughs (Gunn & Peterson 1965) was reported by Becker et al. (2001). The strong evolution in the transmissivity of the high-redshift gas indicates a qualitative change in the ionisation state of the Universe and is consistent with results of models and simulations in which reionisation ends at redshifts $z \gtrsim 6$ (e.g., Fan, Carilli,& Keating 2006).

CMB photons scatter off free electrons produced during reionisation. This smooths fluctuations in the CMB temperature anisotropies and, if the CMB temperature shows a quadrupole anisotropy, generates a polarisation signal on angular scales $\lesssim 10^{\circ}$ corresponding to the scale of the horizon at reionisation (e.g., Zaldarriaga 1997; Hu & White 1997; Kaplinghat et al. 2003; Komatsu et al. 2009). At very small angular scales ($< 0.1^{\circ}$), scattering off free electrons additionally generates anisotropies due to the Sunyaev-Zeldovich effect (Sunyaev & Zeldovich

1980), the Ostriker-Vishniac effect (Ostriker & Vishniac 1986; Vishniac 1987) and patchy reionisation (e.g., Santos et al. 2003). Observations of the CMB and its polarisation may therefore provide important constraints on the reionisation process. Indeed, the most recent analysis of CMB temperature fluctuations (using the observed fluctuations in the polarisation signal to break the degeneracy between the damping of CMB fluctuations due to reionisation and the amplitude of the primordial fluctuation power) that have been measured with the WMAP[7] satellite implies a best-fit reionisation redshift $z = 11.0 \pm 1.4$ (Komatsu et al. 2009; assuming complete instantaneous reionisation).

Observational estimates of the ultra-violet (UV) luminosity density at redshifts $z \gtrsim 6$ (e.g., Stanway, Bunker, & McMahon 2003; Bouwens et al. 2004; Sawicki & Thompson 2006; Bouwens et al. 2008) provide a potential probe of the types of sources that reionised the Universe. At present, it is controversial whether the observed population of galaxies is capable of keeping the Universe at redshifts $z \lesssim 6$ in a highly ionised state (e.g., Gnedin 2008; Bouwens et al. 2008; Yüksel et al. 2008; Pawlik, Schaye, & van Scherpenzeel 2009 and Chapter 2 of this thesis). The ability of galaxies to keep the intergalactic gas ionised depends on the rate at which these galaxies produce ionising photons (which is inferred from their UV luminosity), the fraction of ionising photons that escape into the intergalactic medium and the average recombination rate in the intergalactic gas (Madau, Haardt, & Rees 1999). All these quantities are currently highly uncertain, both from an observer's and from a theorist's perspective. A contribution from quasars and other ionising sources (e.g., Rees 1986; Tegmark, Silk, & Evrard 1993; Mapelli, Ferrara, & Pierpaoli 2006; Dijkstra 2006; Srbinovsky & Wyithe 2007; Loeb 2009), though likely sub-dominant (e.g., Faucher-Giguère et al. 2008; but see Volonteri & Gnedin 2009), can therefore not yet be excluded.

In the (near) future, the detection of the redshifted 21 cm signal from neutral hydrogen will provide a direct view on reionisation (Scott & Rees 1990; Madau, Meiksin, & Rees 1997; Furlanetto, Oh, & Briggs 2006 for a review). Ly-α absorption studies only probe the very last stages of reionisation (when the gas is highly ionised), because the Ly-α optical depth saturates already for trace amounts ($n_{\rm HI}/n_{\rm H} \gtrsim 10^{-4}$) of neutral hydrogen. The analysis of CMB fluctuations provides, on the other hand, mostly integral constraints on the reionisation process, because the electron scattering optical depth towards reionisation is insensitive to the details of the reionisation history. The detection of emission in 21 cm allows, at least in principle, to map out the neutral hydrogen density as a function of redshift in spheres around the observer. Several low-frequency radio arrays (LOFAR, MWA, 21CMA) are now being constructed to measure the statistical properties of the redshifted 21 cm signal. Eventually ($\sim$ 2020), SKA will provide high-resolution tomographic images of the spatial distribution of the neutral hydrogen during reionisation.

1.4 SIMULATING THE EPOCH OF REIONISATION

Cosmological simulations of reionisation are amongst the most promising techniques to study the epoch of reionisation. These simulations combine prescriptions for the gravitational growth of density fluctuations in the expanding Universe and prescriptions for the hydrodynamical evolution of the cosmic gas with recipes for star formation and associated feedback and also follow the propagation of ionising radiation emitted by the first ionising sources (see, e.g., the reviews by Yepes et al. 1997; Bertschinger 1998; Dolag et al. 2008). Unlike analytical or

---

[7] http://map.gsfc.nasa.gov

semi-analytical models, which often rely on the presence of symmetries and which are mostly designed for application with specific scenarios or certain limiting regimes, cosmological simulations enable the investigation of three-dimensional problems in all their complexity. Cosmological simulations therefore constitute the prime choice for investigations into the epoch of reionisation, promising the modelling of the formation and evolution of stars and galaxies and the reionisation of the intergalactic hydrogen from first principles.

It is, however, important to realise that our current ignorance of many of (the details of) the physical processes that determine the formation and evolution of galaxies and their interactions with the surrounding intergalactic gas implies that cosmological simulations often suffer from some of the same systematic limitations as (semi-) analytical models (e.g., Furlanetto, Oh, & Briggs 2006). In fact, most reionisation simulations employ *sub-resolution* models that encode complex physics in an often simplified, sometimes heuristic, manner (e.g., Dolag et al. 2008). This introduces free parameters that require careful calibrations with results from other simulations and/or observations, just as is the case for (semi-) analytical models. Numerical simulations are, moreover, often compromised because of the lack of sufficiently powerful computational algorithms and resources. Simulating reionisation remains a computationally demanding task. In the following we will discuss some of the main challenges posed by the desire to incorporate the transport of ionising radiation into cosmological simulations of structure formation and reionisation.

Representative models of the Universe during reionisation require simulation boxes with sizes of several tens to hundreds of comoving Mpc (e.g., Barkana & Loeb 2004; Iliev et al. 2006). In simulations with smaller boxes, cosmic variance may give rise to results that are not representative of the cosmic mean. For example, the mass of the most massive halo clearly cannot exceed the total mass of the simulated volume. Large simulation boxes are also needed to capture statistically significant samples of ionised regions, which have typical sizes of up to tens of comoving Mpc (e.g., Furlanetto, Zaldarriaga, & Hernquist 2004; Furlanetto, McQuinn, & Hernquist 2006). Simulation boxes must, moreover, be sufficiently large to account for the modulation of density fluctuations by long wavelength modes. This means that the box size must be chosen such that density fluctuations averaged at the scale of the box remain negligible. Large simulation boxes are also important for predictions of the performance of future epoch-of-reionisation observatories, whose field of view will comprise large parts of the sky (e.g., Mellema et al. 2006a).

The hierarchical character of structure formation (Sec. 1.2.2) makes simulating reionisation in large boxes a very computationally demanding task. If cooling by molecular hydrogen is important, the first stars form in halos with masses as small as $\sim 10^6$ $M_\odot$ (Sec. 1.2.3). Even if one assumes that most of the molecular hydrogen is quickly destroyed by Lyman-Werner photons from the very first stars, the mass of the first star-forming halos is only increased to $\sim 10^8$ $M_\odot$ (Sec. 1.2.5), which is still very small. Simulations that aim to resolve the first sites of star formation in large simulations consequently require a large number of resolution elements, which is computationally expensive. The only way to perform such simulations is then to employ simulation methods that are parallelised for use with distributed memory machines.

In addition to very high mass resolution, simulating reionisation requires very high spatial resolution. The first star-forming halos exhibit structure on scales of the order of 10 (proper) kpc and less. Fluctuations in the intergalactic gas may occur on equally small scales (although it helps that Jeans filtering due to reionisation heating erases most of them, see Sec. 1.2.5). Simulating large representative cosmological volumes at such high spatial resolution while keeping the number of resolution elements low to ensure affordable computation times requires the use of spatially adaptive simulation techniques. Fortunately, such techniques, which comprise Adaptive Mesh Refinement (AMR; Berger & Colella 1989) and Smoothed Particle Hydrodynamics (SPH; Gingold & Monaghan 1977; Lucy 1977), are now routinely employed in state-of-the-art cosmological hydrodynamical simulations. We note in passing that SPH currently is arguably the most widely employed technique for large-scale structure formation simulations (see, e.g., Monaghan 2005 and Agertz et al. 2007 for discussions of the advantages and disadvantages of SPH and AMR).

The most severe challenge for simulating reionisation is probably the need to incorporate the transport of ionising radiation into the large spatially adaptive cosmological simulations described above. Computing the ionising intensity throughout the simulation box requires solving the seven-dimensional (three space coordinates, two directional coordinate, frequency and time) radiative transfer equation. This is a formidable task, not only because of the high dimensionality of the problem, but also because of the large number of ionising sources contained in typical cosmological volumes. To accomplish it, existing approaches (e.g., Gnedin & Abel 2001; Ciardi et al. 2001; Nakamoto, Umemura, & Susa 2001; Maselli, Ferrara, & Ciardi 2003; Razoumov & Cardall 2005; Mellema et al. 2006b; Susa 2006; Ritzerveld & Icke 2006; McQuinn et al. 2007; Semelin, Combes, & Baek 2007; Trac & Cen 2007; Pawlik & Schaye 2008; Aubert & Teyssier 2008; Altay, Croft, & Pelupessy 2008; Petkova & Springel 2009; Finlator, Özel, & Davé 2009) to solve the radiative transfer equation in cosmological simulations of reionisation often resort to a number of approximations.

Recently, the accuracy of several existing radiative transfer codes has been assessed in test simulations performed as part of a series of comparison projects (Iliev et al. 2006; Iliev et al. 2009). The results of the comparisons are encouraging, indicating that the participating codes have reached a certain level of maturity and reliability (Iliev et al. 2009). It should, however, be kept in mind that the design of most of the test simulations was kept rather simple in order to facilitate comparisons between different radiative transfer codes. Whether or not the approximations employed by current radiative transfer codes allow the accurate treatment of the radiative transfer problem in the complex setting of large-scale simulations of reionisation thus remains to be seen.

Radiative transfer codes that are both spatially adaptive and parallel on distributed memory are still rare (see Table 1 in Iliev et al. 2006 and Table 1 in Iliev et al. 2009). Most of even the most advanced reionisation simulations are therefore performed on uniform grids that contain relatively few grid points. Combined with the fact that large simulation boxes are necessary to model representative volumes of the Universe, this means that the spatial resolution of state-of-the-art radiative transfer simulations of reionisation is typically far below that of the underlying spatially adaptive hydrodynamical simulations. In fact, many radiative transfer simulations of reionisation ignore hydrodynamical effects altogether and assume the gas traces the dark matter. Small-scale structure in the cosmic gas is therefore often hardly accounted for.

This lack of adequate spatial resolution affects, for instance, the computation of recombination rates, whose precise knowledge is crucial to the understanding of the progress and topology of reionisation (e.g., Choudhury, Haehnelt, & Regan 2009; Chapter 6 of this thesis). At present, the effects of small-scale gas clumpiness on the recombination rate of the intergalactic gas are, at best, only included in a statistical manner by using pre-compiled sets of clumping factors obtained from high-resolution (re-)simulations of small parts of the original cosmological volume (e.g., Iliev et al. 2007; Kohler, Gnedin, & Hamilton 2007). Note that the lack of adequate spatial resolution also implies that the fraction of ionising photons that escape the star-forming galaxies to ionise the intergalactic gas, i.e. the escape fraction, is not computed self-consistently and hence constitutes an additional free parameter. The fact that the escape fractions of star-forming galaxies are degenerate with their ionising luminosities renders estimates of, for instance, the number of photons required to reionise the Universe difficult, if not impossible, and prevents tight constraints on the nature of the ionising sources.

Cosmological simulations typically contain millions of stellar ionising sources (e.g., Iliev et al. 2006). Large numbers of ionising sources pose a challenge to simulations of reionisation because most of the existing radiative transfer methods require computation times that scale linearly with the source number. The usual practice of reducing the number of ionising sources by combining sources that fall into the same cells of a superimposed mesh renders reionisation simulations feasible, but also reduces the spatial resolution at which the radiative transfer is performed. Note that the inclusion of diffuse radiation emitted by recombining ions further increases the number of ionising sources. It is then common to treat this recombination radiation using the on-the-spot approximation (e.g., Osterbrock 1989), assuming it is re-absorbed in the immediate vicinity of the recombining ion. The validity of this approximation in the context of large-scale reionisation simulations remains to be assessed (e.g., Ritzerveld 2005).

Radiative transfer simulations of reionisation are typically performed by post-processing pre-computed static density fields. This static approximation is appropriate for simulating the initial phase of rapid growth of ionised regions, which often proceeds at speeds close to the speed of light, or the propagation of ionisation fronts on cosmological scales (see, e.g., the discussion in Iliev et al. 2006). Once the speed of ionisation fronts becomes comparable to the sound speed of the ionised gas, the static approximation becomes, however, inapplicable and a full radiation-hydrodynamical treatment is required. In any case, the static approximation breaks down after about a sound-crossing time, as the Jeans filtering of the gas can then no longer be ignored. Although thermal feedback from reionisation is known to play a key role (see Sec. 1.2.5), its effects are ignored in almost all of the current large-scale reionisation simulations. Some simulations try to include the effects of reionisation heating at the expense of a detailed treatment of the radiative transfer problem by employing photo-heating rates computed in the optically thin limit (e.g., Gnedin & Abel 2001; Pawlik, Schaye, & van Scherpenzeel 2009 and Chapter 2 of this thesis). The main drawback of such an approach is that it ignores the ability of gas to shadow and self-shield (e.g., Kitayama & Ikeuchi 2000; Susa & Umemura 2004; Dijkstra et al. 2004).

Current cosmological simulations provide invaluable insights into the physics of reionisation and enable first predictions for future observational campaigns. These simulations also reveal the limitations of the currently employed numerical techniques, triggering the exploration of novel approaches to address the numerical challenges outlined above. Several methods are now available to accomplish the transport of ionising radiation in a spatially adaptive manner (e.g., Gnedin & Abel 2001; Susa 2006; Ritzerveld & Icke 2006; Razoumov & Sommer-Larsen 2006; Trac & Cen 2007; Pawlik & Schaye 2008; Altay, Croft, & Pelupessy 2008; Petkova & Springel 2009). Other methods have been designed to avoid the scaling of the computation time with the number of ionising sources (e.g., Gnedin & Abel 2001; Cen 2002; Pawlik & Schaye 2008; Petkova & Springel 2009). Still other radiative transfer methods are available for direct use in step with hydrodynamical simulations (e.g., Gnedin & Abel 2001; Pawlik & Schaye 2008; Altay, Croft, & Pelupessy 2008; Petkova & Springel 2009), and some of these methods even include the radiation-hydrodynamical feedback (Gnedin & Abel 2001; see also table 1 in Iliev et al. 2009). The application of these methods in large-scale cosmological simulations of reionisation is likely to lead to new discoveries and to significantly advance our understanding of one of the last unknown epochs in the history of the Universe.

1.5 THESIS OUTLINE

In this section we give brief summaries of the contents of Chapters 2-7 of this thesis. The main scientific contribution of this thesis is the development of a novel method to solve the radiative transfer problem in large cosmological smoothed particle hydrodynamics simulations (Chapters 4 and 5). This scheme - TRAPHIC (TRAnsport of PHotons In Cones) - is designed to address and overcome the main challenges posed by simulations of reionisation: the huge dynamic range they exhibit, requiring the simultaneous simulation of the physics on both very small and very large scales, and the large number of ionising sources they contain. It is one of the first of a new generation of radiative transfer schemes that are developed to incorporate the spatially adaptive transport of ionising radiation into large-scale structure formation simulations of our Universe in an efficient and accurate manner.

Chapter 2. The critical star formation rate density required to keep the intergalactic hydrogen ionised depends crucially on the average rate of recombinations in the intergalactic medium (IGM). This rate is proportional to the clumping factor $C \equiv \langle\rho_{\rm b}^2\rangle_{\rm IGM}/\langle\rho_{\rm b}\rangle^2$, where $\rho_{\rm b}$ and $\langle\rho_{\rm b}\rangle$ are the local and cosmic mean baryon density, respectively and the brackets $\langle\rangle_{\rm IGM}$ indicate spatial averaging over the recombining gas in the IGM. We perform a suite of cosmological smoothed particle hydrodynamics simulations that include radiative cooling to calculate the volume-weighted clumping factor of the IGM at redshifts $z \geq 6$. We focus on the effect of photo-ionisation heating by a uniform ultra-violet background and find that photo-heating strongly reduces the clumping factor because the increased pressure support smoothes out small-scale density fluctuations. Because the reduction of the clumping factor makes it easier to keep the IGM ionised, photo-heating provides a positive feedback on reionisation. We demonstrate that this positive feedback is in fact very strong: even our most conservative estimate for the clumping factor ($C \approx 6$) is five times smaller than the clumping factor that is usually employed to determine the capacity of star-forming galaxies to keep the $z = 6$ IGM ionised. Our results imply that the observed population of star-forming galaxies at $z \approx 6$ may be sufficient to keep the IGM ionised, provided that the IGM was reheated at $z \gtrsim 9$ and that the fraction of ionising photons that escape the star-forming regions to ionise the IGM is larger than ≈ 0.2.

Chapter 3. Photo-heating associated with reionisation and kinetic feedback from core-collapse supernovae (SNe) have previously been shown to suppress the high-redshift cosmic star formation rate. Here we investigate the interplay between photo-heating and SN feedback using a set of cosmological, smoothed particle hydrodynamics simulations. We show that photo-heating and SN feedback mutually amplify each other's ability to suppress the star formation rate. Our results demonstrate the importance of the simultaneous, non-independent inclusion of these two processes in models of galaxy formation to estimate the strength of the total negative feedback they exert. They may therefore be of particular relevance to semi-analytic models in which the effects of photo-heating and SN feedback are implicitly assumed to act independently of each other.

Chapter 4. We present TRAPHIC, a novel radiative transfer scheme for Smoothed Particle Hydrodynamics (SPH) simulations. TRAPHIC (TRAnsport of PHotons In Cones) is designed for use in simulations exhibiting a wide dynamic range and containing a large number of light sources. It is adaptive both in space and in angle and can be employed for application on distributed memory machines. The (time-dependent) radiative transfer equation is solved by tracing individual photon packets in an explicitly photon-conserving manner directly on the unstructured grid traced out by the set of SPH particles. To accomplish directed transport of radiation despite the irregular spatial distribution of the SPH particles, photons are guided inside cones. The expensive scaling of the computation time with the number of light sources that is encountered in conventional radiative transfer schemes is avoided by introducing a source merging procedure.

Chapter 5. We present and test a parallel numerical implementation of our radiative transfer scheme TRAPHIC, specified for the transport of mono-chromatic hydrogen-ionising radiation, in the smoothed particle hydrodynamics code GADGET-2. The tests comprise several radiative transfer problems of increasing complexity. Some of these tests have been specifically designed to investigate TRAPHIC's ability to solve the radiative transfer problem in the large cosmological reionisation simulations that it was developed for, while others have been designed to demonstrate that TRAPHIC can also be employed in more general contexts. The results of all tests are in excellent agreement with both analytic solutions and numerical reference results obtained with state-of-the-art radiative transfer codes.

Chapter 6. Radiative transfer (RT) simulations coupled to cosmological hydrodynamical simulations are one of the most promising numerical tools to study reionisation, a key epoch in the high-redshift Universe. Current generations of RT schemes are, however, often limited for use with uniform and relatively coarse grids that imply a spatial resolution far below that of state-of-the-art spatially adaptive hydrodynamical simulations. Small-scale structure in the cosmic gas is then, at best, only statistically accounted for. Here we use the spatially adaptive RT scheme TRAPHIC (Chapter 4) to investigate the implications of this approximate approach. We contrast RT simulations performed on spatially adaptive smoothed particle hydrodynamics density fields with RT simulations performed on density fields that are defined on a uniform grid. Comparisons of the evolution of the mean ionised fraction, of the dependence of the ionised fraction on the local gas density and of power spectra of the 21 cm signal from neutral hydrogen reveal substantial differences caused by the difference in the dynamic range employed by the two types of RT simulations. Our results underpin earlier suggestions that ignoring the inhomogeneous distribution of gas on small scales, as is typically done in current RT simulations of reionisation, can give rise to misleading conclusions about the spatial distribution of the ionised gas and hence affect the interpretation of current and the predictions of future observations of reionisation.

Chapter 7. The temperature of the cosmic gas is a key astrophysical observable. The detailed modelling of its evolution with cosmological hydrodynamical simulations requires the use of radiative transfer methods to accurately compute the effects of photo-ionisation and photo-heating on the relevant cooling and heating rates. We extend our implementation of TRAPHIC to compute the non-equilibrium evolution of the temperature of gas exposed to hydrogen-ionising radiation. We verify this extension by comparing TRAPHIC's performance in thermally coupled radiative transfer test simulations with reference solutions obtained with other radiative transfer codes.

REFERENCES

Abel T., Bryan G. L., Norman M. L., 2002, Sci, 295, 93

Agertz O., et al., 2007, MNRAS, 380, 963

Altay G., Croft R. A. C., Pelupessy I., 2008, MNRAS, 386, 1931

Aubert D., Teyssier R., 2008, MNRAS, 387, 295

Barkana R., Loeb A., 1999, ApJ, 523, 54

Barkana R., Loeb A., 2001, PhR, 349, 125

Barkana R., Loeb A., 2004, ApJ, 609, 474

Baugh C. M., 2006, RPPh, 69, 3101

Becker R. H., et al., 2001, AJ, 122, 2850

Benson A. J., Sugiyama N., Nusser A., Lacey C. G., 2006, MNRAS, 369, 1055

Berger M. J., Colella P., 1989, JCoPh, 82, 64

Bergström L., 2000, RPPh, 63, 793

Bertone G., Hooper D., Silk J., 2004, PhR, 405, 279

Bertschinger E., 1998, ARA&A, 36, 599

Blumenthal G. R., Faber S. M., Primack J. R., Rees M. J., 1984, Natur, 311, 517

Bond J. R., Cole S., Efstathiou G., Kaiser N., 1991, ApJ, 379, 440

Booth C. M., Schaye J., 2009, arXiv, arXiv:0904.2572

Bouwens R. J., et al., 2004, ApJ, 606, L25

Bouwens R. J., Illingworth G. D., Franx M., Ford H., 2008, ApJ, 686, 230

Bromm V., Ferrara A., Coppi P. S., Larson R. B., 2001, MNRAS, 328, 969

Bromm V., Kudritzki R. P., Loeb A., 2001, ApJ, 552, 464

Bromm V., Coppi P. S., Larson R. B., 2002, ApJ, 564, 23

Bromm V., Larson R. B., 2004, ARA&A, 42, 79

Carroll S. M., Press W. H., Turner E. L., 1992, ARA&A, 30, 499

Cen R., 2002, ApJS, 141, 211

Chiu W. A., Ostriker J. P., 2000, ApJ, 534, 507

Choudhury T. R., Haehnelt M. G., Regan J., 2009, MNRAS, 394, 960

Ciardi B., Loeb A., 2000, ApJ, 540, 687

Ciardi B., Ferrara A., Marri S., Raimondo G., 2001, MNRAS, 324, 381

Ciardi B., Stoehr F., White S. D. M., 2003, MNRAS, 343, 1101

Ciardi B., Ferrara A., 2005, SSRv, 116, 625

Ciardi B., 2008, AIPC, 990, 353

Clowe D., Bradač M., Gonzalez A. H., Markevitch M., Randall S. W., Jones C., Zaritsky D., 2006, ApJ, 648, L109

Dalla Vecchia C., Schaye J., 2008, MNRAS, 387, 1431

Dijkstra M., Haiman Z., Rees M. J., Weinberg D. H., 2004, ApJ, 601, 666

Dijkstra M., 2006, NewAR, 50, 204

Dolag K., Borgani S., Schindler S., Diaferio A., Bykov A. M., 2008, SSRv, 134, 229

Efstathiou G., 1992, MNRAS, 256, 43P

Fan X., Carilli C. L., Keating B., 2006, ARA&A, 44, 415

Faucher-Giguère C.-A., Lidz A., Hernquist L., Zaldarriaga M., 2008, ApJ, 682, L9

Ferrara A., Salvaterra R., 2004, astro, arXiv:astro-ph/0406554

Finlator K., Özel F., Davé R., 2009, MNRAS, 393, 1090

Fixsen D. J., Cheng E. S., Gales J. M., Mather J. C., Shafer R. A., Wright E. L., 1996, ApJ, 473, 576

Frieman J. A., Turner M. S., Huterer D., 2008, ARA&A, 46, 385

Fukugita M., Hogan C. J., Peebles P. J. E., 1998, ApJ, 503, 518

Fukugita M., Peebles P. J. E., 2004, ApJ, 616, 643

Furlanetto S. R., Zaldarriaga M., Hernquist L., 2004, ApJ, 613, 1

Furlanetto S. R., McQuinn M., Hernquist L., 2006, MNRAS, 365, 115

Furlanetto S. R., Oh S. P., Briggs F. H., 2006, PhR, 433, 181

Gingold R. A., Monaghan J. J., 1977, MNRAS, 181, 375

Glover S. C. O., Brand P. W. J. L., 2003, MNRAS, 340, 210

Gnedin N. Y., Hui L., 1998, MNRAS, 296, 44

Gnedin N. Y., Abel T., 2001, NewA, 6, 437

Gnedin N. Y., 2008, ApJ, 673, L1

Gnedin N. Y., Kravtsov A. V., Chen H.-W., 2008, ApJ, 672, 765

Gunn J. E., Peterson B. A., 1965, ApJ, 142, 1633

Gunn J. E., Gott J. R. I., 1972, ApJ, 176, 1

Guth A. H., 1981, PhRvD, 23, 347

Haiman Z., Thoul A. A., Loeb A., 1996, ApJ, 464, 523

Haiman Z., Rees M. J., Loeb A., 1996, ApJ, 467, 522

Haiman Z., Rees M. J., Loeb A., 1997, ApJ, 476, 458

Haiman Z., Abel T., Madau P., 2001, ApJ, 551, 599

Heger A., Woosley S. E., 2002, ApJ, 567, 532

Hu W., White M., 1997, NewA, 2, 323

Hu W., Dodelson S., 2002, ARA&A, 40, 171

Hui L., Haiman Z., 2003, ApJ, 596, 9

Iliev I. T., Shapiro P. R., Ferrara A., Martel H., 2002, ApJ, 572, L123

Iliev I. T., Shapiro P. R., Raga A. C., 2005b, MNRAS, 361, 405

Iliev I. T., et al., 2006, MNRAS, 371, 1057

Iliev I. T., Mellema G., Pen U.-L., Merz H., Shapiro P. R., Alvarez M. A., 2006, MNRAS, 369, 1625

Iliev I. T., Mellema G., Shapiro P. R., Pen U.-L., 2007, MNRAS, 376, 534

Iliev I. T., et al., 2009, arXiv, arXiv:0905.2920

Inoue A. K., Iwata I., Deharveng J.-M., 2006, MNRAS, 371, L1

Jackson N., 2007, LRR, 10, 4

Kaplinghat M., Chu M., Haiman Z., Holder G. P., Knox L., Skordis C., 2003, ApJ, 583, 24

Kitayama T., Ikeuchi S., 2000, ApJ, 529, 615

Kohler K., Gnedin N. Y., Hamilton A. J. S., 2007, ApJ, 657, 15

Kolb, E. W., Turner, M. S., The Early Universe, Westview Press (1990)

Komatsu E., et al., 2009, ApJS, 180, 330

Lee K.-G., Cen R., Gott J. R. I., Trac H., 2008, ApJ, 675, 8

Liddle, A.;, Lyth, D., Cosmological Inflation and Large-Scale Structure. Cambridge (2000).

Linde A. D., Particle Physics and Inflationary Cosmology, Harwood Academic Publishers (1990)

Loeb A., Barkana R., 2001, ARA&A, 39, 19

Loeb A., 2006, astro, arXiv:astro-ph/0603360

Loeb A., 2009, JCAP, 3, 22

Lucy L. B., 1977, AJ, 82, 1013

Machacek M. E., Bryan G. L., Abel T., 2003, MNRAS, 338, 273

Madau P., Meiksin A., Rees M. J., 1997, ApJ, 475, 429

Madau P., Haardt F., Rees M. J., 1999, ApJ, 514, 648

Madau P., Rees M. J., 2001, ApJ, 551, L27

Maggiore M., Riotto A., 2009, arXiv, arXiv:0903.1249

Mapelli M., Ferrara A., Pierpaoli E., 2006, MNRAS, 369, 1719

Maselli A., Ferrara A., Ciardi B., 2003, MNRAS, 345, 379

McQuinn M., Lidz A., Zahn O., Dutta S., Hernquist L., Zaldarriaga M., 2007, MNRAS, 377, 1043

Mellema G., Iliev I. T., Alvarez M. A., Shapiro P. R., 2006, NewA, 11, 374

Mellema G., Iliev I. T., Pen U.-L., Shapiro P. R., 2006, MNRAS, 372, 679

Meszaros P., 1974, A&A, 37, 225

Milosavljević M., Bromm V., Couch S. M., Oh S. P., 2009, ApJ, 698, 766

Miralda-Escudé J., Rees M. J., 1994, MNRAS, 266, 343

Miralda-Escudé J., Haehnelt M., Rees M. J., 2000, ApJ, 530, 1

Monaghan J. J, 2005, Rep. Prog. Phys. 68 1703-1759

Nabler, G. L., Spacetime and Singularities: An Introduction, Cambridge University Press (1989)

Nakamoto T., Umemura M., Susa H., 2001, MNRAS, 321, 593

Okamoto T., Gao L., Theuns T., 2008, MNRAS, 390, 920

Omukai K., Nishi R., 1998, ApJ, 508, 141

Osterbrock D. E., 1989, Astrophysics of gaseous nebulae and active galactic nuclei, Palgrave Macmillan

Ostriker J. P., Vishniac E. T., 1986, ApJ, 306, L51

Padmanabhan T., Structure Formation in the Universe, Cambridge University Press (1993)

Pawlik A. H., Schaye J., 2008, MNRAS, 389, 651

Pawlik A. H., Schaye J., van Scherpenzeel E., 2009, MNRAS, 394, 1812

Pawlik A. H., Schaye J., 2009, MNRAS, 396, L46

Peacock J. A., Dodds S. J., 1996, MNRAS, 280, L19

Peacock, J. A., Cosmological Physics, Cambridge University Press (1999)

Peebles, P. J. E., The Large-Scale Structure of the Universe, Princeton Series in Physics (1980)

Peebles, P. J. E., Principles of Physical Cosmology, Princeton Series in Physics (1993)

Percival W. J., Cole S., Eisenstein D. J., Nichol R. C., Peacock J. A., Pope A. C., Szalay A. S., 2007, MNRAS, 381, 1053

Perlmutter S., et al., 1999, ApJ, 517, 565

Petkova M., Springel V., 2009, MNRAS, 396, 1383

Press W. H., Schechter P., 1974, ApJ, 187, 425

Rauch M., 1998, ARA&A, 36, 267

Razoumov A. O., Cardall C. Y., 2005, MNRAS, 362, 1413

Razoumov A. O., Sommer-Larsen J., 2006, ApJ, 651, L89

Rees M. J., Ostriker J. P., 1977,MNRAS, 179, 541

Rees M. J., 1986, MNRAS, 222, 27P

Ricotti M., Gnedin N. Y., Shull J. M., 2002, ApJ, 575, 49

Riess A. G., et al., 1998, AJ, 116, 1009

Riess A. G., et al., 2009, arXiv, arXiv:0905.0697

Ritzerveld J., 2005, A&A, 439, L23

Ritzerveld J., Icke V., 2006, PhRvE, 74, 026704

Salvaterra R., et al., 2009, arXiv, arXiv:0906.1578

Santos M. G., Cooray A., Haiman Z., Knox L., Ma C.-P., 2003, ApJ, 598, 756

Sawicki M., Thompson D., 2006, ApJ, 648, 299

Scannapieco C., Tissera P. B., White S. D. M., Springel V., 2006, MNRAS, 371, 1125

Schaerer D., 2002, A&A, 382, 28

Schneider R., Ferrara A., Natarajan P., Omukai K., 2002, ApJ, 571, 30

Scott D., Rees M. J., 1990, MNRAS, 247, 510

Semelin B., Combes F., Baek S., 2007, arXiv, 707, arXiv:0707.2483

Shapiro P. R., Giroux M. L., Babul A., 1994, ApJ, 427, 25
Shapiro P. R., Iliev I. T., Raga A. C., 2004, MNRAS, 348, 753
Sheth R. K., Mo H. J., Tormen G., 2001, MNRAS, 323, 1
Silk J., 1977, ApJ, 211, 638
Srbinovsky J. A., Wyithe J. S. B., 2007, MNRAS, 374, 627
Stanway E. R., Bunker A. J., McMahon R. G., 2003, MNRAS, 342, 439
Sunyaev R. A., Chluba J., 2008, ASPC, 395, 35
Sunyaev R. A., Zeldovich I. B., 1980, MNRAS, 190, 413
Susa H., Umemura M., 2004, ApJ, 600, 1
Susa H., 2006, PASJ, 58, 445
Tassis K., Abel T., Bryan G. L., Norman M. L., 2003, ApJ, 587, 13
Tegmark M., Silk J., Evrard A., 1993, ApJ, 417, 54
Tegmark M., Silk J., Rees M. J., Blanchard A., Abel T., Palla F., 1997, ApJ, 474, 1
Thoul A. A., Weinberg D. H., 1996, ApJ, 465, 608
Tittley E. R., Meiksin A., 2007, MNRAS, 380, 1369
Trac H., Cen R., 2007, ApJ, 671, 1
Trimble V., 1987, ARA&A, 25, 425
Tytler D., O'Meara J. M., Suzuki N., Lubin D., 2000, PhST, 85, 12
Valageas P., Silk J., 1999, A&A, 347, 1
Vishniac E. T., 1987, ApJ, 322, 597
Volonteri M., Rees M. J., 2005, ApJ, 633, 624
Volonteri M., Gnedin N., 2009, arXiv, arXiv:0905.0144
Wald, R. M., General Relativity, The University of Chicago Press (1984)
Whalen D., van Veelen B., O'Shea B. W., Norman M. L., 2008, ApJ, 682, 49
White S. D. M., Rees M. J., 1978, MNRAS, 183, 341
White S. D. M., Frenk C. S., 1991, ApJ, 379, 52
Wiersma R. P. C., Schaye J., Smith B. D., 2009, MNRAS, 393, 99
Wise J. H., Abel T., 2005, ApJ, 629, 615
Wise J. H., Cen R., 2009, ApJ, 693, 984
Woosley S. E., Heger A., Weaver T. A., 2002, RvMP, 74, 1015
Yepes G., 1997, ASPC, 126, 279
Yepes G., Kates R., Khokhlov A., Klypin A., 1997, MNRAS, 284, 235
Yoshida N., Abel T., Hernquist L., Sugiyama N., 2003, ApJ, 592, 645
Yüksel H., Kistler M. D., Beacom J. F., Hopkins A. M., 2008, ApJ, 683, L5
Zaldarriaga M., 1997, PhRvD, 55, 1822

> –Est-ce que vous l'avez déjà lu quelque part ? –Mais non, certainement. –Vraiment, jamais nulle part ? Alors monsieur, dit-il rembruni, c'est que cela n'est pas vrai. Si c'était vrai, quelqu'un l'aurait déjà pensé.
>
> Sartre, La nausée

CHAPTER 2

Keeping the Universe ionised: photo-heating and the clumping factor of the high-redshift intergalactic medium

Andreas H. Pawlik, Joop Schaye, & Eveline van Scherpenzeel

MNRAS 394 (2009), 1812

THE critical star formation rate density required to keep the intergalactic hydrogen ionised depends crucially on the average rate of recombinations in the intergalactic medium (IGM). This rate is proportional to the clumping factor $C \equiv \langle \rho_{\rm b}^2 \rangle_{\rm IGM} / \langle \rho_{\rm b} \rangle^2$, where $\rho_{\rm b}$ and $\langle \rho_{\rm b} \rangle$ are the local and cosmic mean baryon density, respectively and the brackets $\langle \rangle_{\rm IGM}$ indicate spatial averaging over the recombining gas in the IGM. We perform a suite of cosmological smoothed particle hydrodynamics simulations that include radiative cooling to calculate the volume-weighted clumping factor of the IGM at redshifts $z \geq 6$. We focus on the effect of photo-ionisation heating by a uniform ultra-violet background and find that photo-heating strongly reduces the clumping factor because the increased pressure support smoothes out small-scale density fluctuations. Because the reduction of the clumping factor makes it easier to keep the IGM ionised, photo-heating provides a positive feedback on reionisation. We demonstrate that this positive feedback is in fact very strong: even our most conservative estimate for the clumping factor ($C \approx 6$) is five times smaller than the clumping factor that is usually employed to determine the capacity of star-forming galaxies to keep the $z = 6$ IGM ionised. Our results imply that the observed population of star-forming galaxies at $z \approx 6$ may be sufficient to keep the IGM ionised, provided that the IGM was reheated at $z \gtrsim 9$ and that the fraction of ionising photons that escape the star-forming regions to ionise the IGM is larger than ≈ 0.2.

2.1 INTRODUCTION

The absence of a Gunn-Peterson trough in the observed absorption spectra towards high-redshift quasars suggests that the reionisation of intergalactic hydrogen was completed at a redshift $z \gtrsim 6$ (see Fan, Carilli,& Keating 2006 for a recent review) and that it remained highly ionised ever since. Current observational estimates of the ultra-violet (UV) luminosity density at redshifts $z \lesssim 6$ (e.g. Stanway, Bunker, & McMahon 2003; Lehnert & Bremer 2003; Bunker et al. 2004; Bouwens et al. 2004; Yan & Windhorst 2004; Sawicki & Thompson 2006; Bouwens et al. 2006; Mannucci et al. 2007; Oesch et al. 2008; Bouwens et al. 2008), on the other hand, may imply star formation rate (SFR) densities several times lower than the critical SFR density required to keep the intergalactic medium (IGM) ionised (but see, e.g., Stiavelli, Fall, & Panagia 2004; Malhotra et al. 2005; Panagia et al. 2005). Taken at face value, these low SFR densities pose a severe challenge to commonly employed theoretical models in which the observed population of star-forming galaxies is the only source of ionising radiation in the high-redshift Universe.

There are, however, large uncertainties associated with both the observationally inferred (see, e.g., the comprehensive analysis of Bouwens et al. 2007) and the critical SFR densities. The critical SFR density,

$$\begin{aligned}\dot{\rho}_* &\approx 0.027\ \mathrm{M}_\odot\ \mathrm{yr}^{-1}\ \mathrm{Mpc}^{-3} \\ &\times\ {f_{\mathrm{esc}}}^{-1}\left(\frac{C}{30}\right)\left(\frac{1+z}{7}\right)^3\left(\frac{\Omega_{\mathrm{b}} h_{70}^2}{0.0465}\right)^2, \end{aligned} \tag{2.1}$$

here rescaled to match the most recent WMAP estimate for the cosmic baryon density (Komatsu et al. 2008), has been derived by Madau, Haardt, & Rees (1999) using an early version of the Bruzual & Charlot (2003) population synthesis code, assuming a Salpeter initial stellar mass function (IMF) and solar metallicity.

The critical SFR is inversely proportional to the escape fraction f_{esc}, i.e. the fraction of ionising photons produced by star-forming galaxies that escape the interstellar medium (ISM) to ionise the IGM, and proportional to the average recombination rate in the IGM. The latter is parametrised using the dimensionless clumping factor $C \equiv \langle \rho_{\mathrm{b}}^2 \rangle_{\mathrm{IGM}} / \langle \rho_{\mathrm{b}} \rangle^2$, where ρ_{b} is the baryon density, $\langle \rho_{\mathrm{b}} \rangle$ is the mean baryon density of the Universe and the brackets $\langle\rangle_{\mathrm{IGM}}$ indicate spatial averaging over the gas constituting the recombining IGM. Under the assumption of a uniformly ionised IGM, the clumping factor expresses the spatially averaged number of recombinations occurring per unit time and unit volume in the ionised IGM, relative to that in gas at the cosmic mean density $\langle \rho_{\mathrm{b}} \rangle$. A larger escape fraction implies a smaller critical SFR density, as more photons are available to ionise the IGM. On the other hand, a larger clumping factor implies a larger critical SFR density since more ionising photons are required to compensate for the increased number of recombinations.

Most observational studies that compare[1] the SFR density derived from estimates of the UV luminosity density at redshift $z \approx 6$ to the critical SFR density assume an escape fraction $f_{\mathrm{esc}} \lesssim 0.5$ and a clumping factor $C = 30$. While a variety of both observational and theoretical studies (e.g. Inoue, Iwata, & Deharveng 2006 and references therein; Razoumov & Sommer-Larsen 2006; Gnedin, Kravtsov, & Chen 2008a) have ruled out larger escape fractions, the estimate for the clumping factor comes from a single cosmological simulation performed more than 10

---

[1] Note that although the critical SFR density is sensitive to the IMF, this comparison is insensitive to the IMF provided the same IMF is used to compute the critical and observationally derived SFR densities. This is because the UV luminosity density is dominated by the same massive stars that are responsible for the emission of ionising photons with energies > 13.6 eV (Madau, Haardt, & Rees 1999).

years ago (Gnedin & Ostriker 1997). It is on the basis of these values for the escape fraction and the clumping factor that the observed population of galaxies has been found to be incapable of keeping the intergalactic hydrogen ionised, forming massive stars at a rate which is up to an order of magnitude lower than required by Eq. 2.1.

It has been pointed out that this discrepancy between the inferred and critical SFR densities could be resolved if the employed clumping factor were too high (e.g. Sawicki & Thompson 2006; see also the discussion in Bouwens et al. 2007). Indeed, in most (but not all) of the more recent theoretical theoretical studies (e.g. Valageas & Silk 1999; Miralda-Escudé, Haehnelt, & Rees 2000; Gnedin 2000a; Haiman, Abel, & Madau 2001; Benson et al. 2001; Chiu, Fan, & Ostriker 2003; Iliev et al. 2007; Srbinovsky & Wyithe 2007; Kohler, Gnedin, & Hamilton 2007; Bolton & Haehnelt 2007; Maio et al. 2007; Furlanetto, Haiman, & Oh 2008) significantly lower clumping factors were derived. On the other hand, it is sometimes emphasised that simulations underestimate the clumping factor, due to a lack of resolution (see, e.g., Madau, Haardt, & Rees 1999). In this work we perform a set of cosmological Smoothed Particle Hydrodynamics (SPH) simulations that include radiative cooling and photo-ionisation by a uniform UV background in the optically thin limit to study the clumping factor of the IGM.

We focus on the effect of photo-ionisation heating on the evolution of the clumping factor. Previous investigations of the impact of photo-heating on the reionisation of the IGM have almost exclusively come to the conclusion that it acts as to provide a negative feedback. Photo-heating boils the gas out of the potential wells of dark matter (DM) halos with virial temperatures $T_{\rm vir} \lesssim 10^4$ K (e.g. Thoul & Weinberg 1996; Navarro & Steinmetz 1997; Barkana & Loeb 1999; Kitayama & Ikeuchi 2000; Gnedin 2000b; Dijkstra et al. 2004; Shapiro, Iliev, & Raga 2004; Hoeft et al. 2006; Crain et al. 2007; Mesinger & Dijkstra 2008; Okamoto, Gao, & Theuns 2008; Pawlik & Schaye 2009b). This inhibits the formation of stars in these low-mass halos and thus decreases the ionising emissivity, which makes it more difficult to reionise the Universe. The same mechanism that reduces the number of ionising photons that are emitted into the IGM does, however, also affect the evolution of the clumping factor (e.g. Haiman, Abel, & Madau 2001; Oh & Haiman 2003; Kuhlen & Madau 2005; Wise & Abel 2005; Furlanetto, Oh, & Briggs 2006; Ciardi & Salvaterra 2007).

In this chapter we demonstrate that photo-heating significantly lowers the clumping factor and hence the average recombination rate in the IGM. While photo-ionisation heating undoubtedly impedes the production of ionising photons, our results imply that it also makes it much easier to keep the IGM ionised. By comparing our estimate of the critical SFR with observationally inferred SFRs we argue that the observed population of UV galaxies may well be capable of keeping the Universe at redshift $z \approx 6$ ionised.

Note that the critical SFR results from simply equating the spatially averaged rate at which ionising photons are emitted into the IGM to the spatially averaged rate at which the intergalactic gas recombines. Eq. 2.1 is therefore incapable of capturing a number of potentially important physical effects. Some ionising photons will, for instance, redshift below the ionisation threshold before ionising and some ionising photons will have been emitted longer than a recombination time ago upon impact with a neutral atom, so that equating instantaneous rates is not appropriate and one even may have to take source evolution into account. It is therefore important to keep in mind that Eq. 2.1 is likely only accurate within factors of a few. We will discuss other uncertainties associated with our work in Section 2.4.

The chapter is structured as follows. In Section 2.2 we give a detailed description of our set of simulations. In Section 2.3 we use our simulations to compute the clumping factor of the IGM. Finally, in Section 2.4, we discuss our results and their implications.

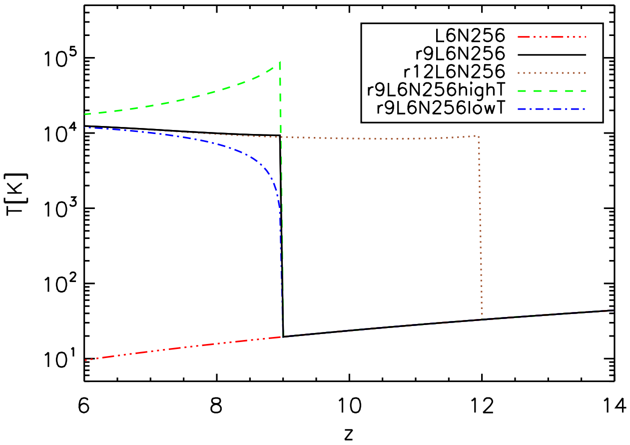

Figure 2.1: Thermal evolution of gas with overdensity $\Delta = 1$ for characteristic choices of the reheating parameters z_r and ϵ_r, which are listed in Table 2.1 for the simulations indicated in the legend. Note that even in the absence of an additional energy input at redshift $z = z_\mathrm{r}$, i.e. for $\epsilon_\mathrm{r} = 0$, as it is the case for simulation *r9L6N256lowT*, the gas is quickly heated by the UV background to a temperature $T \sim 10^4$ K.

2.2 SIMULATIONS

We use a modified version of the N-body/TreePM/SPH code GADGET-2 (Springel 2005) to perform a suite of cosmological SPH simulations including radiative cooling.

The initial particle positions and velocities are obtained from glass-like initial conditions using CMBFAST (version 4.1; Seljak & Zaldarriaga 1996) and employing the Zeldovich approximation to linearly evolve the particles down to redshift z = 127. We assume a flat ΛCDM universe and employ the set of cosmological parameters $[\Omega_\mathrm{m}, \Omega_\mathrm{b}, \Omega_\Lambda, \sigma_8, n_\mathrm{s}, h]$ given by [0.258, 0.0441, 0.742, 0.796, 0.963, 0.719], in agreement with the WMAP 5-year observations (Komatsu et al. 2008). For comparison, we also perform some simulations employing the set of cosmological parameters [0.238, 0.0418, 0.762, 0.74, 0.951, 0.73] and [0.25, 0.045, 0.75, 0.9, 1, 0.73], consistent with WMAP 3-year (Spergel et al. 2007) and WMAP 1-year (Spergel et al. 2003) observations, respectively. Data is generated at 50 equally spaced redshifts between $z = 20$ and $z = 6$. The parameters of the simulations employed for the present work are summarised in Table 2.1.

The gravitational forces are softened over a length of $1/25$ of the mean dark matter interparticle distance. We employ the star formation recipe of Schaye & Dalla Vecchia (2008), to which we refer the reader for details. Briefly, gas with densities exceeding the critical density for the onset of the thermo-gravitational instability (hydrogen number densities $n_\mathrm{H} = 10^{-2} - 10^{-1}$ cm^{-3}) is expected to be multiphase and star-forming (Schaye 2004). We therefore impose an effective equation of state (EoS) with pressure $P \propto \rho^{\gamma_\mathrm{eff}}$ for densities $n_\mathrm{H} > n_\mathrm{H}^*$, where $n_\mathrm{H}^* \equiv 10^{-1}$ cm^{-3}, normalised to $P/k = 10^3$ cm^{-3} K at the critical density n_H^*. We use $\gamma_\mathrm{eff} = 4/3$ for which both the Jeans mass and the ratio of the Jeans length and the SPH kernel are independent of the density, thus preventing spurious fragmentation due to a lack of numerical resolution. Gas on the effective EoS is allowed to form stars using a pressure-dependent rate that reproduces the observed Kennicutt-Schmidt law (Kennicutt 1998), renormalised by a factor[2] of $1/1.65$ to account for the fact that it assumes a Salpeter IMF whereas we are using a Chabrier IMF.

---

[2] This conversion factor between SFRs has been computed using the Bruzual & Charlot (2003) population synthesis code for model galaxies of age $> 10^7$ yr forming stars at a constant rate and is insensitive to the assumed metallicity.

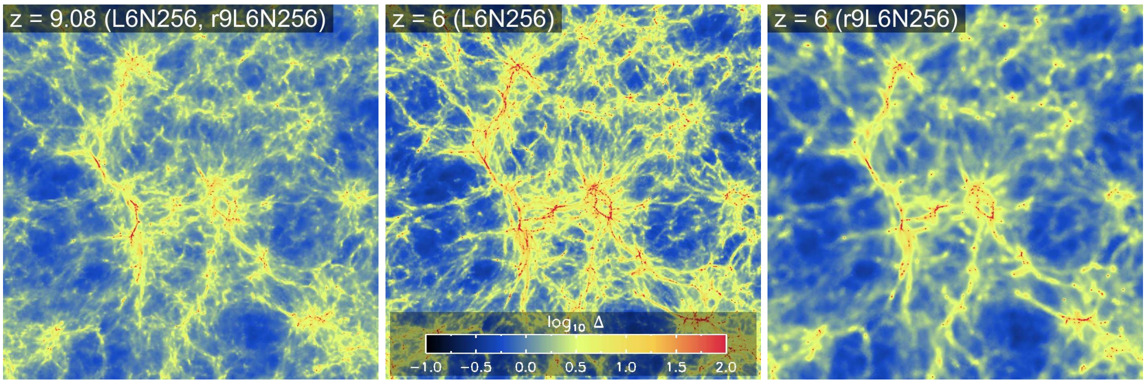

Figure 2.2: Slices (of thickness $1.25\ h^{-1}$ comoving Mpc) through the centre of the simulation box, showing the SPH overdensity field in the simulations *L6N256* and *r9L6N256* at redshifts $z = 9.08$ (left-hand panel; where they are identical) and $z = 6$ (middle panel: *L6N256*, right-hand panel: *r9L6N256*). The inclusion of photo-heating in *r9L6N256* leads to a strong smoothing of the density field (right-hand panel). *See Fig. 2 in the appendix at the end of this thesis for a coloured version.*

The gas is of primordial composition, with a hydrogen mass fraction $X = 0.752$ and a helium mass fraction $Y = 1 - X$. Radiative cooling and heating are included assuming ionisation equilibrium, using tables generated with the publicly available package CLOUDY (version 05.07 of the code last described by Ferland et al. 1998), as described in Wiersma, Schaye & Smith (2008). The gas is allowed to cool by collisional ionisation and excitation, emission of free-free and recombination radiation and Compton cooling off the cosmic microwave background.

We perform a set of simulations including photo-ionisation by a uniform UV background in the optically thin limit at redshifts below the reheating redshift $z_{\rm r}$. These simulations are denoted with the prefix *r* (see Table 2.1). To study the effect of reionisation reheating, we compare these simulations to a simulation that does not include photo-ionisation (*L6N256*). Note that the photo-ionisation changes the density of free electrons and the ionic abundances. Both the cooling and heating rates are therefore affected by the inclusion of a UV background (e.g. Efstathiou 1992; Wiersma, Schaye & Smith 2008).

The properties of the UV background depend on the redshift of reheating. If $z_{\rm r} \leq 9$, we employ the evolving UV background from quasars and galaxies tabulated by Haardt & Madau (2001) for $z \leq z_{\rm r}$. If $z_{\rm r} > 9$, we use the $z = 9$ Haardt & Madau (2001) UV background for all redshifts $9 < z \leq z_{\rm r}$, and employ the evolving Haardt & Madau (2001) UV background for redshifts $z \leq 9$. This is necessary because Haardt & Madau (2001) only tabulate up to $z = 9$. For $z > z_{\rm r}$, we employ the $z = 9$ Haardt & Madau (2001) UV background but with its intensity at energies equal to and larger than 13.6 eV set to zero. Molecular hydrogen and deuterium and their catalysts are kept photo-dissociated by this soft UV background at all redshifts and therefore never contribute to the cooling rate. Our approach is motivated in the context of reionisation because the weak UV background established by the very first ionising sources is already sufficient to efficiently suppress the formation of molecular hydrogen (e.g. Haiman, Rees, & Loeb 1997 and references therein; Glover 2007; Chuzhoy, Kuhlen, & Shapiro 2007).

The reheating redshift $z_{\rm r}$ is a parameter in our simulations. The most recent determination of the Thomson optical depth towards reionisation from the WMAP (5-year) experiment implies a reionisation redshift $z_{\rm reion} = 11.0 \pm 1.4$, assuming that the transition from the neutral to the fully ionised Universe was instantaneous (Komatsu et al. 2008). The Thomson optical depth towards reionisation provides, however, only an integral constraint on the Epoch of Reionisation. The reionisation history may therefore have been considerably more intricate. An early population of X-ray sources, for example, could reheat the IGM to temperatures $\sim 10^4$ K already at much higher redshifts (e.g. Collin-Souffrin 1991; Madau & Efstathiou 1999; Oh 2001; Venkatesan, Giroux, & Shull 2001; Machacek, Bryan, & Abel 2003; Madau et al. 2004; Ricotti & Ostriker 2004). We therefore study a range of thermal histories, performing simulations using $z_{\rm r} = 7.5, 9, 10.5, 12, 13.5, 15$ and 19.5. To be conservative, we use the relatively low reheating redshift $z_{\rm r} = 9$ as our default value.

In our simulations we compute the photo-heating rates in the optically thin limit, which means that we underestimate the temperature of the IGM during reionisation (e.g. Abel & Haehnelt 1999). We therefore inject an additional thermal energy $\epsilon_{\rm r}$ per proton at $z = z_{\rm r}$ (see, e.g., Thoul & Weinberg 1996). By varying the parameter $\epsilon_{\rm r}$, we will investigate the sensitivity of our results to the temperature of the reheated IGM. Our default simulation employs $\epsilon_{\rm r} = 2$ eV. Fig. 2.1 shows the thermal evolution of gas at the cosmic mean baryon density $\langle\rho_{\rm b}\rangle$, i.e. of gas with overdensity $\Delta \equiv \rho_{\rm b}/\langle\rho_{\rm b}\rangle = 1$, for different values of $\epsilon_{\rm r}$ and $z_{\rm r}$. At $z = z_{\rm r}$, the gas is heated to $T_{\rm r} \approx 10^4$ K for $\epsilon_{\rm r} = 2$ eV, whereas the gas temperature is about an order of magnitude higher (lower) for $\epsilon_{\rm r} = 20$ eV ($\epsilon_{\rm r} = 0$ eV). After reheating the gas quickly looses memory of its initial temperature and by $z = 6$ the gas temperature is $T \approx 10^4$ K in all cases.

In one of our simulations (*r9L6N256winds*) we include kinetic feedback from star formation. We employ the prescription of Dalla Vecchia & Schaye (2008), which is a variation of the Springel & Hernquist (2003) recipe for kinetic feedback. In this prescription, core-collapse supernovae locally inject kinetic energy and kick gas particles into winds. The feedback is specified by two parameters, the mass loading $\eta \equiv \dot{M}_{\rm w}/\dot{M}_*$, which describes the initial wind mass loading $\dot{M}_{\rm w}$ in units of the cosmic SFR $\dot{M}_*$, and the initial wind velocity $v_{\rm w}$. We use $\eta = 2$ and $v_{\rm w} = 600$ km s^{-1}, consistent with observations of local (e.g. Veilleux, Cecil, & Bland-Hawthorn 2005) and redshift $z \approx 3$ (Shapley et al. 2003) starburst galaxies. Note that wind particles are not hydrodynamically decoupled and that they are launched local to the star formation event, different from the Springel & Hernquist (2003) recipe.

2.3 RESULTS

In this section we employ the set of simulations described in Section 2.2 and summarised in Table 2.1 to calculate the clumping factor of the IGM. We start in Section 2.3.1 with analysing the distribution of the gas in our default simulation *r9L6N256* and in the simulation *L6N256*, which is identical to our default simulation except for the fact that it does not include a photo-ionising background. In Section 2.3.2 we discuss the definition of the clumping factor and compare the clumping factors derived from our default simulation *r9L6N256* to that derived from simulation *L6N256*. We discuss the convergence of our results with respect to variations in the mass resolution and in the size of the simulation box in Section 2.3.2. In Section 2.3.2 we vary the redshift at which the ionising UV background is turned on and in Section 2.3.2 we demonstrate that our conclusions are robust with respect to our choice for the temperature to which the IGM is photo-heated. In Section 2.3.2 we discuss how kinetic feedback from supernova winds affects our results and quote the clumping factors obtained from the simulations employing WMAP 3-year and 1-year cosmological parameters. We conclude with a brief comparison to previous work.

Table 2.1: Simulation parameters: comoving size of the simulation box, $L_{\rm box}$ (default value: $6.25\ h^{-1}$ Mpc); number of DM particles, $N_{\rm dm}$ (default value: 256^3); mass of dark matter particles, $m_{\rm dm}$ (default value: $8.6 \times 10^5\ h^{-1}\ {\rm M}_\odot$); additional reheating energy per proton, $\epsilon_{\rm r}$ (default value: 2 eV); reheating redshift, $z_{\rm r}$ (default value: 9); kinetic feedback from supernova winds, winds (default: no); cosmological parameters, WMAP (default: 5-year). The number of SPH particles initially equals $N_{\rm dm}$ (it decreases during the simulation due to star formation). Bold font indicates our default simulation.

Simulation	$L_{\rm box}$ [h^{-1} comoving Mpc]	$N_{\rm dm}$	$m_{\rm dm}$ [$10^5\ h^{-1}\ {\rm M}_\odot$]	$\epsilon_{\rm r}$ [eV]	$z_{\rm r}$	winds	WMAP year
r9L6N256	**6.25**	$\mathbf{256^3}$	**8.6**	**2**	**9**	**no**	**5**
L6N256	6.25	256^3	8.6	0	0	no	5
r[$z_{\rm r}$]L6N256	6.25	256^3	8.6	2	$[7.5, 10.5, 12, 13.5, 15, 19.5]$	no	5
r9L6N256highT	6.25	256^3	8.6	20	9	no	5
r9L6N256lowT	6.25	256^3	8.6	0	9	no	5
r9L6N256winds	6.25	256^3	8.6	2	9	yes	5
r9L6N256W1	6.25	256^3	8.3	2	9	no	1
r9L6N256W3	6.25	256^3	7.9	2	9	no	3
r9L12N256	12.5	256^3	69.1	2	9	no	5
r9L6N128	6.25	128^3	69.1	2	9	no	5
r9L6N064	6.25	64^3	552.8	2	9	no	5
r9L3N064	3.125	64^3	69.1	2	9	no	5

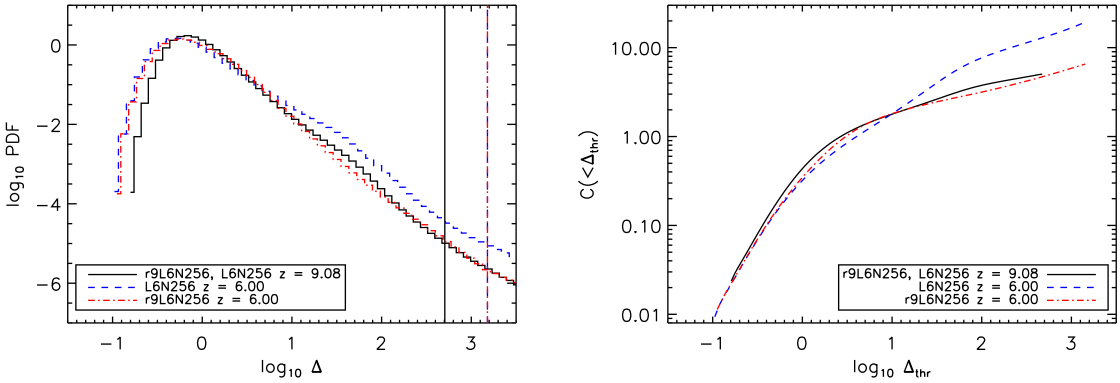

Figure 2.3: *Left-hand panel:* Volume-weighted PDF of the baryon overdensity Δ per unit $\log_{10}\Delta$ for simulations *r9L6N256* and *L6N256* at redshifts $z = 9.08$ and $z = 6$, as indicated in the legend. Photo-heating destroys the bump around overdensities $1 \lesssim \log_{10}\Delta \lesssim 2$, which mark the gas that accretes onto DM halos. The vertical lines (which match the colour and style of the corresponding PDFs) indicate the overdensities corresponding to the onset of star formation. *Right-hand panel:* Clumping factor $C(<\Delta_{\rm thr})$ of gas with overdensity $\Delta < \Delta_{\rm thr}$ for the simulations shown in the left-hand panel. The inclusion of photo-heating in *r9L6N256* leads to a clumping factor that is substantially smaller than that obtained from *L6N256*, for threshold overdensities $\Delta_{\rm thr} > 10$. Note that the maximum threshold overdensities we consider for the calculation of the clumping factor are given by the critical density $n_{\rm H}^* \equiv 10^{-1}$ cm^{-3} for the onset of star-formation (the vertical lines shown in the left-hand panel).

2.3.1 The gas density distribution

Here we compare the gas distributions in our default simulation *r9L6N256* (in which the UV background is turned on at redshift $z_{\rm r} = 9$) and in the simulation *L6N256* (which does not include photo-ionisation heating).

Figure 2.2 shows the overdensities at redshifts $z = 9.08$ and $z = 6$ in a slice through the simulation box for these simulations. Heating by the photo-ionising background almost instantaneously increases the gas temperatures to $T_{\rm r} \sim 10^4$ K (see Fig. 2.1) and accordingly raises the cosmological Jeans mass. Gas that had already settled into the potential wells of DM halos with virial temperature $T_{\rm vir} \lesssim T_{\rm r}$ is driven back into the diffuse IGM by the increased pressure gradient forces (e.g. Barkana & Loeb 1999; Shapiro, Iliev, & Raga 2004). The large cosmological Jeans mass prevents any re-accretion of gas or infall of previously unbound gaseous material into these low-mass halos and keeps the IGM diffuse. Comparing the middle panel with the right-hand panel of Fig. 2.2, this *Jeans filtering* (e.g. Shapiro, Giroux, & Babul 1994; Gnedin & Hui 1998; Gnedin 2000b; Okamoto, Gao, & Theuns 2008) in the presence of photo-heating leads to a strong smoothing of the small-scale density fluctuations by $z = 6$.

A detailed analysis of the overdensity distribution in the simulations can be obtained by studying $\mathcal{P}_{\rm V}(\Delta)$, the volume-weighted probability density function (PDF) for Δ. We show the PDF (per unit $\log_{10}\Delta$ and normalised according to $\int_0^\infty d\Delta\, \mathcal{P}_{\rm V}(\Delta) = 1$) in the left-hand panel of Fig. 2.3. It is important to be aware of the fact that the finite numerical resolution of our simulations implies an unavoidable intrinsic smoothing of the gas density distribution on the scale of the SPH kernel or the scale over which the gravitational forces are softened, whichever is larger. A numerical smoothing on scales larger than the Jeans filtering scale (below which the gas density distribution is physically smoothed) would prevent us from obtaining converged results.

We will discuss the convergence of our simulations with respect to resolution in Section 2.3.2.

At redshift $z = 9.08$ (black solid histogram), the gravitational amplification of the overdensities present in the initial conditions has produced a significant deviation of the PDF from its primordial Gaussian shape. The flattening of the slope of the PDF for overdensities $1 \lesssim \log_{10} \Delta \lesssim 2$ can be attributed to the shock-heating of gas falling into the potential wells of dark matter halos, most of which have virial temperatures $\lesssim 10^4$ K, which we refer to as low-mass halos. The shape of the PDF is determined by the effective EoS once the gas reaches the critical density for the onset of star formation ($n_{\rm H}^* \equiv 10^{-1}$ cm^{-3}, see Section 2.2; indicated by the vertical lines).

At redshifts $z < z_{\rm r}$, the shape of the PDF strongly depends on whether photo-heating by the ionising background is included or not. In the absence of such a background (*L6N256*, blue dashed histogram), gravitational collapse proceeds unimpeded, increasing the PDF at $\log_{10} \Delta \gtrsim 1$. Since the gas that accretes onto DM halos must originate from the reservoir at $\log_{10} \Delta \lesssim 1$ (the diffuse IGM), the PDF decreases over this range of overdensities. As a result, the maximum of the PDF shifts to lower overdensities. At the same time, the gravitational amplification of large-scale underdense regions leads to an increase in the PDF around overdensities $\log_{10} \Delta \sim -1$.

Photo-heating in the presence of the ionising background photo-evaporates the gas in DM halos, as described above. The bump in the PDF around $1 \lesssim \log_{10} \Delta \lesssim 2$ therefore disappears (red dot-dashed histogram). Note that the redistribution of the baryons due to photo-heating also slightly increases the minimum overdensity that is present in the simulation. In Appendix 2.A.2 we compare the PDF obtained from our default simulation to the fit provided by Miralda-Escudé, Haehnelt, & Rees (2000), which is often employed to compute the clumping factor in (semi-)analytical studies of the epoch of reionisation.

2.3.2 The clumping factor

In this section we demonstrate how the clumping factor, $C \equiv \langle \rho_{\rm b}^2 \rangle_{\rm IGM} / \langle \rho_{\rm b} \rangle^2$, depends on the definition of the IGM and compute it for our default simulation *r9L6N256* and for the simulation *L6N256*. This allows us to investigate how the clumping factor is affected by the inclusion of a photo-ionising background.

Our main motivation for computing the clumping factor of the IGM is to evaluate the critical SFR density required to keep the IGM ionised. The critical SFR density describes the balance between the number of ionising photons escaping into the IGM (parametrised by the escape fraction) and the number of ionising photons that are removed from the IGM due to photo-ionisations of recombining hydrogen ions (parametrised by the clumping factor). When the ratio of photon escape rate to recombination rate is larger than unity, the rate at which galaxies form stars exceeds the critical SFR density and is thus sufficient to keep the IGM ionised.

It is important to realise that only recombinations leading to the removal of ionising photons *which escaped the ISM of the star-forming regions* contribute to the balance that gives rise to the definition of the critical SFR density. To separate the gas in the ISM from the gas in the IGM, a simple threshold density criterion is often employed (e.g. Miralda-Escudé, Haehnelt, & Rees 2000; see also the discussion in Miralda-Escudé 2003). Ionising photons are counted as escaped once they enter regions with gas densities $\rho_{\rm b} < \rho_{\rm thr}$. Consequently, only gas with densities $\rho_{\rm b} < \rho_{\rm thr}$, or equivalently, gas with overdensities $\Delta < \Delta_{\rm thr} \equiv \rho_{\rm thr} / \langle \rho_{\rm b} \rangle$ should be considered in the evaluation of the clumping factor.

The threshold density $\rho_{\rm thr}$ depends on which gas is considered to be part of the ISM, and which gas is considered to be part of the IGM. As long as the definition of the escape fraction and that of the clumping factor refer to the same decomposition of the gas into IGM and ISM, its value can be chosen arbitrarily. We therefore treat the threshold density as a parameter and compute the clumping factor as a function of $\Delta_{\rm thr}$ (cp. Miralda-Escudé, Haehnelt, & Rees 2000),

$$C(<\Delta_{\rm thr}) \equiv \int_0^{\Delta_{\rm thr}} d\Delta\ \Delta^2\ \mathcal{P}_{\rm V}(\Delta), \tag{2.2}$$

where $\mathcal{P}_{\rm V}(\Delta)$ is normalised according to $\int_0^{\Delta_{\rm thr}} d\Delta\ \mathcal{P}_{\rm V}(\Delta) = 1$. In practice, we calculate $C(<\Delta_{\rm thr})$ by performing a volume-weighted summation over all SPH particles with overdensities $\Delta_i < \Delta_{\rm thr}$, i.e

$$C(<\Delta_{\rm thr}) = \frac{\sum_{\Delta_i<\Delta_{\rm thr}} h_i^3 \Delta_i^2}{\sum_{\Delta_i<\Delta_{\rm thr}} h_i^3}, \tag{2.3}$$

where h_i is the radius of the SPH smoothing kernel associated with SPH particle i. We verified that replacing h_i^3 with m_i/ρ_i as an estimate for the volume occupied by SPH particle i (with mass m_i) gives nearly indistinguishable results.

By definition, $C(<\Delta_{\rm thr})$ increases monotonically with the threshold density $\rho_{\rm thr}$. Here, we set an upper limit to $\Delta_{\rm thr}$, corresponding to the threshold density $n_{\rm H}^* \equiv 10^{-1}\ {\rm cm}^{-3}$ for the onset of star formation that we employ in our simulations. Since we impose an effective EoS for gas with densities larger than $n_{\rm H}^*$ (Section 2.2), its PDF is not expected to reflect the PDF of real star-forming regions, motivating our choice for the maximum threshold density. The choice is conservative, leading to an overestimate rather than an underestimate of the critical SFR density, since the threshold density marking the escape of ionising photons and hence the clumping factor of the IGM to be used in Eq. 2.1 is likely to be lower (see, e.g., the discussion in Gnedin 2008b).

In the right-hand panel of Fig. 2.3 we show $C(<\Delta_{\rm thr})$ for the simulations *r9L6N256* and *L6N256* at redshifts shortly before (at $z = 9.08$, when *r9L6N256* and *L6N256* are identical) and well after (at $z = 6$, when they differ by the presence and absence of an ionising background, respectively) the reheating redshift $z_{\rm r} = 9$. In agreement with our discussion above, the clumping factor increases monotonically with the threshold density. Its dependence on redshift can be understood by looking at the evolution of the shape of the PDF, which we discussed in the previous section.

For *L6N256*, i.e. in the absence of photo-heating, the clumping factor for threshold overdensities $\log_{10}\Delta_{\rm thr} > 1$ is larger at $z = 6$ than at $z = 9.08$, due mainly to the growth of the bump present in the PDF for overdensities $1 \lesssim \log_{10}\Delta \lesssim 2$. For $\log_{10}\Delta_{\rm thr} \sim 0$, on the other hand, the clumping factor is slightly smaller at $z = 6$ than at $z = 9.08$, which is caused by the depletion of the diffuse IGM through accretion onto DM halos. Note that at $z = 6$ the clumping factor reaches a maximum value of $C \approx 20$, which is significantly smaller than the value quoted by Gnedin & Ostriker (1997), which is commonly employed in observational studies. This is probably because Gnedin & Ostriker (1997) computed the clumping factor including gas of any density, i.e. using a density threshold implicitly set by the maximum overdensity resolved in their simulation.

The evolution of the clumping factor in *r9L6N256*, i.e. in the presence of the ionising background, is very different. At $z = 6$ it is close to that at $z = 9.08$ for all threshold overdensities. Compared to *L6N256*, the difference between the clumping factors for $z = 6$ and $z = 9.08$ is greatly reduced and the clumping factor at redshift $z = 6$ never reaches values larger than $C \approx 6$.

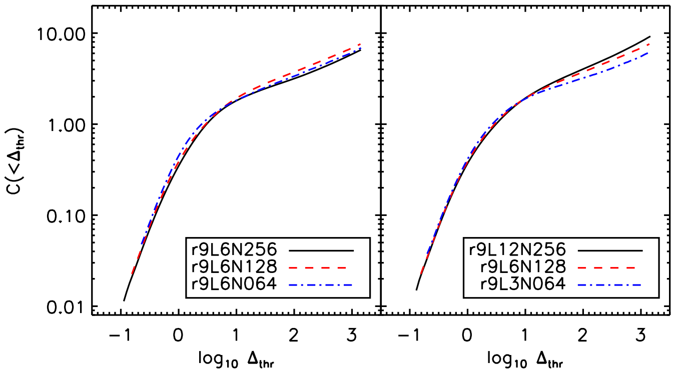

Figure 2.4: Clumping factor $C(<\Delta_{\rm thr})$ of gas with overdensities $\Delta < \Delta_{\rm thr}$ and its dependence on resolution (at fixed box size, left-hand panel) and on box size (at fixed resolution, right-hand panel). The clumping factor obtained from our default simulation *r9L6N256* is converged with respect to the employed resolution for all threshold overdensities shown. With respect to the size of the simulation box, it is converged for threshold overdensities $\log_{10}\Delta_{\rm thr} \lesssim 2$. For larger threshold overdensities, full convergence may require the use of simulation boxes even larger than $12.5\,h^{-1}$ comoving Mpc, the size of the largest box employed here.

Convergence tests

In this section we check whether our results are converged. Generally, one expects the clumping factor to increase with both the spatial resolution and the size of the simulation box. The spatial resolution determines the smallest scale on which fluctuations in the density field may be identified, whereas the size of the simulation box sets a cut-off to the largest scale on which the overdensity field can be non-zero. Moreover, the size of the simulation box limits the mass of the largest halo present in the simulation. Fig. 2.4 demonstrates that our default simulation (*r9L6N256*) is of sufficiently high resolution and employs a sufficiently large box to allow a faithful computation of the clumping factor of the reheated IGM at $z = 6$. In the left-hand panel we show the clumping factor in three simulations that use the same box size, but have mass resolutions that differ by multiples of 2^3, whereas in the right-hand panel we show the clumping factor in three simulations that employ the same resolution, but have box sizes that differ by multiples of 2.

When compared to our default simulation *r9L6N256*, decreasing the mass resolution by factors of 8 (*r9L6N128*) and 64 (*r9L6N064*) only leads to insignificant and unsystematic[3] changes in the clumping factor (left-hand panel). This can be understood by noting that the virial mass of halos corresponding to a virial temperature $T_{\rm vir} = T_{\rm r}$ is resolved with $\gtrsim 100$ particles for redshifts $z < 9$. Any further increase in resolution would therefore mostly affect the abundance of DM halos with $T_{\rm vir} \ll T_{\rm r}$. In the presence of the UV background the gas in these halos is, however, quickly photo-evaporated (if formed at $z > z_{\rm r}$) or prevented from accreting by the large Jeans mass associated with the photo-heated gas (for $z < z_{\rm r}$). At redshifts well below the reheating redshift $z_{\rm r}$, i.e. when sufficient time has passed to accomplish the photo-evaporation of halos and to allow the gas to respond hydrodynamically to the jump in the Jeans mass (i.e. to Jeans-filter the IGM), the observed convergence with respect to mass resolution is therefore expected[4].

---

[3] Note that the clumping factor is even slightly larger in *r9L6N128* than in *r9L6N256*, although the latter has an 8 times higher mass resolution.

[4] We note that in the absence of a photo-ionising background, convergence may be more difficult to achieve, requiring a higher mass resolution than employed here. Convergence will be easier to achieve for lower threshold

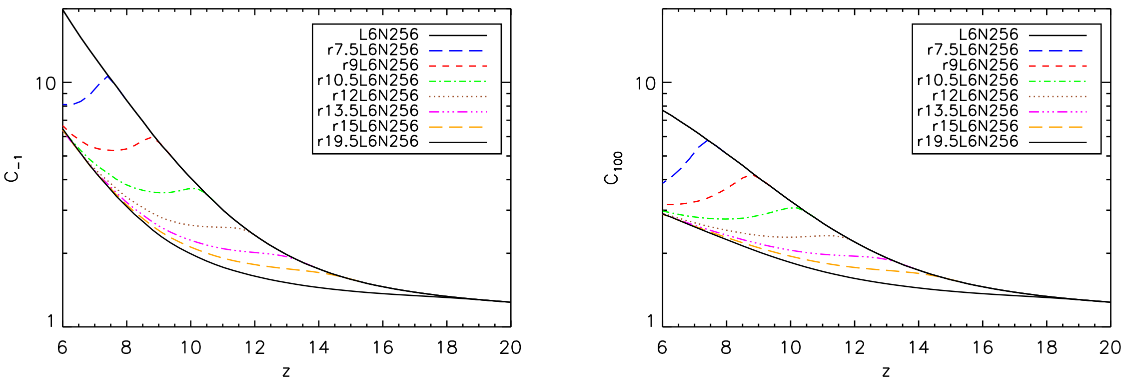

Figure 2.5: Evolution of the clumping factors C_{-1} (left-hand panel) and C_{100} (right-hand panel) for different reheating redshifts $z_{\rm r}$, as indicated in the legends. Note that $C_{-1}(z)$ and $C_{100}(z)$ in all reheating simulations evolve towards the clumping factors obtained in the simulation with reheating at $z_{\rm r} = 19.5$ (bottom black solid curves). At $z = 6$, the clumping factors are therefore insensitive to the reheating redshift provided that $z_{\rm r} \gtrsim 9$, with $C_{-1}(z = 6) \approx 6$ and $C_{100}(z = 6) \approx 3$. Fits to the evolution of the clumping factors are given in Appendix 2.A.1.

Since the clumping factor has already converged for the spatial resolution used in simulation *r9L6N128*, we can employ this simulation to verify whether the size of the box of our default simulation *r9L6N256* is sufficiently large to enable an unbiased estimate of the clumping factor (right-hand panel). Overall, increasing the box size (at fixed resolution) from $6.25\ h^{-1}$ comoving Mpc by a factor of two to $12.5\ h^{-1}$ comoving Mpc leaves the clumping factor almost unaffected. For threshold densities $\log_{10}\Delta_{\rm thr} \gtrsim 2$ the clumping factor may, however, not yet have fully converged, indicating that even larger simulation boxes than that considered here may be required for its computation (see also the discussion in Barkana & Loeb 2004).

Varying the reheating redshift

To study the effect of photo-heating on the evolution of the clumping factor in more detail, we make use of the clumping factors

$$C_{-1} \equiv C(< 10^{-1}\ {\rm cm}^{-3} m_{\rm H}/(X\langle\rho_{\rm b}\rangle)) \qquad (2.4)$$

and

$$C_{100} \equiv C(< \min(100, 10^{-1}\ {\rm cm}^{-3} m_{\rm H}/(X\langle\rho_{\rm b}\rangle))). \qquad (2.5)$$

C_{-1} is the clumping factor for gas with densities below $n_{\rm H} = n_{\rm H}^* \equiv 10^{-1}\ {\rm cm}^{-3}$, the maximum threshold density we consider. For redshifts $z < 16.3$, C_{100} fixes the threshold overdensity to a value between the mean overdensity of spherical top-hat DM halos, ($\approx 18\pi^2$; e.g. Padmanabhan 1993) and the overdensity at the virial radius of an isothermal DM halo (≈ 60; Lacey & Cole 1994) and closely agrees with the threshold densities commonly employed in the literature to calculate the clumping factor of the IGM. For larger redshifts, the threshold overdensity $\Delta_{\rm thr} = 100$ corresponds to a density $n_{\rm H} > n_{\rm H}^* \equiv 10^{-1}\ {\rm cm}^{-3}$, which is larger than the critical density for the onset of star formation in our simulations. The definition Eq. 2.5 ensures that

---

densities.

the maximum density that we consider for the computation of C_{100} is always smaller than $n_{\rm H}^{*}$. Note that C_{-1} refers to the clumping factor of gas with densities below a fixed proper density, while C_{100} refers to the clumping factor of gas with densities below a fixed overdensity for redshifts $z < 16.3$ and is identical to C_{-1} for larger redshifts.

The evolution of C_{-1} and C_{100} is shown, respectively, in the left-hand and right-hand panels of Fig. 2.5 for the simulations *r9L6N256* (i.e. reheating at redshift $z_{\rm r} = 9$) and *L6N256* (i.e. no reheating). In the same figure we also include the evolution of C_{-1} and C_{100} obtained from the set of simulations *r[*$z_{\rm r}$*]L6N256*, where $z_{\rm r} = 7.5, 10.5, 12, 13.5, 15$ and 19.5. While the simulations are identical for $z > z_{\rm r}$, the ionising background strongly affects the evolution of $C_{-1}(z)$ and $C_{100}(z)$ for $z < z_{\rm r}$. Whereas in *L6N256* the clumping factors reach $C_{-1} \approx 20$ and $C_{100} \approx 8$ at $z = 6$, they only reach $C_{-1} \approx 6$ and $C_{100} \approx 3$ in *r9L6N256*, which are smaller than in *L6N256* by roughly a factor of three. Note that because the clumping factor obtained from simulation *L6N256* is likely to be not fully converged with respect to resolution (see footnote 4), we may even have underestimated the magnitude of the decrease in the clumping factor due to photo-heating.

Interestingly, the clumping factor at $z = 6$ is insensitive to the redshift $z_{\rm r}$ at which the UV background is turned on, as long as $z_{\rm r} \gtrsim 9$. This is because, after an initial transitory phase, the evolution of the clumping factor obtained for reheating at redshift $z_{\rm r}$ approaches that obtained for reheating at $z_{\rm r} = 19.5$. Note that the difference between the clumping factors obtained from *r[*$z_{\rm r}$*]L6N256* and *r19.5L6N256* becomes smaller with increasing reheating redshift $z_{\rm r}$. In particular, the clumping factors obtained for reheating at $z_{\rm r} = 15$ are nearly identical to those obtained for reheating at $z_{\rm r} = 19.5$ at all redshifts. The evolution of the clumping factors obtained from *r19.5L6N256* can therefore be considered to reflect the evolution of the clumping factor in the limit of reheating at very high redshift, $z_{\rm r} \gg 19.5$.

In Appendix 2.A.1 we provide fits to the evolution of the clumping factor over the redshift range $6 \leq z \leq 20$ for a range of (over-)density thresholds and reheating redshifts. These fits (Eqs. 2.7 and 2.8) may be employed in (semi-)analytic models of the epoch of reionisation. Many such models assume that reionisation heating provides only a negative feedback on the reionisation process, reducing the star formation rate due to the photo-evaporation of gas in low-mass halos. However, as we have shown here, photo-heating decreases the clumping factor, and hence the average recombination rate. Since this makes it easier to keep the IGM ionised, reionisation heating also provides a positive feedback on the process of reionisation. Although the relative importance of both can only be assessed using larger hydrodynamical simulations of higher resolution[5], it is clear that models that do not account for this positive feedback will underestimate the efficiency with which star-forming galaxies are able to reionise the IGM.

Dependence on the reheating temperature

In this section we investigate the robustness of our results with respect to our simplified treatment of photo-ionisation heating.

We have considered photo-heating by a uniform ionising background in the optically thin

---

[5] At $z = 6$, the cosmic SFR density (the stellar mass) in *r9L6N256* is smaller than that in *L6N256* by a factor 1.26 (1.17). In our simulations, photo-heating thus decreases the SFR density less strongly than it reduces the clumping factor, which would imply that the positive feedback is more important. The SFR densities in both *r9L6N256* and *L6N256* are, however, not fully converged with respect to resolution and box size. A final assessment as to whether the negative or the positive feedback is stronger must therefore be deferred to future studies using simulations with higher resolution and larger box sizes.

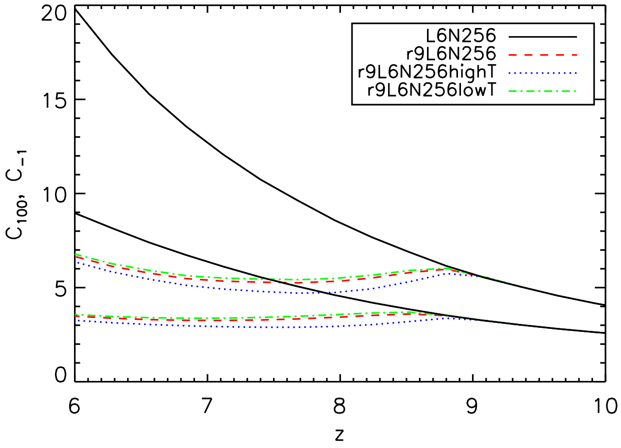

Figure 2.6: The dependence of C_{-1} (upper set of curves) and C_{100} (lower set of curves) on the value for the reheating energy $\epsilon_{\rm r}$. Both *r9L6N256highT* ($\epsilon_{\rm r} = 20$ eV) and *r9L6N256lowT* ($\epsilon_{\rm r} = 0$ eV) give results very similar to that obtained from the default run, *r9L6N256* ($\epsilon_{\rm r} = 2$ eV), which demonstrates the robustness of our conclusions with respect to changes in the reheating temperature.

limit. In reality, the reionisation process is likely to be driven by inhomogeneously distributed sources in an initially optically thick medium. The temperature to which the IGM is reheated will then not only depend on the spectrum of the ionising sources, but also on the amount of spectral hardening due to the preferential absorption of the less energetic ionising photons (e.g. Abel & Haehnelt 1999; Bolton, Meiksin, & White 2004). Moreover, the speed at which a particular patch of the IGM is reionised determines the duration during which its gas can cool efficiently, as the cooling is dominated by inelastic collisions between free electrons and neutral atoms. Different reionisation histories may therefore result in different IGM temperatures (e.g. Miralda-Escudé & Rees 1994; Theuns et al. 2002; Hui & Haiman 2003; Tittley & Meiksin 2007).

To bracket possible scenarios, we have performed two additional simulations in which we varied the amount of energy transferred to the baryons during the photo-ionisation process, *r9L6N256highT* and *r9L6N256lowT*. Whereas in the former we employ an additional energy input that is ten times larger than our default value ($\epsilon_{\rm r} = 20$ eV), in the latter no additional energy is injected ($\epsilon_{\rm r} = 0$ eV). We show in Fig. 2.6 that the evolution of C_{-1} and C_{100} obtained from these two simulations is very similar to that obtained from our default run, *r9L6N256*. The dependence on the reheating temperature $T_{\rm r} > 10^4$ K is weak, because halos with virial temperatures $T_{\rm vir} \lesssim 10^4$ K are already efficiently destroyed for $T_{\rm r} \approx 10^4$ K. A further increase in the reheating temperature mostly affects the fraction of mass in halos with larger virial temperatures, which is small. Moreover, Fig. 2.1 shows that the gas in the simulations *r9L6N256highT* and *r9L6N256lowT* quickly loses memory of its thermal state at some higher redshift, which is another reason for the similarity in the results obtained using different values for the reheating energy $\epsilon_{\rm r}$.

Effect of kinetic supernova feedback and dependence on cosmological parameters

The inclusion of kinetic feedback from supernovae in *r9L6N256winds* only weakly affects the evolution of the clumping factors. At redshift $z = 6$, C_{-1} and C_{100} are slightly larger (by factors 1.1 and 1.18, resp.) in *r9L6N256winds* than in our default simulation, *r9L6N256*, which does not include kinetic feedback. The reason for the slight increase in the clumping factors is that winds move gas from regions of densities larger than the critical density for the onset of star formation to regions of lower density that contribute to the calculation of the clumping factors. We note that the inclusion of kinetic feedback does, on the other hand, strongly affect the cosmic SFR. At $z = 6$, the cosmic SFR (the stellar mass) is lower in the simulation that includes kinetic feedback (*r9L6N256winds*) than in our default simulation (*r9L6N256*) by a factor of 6.1 (3.4).

Finally, we quote the clumping factors obtained from the simulations $r9L6N256W3$ and $r9L6N256W1$, which employed cosmological parameters consistent with the WMAP 3-year and 1-year observations, respectively. We find that at redshift $z = 6$, the clumping factors C_{-1} and C_{100} are larger in $r9L6N256$ than in $r9L6N256W3$ by factors of 1.31 and 1.16, respectively. They are smaller in $r9L6N256$ than in $r9L6N256W1$ by factors of 0.74 and 0.84. In summary, with respect to $r9L6N256$, the clumping factors are larger in $r9L6N256W1$ and smaller in $r9L6N256W3$, as expected from the corresponding values of σ_8, which set the average absolute amplitude of the overdensity fluctuations.

Comparison with previous work

We conclude our study of the clumping factor with a brief comparison with previous work, shown in Fig. 2.7. The evolution of the clumping factors in our simulations *L6N256* and *r9L6N256* is shown by the black solid and red dashed curves, respectively, where the upper (lower) set of curves shows C_{-1} (C_{100}). We compare it to the evolution of the clumping factor presented in Miralda-Escudé, Haehnelt, & Rees (2000) and Iliev et al. (2007), which are amongst the most commonly employed works on the clumping factor and make use of sufficiently different techniques to bracket a range of possible cases. We caution the reader that such a direct comparison is difficult and of limited validity because of the very different assumptions underlying the individual works.

Miralda-Escudé, Haehnelt, & Rees (2000) used the L10 hydrodynamical simulation presented in Miralda-Escudé et al. (1996) to obtain the PDF of the gas density at redshifts $z = 2, 3$ and 4. The simulation was performed using the TVD hydrodynamical scheme described in Ryu et al. (1993). It used a box of size $10\ h^{-1}$ comoving Mpc, 144^3 dark matter particles and 288^3 gas cells and employed cosmological parameters consistent with the first-year COBE normalization. The simulation included photo-heating from a uniform UV background, computed from the emissivities of the sources in the simulation. We refer the reader to Miralda-Escudé et al. (1996) for more details. Miralda-Escudé, Haehnelt, & Rees (2000) also provided fits to the gas density PDF and presented a prescription for its extrapolation to redshifts $z > 4$. We employed this prescription to compute the clumping factor evolution using Eq. 2.2.

The evolution of the clumping factors C_{-1} and C_{100} obtained from the Miralda-Escudé, Haehnelt, & Rees (2000) PDFs is shown, respectively, by the top and bottom blue long-dashed curves. For redshifts $z \gtrsim 9$, it closely agrees with the corresponding evolution obtained from our simulation *r9L6N256*. For lower redshifts the agreement is less good, although the clumping factors never differ by more than factors ~ 2. The differences between their and our results are probably due to the use of different hydrodynamical schemes, different cosmological parameters and different prescriptions for the UV background. The change in the slope of the clumping factor growth that can be seen at redhift $z \approx 9$ is likely due to the inclusion of photo-heating. That this change is much less pronounced than in our simulation *r9L6N256* may be due to a more gradual build-up of the ionising background in the Miralda-Escudé, Haehnelt, & Rees (2000) simulation.

Iliev et al. (2007) computed the clumping factor from a pure dark matter simulation. The simulation employed a box of size $3.5\ h^{-1}$ comoving Mpc and 1624^3 particles and was initialized with cosmological parameters consistent with the WMAP 3-year results[6]. The clumping factor was computed by averaging over all dark matter densities, and hence only implicitly makes use of an overdensity threshold (determined by the maximum overdensity present in their simulation). We refer the reader to the original description in Iliev et al. (2007) for more details.

Iliev et al. (2007) provided the following fit to the evolution of the clumping factor in their simulation,

$$C_{\rm Iliev07}(z) = 26.2917\exp(-0.1822z + 0.003505z^2), \tag{2.6}$$

which is valid over the range $6 < z < 30$. It is shown by the green dotted curve. Since it was derived from a pure dark matter simulation, Eq. 2.6 does not capture the hydrodynamical response due to reionisation heating. It should therefore be compared to the evolution of the clumping factor obtained from our simulation *L6N256*, which did not include photo-heating. A direct interpretation of such a comparison is, however, difficult, because Eq. 2.6 does not explicitly refer to an overdensity threshold.

Our comparison clearly illustrates that there is a considerable spread in the clumping factor values quoted in the literature. The interpretation of many studies is complicated by the fact that they do not refer to a density threshold, which means that the result is determined by the numerical resolution of their simulations.

2.4 DISCUSSION

Several observational studies have claimed that the star formation rate (SFR) density at redshift $z \approx 6$ is smaller than the critical SFR density required to keep the intergalactic medium (IGM) ionised. In the absence of a large population of unseen sources of ionising radiation, this discrepancy between the two SFR densities would be in direct conflict with the high degree of ionisation inferred from the non-detection of a Gunn-Peterson trough in the majority of the line-of-sight spectra towards $z \lesssim 6$ quasars.

The critical SFR density is inversely proportional to the spatially averaged fraction of ionising photons that escape into the IGM per unit time and proportional to the clumping factor $C \equiv \langle\rho_{\rm b}^2\rangle_{\rm IGM}/\langle\rho_{\rm b}\rangle^2$, a measure for the average recombination rate in the IGM. One may therefore ask whether the discrepancy between the observed and critical SFR densities could be resolved by changing the assumptions about the values of either of these two quantities. In this work we considered the hypothesis that most observational studies overestimate the critical SFR density because they employ a clumping factor that is too large.

We re-evaluated the clumping factor, analysing the gas density distributions in a set of cosmological smoothed particle hydrodynamics simulations that include radiative cooling and photo-ionisation by a uniform UV background in the optically thin limit. The clumping factor of the IGM depends critically on the definition of which gas is considered to be part of the IGM. Following Miralda-Escudé, Haehnelt, & Rees (2000), we assumed that all gas with densities below a threshold density constitutes the IGM and computed the clumping factor as a function of this threshold density. In addition, we introduced two physically well-motivated definitions, C_{100}, the clumping factor of gas with overdensities $\Delta < 100$ and C_{-1}, the clumping factor of gas with proper densities below $n_{\rm H} = n_{\rm H}^* \equiv 10^{-1}$ cm^{-3}, our threshold density for the onset of star formation.

---

[6] We note that they also computed the clumping factor in a similar simulation that was initialized with cosmological parameters consistent with the WMAP 1-year results.

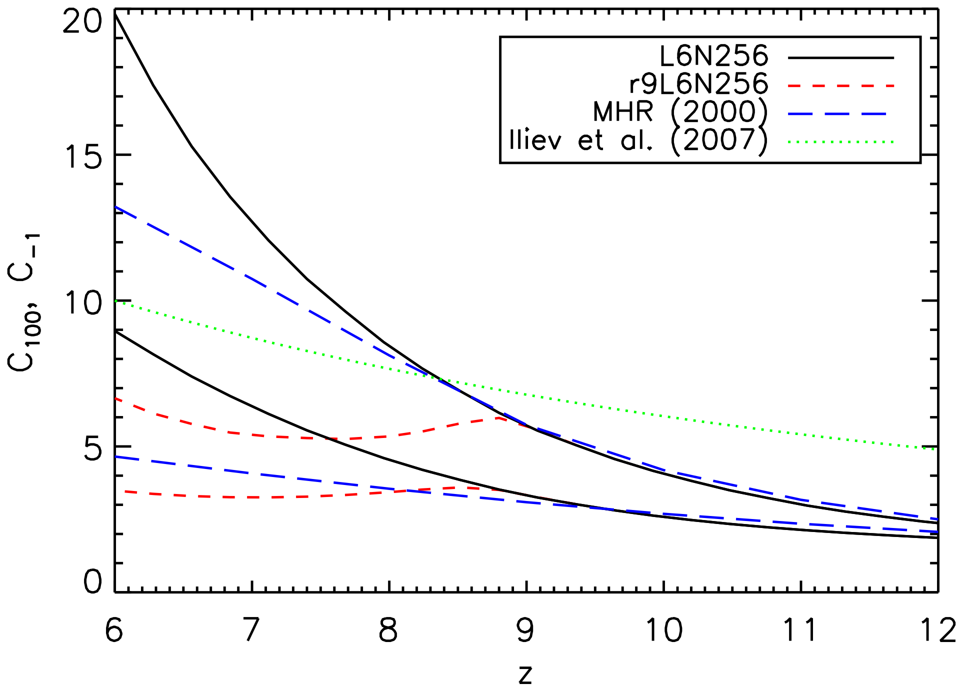

Figure 2.7: Clumping factor evolution: comparison with previous work. The black solid and red dashed curves are the clumping factors C_{-1} (upper set of curves) and C_{100} (lower set of curves) obtained from our simulations *L6N256* and *r9L6N256*. The blue dashed curves show the evolution of the clumping factors C_{-1} (upper curve) and C_{100} (lower curve) derived from the gas density PDFs presented in Miralda-Escudé, Haehnelt, & Rees (2000), which implicitly incorporate the effects of photo-heating. The green dotted curve shows the evolution of the clumping factor (defined without explicitly referring to a (over-)density threshold; instead, the overdensity threshold was set by the numerical resolution) the dark matter simulation of Iliev et al. (2007), which does not include the effects of photo-heating. In both cases a direct comparison is difficult, because of the different assumptions underlying the individual works.

By comparing simulations that include photo-ionisation by a uniform UV background to one that does not, we showed that photo-heating strongly influences the evolution of the clumping factor of the IGM. Photo-ionisation heating expels the gas from within halos of virial temperatures $T_{\rm vir} \lesssim 10^4$ K and prevents its further accretion by raising the Jeans mass in the IGM. By suppressing the formation of stars in these low-mass halos, photo-heating from reionisation decreases the rate at which ionising photons are emitted into the IGM and is therefore correctly said to exert a negative feedback on the reionisation process. The fact that photo-heating also leads to a decrease in the clumping factor and hence provides a strong positive feedback by making it easier to keep the IGM ionised, is however often overlooked (but see, e.g., Haiman, Abel, & Madau 2001; Oh & Haiman 2003; Kuhlen & Madau 2005; Wise & Abel 2005; Furlanetto, Oh, & Briggs 2006; Ciardi & Salvaterra 2007).

At redshift $z = 6$, we find that $C_{-1} \approx 6$ and $C_{100} \approx 3$ and that these values are insensitive to the redshift $z_{\rm r}$ at which the UV background is turned on, as long as $z_{\rm r} \gtrsim 9$. These values for C_{-1} and C_{100} are at least three times smaller than they would be in the absence of photo-heating. We demonstrated that our default simulation is converged at $z = 6$ with respect to the employed resolution. It is converged with respect to changes in the box size for threshold overdensities $\log_{10}\Delta_{\rm thr} \lesssim 2$. In Appendix 2.A we provide fits to the evolution of the clumping factor for various (over-)density thresholds and reheating redshifts. There we also compare the probability density function (PDF) of the gas densities at $z = 6$ obtained from our default simulation to the widely used fit provided by Miralda-Escudé, Haehnelt, & Rees (2000). We update their fitting parameters to best fit the PDF from our default simulation. Finally, we compared our results for the clumping factor of the IGM to those obtained in previous works.

Since even our most conservative estimate for the clumping factor ($C_{-1} \approx 6$) is five times smaller than the clumping factor that is usually employed to determine the capacity of star-forming galaxies to keep the $z = 6$ IGM ionised, our results may have important implications for the understanding of the reionisation process. Setting $C = 6$ in Eq. 2.1, the critical SFR density becomes $\dot{\rho}_* = 0.005\ f_{\rm esc}^{-1}\ {\rm M}_\odot\ {\rm yr}^{-1}\ {\rm Mpc}^{-3}$. This is smaller than recent observational estimates for the SFR density at $z \approx 6$, $\dot{\rho}_* = 0.022 \pm 0.004\ {\rm M}_\odot\ {\rm yr}^{-1}\ {\rm Mpc}^{-3}$ (integrated to the observed $z \approx 6$ faint-end limit $L > 0.04\ L^*_{z=3}$ and dust-corrected; Bouwens et al. 2007), provided that $f_{\rm esc} \gtrsim 0.2$.

Our study thus suggests that the observed population of star-forming galaxies may be capable of keeping the IGM ionised, relaxing the tension between observationally inferred and critical SFR density in view of the observation of a highly ionised IGM at redshifts $z \lesssim 6$. We note that at $z \approx 7$, the SFR density is estimated to be $\dot{\rho}_* = 0.004 \pm 0.002\ {\rm M}_\odot\ {\rm yr}^{-1}\ {\rm Mpc}^{-3}$ (integrated to the observed $z \approx 7$ faint-end limit $L > 0.2\ L^*_{z=3}$ and dust-corrected; Bouwens et al. 2008), whereas the critical SFR density is $\dot{\rho}_* = 0.008\ f_{\rm esc}^{-1}\ {\rm M}_\odot\ {\rm yr}^{-1}\ {\rm Mpc}^{-3}$ (using $C = 6$). The observed population of star-forming galaxies at $z \approx 7$ is therefore not able to keep the IGM ionised. If the Universe were ionised by this redshift, then the sources that were responsible remain to be discovered.

We caution the reader that the comparison of the critical and observed SFRs is subject to considerable uncertainty. First, the SFR inferred from UV galaxy counts probably underestimates the true SFR, because these counts miss UV galaxies fainter than the faint-end limit implied by their sensitivities. These galaxies may, however, significantly contribute to the UV luminosity density if the faint-end slope of the UV luminosity function is sufficiently steep. Complementary estimates of the high-redshift star formation rate based on measurements of the high-redshift ($z = 4 - 7$) gamma ray burst rate (Yüksel et al. 2008) and measurements of the Lyman-alpha forest opacity at redshifts $z \sim 3$ (Faucher-Giguère et al. 2008) indeed suggest $z \sim 6$ SFRs that exceed those inferred from UV galaxy counts by factors of a few.

Second, the expression for the critical SFR (Eq. 2.1) is only approximate. As already mentioned in the introduction, this expression is based on equating the rate at which ionising photons escape into the intergalactic medium to the rate at which the intergalactic gas is recombining, both averaged in space. It neglects effects like the cosmological redshifting of photons below the ionisation threshold energy and evolution of the ionising sources during a recombination time. Because the cross-section $\sigma_{\rm HI} \sim \nu^{-3}$ for absorption of ionising photons by neutral hydrogen decreases with increasing photon frequency ν, these effects may become important for photons whose mean free path is comparable to the cosmic horizon. Our limit on the escape fraction required to keep the Universe at $z \approx 6$ ionised may therefore only be accurate within a factor of a few.

Our simulations demonstrate that radiation-hydrodynamical feedback due to photo-ionisation heating plays a key role in shaping the properties of the IGM at redshifts $z \gtrsim 6$. We have studied the impact of photo-ionisation heating on the clumping factor of the IGM assuming a uniform ionising UV background in the optically thin limit. In reality the reionisation process will, however, be more complex. We have demonstrated the robustness of our conclusions with respect to uncertainties in the temperature of the IGM resulting from our simplified treatment of the reionisation heating, but there are other factors whose importance is more difficult to assess.

Our use of the optically thin approximation neglects self-shielding, a radiative transfer effect due to which halos that would otherwise be completely photo-evaporated could keep some of their gas (e.g., Kitayama & Ikeuchi 2000; Susa & Umemura 2004; Dijkstra et al. 2004). Since the self-shielded gas remains neutral, it should be excluded when computing the clumping factor. Self-shielding becomes important for $N_{\rm HI} \gtrsim 10^{18}$ cm^{-2}, which for self-gravitating gas clouds corresponds to densities (Schaye 2001) $n_{\rm H} \gtrsim 10^{-2}$ cm$^{-3}(\Gamma/10^{-12}$ s$^{-1})$, where Γ is the HI photo-ionisation rate. In our discussion of the critical SFR we have conservatively adopted the clumping factor C_{-1}, defined using a threshold density $n_{\rm H} = 10^{-1}$ cm^{-3}, which is an order of magnitude larger than the critical density for self-shielding.

Self-shielding might affect our results because it may lower the speed with which halos are photo-evaporated. The work by Iliev, Shapiro, & Raga (2005b) (in combination with the work by Shapiro, Iliev, & Raga 2004) shows that photo-evaporation times obtained in simulations that employ an optically thin UV background may differ by factors of a few from those obtained in detailed radiation-hydrodynamical simulations. However, if any halos would resist photo-evaporation much longer than predicted by our approximate treatment of photo-heating, then the clumping factor of the IGM would be even lower, because self-shielding locks the gas that would otherwise contribute to the clumping factor of the IGM in its neutral state.

If absorption by optically thick (self-shielded) clouds becomes important, then the mean free path of ionising photons may be set by the mean distance between these clouds (Zuo & Phinney 1993) instead of by the opacity of the diffuse IGM. In this case it might be appropriate to supplement the Miralda-Escudé, Haehnelt, & Rees 2000 model for the computation of the average recombination rate with a more direct account for these clouds as discrete photon sinks (e.g., Iliev, Scannapieco, & Shapiro 2005a; Ciardi et al. 2006). The effect of absorption by optically thick clouds is, however, largely degenerate with the ionising efficiency of the population of star-forming galaxies, as explained in Iliev et al. (2007). If, on the one hand, these clouds are ionising sources themselves, then their contribution to the average recombination rate can be described by their escape fractions. If, on the other hand, these clouds do not host ionising sources, then their contribution to the average recombination can be accommodated by changes in the ionising efficiency of star-forming galaxies because of their biased clustering around these galaxies. The effects of optically thick clouds can therefore approximately be accounted for by adjusting the properties of the ionising sources.

Self-shielding is only one example of the physical effects that we are ignoring. The inclusion of metals and molecules, for instance, would increase the ability of the gas to cool, which may lead to an increase in the clumping factor (e.g. Maio et al. 2007). In the presence of photo-heating and for the threshold densities we employ to compute the clumping factors we however expect this effect to be very small. A more efficient cooling due to metals and molecules may also enable star formation and associated kinetic feedback in low-mass haloes with virial temperatures $T_{\rm vir} < 10^4$ K. Both are processes that we have ignored but which are likely to affect the clumping factor evolution (e.g. Wise & Abel 2008).

The evolution of the clumping factor will also depend on the morphology of the reionisation transition. Our treatment implicitly assumed that all gas with overdensities smaller than a threshold overdensity is uniformly ionised, while all gas with larger overdensities is fully neutral. This picture probably only applies to the late stages of reionisation, when individual ionised regions start to overlap and the only neutral gas that remains to be ionised is locked up in regions of high gas overdensities. Before overlap, other reionisation models may be more useful for the description of the clumping factor evolution. For example, Furlanetto & Oh (2005) point out that if the large-scale dense regions are ionised first, the clumping factor may be somewhat larger than one would otherwise expect, because the photons are initially confined to these dense regions. Moreover, Furlanetto, Haiman, & Oh (2008) show that in fossil ionised regions, that is, regions in which the gas freely recombines, the clumping factor will generally be smaller than for regions in photo-ionisation equilibrium, because the densest gas which contributes most to the clumping factor becomes neutral first.

The clumping factor is an important ingredient of (semi-)analytic treatments of reionisation. It would therefore be highly desirable to evaluate the approximations we have employed in our simplified treatment of the photo-heating process using large high-resolution radiation-hydrodynamical simulations of reionisation that include cooling by metals and molecules and feedback from star formation. At the moment such simulations are, however, not yet feasible.

In fact, current state-of-the-art radiative transfer simulations typically make use of clumping factors in their "sub-grid" modules because they lack the resolution to resolve the clumpiness of the gas directly. In addition, they typically do not include the effect of photo-heating. In fact, many radiative transfer simulations ignore hydrodynamics altogether and assume the gas to trace the dark matter.

With this work we hope to have presented a conservative assessment of the clumping factor of the post-reionisation IGM that may provide a useful input to future (semi-)analytic models and simulations of the reionisation process.

ACKNOWLEDGMENTS

We thank Rychard Bouwens, Steven Furlanetto and Jordi Miralda-Escudé for valuable communications. We thank the anonymous referee for his/her constructive contribution that greatly improved the discussion of our results. We are grateful to Claudio Dalla Vecchia for help with running the simulations, Rob Wiersma for useful discussions on the cooling tables and Marcel Haas and Freeke van de Voort for a thorough reading of the draft of Pawlik, Schaye, & van Scherpenzeel (2009a). The simulations presented here were run on the Cosmology Machine at the Institute for Computational Cosmology in Durham as part of the Virgo Consortium research programme and on Stella, the LOFAR BlueGene/L system in Groningen. This work was supported by Marie Curie Excellence Grant MEXT-CT-2004-014112.

REFERENCES

Abel T., Haehnelt M. G., 1999, ApJ, 520, L13

Barkana R., Loeb A., 1999, ApJ, 523, 54

Barkana R., Loeb A., 2001, PhR, 349, 125

Barkana R., Loeb A., 2004, ApJ, 609, 474

Benson A. J., Nusser A., Sugiyama N., Lacey C. G., 2001, MNRAS, 320, 153

Bolton J., Meiksin A., White M., 2004, MNRAS, 348, L43

Bolton J. S., Haehnelt M. G., 2007, MNRAS, 382, 325

Bouwens R. J., et al., 2004, ApJ, 606, L25

Bouwens R. J., Illingworth G. D., Blakeslee J. P., Franx M., 2006, ApJ, 653, 53

Bouwens R. J., Illingworth G. D., Franx M., Ford H., 2007, ApJ, 670, 928

Bouwens R. J., Illingworth G. D., Franx M., Ford H., 2008, preprint (arXiv:0803.0548)

Bruzual G., Charlot S., 2003, MNRAS, 344, 1000

Bunker A. J., Stanway E. R., Ellis R. S., McMahon R. G., 2004, MNRAS, 355, 374

Chabrier G., 2003, PASP, 115, 763

Chiu W. A., Fan X., Ostriker J. P., 2003, ApJ, 599, 759

Ciardi B., Scannapieco E., Stoehr F., Ferrara A., Iliev I. T., Shapiro P. R., 2006, MNRAS, 366, 689

Ciardi B., Salvaterra R., 2007, MNRAS, 381, 1137

Collin-Souffrin S., 1991, A&A, 243, 5

Chuzhoy L., Kuhlen M., Shapiro P. R., 2007, ApJ, 665, L85

Crain R. A., Eke V. R., Frenk C. S., Jenkins A., McCarthy I. G., Navarro J. F., Pearce F. R., 2007, MNRAS, 377, 41

Dalla Vecchia C., Schaye J., 2008, MNRAS, 387, 1431

Dijkstra M., Haiman Z., Rees M. J., Weinberg D. H., 2004, ApJ, 601, 666

Efstathiou G., 1992, MNRAS, 256, 43P

Fan X., Carilli C. L., Keating B., 2006, ARA&A, 44, 415

Faucher-Giguère C.-A., Lidz A., Hernquist L., Zaldarriaga M., 2008, ApJ, 688, 85

Ferland G. J., Korista K. T., Verner D. A., Ferguson J. W., Kingdon J. B., Verner E. M., 1998, PASP, 110, 761

Furlanetto S. R., Oh S. P., 2005, MNRAS, 363, 1031

Furlanetto S. R., Oh S. P., Briggs F. H., 2006, PhR, 433, 181

Furlanetto S. R., Haiman Z., Oh S. P., 2008, ApJ, 686, 25

Glover S. C. O., Brand P. W. J. L., 2003, MNRAS, 340, 210

Glover S. C. O., 2007, MNRAS, 379, 1352

Gnedin N. Y., Ostriker J. P., 1997, ApJ, 486, 581

Gnedin N. Y., Hui L., 1998, MNRAS, 296, 44

Gnedin N. Y., 2000a, ApJ, 535, 530

Gnedin N. Y., 2000b, ApJ, 542, 535

Gnedin N. Y., Kravtsov A. V., Chen H.-W., 2008, ApJ, 672, 765

Gnedin N. Y., 2008, ApJ, 673, L1

Haardt F., Madau P., 2001, in the proceedings of XXXVI Rencontres de Moriond, preprint (astroph/0106018)

Haiman Z., Rees M. J., Loeb A., 1997, ApJ, 476, 458

Haiman Z., Abel T., Madau P., 2001, ApJ, 551, 599

Hoeft M., Yepes G., Gottlöber S., Springel V., 2006, MNRAS, 371, 401

Hui L., Haiman Z., 2003, ApJ, 596, 9

Iliev I. T., Scannapieco E., Shapiro P. R., 2005a, ApJ, 624, 491

Iliev I. T., Shapiro P. R., Raga A. C., 2005b, MNRAS, 361, 405

Iliev I. T., Mellema G., Shapiro P. R., Pen U.-L., 2007, MNRAS, 376, 534

Inoue A. K., Iwata I., Deharveng J.-M., 2006, MNRAS, 371, L1

Kennicutt R. C., Jr., 1998, ApJ, 498, 541

Kitayama T., Ikeuchi S., 2000, ApJ, 529, 615

Kohler K., Gnedin N. Y., Hamilton A. J. S., 2007, ApJ, 657, 15

Komatsu E., et al., 2008, preprint (arXiv:0803.0547)

Kuhlen M., Madau P., 2005, MNRAS, 363, 1069

Lacey C., Cole S., 1994, MNRAS, 271, 676

Lehnert M. D., Bremer M., 2003, ApJ, 593, 630

Machacek M. E., Bryan G. L., Abel T., 2003, MNRAS, 338, 273

Madau P., Efstathiou G., 1999, ApJ, 517, L9

Madau P., Haardt F., Rees M. J., 1999, ApJ, 514, 648

Madau P., 2000, RSPTA, 358, 2021

Madau P., Rees M. J., Volonteri M., Haardt F., Oh S. P., 2004, ApJ, 604, 484

Maio U., Dolag K., Ciardi B., Tornatore L., 2007, MNRAS, 379, 963

Malhotra S., et al., 2005, ApJ, 626, 666

Mannucci F., Buttery H., Maiolino R., Marconi A., Pozzetti L., 2007, A&A, 461, 423

Mesinger A., Dijkstra M., 2008, preprint (arXiv:0806.3090)

Miralda-Escudé J., Rees M. J., 1994, MNRAS, 266, 343

Miralda-Escudé J., Cen R., Ostriker J. P., Rauch M., 1996, ApJ, 471, 582

Miralda-Escudé J., Haehnelt M., Rees M. J., 2000, ApJ, 530, 1

Miralda-Escudé J., 2003, ApJ, 597, 66

Navarro J. F., Steinmetz M., 1997, ApJ, 478, 13

Oesch P. A., et al., 2008, preprint (arXiv:0804.4874)

Oh S. P., 2001, ApJ, 553, 499

Oh S. P., Haiman Z., 2003, MNRAS, 346, 456

Okamoto T., Gao L., Theuns T., 2008, preprint (arXiv:0806.0378)

Padmanabhan T., Structure Formation in the Universe, Cambridge University Press (1993)

Panagia N., Fall S. M., Mobasher B., Dickinson M., Ferguson H. C., Giavalisco M., Stern D., Wiklind T., 2005, ApJ, 633, L1

Pawlik A. H., Schaye J., van Scherpenzeel E., 2009, MNRAS, 394, 1812

Pawlik A. H., Schaye J., 2009, MNRAS, L228

Razoumov A. O., Sommer-Larsen J., 2006, ApJ, 651, L89

Ricotti M., Ostriker J. P., 2004, MNRAS, 352, 547

Ryu D., Ostriker J. P., Kang H., Cen R., 1993, ApJ, 414, 1

Sawicki M., Thompson D., 2006, ApJ, 648, 299

Schaye J., 2001, ApJ, 559, 507

Schaye J., 2004, ApJ, 609, 667

Schaye J., Dalla Vecchia C., 2008, MNRAS, 383, 1210

Seljak U., Zaldarriaga M., 1996, ApJ, 469, 437

Shapiro P. R., Giroux M. L., Babul A., 1994, ApJ, 427, 25

Shapiro P. R., Iliev I. T., Raga A. C., 2004, MNRAS, 348, 753

Shapley A. E., Steidel C. C., Pettini M., Adelberger K. L., 2003, ApJ, 588, 65

Spergel D. N., et al., 2007, ApJS, 170, 377

Spergel D. N., et al., 2003, ApJS, 148, 175

Springel V., Hernquist L., 2003, MNRAS, 339, 289

Springel V., 2005, MNRAS, 364, 1105

Srbinovsky J. A., Wyithe J. S. B., 2007, MNRAS, 374, 627

Stanway E. R., Bunker A. J., McMahon R. G., 2003, MNRAS, 342, 439

Stiavelli M., Fall S. M., Panagia N., 2004, ApJ, 610, L1

Susa H., Umemura M., 2004, ApJ, 600, 1

Theuns T., Schaye J., Zaroubi S., Kim T.-S., Tzanavaris P., Carswell B., 2002, ApJ, 567, L103

Thoul A. A., Weinberg D. H., 1996, ApJ, 465, 608

Tittley E. R., Meiksin A., 2007, MNRAS, 380, 1369

Valageas P., Silk J., 1999, A&A, 347, 1

Veilleux S., Cecil G., Bland-Hawthorn J., 2005, ARA&A, 43, 769

Venkatesan A., Giroux M. L., Shull J. M., 2001, ApJ, 563, 1

Wiersma R. P. C., Schaye J., Smith B. D., 2008, MNRAS, in press, preprint (arXiv:0807.3748)

Wise J. H., Abel T., 2005, ApJ, 629, 615

Wise J. H., Abel T., 2008, ApJ, 684, 1

Yan H., Windhorst R. A., 2004, ApJ, 600, L1

Yüksel H., Kistler M. D., Beacom J. F., Hopkins A. M., 2008, ApJ, 683, L5

Zuo L., Phinney E. S., 1993, ApJ, 418, 28

2.A FITTING FORMULAS

Here we provide fits to the evolution of the clumping factor for a range of overdensity thresholds and all reheating redshifts considered for use with (semi-)analytical models of reionisation. We also compare the probability density function of the gas densities at redshift $z = 6$ obtained from our default simulation to the fit provided by Miralda-Escudé, Haehnelt, & Rees (2000).

2.A.1 Clumping factor

In this section we fit the evolution of the clumping factors C_{-1} and C_{100} over the redshift range $6 \leq z \leq 20$, based on the data presented in Fig. 2.5. In addition, we give fits to the evolution of the clumping factors C_{-2} and $C_{1000}, C_{500}, C_{200}$ and C_{50}, where $C_{-2} \equiv C(< 10^{-2}~\mathrm{cm}^{-3} m_{\mathrm{H}}/(X\langle\rho_{\mathrm{b}}\rangle))$ and $C_{1000} \equiv C(< \min(1000, 10^{-1}~\mathrm{cm}^{-3} m_{\mathrm{H}}/(X\langle\rho_{\mathrm{b}}\rangle)))$ and similar for C_{500}, C_{200} and C_{50}. We first give fits to the evolution of the clumping factors for the simulations *L6N256* and *r19.5L6N256*, i.e. the simulations without reheating and with reheating at the highest redshift we considered. These fits are then used to obtain fits to the evolution of the clumping factors for reheating at the intermediate redshifts $z_{\mathrm{r}} = 7.5, 9.0, 10.5, 12, 13.5$ and 15.0 by interpolation.

We approximate the evolution of the clumping factors for the simulations *L6N256* and *r19.5L6N256* by

$$C(z) \quad = \quad z^{\beta} e^{-\gamma z + \delta} + \alpha, \tag{2.7}$$

where C is either $C_{-1}, C_{-2}, C_{1000}, C_{500}, C_{200}, C_{100}$ or C_{50} and similar for α, β, γ, δ. The values for the parameters α, β, γ, δ are listed in Tables 2.2 and 2.3. The fit (Eq. 2.7) is accurate to within $\lesssim 10\%$. We emphasize that it is only strictly valid over the fitting range $6 \leq z \leq 20$. For $C_{1000}, C_{500}, C_{200}, C_{100}$ and C_{50}, i.e. for the clumping factors that are defined using an overdensity threshold, we forced, however, the fits to approach the correct high-z limit, i.e. $C \rightarrow 1$, by fixing $\alpha = 1$ during the fitting procedure. Note that the threshold densities used with C_{-1} and C_{-2} correspond to threshold overdensities $\Delta_{\mathrm{thr}} < 1$ for redshifts $z > 79.4$ and $z > 36.3$, respectively and that $C_{1000}, C_{500}, C_{200}, C_{100}$ and C_{50} become identical to C_{-1} for redshifts $z > 7.0, 9.1, 12.7, 16.3$ and 20.8, respectively.

Table 2.2: Parameter values α, β, γ and δ to be used in Eq. 2.7 in order to fit the evolution of the clumping factors C_{-1} and C_{-2} obtained from the simulations *L6N256* and *r19.5L6N256* (see also Fig. 2.5).

	L6N256	*r19.5L6N256*
α_{-1}	1.29	1.21
β_{-1}	0.00	−3.66
γ_{-1}	0.47	0.00
δ_{-1}	5.76	8.25
α_{-2}	1.29	1.16
β_{-2}	0.00	−2.47
γ_{-2}	0.44	0.00
δ_{-2}	4.68	5.16

The values of C for reheating at redshifts $z_{\rm r} = 7.5, 9.0, 10.5, 12, 13.5$ and 15.0 (hereafter $C^{z_{\rm r}}$) are fitted by interpolating between the fits (Eq. 2.7) to the evolution of the clumping factors obtained from *L6N256* (hereafter C^0) and *r19.5L6N256* (hereafter $C^{19.5}$). That is, we write

$$C^{z_{\rm r}}(z) = w(z)C^0(z) + [1 - w(z)]C^{19.5}(z), \tag{2.8}$$

where

$$w(z) = \frac{1}{2}\left[\text{erf}\left(\frac{z - \zeta^{z_{\rm r}}}{\tau^{z_{\rm r}}}\right) + 1\right], \tag{2.9}$$

and erf is the error function,

$$\text{erf}(z) = \frac{2}{\sqrt{\pi}}\int_0^z d\tilde{z}\ \exp\left(-\tilde{z}^2\right). \tag{2.10}$$

The constants $\zeta^{z_{\rm r}}$ and $\tau^{z_{\rm r}}$ are listed in Tables 2.4 and 2.5. Eq. 2.8 fits the data to within $\lesssim 10\%$.

2.A.2 Probability density function

Miralda-Escudé, Haehnelt, & Rees (2000) gave a convenient four-parameter fit to the volume-weighted probability density function (PDF) of the gas density at redshifts $z = 2, 3$ and 4 obtained from the L10 hydrodynamical simulation described in Miralda-Escudé et al. (1996). In addition, they provided a prescription for extrapolating this fit to higher redshifts. Here we compare the volume-weighted PDF obtained from our default simulation (*r9L6N256*) at $z = 6$ to their fit. Because we find that their set of fitting parameters provides a somewhat poor description of this PDF, we also provide an updated set of parameters that yields a fit which more accurately describes the one-point distribution of gas densities at $z = 6$ in our default simulation.

In Fig. 2.8 we show the volume-weighted PDF of the gas density per unit $\log_{10}\Delta$. We have investigated the convergence of this PDF with respect to the resolution and the size of the simulation box, using the same set of simulations that we employed to study the convergence of the clumping factor in Section 2.3.2. We find that the PDF is converged with respect to changes in the resolution. It is converged with respect to changes in the size of the simulation box for overdensities $\log_{10}\Delta \lesssim 2$. For larger overdensities, the values of the PDF obtained from our default simulation may not yet be fully converged. We note that at $z = 6$ the PDFs obtained from the simulations *r[*$z_{\rm r}$*]L6N256z* that employ a reheating redshift $z_{\rm r} > 9$ are almost undistinguishable from that obtained from our default simulation.

Table 2.3: Parameter values α, β, γ and δ to be used in Eq. 2.7 in order to fit the evolution of the clumping factors $C_{1000}, C_{500}, C_{200}, C_{100}$ and C_{50} obtained from the simulations *L6N256* and *r19.5L6N256* (see also Fig. 2.5).

	L6N256	*r19.5L6N256*
α_{1000}	1.00	1.00
β_{1000}	-1.00	-2.89
γ_{1000}	0.28	0.00
δ_{1000}	6.29	6.76
α_{500}	1.00	1.00
β_{500}	0.00	-2.44
γ_{500}	0.34	0.00
δ_{500}	4.60	5.68
α_{200}	1.00	1.00
β_{200}	0.00	-1.99
γ_{200}	0.30	0.00
δ_{200}	4.04	4.49
α_{100}	1.00	1.00
β_{100}	0.00	-1.71
γ_{100}	0.28	0.00
δ_{100}	3.59	3.76
α_{50}	1.00	1.00
β_{50}	0.00	-1.47
γ_{50}	0.23	0.00
δ_{50}	2.92	3.08

Table 2.4: Parameter values $\zeta^{z_{\rm r}}$ and $\tau^{z_{\rm r}}$ to be used in Eq. 2.8 in order to fit the evolution of the clumping factors C_{-1} and C_{-2} obtained from the simulations *r[*$z_{\rm r}$*]L6N256* (see also Fig. 2.5).

$z_{\rm r}$	$\zeta_{-1}^{z_{\rm r}}$	$\tau_{-1}^{z_{\rm r}}$	$\zeta_{-2}^{z_{\rm r}}$	$\tau_{-2}^{z_{\rm r}}$
7.5	6.83	0.83	6.61	0.80
9.0	8.10	1.25	7.78	1.26
10.5	9.41	1.71	8.92	1.65
12.0	10.77	2.16	10.02	1.96
13.5	12.10	2.45	11.09	2.24
15.0	13.27	2.43	12.20	2.48

Table 2.5: Parameter values $\zeta^{z_{\rm r}}$ and $\tau^{z_{\rm r}}$ to be used in Eq. 2.8 in order to fit the evolution of the clumping factors $C_{1000}, C_{500}, C_{200}, C_{100}$ and C_{50} obtained from the simulations *r[*$z_{\rm r}$*]L6N256* (see also Fig. 2.5).

$z_{\rm r}$	$\zeta_{1000}^{z_{\rm r}}$	$\tau_{1000}^{z_{\rm r}}$	$\zeta_{500}^{z_{\rm r}}$	$\tau_{500}^{z_{\rm r}}$	$\zeta_{200}^{z_{\rm r}}$	$\tau_{200}^{z_{\rm r}}$	$\zeta_{100}^{z_{\rm r}}$	$\tau_{100}^{z_{\rm r}}$	$\zeta_{50}^{z_{\rm r}}$	$\tau_{50}^{z_{\rm r}}$
7.5	6.71	0.68	6.74	0.76	6.71	0.83	6.60	0.75	6.53	0.85
9.0	7.98	1.29	7.96	1.22	7.93	1.32	7.75	1.72	7.67	1.37
10.5	9.49	2.00	9.50	2.12	9.33	2.03	8.99	1.71	8.94	2.03
12.0	11.10	2.58	11.33	3.05	10.98	2.90	10.39	2.38	10.40	2.84
13.5	12.36	2.35	13.12	3.63	12.75	3.72	11.93	3.07	12.02	3.69
15.0	13.27	1.77	14.36	3.26	14.64	4.49	13.66	3.75	13.86	4.60

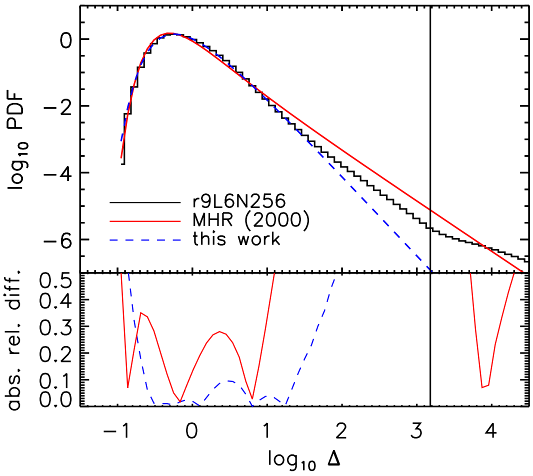

Figure 2.8: Top panel: Volume-weighted PDF of the baryon overdensity Δ (per unit $\log_{10} \Delta$) at $z = 6$ obtained from our default simulation *r9L6N256* (black solid histogram). For comparison, the red solid line shows the four-parameter fit given by Eq. 2.11, with the parameter values taken from Miralda-Escudé, Haehnelt, & Rees (2000). The blue dashed line shows our best fit of Eq. 2.11 to the PDF. Bottom panel: Absolute value of the relative differences of the fits with respect to the PDF. In both panels, the vertical line indicates the overdensity corresponding to the onset of star formation.

We compare the PDF to the fit given by Miralda-Escudé, Haehnelt, & Rees (2000),

$$\mathcal{P}_{\rm V}(\Delta)d\Delta = A \exp\left[-\frac{(\Delta^{-2/3} - C_0)^2}{2(2\delta_0/3)^2}\right] \Delta^{-\beta} d\Delta, \tag{2.11}$$

using their values for the parameters[7] $A = 0.375, \delta_0 = 1.09, \beta = 2.50$ and $C_0 = 0.880$. As can be seen from Fig. 2.8, for overdensities $1 \lesssim \log_{10} \Delta \lesssim 2$ the PDF obtained from our default simulation is significantly steeper than predicted by the fit. Using the simulations *r9L6N256W3* and *r9L6N256W1*, we verified that the steepness of the slope of the PDF over this range of overdensities is sensitive to the cosmological parameters employed. Note that the PDF does also not asymptote to $\mathcal{P}_{\rm V}(\Delta) \propto \Delta^{-\beta}$, as predicted by Eq. 2.11. For overdensities larger than the overdensity for the onset of star formation, the PDF is instead governed by the effective equation of state characteristic for the multi-phase star-forming gas.

We fitted Eq. 2.11 to our PDF over the range $-1 \leq \log_{10} \Delta \leq 2$, constraining the parameters A and C_0 by the requirement that the total integral over the volume- and mass-weighted PDF must be normalized to unity. This yields values $A = 3.038, \delta_0 = 1.477, \beta = 3.380$ and $C_0 = -0.932$. Note that the fit based on these parameter values still does not provide a good description of the PDF for overdensities $\log_{10} \Delta \gtrsim 2$.

---

[7] Note that the value for A given in Miralda-Escudé, Haehnelt, & Rees (2000) is too large by a factor of $\ln 10$.

> Eine solche Skizze braucht nicht im
> höchsten Grade ausgeführt und
> vollendet zu sein, wenn sie gut gesehen,
> gedacht und fertig ist, so ist sie für den
> Liebhaber oft reizender als ein größeres
> ausgeführtes Werk.
>
> Goethe, Maximen und Reflexionen

CHAPTER 3

Photo-heating and supernova feedback amplify each other's effect on the cosmic star formation rate

Andreas H. Pawlik & Joop Schaye

MNRAS 396 (2009) L46

Photo-heating associated with reionisation and kinetic feedback from core-collapse supernovae have previously been shown to suppress the high-redshift cosmic star formation rate. Here we investigate the interplay between photo-heating and supernova feedback using a set of cosmological, smoothed particle hydrodynamics simulations. We show that photo-heating and supernova feedback mutually amplify each other's ability to suppress the star formation rate. Our results demonstrate the importance of the simultaneous, non-independent inclusion of these two processes in models of galaxy formation to estimate the strength of the total negative feedback they exert. They may therefore be of particular relevance to semi-analytic models in which the effects of photo-heating and supernova feedback are implicitly assumed to act independently of each other.

3.1 INTRODUCTION

The cosmic star formation rate (SFR) is an important observable of our Universe. It is affected by a variety of physical processes, many of which are in turn regulated by the SFR, giving rise to so-called feedback loops (for an overview see, e.g., Ciardi & Ferrara 2005). Photo-ionisation heating due to the absorption of ionising photons from star-forming regions and the injection of kinetic energy from supernova (SN) explosions of massive stars provide two such feedback loops. Their implications for the assembly of the first generation of galaxies have been extensively discussed in studies of the epoch of reionisation (for a review of this epoch see, e.g., Loeb & Barkana 2001).

Photo-heating associated with reionisation increases the mean temperature of the intergalactic medium (IGM) to $\sim 10^4$ K (e.g., Hui & Gnedin 1997) and reduces the rate at which hotter gas can cool (Efstathiou 1992; Wiersma, Schaye, & Smith 2009). The increase in the gas temperature keeps the IGM smooth and prevents the assembly of low-mass galaxies, that is, galaxies with masses corresponding to a virial temperature $\lesssim 10^4$ K (e.g., Shapiro, Giroux, & Babul 1994; Gnedin & Hui 1998). Moreover, the gas in galaxies that have already collapsed is relatively quickly photo-evaporated (e.g., Shapiro, Iliev, & Raga 2004; Iliev, Shapiro, & Raga 2005), strongly decreasing the gas fraction of low-mass halos (e.g., Thoul & Weinberg 1996; Barkana & Loeb 1999; Dijkstra et al. 2004; Susa & Umemura 2006). Indeed, the cosmic SFR has been predicted to exhibit a distinct drop around the redshift of reionisation (Barkana & Loeb 2000). Photo-ionisation heating is therefore said to provide a negative feedback on reionisation.[1]

SN explosions of massive stars typically inject a few solar masses of gas with velocity of $\sim 10^4$ km s^{-1}, corresponding to a kinetic energy of $\sim 10^{51}$ erg. The ejected material sweeps up and shock-heats the surrounding gas, entraining outflows sufficiently powerful to, at least temporarily, substantially reduce the gas fractions for galaxy-scale dark matter halos (e.g., Yepes et al. 1997; Scannapieco et al. 2006). Since this leads to a suppression of the SFR, SN explosions, like photo-heating from reionisation, provide a negative feedback on reionisation. In addition to the depth of the gravitational potential, the ability of SN feedback to reduce the gas fractions generally depends on the geometry of the gas distribution (e.g., Mac Low & Ferrara 1999).

Studies of the effects of photo-heating and SN feedback on the SFR that considered each process in isolation have been augmented by studies that included both photo-heating and SN feedback. These studies include simulations of the formation of the first stars (e.g., Greif et al. 2007; Wise & Abel 2008; Whalen et al. 2008), of the evolution of isolated galaxies (e.g., Fujita et al. 2004; Dalla Vecchia & Schaye 2008, Tasker & Bryan 2008), and of galaxies in a cosmological volume (e.g., Tassis et al. 2003). Some of these studies also investigate the interplay between photo-heating and SN feedback. For example, Kitayama & Yoshida (2005) demonstrated in a one-dimensional hydrodynamical study that a previous episode of photo-heating may increase the efficiency of the evacuation of dark matter halos by (thermal) SN feedback and enable the destruction of galaxies out to much larger masses. In this chapter we report on another interaction of star formation feedbacks, using three-dimensional galaxy formation simulations.

We employ a set of Smoothed Particle Hydrodynamics (SPH) cosmological simulations that include star formation, and photo-ionisation heating from a uniform ultraviolet (UV) background and/or kinetic feedback from core-collapse SNe. We investigate how photo-heating af-

---

[1] As pointed out by Pawlik, Schaye, & van Scherpenzeel (2008), photo-heating also provides a strong positive feedback on reionisation because the increase in the gas temperature smoothes out density fluctuations, reducing the recombination rate.

Table 3.1: Simulation parameters. From left to right, table entries are: simulation label; comoving size of the simulation box, $L_{\rm box}$; number of DM particles, $N_{\rm dm}$; mass of dark matter particles, $m_{\rm dm}$. A prefix *r9* indicates the inclusion of photo-heating in the optically thin limit from a uniform UV background (for $z \leq 9$) and a suffix *winds* indicates the inclusion of SN feedback (with initial wind velocity $v_{\rm w} = 600$ km s^{-1} and mass loading $\eta = 2$). A bold font marks our set of reference simulations.

simulation	$L_{\rm box}$ [h^{-1} Mpc]	$N_{\rm dm}$	$m_{\rm dm}$ [$10^5\ h^{-1}$ M$_\odot$]
L6N256	**6.25**	$\mathbf{256^3}$	**8.6**
r9L6N256	**6.25**	$\mathbf{256^3}$	**8.6**
L6N256winds	**6.25**	$\mathbf{256^3}$	**8.6**
r9L6N256winds	**6.25**	$\mathbf{256^3}$	**8.6**
L3N256	3.125	256^3	1.1
r9L3N256	3.125	256^3	1.1
L3N256winds	3.125	256^3	1.1
r9L3N256winds	3.125	256^3	1.1
L3N128	3.125	128^3	8.6
r9L3N128	3.125	128^3	8.6
L3N128winds	3.125	128^3	8.6
r9L3N128winds	3.125	128^3	8.6

fects the high-redshift ($z \geq 6$) SFR in the presence and absence of SN feedback and, conversely, how SN feedback affects the cosmic SFR in the presence and absence of a photo-ionising background. We find that the inclusion of SN feedback amplifies the suppression of the cosmic SFR due to the inclusion of photo-heating. On the other hand, the inclusion of photo-heating amplifies the suppression of the cosmic SFR due to the inclusion of SN feedback.

Photo-heating and SN feedback therefore mutually amplify each other in suppressing the SFR. Our results are relevant to current implementations of (semi-) analytic models of galaxy formation (see Baugh 2006 for a review), in which the effects of photo-heating and SN feedback are implicitly assumed to act independently of each other. These models may thus underestimate the strength of the combined negative feedback from photo-heating and SNe.

We emphasise that none of our simulations has a sufficiently high resolution to achieve convergence in the cosmic SFR. Future simulations will therefore be required to quantify our qualitative statement. We show, however, that the factor by which photo-heating and SN feedback amplify each other's ability to suppress the cosmic SFR becomes larger with increasing resolution, giving credibility to our main conclusion.

This chapter is organised as follows. We present our simulation method in §3.2 and we illustrate our main result in §3.3. Finally, we summarize our conclusions and discuss the caveats inherent to the present work in §3.4.

3.2 SIMULATIONS

Our simulation method is identical to that employed in Pawlik, Schaye, & van Scherpenzeel (2008), to which we refer the reader for more details. We use a modified version of the N-body/TreePM/SPH code GADGET-2 (Springel 2005) to perform a total of 12 cosmological SPH simulations at different resolutions, using different box sizes. We employ the set of cosmological parameters $[\Omega_{\rm m}, \Omega_{\rm b}, \Omega_\Lambda, \sigma_8, n_{\rm s}, h]$ given by $[0.258, 0.0441, 0.742, 0.796, 0.963, 0.719]$, in agreement with the WMAP 5-year observations (Komatsu et al. 2008). The simulations include radiative cooling, star formation and, optionally, photo-heating by a uniform UV background and/or kinetic feedback from SNe (see Table 3.1).

The gas is of primordial composition and is allowed to cool by collisional ionisation and excitation, emission of free-free and recombination radiation and Compton cooling off the cosmic microwave background. Molecular hydrogen is kept photo-dissociated at all times by the inclusion of a soft UV background. We employ the star formation recipe of Schaye & Dalla Vecchia (2008), to which we refer the reader for details. According to this recipe, gas forms stars at a pressure-dependent rate that reproduces the observed Kennicutt-Schmidt law (Kennicutt 1998).

Photo-ionisation (heating) is included in the optically thin limit using a uniform Haardt & Madau (2001) UV background from quasars and galaxies for redshifts $z \leq z_{\rm r} = 9$. The value for $z_{\rm r}$ is consistent with the most recent determination of the Thomson optical depth towards reionisation from the WMAP (5-year) experiment (Komatsu et al. 2008). We inject an additional thermal energy of 2 eV per proton at $z = z_{\rm r}$. In the absence of shocks, gas particles at the cosmic mean density are therefore kept at a temperature $T \approx 10^4$ K for $z < z_{\rm r}$ (see Fig. 1 of Pawlik, Schaye, & van Scherpenzeel 2008).

We model kinetic feedback from star formation using the prescription of Dalla Vecchia & Schaye (2008), according to which core-collapse SNe locally inject kinetic energy and kick gas particles into winds. The feedback is specified by two parameters, the initial wind mass loading in units of the newly formed stellar mass, η, and the initial wind velocity $v_{\rm w}$. We adopt $\eta = 2$ and $v_{\rm w} = 600~{\rm km\,s^{-1}}$, consistent with observations of local (e.g. Veilleux, Cecil, & Bland-Hawthorn 2005) and redshift $z \approx 3$ (e.g. Shapley et al. 2003) starburst galaxies. This choice of parameters implies that 40 per cent of the energy available from core-collapse SNe is injected as kinetic energy (assuming a Chabrier initial mass function in the range $0.1 \leq M/M_\odot \leq 100$ and $10^{51}~{\rm erg}$ per $M > 6~M_\odot$ star), while the remaining 60 per cent are implicitly assumed to be lost radiatively.

We use a Friends-of-Friends halo finder (Davis et al. 1985) with linking length $b = 0.2$ to obtain a list of dark matter halos contained in each of our simulation outputs. Only halos containing more than 100 dark matter particles are included in these lists. For each simulation output we compute the SFR associated with dark matter halo as follows. First, gas particles are attached to the nearest dark matter particle. Second, the SFR of a dark matter halo is the sum of the SFRs of the gas particles that were attached to the dark matter particles it contains.

3.3 RESULTS

Our main result is shown in Fig. 3.1. The top panel shows the evolution of the total SFR, defined as the sum of the star formation rates over all halos, for our set of reference simulations. We use $\dot{\rho}_{*,\rm wh}$, $\dot{\rho}_{*,\rm h}$ and $\dot{\rho}_{*,\rm w}$ to denote, respectively, the SFR densities in the simulations with both SN feedback and photo-heating (red dashed curve, *r9L6N256winds*), with photo-heating but without SN feedback (red solid curve, *r9L6N256*) and with SN feedback but without photo-heating (blue dashed curve, *L6N256winds*). We denote the SFR density in the simulation that included neither photo-heating nor wind feedback with $\dot{\rho}_*$ (blue solid curve, *L6N256*).

Both the inclusion of photo-heating and the inclusion of kinetic feedback from SNe lead to a significant suppression of the SFR. The factor $s_{\rm h} \equiv \dot{\rho}_*/\dot{\rho}_{*,\rm h}$ by which the SFR is suppressed due to photo-heating is smaller than the factor $s_{\rm w} \equiv \dot{\rho}_*/\dot{\rho}_{*,\rm w}$ by which the SFR is suppressed due to

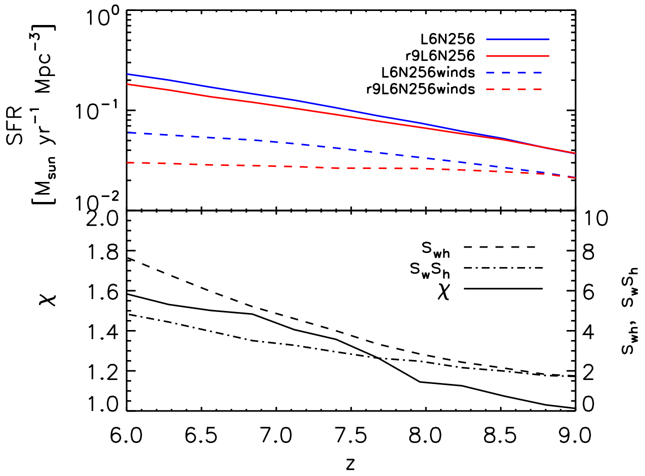

Figure 3.1: Top panel: evolution of the total SFRs in our set of reference simulations. Photo-heating and SN feedback were included for the red and dashed curves, respectively. Star formation is strongly suppressed when photo-heating and/or kinetic feedback from SNe are included. Bottom panel: Suppression factors $s_{\rm wh}$ and $s_{\rm w}s_{\rm h}$ (right y-axis) and feedback amplification factor $\chi \equiv s_{\rm wh}/(s_{\rm w}s_{\rm h})$ (left y-axis). The fact that $\chi > 1$ implies that photo-heating and SN feedback amplify each other's ability to suppress the SFR.

kinetic feedback. As expected, the simultaneous inclusion of photo-heating and feedback from SNe leads to a suppression of the SFR by a factor $s_{\rm wh} \equiv \dot{\rho}_*/\dot{\rho}_{*,\rm wh}$ that is larger than the factors $s_{\rm h}$ and $s_{\rm w}$ by which the SFRs are suppressed due to the sole inclusion of either photo-heating or SN feedback.

Interestingly, the factor by which the SFR is suppressed due to photo-heating is larger in the presence (set of dashed curves) than in the absence (set of solid curves) of SN feedback. Conversely, the factor by which the SFR is suppressed due to SN feedback is larger in the presence (set of red curves) than in the absence (set of blue curves) of photo-heating.

Photo-heating and SN feedback thus mutually amplify each other in suppressing the SFR. This amplification probably arises because the inclusion of photo-heating keeps the gas diffuse, which makes it easier for the winds to drag it out of halos. Winds, on the other hand, move gas from the central to the outer parts of halos, where it is more susceptible to the photo-evaporation process. Models that implicitly ignore this interaction between photo-heating and SN feedback, like for example (semi-) analytic models of galaxy formation (e.g., Khochfar & Ostriker 2008; Monaco, Fontanot, & Taffoni 2007; Benson et al. 2006; Croton et al. 2006; Benson et al. 2002; Somerville 2002), thus may underestimate the strength of the feedback these processes exert.

We now define the feedback amplification factor $\chi \equiv s_{\rm wh}/(s_{\rm w}s_{\rm h})$. A value $\chi = 1$ would indicate that photo-heating and SN feedback suppress the SFR independently of each other. A value $\chi > 1$ ($\chi < 1$) would indicate that photo-heating and SN feedback amplify (weaken) each other's ability to suppress the SFR. The evolution of the amplification factor χ is shown in the bottom panel of Fig. 3.1, together with that of $s_{\rm wh}$ and $s_{\rm w}s_{\rm h}$. The fact that $\chi > 1$ for $z < 9$ implies that photo-heating and SN feedback amplify each other in suppressing star formation.[2]

To demonstrate that this amplification is indeed mutual, we write $s_{\rm wh} \equiv s_{\rm w|h}s_{\rm h} \equiv s_{\rm h|w}s_{\rm w}$. This defines the suppression factors $s_{\rm w|h} = \dot{\rho}_{*,\rm h}/\dot{\rho}_{*,\rm wh}$ and $s_{\rm h|w} = \dot{\rho}_{*,\rm w}/\dot{\rho}_{*,\rm wh}$. Thus, $s_{\rm w|h}$ is the factor by which SN feedback suppresses the SFR in simulations that include photo-heating and $s_{\rm h|w}$ is the factor by which photo-heating suppresses the SFR in simulations that include SN feedback. We have

$$\frac{s_{\rm w|h}}{s_{\rm w}} = \frac{\dot{\rho}_{*,\rm h}/\dot{\rho}_{*,\rm wh}}{\dot{\rho}_*/\dot{\rho}_{*,\rm w}} = \frac{\dot{\rho}_{*,\rm w}/\dot{\rho}_{*,\rm wh}}{\dot{\rho}_*/\dot{\rho}_{*,\rm h}} = \frac{s_{\rm h|w}}{s_{\rm h}}. \tag{3.1}$$

---

[2] Note that in our simulations $s_{\rm h} = 1 = \chi$ for $z \geq 9$ because there is no photo-heating at these redshifts.

This shows explicitly that the amplification of the suppression of the SFR due to photo-heating in simulations that include SN feedback is equal to the amplification of the suppression of the SFR due to SN feedback in simulations that include photo-heating. It implies that we cannot determine whether photo-heating amplifies the effect of SN feedback or vice versa.

Fig. 3.2 shows, for our set of reference simulations, the dependence of the suppression of the SFR due to photo-heating and/or SN feedback on halo mass. The top panel shows the cumulative SFR at $z = 6$ in dark matter halos less massive than $M_{\rm dm}$. The bottom panel shows, similar to the bottom panel of Fig. 3.1, the feedback amplification factor χ obtained from analogous definitions of the suppression factors $s_{\rm h}, s_{\rm w}$ and $s_{\rm wh}$ applied to the cumulative SFR at $z = 6$ shown in the top panel. The vertical dotted lines indicate the dark matter mass corresponding to a virial temperature $T_{\rm vir} = 10^4$ K.

While photo-heating strongly decreases the SFR in halos with virial temperatures $T_{\rm vir} \lesssim 10^4$ K, the inclusion of SN feedback leads to a strong decrease in the SFR in halos with $T_{\rm vir} \gtrsim 10^4$ K. Radiative and kinetic feedback thus act mostly over complementary mass ranges. This dichotomy arises because photo-evaporation mainly affects the gas fractions of halos with masses that correspond to virial temperatures that are of order of or smaller than the thermal temperature to which the gas is photo-heated, $T_{\rm vir} \lesssim 10^4$ K. In contrast, star formation and the associated SN feedback become only efficient for halos with masses corresponding to $T_{\rm vir} \gtrsim 10^4$ K, because our simulations do not include radiative cooling from metals and molecules (and because of our limited resolution), which could potentially enable star formation in halos of much smaller virial temperatures.

The left-hand (right-hand) panels of Fig. 3.3 show the evolution (mass-dependence) of the feedback amplification factor χ obtained from simulations for which we have varied the size of the simulation box and/or the resolution. Note that the solid, black curves in the left-hand and right-hand panels are identical to the solid, black curves shown in the bottom panels of Figs. 3.1 and 3.2, respectively.

Changing the size of the simulation box by a factor of two (at fixed resolution; solid curves) has little effect. On the other hand, increasing the resolution by a factor of two (while keeping the size of the simulation box fixed; red curves) significantly increases χ. The increase in χ with increasing resolution is likely due to both an increase in the fraction of galaxies that are subject to photo-evaporation and an increase in the SFR (and thus associated SN feedback) of all galaxies.

3.4 DISCUSSION

Photo-heating from reionisation and supernova (SN) feedback are key processes that determine the star formation rate (SFR) in the high-redshift Universe. Using a set of cosmological SPH simulations that include radiative cooling and star formation, we analysed the $z \geq 6$ star formation history in the presence of photo-ionisation heating from a uniform UV background and/or kinetic feedback from core-collapse SNe. The inclusion of photo-heating and SN feedback both lead to a suppression of the SFR.

We showed that the factor by which the SFR is suppressed due to photo-heating is larger in the presence than in the absence of SN feedback. We also showed that the factor by which the SFR is suppressed due to the inclusion of SN feedback is larger in the presence than in the absence of photo-heating. This mutual amplification of SN feedback and reionisation heating is the central result of the present work.

We caution the reader that our simulations have not fully converged with respect to res-

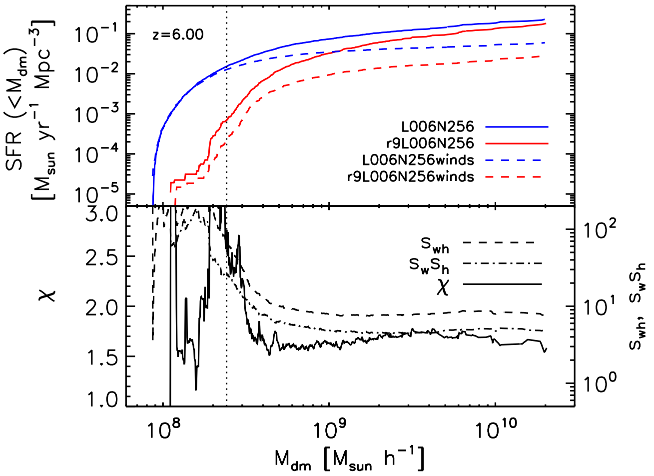

Figure 3.2: Top panel: cumulative SFRs as function of dark matter halo mass at $z = 6$ for our set of reference simulations. Photo-heating and SN feedback suppress the SFR over roughly complementary mass ranges. Bottom panel: similar to the bottom panel of Fig. 3.1, but now for the cumulative SFRs shown in the top panel. The vertical dotted lines indicate the dark matter mass corresponding to a virial temperature $T_{\rm vir} = 10^4$ K.

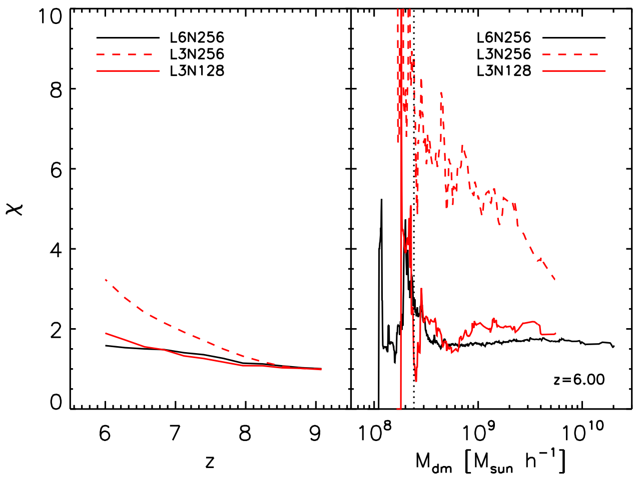

Figure 3.3: Evolution (left-hand panel) and mass-dependence (at $z = 6$; right-hand panel) of the feedback amplification factor χ for different choices of the box size and resolution. The vertical, dotted line in the right panel indicates the dark matter mass corresponding to a virial temperature $T_{\rm vir} = 10^4$ K. The feedback amplification factor is insensitive to the size of the simulation box but increases strongly with resolution.

olution and that we have ignored some potentially important physical processes. This result will therefore need to be confirmed and quantified with future simulations. In what follows we briefly discuss the most important physical effects that our analysis ignored.

We computed photo-heating rates from a uniform UV background in the optically thin limit. Our simulations therefore do not account for the self-shielding of gas from ionising radiation. This may lower the fraction of the gas that is photo-evaporated (e.g., Kitayama et al. 2000; Susa & Umemura 2004; Dijkstra et al. 2004). Iliev, Shapiro, & Raga (2005) (extending the work of Shapiro, Iliev, & Raga 2004) have, however, pointed out that regions that are initially self-shielded will eventually also be photo-evaporated: as subsequent layers of gas are photo-evaporated, previously self-shielded regions become exposed to ionising radiation and are eventually stripped away. Moreover, the evaporation of the initially self-shielded gas may proceed at a speed comparable to the speed predicted by simulations that compute photo-heating rates in the optically thin limit (Fig. 3 in Iliev, Shapiro, & Raga 2005). Note also that because SN explosions decrease the gas density, the effects of self-shielding may be less prominent in simulations that include this type of feedback. Clearly, the importance of self-shielding and the applicability of the optically thin limit to the present problem need to be critically assessed using cosmological radiation-hydrodynamical simulations.

Although all of our simulations employ a sufficiently high resolution to resolve all halos with virial temperatures $T_{\rm vir} \gtrsim 10^4$ K with at least 100 particles, none of them has the resolution to properly reproduce the properties of the multi-phase medium associated with the star-forming regions these halos host. The factors by which photo-heating and SN feedback suppress the SFR are therefore not yet converged. We have, however, demonstrated that the effect of mutual amplification of photo-heating and SN feedback becomes only stronger with increasing resolution.

Because we have assumed the presence of a photo-dissociating background, the formation of molecular hydrogen is suppressed in our simulations. In reality, the gas may contain a significant fraction of molecular hydrogen before reionisation (but see, e.g., Haiman, Rees, & Loeb 1997). Star formation and the associated kinetic feedback would then already be efficient in halos with virial temperatures much smaller than 10^4 K (e.g., Tegmark et al. 1997). Because the gas fraction in these halos would be affected by both photo-heating and SN feedback, we expect that the inclusion of molecular hydrogen would only strengthen our main result.

We have also ignored the existence of atoms and ions heavier than helium. SN explosions may, however, quickly enrich the interstellar and intergalactic gas with metals (e.g., Bromm, Yoshida, & Hernquist 2003), which would increase its ability to cool. Metal enrichment thus provides a positive feedback that may partially offset the negative kinetic feedback from SN explosions.

None of the caveats we discussed seems, however, likely to invalidate our main qualitative conclusion that photo-heating and SN explosions amplify each other's effect on the cosmic SFR. Galaxy formation models that treat the effects of photo-heating and SN explosions independently of each other, like e.g. (semi-) analytic models, may therefore significantly underestimate the effect of these feedback processes on the SFR. Because photo-heating and SN feedback are important processes that affect the gas in low mass-halos at all epochs, our findings may also have implications for the understanding of the properties of low-redshift galaxies, e.g. in the context of the missing satellite problem (for a recent discussion see, e.g., Koposov et al. 2009).

ACKNOWLEDGMENTS

We are grateful to Volker Springel for letting us use his implementation of a Friends-of-Friends halo finder and we thank Claudio Dalla Vecchia for his implementation of additional variables. Some of the simulations were run on the Cosmology Machine at the Institute for Computational Cosmology in Durham as part of the Virgo Consortium research programme. This work was supported by Marie Curie Excellence Grant MEXT-CT-2004-014112.

REFERENCES

Barkana R., Loeb A., 1999, ApJ, 523, 54

Barkana R., Loeb A., 2000, ApJ, 539, 20

Baugh C. M., 2006, RPPh, 69, 3101

Benson A. J., Sugiyama N., Nusser A., Lacey C. G., 2006, MNRAS, 369, 1055

Benson A. J., Lacey C. G., Baugh C. M., Cole S., Frenk C. S., 2002, MNRAS, 333, 156

Bromm V., Yoshida N., Hernquist L., 2003, ApJ, 596, L135

Ciardi B., Ferrara A., 2005, SSRv, 116, 625

Croton D. J., et al., 2006, MNRAS, 365, 11

Dalla Vecchia C., Schaye J., 2008, MNRAS, 387, 1431

Davis M., Efstathiou G., Frenk C. S., White S. D. M., 1985, ApJ, 292, 371

Dijkstra M., Haiman Z., Rees M. J., Weinberg D. H., 2004, ApJ, 601, 666

Efstathiou G., 1992, MNRAS, 256, 43P

Fujita A., Mac Low M.-M., Ferrara A., Meiksin A., 2004, ApJ, 613, 159

Gnedin N. Y., Hui L., 1998, MNRAS, 296, 44

Greif T. H., Johnson J. L., Bromm V., Klessen R. S., 2007, ApJ, 670, 1

Haardt F., Madau P., 2001, in Neumann D. M.,Van J. T. T., eds, Proc.XXXVI Rencontres de Moriond, Clusters of Galaxies and the High Redshift Universe Observed in X-Rays, preprint (astro-ph/0106018)

Haiman Z., Rees M. J., Loeb A., 1997, ApJ, 476, 458

Hui L., Gnedin N. Y., 1997, MNRAS, 292, 27

Iliev I. T., Shapiro P. R., Raga A. C., 2005, MNRAS, 361, 405

Kennicutt R. C., Jr., 1998, ApJ, 498, 541

Kitayama T., Tajiri Y., Umemura M., Susa H., Ikeuchi S., 2000, MNRAS, 315, L1

Kitayama T., Yoshida N., 2005, ApJ, 630, 675

Khochfar S., Ostriker J. P., 2008, ApJ, 680, 54

Komatsu E., et al., 2008, preprint (arXiv:0803.0547)

Koposov S. E., Yoo J., Rix H.-W., Weinberg D. H., Macciò A. V., Miralda-Escudé J., 2009, preprint (arXiv:0901.2116)

Loeb A., Barkana R., 2001, ARA&A, 39, 19

Mac Low M.-M., Ferrara A., 1999, ApJ, 513, 142

Monaco P., Fontanot F., Taffoni G., 2007, MNRAS, 375, 1189

Pawlik A. H, Schaye J., van Scherpenzeel, E., MNRAS, in press, preprint (arXiv:0807.3963)

Scannapieco C., Tissera P. B., White S. D. M., Springel V., 2006, MNRAS, 371, 1125

Schaye J., Dalla Vecchia C., 2008, MNRAS, 383, 1210

Shapiro P. R., Giroux M. L., Babul A., 1994, ApJ, 427, 25

Shapiro P. R., Iliev I. T., Raga A. C., 2004, MNRAS, 348, 753

Shapley A. E., Steidel C. C., Pettini M., Adelberger K. L., 2003, ApJ, 588, 65

Somerville R. S., 2002, ApJ, 572, L23

Springel V., 2005, MNRAS, 364, 1105

Susa H., Umemura M., 2004, ApJ, 600, 1

Susa H., Umemura M., 2006, ApJ, 645, L93

Tasker E. J., Bryan G. L., 2008, ApJ, 673, 810

Tassis K., Abel T., Bryan G. L., Norman M. L., 2003, ApJ, 587, 13

Tegmark M., Silk J., Rees M. J., Blanchard A., Abel T., Palla F., 1997, ApJ, 474, 1

Thoul A. A., Weinberg D. H., 1996, ApJ, 465, 608

Veilleux S., Cecil G., Bland-Hawthorn J., 2005, ARA&A, 43, 769

Wiersma R. P. C., Schaye J., Smith B. D., 2009, MNRAS, 393, 99

Whalen D., van Veelen B., O'Shea B. W., Norman M. L., 2008, ApJ, 682, 49

Wise J. H., Abel T., 2008, ApJ, 685, 40

Yepes G., Kates R., Khokhlov A., Klypin A., 1997, MNRAS, 284, 235

> Dies ist ein Seidel vorher, aber du kannst
> auch Spucke dazu sagen, dann müssen
> vielleicht alle Spucke dazu sagen,
> getrunken wird aber doch daraus.
>
> Döblin, Berlin Alexanderplatz

CHAPTER 4

TRAPHIC - radiative transfer for smoothed particle hydrodynamics simulations

Andreas H. Pawlik & Joop Schaye

This chapter contains material that has been published together with the material presented in the next chapter, Chapter 5, in MNRAS 389 (2008), 651-677. It provides an updated version of Sections 1-4 in that publication.

We present TRAPHIC, a novel radiative transfer scheme for Smoothed Particle Hydrodynamics (SPH) simulations. TRAPHIC (TRAnsport of PHotons In Cones) is designed for use in simulations exhibiting a wide dynamic range and containing a large number of light sources. It is adaptive both in space and in angle and can be employed for application on distributed memory machines. The (time-dependent) radiative transfer equation is solved by tracing individual photon packets in an explicitly photon-conserving manner directly on the unstructured grid traced out by the set of SPH particles. To accomplish directed transport of radiation despite the irregular spatial distribution of the SPH particles, photons are guided inside cones. The expensive scaling of the computation time with the number of light sources that is encountered in conventional radiative transfer schemes is avoided by introducing a source merging procedure. In this chapter we limit ourself to the description of the radiative transfer scheme. Its implementation for use with state-of-the-art SPH simulations will be described and tested in Chapter 5.

4.1 INTRODUCTION

Radiation is one of the fundamental constituents of our Universe. Its interaction with baryons may lead to an energy exchange that can both heat and cool the matter, initiating pressure forces that may strongly influence the subsequent hydrodynamical evolution. Radiation may also exert a direct pressure force upon the matter through the exchange of momentum. Radiative interactions are furthermore often the dominating process in governing the excitation and ionization state of atoms and molecules. The inclusion of the transport of radiation into hydrodynamical simulations may therefore provide the key for interpreting the outcome of physical experiments and observational campaigns.

To perform hydrodynamical simulations, the Lagrangian technique Smoothed Particle Hydrodynamics (SPH; Gingold & Monaghan 1977; Lucy 1977) is often employed. In SPH, the continuum fluid is discretized using a finite set of point particles, each carrying its own collection of variables. The deformation of the fluid by internal and external processes manifests itself in a steady redistribution of the point particles in space. All it takes to determine the values of physical field variables at a given point in the simulation box is to perform a weighted average over the values these variables take on the particles in its surrounding. This elegant simplicity of the SPH technique is one of the many reasons for its success.

Although the first radiative transfer calculation was already included in SPH at the very birth of this numerical technique more than thirty years ago (Lucy 1977), the detailed treatment of radiation transport in SPH is still an enormous challenge. One of the main reasons for this is certainly the high dimensionality of the problem. In fact, the radiative transfer equation depends on no less than seven variables (three space coordinates, two angles, frequency and time). Moreover, existing numerical schemes to solve the radiative transfer equation have most often only been formulated for use with uniform grids. Despite these difficulties, there has been encouraging progress over the last years, with several interesting and rather different approaches (see Sec. 4.3). In this chapter we present a novel method to solve the radiative transfer equation in SPH. We specifically designed our method for use in hydrodynamical simulations exhibiting a wide dynamic range in physical length scales and containing a large number of light sources.

A prominent example for such simulations are cosmological simulations of large-scale structure formation. Performing cosmological simulations is an exceedingly demanding computational task. Difficulties in describing the growth of the initially tiny matter density perturbations produced before and during the event of recombination and their metamorphosis into the rich structure observable today do not only arise because of our ignorance of how to properly model the governing physical processes. Often, it is simply the lack of computational power which prevents us from faithfully representing the basic actions involved: Cosmological simulations are both time consuming and memory exhaustive. To overcome these computational challenges, one can make use of advanced techniques and resort to clever approximations, reducing the computational effort.

Consider the wide range of scales encountered in cosmological hydrodynamical simulations. According to the hierarchical model of structure formation, the first structures and building blocks of the evolving universe are expected to form at small scales. The non-linear evolution at these scales shapes the distribution of the matter at all times, thus necessitating simulations of high spatial resolution. On the other hand, we also require sufficiently large simulation boxes in order to properly account for the modulation of the small-scale nonlinear evolution by the large-scale structure formation processes (e.g. Barkana & Loeb 2004) and not to be deceived by the cosmic scatter.

To accommodate these two antithetic demands while keeping the number of particles representing the matter low enough to be computationally manageable, *spatially adaptive* SPH simulations have been invoked. It is then immediately clear that when solving the transport of radiation along with the gravito-hydrodynamics of the matter, one requires the radiative transfer scheme to be adaptive, too. Even spatially adaptive cosmological SPH simulations, however, make use of hundreds of millions of particles and are therefore still extremely memory-consuming. It is then indispensable to distribute the computational load over a large number of machines. For this reason, we require a radiative transfer scheme that is *parallel on distributed memory* machines.

When performing radiative transfer simulations, sources of light are assigned a special importance. As a result, the computation time of most of the available radiative transfer schemes scales linearly with the number of sources in the simulation box. However, in cosmological simulations, even at times as early as 1 billion years after the Big Bang, i.e. at a redshift of $z \sim 6$, a non-negligible amount ($\gtrsim 1$ per cent) of baryonic matter has undergone star formation. In addition to these stellar sources of light, the intergalactic gas emits photons too, producing a radiation component often referred to as diffuse radiation. Hence, without *breaking the linear scaling* with the number of light sources, radiative transfer simulations at the resolution of state-of-the-art cosmological hydrodynamic simulations need to be dispatched to the realm of the future.

In this paper we present a radiative transfer scheme for use in SPH simulations that is adaptive, parallel on distributed memory and that avoids the linear scaling of the computation time with the number of sources. Hence, it is ideally suited for application in large simulations covering a wide range of length scales and containing many sources. In our scheme we follow the propagation of individual photon packets. It is *explicitly photon-conserving* (Abel, Norman, & Madau 1999) and can be applied to solve the *time-dependent* radiative transfer equation. Because the photon packets are traced in cones, we refer to our scheme as TRAPHIC - TRAnsport of PHotons In Cones. The introduction of cones is required in order to perform the transport of photon packets directly on the unstructured grid defined by the SPH particles.

Although we have designed our radiative transfer scheme to be readily coupled to the hydrodynamic evolution of the matter in SPH simulations, here we limit ourselves to the description of the radiative transfer scheme itself. We will present and tests its implementation in a state-of-the-art SPH code in Chapter 5. We will report on fully coupled radiation-hydrodynamical SPH simulations employing our implementation of TRAPHIC in future work.

The outline for the rest of this chapter is as follows. We start with a brief review of the principles of SPH that we consider crucial for the understanding of the present work. In Sec. 4.3 we then recall the radiative transfer equation and place our radiative transfer method in context by reviewing the approaches that have been used to solve the radiative transfer problem in SPH so far. In Section 4.4 we give a detailed description of the ideas behind our method. This is done in two steps: a brief overview over the method is followed by a more detailed discussion. Throughout we will emphasise how we satisfy the requirements set by our primary aim of performing radiative transfer in simulations exhibiting a wide range in length scales and a large number of light sources. Finally, in Sec. 4.5 we summarise our approach and conclude with an outlook.

4.2 SMOOTHED PARTICLE HYDRODYNAMICS

Excellent reviews of SPH exist (see e.g. Monaghan 2005; Monaghan 1992; Price 2005). Here, we just briefly outline the basic principles we consider critical for the understanding of our radiative transfer method.

At the basis of SPH lies the representation of a field $A(\mathbf{r})$ by its integral interpolant $A_{\mathrm{I}}(\mathbf{r})$,

$$A_{\mathrm{I}}(\mathbf{r}) = \int d^3r' \, A(\mathbf{r}')W(\mathbf{r}-\mathbf{r}', h), \tag{4.1}$$

where the smoothing length h determines the spatial resolution. The interpolation kernel W satisfies

$$\begin{aligned} \int d^3r' \, W(\mathbf{r}-\mathbf{r}', h) &= 1 \qquad (4.2)\\ \lim_{h\to 0} W(\mathbf{r}-\mathbf{r}', h) &= \delta_{\mathrm{D}}(\mathbf{r}-\mathbf{r}'), \qquad (4.3) \end{aligned}$$

where δ_{D} is the Dirac delta function, such that $A_{\mathrm{I}}(\mathbf{r})$ coincides with $A(\mathbf{r})$ in the limit $h \to 0$. The last two conditions do not fix the functional form for W. An often adopted choice is the spherically symmetric compact spline

$$W(\mathbf{r}-\mathbf{r}', h) = \frac{8}{\pi h^3} \begin{cases} 1 - 6\left(\frac{r}{h}\right)^2 + 6\left(\frac{r}{h}\right)^3, & 0 \le \frac{r}{h} \le \frac{1}{2} \\ 2\left(1-\frac{r}{h}\right)^3, & \frac{1}{2} < \frac{r}{h} \le 1 \\ 0, & \frac{r}{h} > 1, \end{cases} \tag{4.4}$$

where $r = |\mathbf{r}-\mathbf{r}'|$. From here on, when referring to the interpolation kernel W, we assume that it is of this form. The discrete representation of a fluid by SPH particles is achieved by approximating the integral interpolant (Eq. 4.1) by the summation interpolant,

$$A_{\mathrm{I}}(\mathbf{r}) \approx A_{\mathrm{S}}(\mathbf{r}) = \sum_j \frac{m_j}{\rho_j} A(\mathbf{r}_j)W(\mathbf{r}-\mathbf{r}_j, h), \tag{4.5}$$

where the summation is over the particles of mass m and mass density ρ. For a self-contained numerical treatment, any field needs to be discretized only at the positions of the particles i representing the fluid,

$$A_i \equiv A_{\mathrm{S}}(\mathbf{r}_i) = \sum_j \frac{m_j}{\rho_j} A(\mathbf{r}_j)W(\mathbf{r}_i-\mathbf{r}_j, h). \tag{4.6}$$

Since the kernel W is compact, only local information needs to be accessed for the evaluation of the last sum, which can be carried out in a computationally efficient manner in parallel on distributed memory machines.

For the interpretation of Eq. 4.6, two main approaches can be taken, depending on the choice for h (Hernquist & Katz 1989). In the scattering approach each particle j is considered as a cloud of radius h_j and contributes to the field at the position of particle i with the weight $W(\mathbf{r}_i-\mathbf{r}_j, h_j)$. In the gathering approach, each particle i searches the sphere of radius h_i (in the following referred to as the sphere of influence, or *neighbourhood*) for particles (its *neighbours*) and obtains an estimate of the field value at its position by summing the field values at the positions of the neighbours j, each weighted by $W(\mathbf{r}_i-\mathbf{r}_j, h_i)$.

The two interpretations are identical only if the spatial resolution is fixed throughout the fluid, i.e. if $h_i = h_j = h$. However, the SPH formalism only unfolds its true strength by allowing the resolution to vary in space, according to the local density field. This is usually achieved by either directly fixing the number of neighbours N_{ngb} for all particles, or by requiring that the kernel volume contains a constant mass (Springel & Hernquist 2002).

4.3 RADIATIVE TRANSFER IN SPH - PREVIOUS WORK

Before describing TRAPHIC, our method to solve the radiative transfer equation in SPH, we briefly recall the radiative transfer equation and give a short overview of the main numerical methods that have been employed so far to obtain its solution in SPH simulations.

The classical equation of radiative transfer reads (see e.g. Mihalas & Weibel Mihalas 1984)

$$\frac{1}{c}\frac{\partial I_\nu}{\partial t} + \mathbf{n}\cdot\nabla I_\nu = \epsilon_\nu - \kappa_\nu \rho I_\nu. \tag{4.7}$$

In Eq. 4.7, $I_\nu \equiv I_\nu(\mathbf{r},\mathbf{n},t)$ is the monochromatic intensity (units ergs cm^{-2} s^{-1} Hz^{-1} sr^{-1}) of frequency ν at position $\mathbf{r}$, $\mathbf{n}$ is a unit vector along the direction of light propagation and c is the speed of light. Sources and sinks of radiation are described by the emissivity ϵ_ν (units ergs cm^{-3} s^{-1} Hz^{-1} sr^{-1}) and the mass absorption coefficient κ_ν (units cm^2 g^{-1}), respectively. In general, both ϵ_ν and κ_ν are functions of $\mathbf{r},\mathbf{n}$ and time t.

If we define the photon number density ψ_ν such that $\psi_\nu d\Omega d\nu$ is the number of photons per unit volume with frequencies $(\nu, \nu + d\nu)$ travelling with velocity c into a solid angle $d\Omega$ around $\mathbf{n}$, the intensity is given by $I_\nu = ch_{\rm p}\nu\psi_\nu$, where $h_{\rm p}$ is the Planck constant. Eq. 4.7 is a partial differential equation depending on seven variables, which in general is hard to solve. Different approximations have been employed to obtain its solution, giving rise to different numerical approaches. Below we discuss the main approaches that have been taken so far to accomplish the transport of radiation in SPH simulations.

In his study of optically thick proto-stars, Lucy (1977) modelled the transport of radiation as a diffusion process by including a corresponding term in the SPH formulation of the energy equation. Brookshaw (1994) pointed out drawbacks of the particular formulation used in Lucy (1977), and re-phrased the diffusion equation in SPH such as to reduce its sensitivity to particle disorder. This new formulation of the diffusion equation was employed by Viau, Bastien, & Cha (2006) to perform collapse simulations of centrally condensed clouds.

Treating the transport of radiation in the diffusion limit is, however, only a good approximation in optically thick media. In the optically thin regime, infinite signal propagation speeds result, since the diffusion equation is a partial differential equation of parabolic type. This defect can be remedied by supplementing the diffusion equation with a so-called flux-limiter. SPH simulations with flux-limited diffusion have been carried out by e.g. Herant et al. (1994), Whitehouse & Bate (2006), Fryer, Rockefeller, & Warren (2006) and Mayer et al. (2007), covering a wide range of physical applications, from supernovae explosions and proto-stellar collapse to the study of proto-planetary disks. The (flux-limited) diffusion approach to solve the radiative transfer equation fails in complex geometries. In particular, opaque obstacles illuminated by a point source do not cast sharp shadows, because the shadow region is filled in by the diffusion.

To solve the radiative transfer equation without being restricted to the optically thick regime or simple geometries, Monte Carlo techniques can be employed (Oxley & Woolfson 2003, Stamatellos & Whitworth 2005, Croft & Altay 2007, Semelin, Combes, & Baek 2007, Altay, Croft, & Pelupessy 2008). In Monte Carlo radiative transfer, individual photon packets emitted by each source are directly followed as they pass through the matter, thus simulating the physical process of radiation transport as encountered in nature. While Monte Carlo simulations allow realistic shadows to be cast behind opaque obstacles, they are computationally very demanding, since the Poisson noise inherent to the statistical description of the radiation field leads to a signal-to-noise ratio that grows only with the square-root of the number of photon packets emitted.

Ray-tracing schemes keep the advantages of Monte Carlo radiative transfer simulations, whilst not being affected by the statistical noise. In short, in ray-tracing schemes rays are cast from each source throughout the simulation box. The optical depth to each point in space is calculated along theses rays, and the attenuation of the flux emitted by the sources is obtained. Variants of ray-tracing working with photons instead of fluxes blur the differences with Monte-Carlo schemes.

Ray-tracing schemes are most easily implemented on a regular grid superimposed on the SPH density field. However, this implies that all information about substructure on scales smaller than the size of the grid cells is ignored. As a cure, adaptive grids have been invoked (e.g. Razoumov & Sommer-Larsen 2006, Alvarez, Bromm, & Shapiro 2006). In SPH, *grid-less* ray-tracing has been introduced by Kessel-Deynet & Burkert (2000) to investigate the effects of ionizing UV radiation by massive stars on the surrounding interstellar medium. The Strömgren volume method (Dale, Ercolano, & Clarke 2007, compare also Johnson, Greif, & Bromm 2007) and the ionization front tracking technique employed by Yoshida et al. (2007) are related approaches. Another grid-less radiation tracing scheme that has been applied to SPH simulations is presented in Ritzerveld & Icke (2006). Inspired by the Kessel-Deynet & Burkert (2000) approach, Susa (2006) describes a radiation-hydrodynamics scheme for the transport of ionizing radiation in cosmological simulations of structure formation.

One major drawback most ray-tracing schemes share with the Monte-Carlo technique is that the computational effort to solve the radiative transfer equation scales linearly with the number of sources in the simulation box, because rays are traced for each source in turn (but see Sec.4.4.2 later on). For this reason, SPH radiation-hydrodynamical simulations employing the ray-tracing approach have mostly been restricted to the study of problems involving only a few sources.

Recently, so-called moment methods have also been implemented for use with SPH simulations (Petkova & Springel 2008 for an adaptive, grid-less implementation; Finlator, Özel, & Davé 2009 for an implementation on a super-imposed grid). These methods work by forming an infinite hierarchy of moments of the radiative transfer equation, which is then solved. The moment approach allows for a straight-forward merging of sources, which renders its computation time independent of the source number. Its numerical solution requires, however, a closure relation that cuts the moment hierarchy to obtain a finite number of moments. Practically feasible choices for this closure relation shift the hyperbolic character of the radiative transfer equation to become diffusion-like. Moment methods therefore typically do not produce shadows behind opaque obstacles.

In the following sections we will describe TRAPHIC, a novel method to solve the radiative transfer equation in SPH. TRAPHIC employs a photon tracing technique that works directly on the discrete set of irregularly distributed SPH particles. It is designed to overcome the challenges set by our goal of carrying out large radiation-hydrodynamics SPH simulations exhibiting a wide dynamic range in length scales and containing a large number of light sources.

4.4 TRAPHIC - TRANSPORT OF PHOTONS IN CONES

In this section we give a detailed description of TRAPHIC, our method to solve the radiative transfer equation in SPH. We start the presentation of our radiative transfer scheme by sketching the main idea, in order to give an overview and to introduce the reader to the underlying concepts, which will be illustrated and explained in more detail in the subsequent sections. TRAPHIC is designed to solve the radiative transfer equation in three-dimensional SPH simulations. When illustrating concepts with schematic figures we will, however, restrict ourselves to two dimensions for the sake of clarity.

Although we ultimately aim at performing simulations in which the radiation transport is fully coupled to the hydrodynamics, here we assume that the SPH density field is static and that the radiation does not exert any thermodynamical or hydrodynamical feedback on the matter. We will report on the coupling of radiation and hydrodynamics in future work.

4.4.1 Overview

We solve the radiative transfer equation (Eq. 4.7) in finite steps $(t_{\mathrm{r}}, t_{\mathrm{r}} + \Delta t_{\mathrm{r}})$, where t_{r} is the current simulation time, by tracing photon packets radially away from their location of emission until a certain stopping criterion is fulfilled. We do not introduce a grid on which the photons are propagated. Instead, we propagate the photons directly on the discrete set of particles in the simulation. For the transport of photons we employ the same particle-to-neighbour communication scheme that is already used in the SPH simulation to solve the equations of hydrodynamics. That is, we accomplish the global transport of photons by propagating them only locally, between a particle and its $\tilde{N}_{\mathrm{ngb}}$ neighbours. We allow $\tilde{N}_{\mathrm{ngb}}$ to be different from N_{ngb}, the number of neighbours used during the SPH calculations. In SPH, N_{ngb} determines the adaptive spatial resolution of the hydrodynamical simulation. Similarly, in our scheme, $\tilde{N}_{\mathrm{ngb}}$ sets the adaptive spatial resolution of the radiation transport. It is the first of two numerical parameters in our method (see also the left-hand panel of Fig. 4.1).

Working directly on the set of SPH particles, our scheme exploits the full spatial resolution of the hydrodynamical simulation. A further advantage of our approach is that the radiation transport is automatically parallel on distributed memory, as long as the SPH simulation itself is parallel on distributed memory. This is in contrast to radiation-hydrodynamical schemes that employ individual communication schemes for the transport of radiation and the SPH computations. Our radiative transfer scheme can hence be coupled to the SPH simulation without introducing any additional computational structures.

The main challenge we face when performing radiation transport by propagating photons only from a particle to its neighbours is achieving a transport that is directed: Photons travel along straight rays, while the spatial distribution of the SPH particles is generally highly irregular. In the following we give an overview of the concepts employed in our scheme and describe how we overcome this and other challenges to accomplish the transport of radiation in SPH simulations.

We distinguish two types of particles present in SPH simulations that are relevant for the transport of photons: star particles and SPH (gas) particles. Only gas particles can interact with photons, via absorptions and scatterings. We assume, however, that both star and gas particles can be sources of photons and will therefore refer to them as source particles, or simply sources.

The transport of radiation at simulation time t_{r} over a single radiative transfer time step Δt_{r} starts with the emission of photons by the source particles. Subsequently, these photons are propagated downstream, radially away from the source, simultaneously for all sources. In our particle-to-neighbour transport scheme photons are propagated from gas particle to gas particle. On their way, photons may interact with the matter field discretized by the gas particles. Each gas particle can simultaneously receive photons, possibly emitted at different times, from multiple (in principle all) sources in the simulation. Their further propagation would require a loop over all propagation directions. We explicitly avoid the resulting linear scaling of the computation effort with the total number of sources by introducing a source merging procedure.

The distribution of photons amongst the neighbours of the source particles must respect the angular dependence of the source emissivity. We achieve this by introducing for each source a set of randomly oriented, tessellating *emission cones*[1](Sec.4.4.2), as illustrated in the middle panel of Fig. 4.1. The fraction of the total number of photons emitted into each cone is proportional to its solid angle. The emission direction (which we will equivalently refer to as the propagation direction) associated with each emitted photon packet is determined by the central axis of the emission cone. The number of cones used in the emission cone tessellation, N_c, is the second numerical parameter in our method. It sets the angular resolution. The random orientation given to the cones ensures that photons are not restricted to propagate along a fixed number of directions and prevents artefacts introduced by the shape of the emission cones.

Some of the emission cones may not contain any neighbours, as is the case for the bottom-right cone of the tessellation shown in the middle panel of Fig. 4.1. To nevertheless emit photons into the corresponding directions, we create additional neighbours to which the photons can then be transferred (Fig. 4.1, right-hand panel). We refer to these neighbours as virtual particles (ViPs), since they do not take part in the SPH simulation. The properties of the ViPs are obtained from those of the neighbouring SPH particles using SPH interpolation. ViPs compensate for the lack of neighbours in certain solid angles around the emitting source. Hence, by employing ViPs we introduce the freedom of choosing emission directions independently of the geometry of the SPH particle distribution. As we will argue in Section 4.4.2 and investigate in more detail in Appendix 4.A, this freedom is a necessary requirement for achieving a desired angular dependence of the transport process, e.g. the isotropic emission of photons by star particles, in any particle-to-neighbour transport scheme.

The photon packets distributed amongst the neighbours of the sources are further transferred downstream until they experience an interaction. In contrast to the emission of photons by source particles, gas particles distribute photons only amongst the subset of neighbours located in the downstream direction (see Fig. 4.2). We distinguish this directed particle-to-neighbour transport from the emission process by referring to it as *transmission* (Sec.4.4.2). In more detail, each gas particle transmits photons downstream by distributing photon packets amongst the subset of neighbours located in certain regular cones only. These so-called transmission cones are centred on the emission (propagation) direction associated with each photon packet and have an opening angle determined by the angular resolution, i.e. by N_c. They confine the photon packets to the cone into which they were emitted by the corresponding source particle. As a result, the photon packets are propagated radially away from the sources, in a manner that is independent of the geometry of the SPH particle distribution. Like emission cones, transmission cones might not contain any neighbours. Again we employ ViPs to accomplish the photon transport into the corresponding directions.

By keeping the opening angle of the cones fixed, the solid angle subtended by a transmission cone as viewed from the original source decreases with the distance from the source. As a result, the photon transport becomes adaptive in angle, as in the ray-splitting technique employed in ray-tracing schemes (e.g. Abel & Wandelt 2002). We will demonstrate later on, when testing a numerical implementation of our scheme (see Chapter 5), that the use of implicitly adaptive transmission cones confining the photon propagation yields sharp shadows behind opaque obstacles.

Gas particles receive photon packets from other particles through the processes of emission

---

[1] We use the word cone in a general sense. It does not necessarily describe, but includes in its meaning, a regular cone, which is defined as a pyramid with a circular cross section.

and transmission described above. A given gas particle can simultaneously receive multiple photon packets, which may each be associated with a different emission direction. In fact, our assumption that all star and gas particles in the simulation box can be source particles would imply that the number of directions from which photon packets can be simultaneously received by a given gas particle would scale linearly with the total number of particles in the simulation. The computational effort to accomplish the subsequent photon transmission along the associated directions would then also scale linearly with the total number of particles. Since this consideration applies to the transmission of photons by any SPH particle in the simulation, the total computational effort to solve the radiative transfer equation would scale no less than quadratically with the total number of SPH particles.

To avoid this computationally expensive scaling, we introduce a source *merging* procedure (cp. Fig. 4.4, which will be explained in more detail in Sec.4.4.2). We make use of the fact that source particles that are seen as close (in angle) to each other from a given gas particle can be approximated by, or merged into, a single point source. We average the emission directions associated with the photon packets received from sources in solid angle bins defined by a so-called reception cone tessellation which, except for a random rotation, is identical to the cone tessellation employed for the emission process. Consequently, photon packets need to be transmitted into at most $N_{\rm c}$ directions.

We distinguish two types of interactions with the matter field sampled by gas particles and ViPs that photons may experience. Absorption interactions change the number of photons contained in each packet. Scattering interactions change the propagation direction (and possibly the frequency) of the photons in a packet. All interactions are taken into account in an explicitly photon-conserving manner. We give a detailed description of interactions in Sec.4.4.3.

4.4.2 Transport of photons

We now expand on the description of our radiative transfer scheme given above. We comment in detail on the main concepts underlying TRAPHIC, i.e. the emission of photons by source particles, the transmission of photons by gas particles and the source merging procedure. The description of how these concepts are employed to advance the solution of the radiative transfer equation in time is deferred to Sec.4.4.4.

Photon emission by source particles

In this section we describe the emission of photons by source particles. Star particles emit photons according to their intrinsic luminosity, which can for instance be obtained from population synthesis models. An example of the emission of photons by gas particles is the emission of recombination radiation by a recombining ion.

Let us consider the emission of photons by source particle i, located at $\mathbf{r}_i$. We denote the number of photons emitted per unit time per unit frequency ν per unit solid angle Ω around the unit direction vector $\mathbf{n}$ by $\dot{\mathcal{N}}_{\nu,i}(\mathbf{n},\mathbf{r},t)$, or simply $\dot{\mathcal{N}}_{\nu,\mathbf{n},i}$. With this notation, the number of photons $\dot{\mathcal{N}}_{\nu,i}$ emitted per unit time at frequency ν is $\dot{\mathcal{N}}_{\nu,i} \equiv \int d\Omega\, \dot{\mathcal{N}}_{\nu,\mathbf{n},i}$, and the total number of photons emitted per unit time is $\dot{\mathcal{N}}_{\gamma,i} \equiv \int d\nu \;\int d\Omega\, \dot{\mathcal{N}}_{\nu,\mathbf{n},i}$.

Source particle i emits $\int_t^{t+\Delta t_{\rm r}} \dot{\mathcal{N}}_{\gamma,i}$ photons over the radiative transfer time step $\Delta t_{\rm r}$. In agreement with our particle-to-neighbour based transport approach, the emission process is modelled by distributing these photons amongst the $\tilde{N}_{\rm ngb}$ nearest gas particles, residing in a sphere of radius $\tilde{h}_i$ centred on $\mathbf{r}_i$. This sphere is schematically depicted in the left-hand panel of Fig. 4.1.

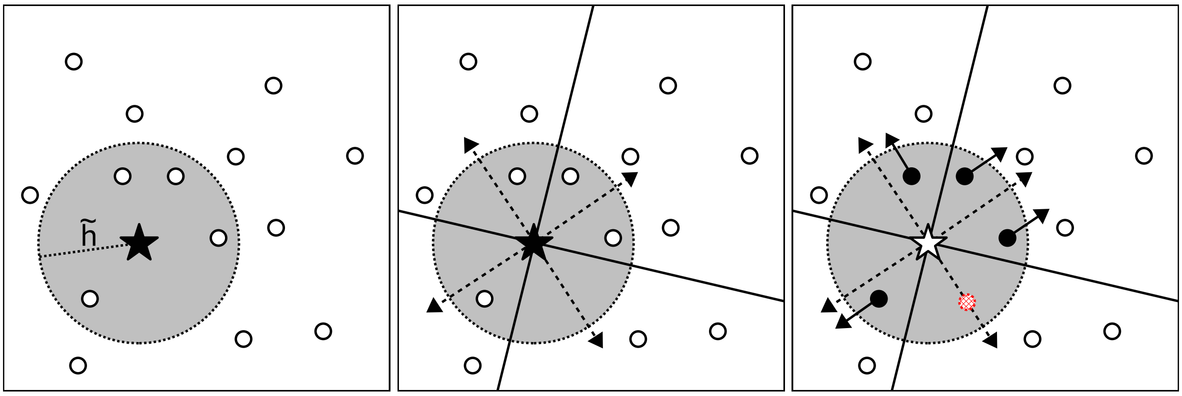

Figure 4.1: Emission of photon packets by source particles. *Left-hand panel:* A source particle (black star) and its neighbourhood (big grey disc). In this example the radius $\tilde{h}$ of the neighbourhood is defined such that there are $\tilde{N}_{\rm ngb} = 4$ neighbouring gas particles (white discs). *Middle panel:* The randomly oriented emission cone tessellation of the source particle (solid lines) is shown for the case $N_{\rm c} = 4$. The dashed arrows indicate the central axes of the cones. Note that the bottom-right cone does not contain a neighbouring gas particle. *Right-hand panel:* The source particle has transferred its photon packets to its neighbours (black discs). The emission direction (small solid arrows) associated with each packet points in the direction of the axis of the cone in which the neighbour resides. For the empty cone, a virtual particle is created (red hatched disc), placed randomly along the central axis of the cone.

Source particle i distributes its photons amongst its neighbours with the help of a set of space-filling emission cones, defined as follows (middle panel of Fig. 4.1). We tessellate the simulation box into $N_{\rm c}$ cones of (generally not identical) solid angles Ω_i^k, $k = 1, 2, ..., N_{\rm c}$, with the apexes located at the position $\mathbf{r}_i$ of particle i. The number of neighbours $\tilde{N}^k_{{\rm ngb},i}$ in each cone k is determined, taking values in the range $0 \le \tilde{N}^k_{{\rm ngb},i} \le \tilde{N}_{\rm ngb}$.

For what follows we consider the emission of photons for each frequency ν separately. To each neighbour j in cone k a photon packet of characteristic frequency ν is emitted. The packet contains a fraction $w_i^{kj} > 0$ ($j = 1...\tilde{N}^k_{{\rm ngb},i}$) of the total number of photons $\dot{\mathcal{N}}_{\nu,i}$ to be emitted per unit time at frequency ν, with

$$w_i^{kj} = \frac{\int_{\Omega_i^k} d\Omega\, \dot{\mathcal{N}}_{\nu,\mathbf{n},i}}{\int d\Omega\, \dot{\mathcal{N}}_{\nu,\mathbf{n},i}} \times \frac{w_i^j}{\sum_{l=1}^{\tilde{N}^k_{{\rm ngb},i}} w_i^l}, \tag{4.8}$$

where w_i^j are weights attached to neighbour j in cone k. The first factor on the right-hand side of Eq. 4.8 determines which fraction of the total number of photons is emitted into cone k, whereas the second factor controls the fraction of photons that is transferred to neighbour j, that is, it controls the distribution of photons amongst the particles within cone k. Here we set $w_i^j = 1$, i.e. equal weights for all neighbours in a given cone. The number of cones used in the tessellation, the parameter $N_{\rm c}$, determines the angular resolution of the radiation transport. A cone tessellation may consist of cones with different solid angles. We therefore define the angular resolution to be the size of the average solid angle, $\langle\Omega\rangle = 4\pi/N_{\rm c}$.

For each emission cone k the central axis is defined, characterised by the unit vector $\mathbf{n}_k$ pointing away from the source (Fig. 4.1, middle panel). We refer to this vector as the emission direction associated to photon packets emitted into cone k. When a photon packet is emitted to a neighbouring gas particle, the emission direction is transferred in addition to the number of photons it contains (Fig. 4.1, right-hand panel). Since the orientation of the emission cone tessellation is randomised by applying a random rotation at each emission, there is no a priori limit on the values the emission directions can take. Note that while we transfer the emission direction, we do not transfer the position of the source. Photon packets are traced further downstream based on their emission direction only, as we will explain in Sec.4.4.2. Each photon packet has also an associated *clock* $t^\star$. At emission the clock time is set to the time of the simulation, $t^\star = t_\mathrm{r}$. In Sec.4.4.4 we will see that the clock can be employed to propagate the photon packets at the speed of light.

Some cones may not contain any neighbouring gas particles. This is for instance the case for the bottom right cone in the middle panel of Fig. 4.1. For a fixed number of neighbours these empty cones will occur more frequently if the angular resolution is higher (i.e. if the solid angles of the cones are smaller). On the other hand, for a fixed angular resolution N_c, empty cones will occur more frequently if the number of neighbours $\tilde{N}_\mathrm{ngb}$ is smaller. Spatial clustering of the neighbours also increases the probability of the occurrence of empty emission cones. In the absence of a neighbouring gas particle photons cannot be transported along the emission direction of the empty cone. We therefore create a new neighbour, a so-called virtual particle (ViP), to which the photons are transferred. The ViP is placed along the cone axis at a random distance $< \tilde{h}_i$ from the source particle, such that the volume of the cone is uniformly sampled (see the right-hand panel of Fig. 4.1). The properties of ViPs (e.g. density) are determined from their neighbouring gas particles using SPH interpolation. ViPs are only employed for the transport of photons. We stress that ViPs are not used by the SPH simulation.

We emphasise that the introduction of cones is essential for accomplishing the emission process in our particle-to-neighbour transport scheme. To see this, consider the alternative of distributing the photons directly amongst the neighbours of gas particle i. This amounts to setting $\Omega_i^1 = 4\pi$ and $\Omega_i^j = 0$ for $j > 1$ in Eq. 4.8. Without any reference system, the emission directions associated to the photon packets would then be given by the unit vectors pointing from source i to neighbour j. In Appendix 4.A we show that in this case the net emission direction in general would correlate with the direction towards the centre of mass of the neighbours. As a result, the emission process would depend on the clustering of the neighbours in space as set by the geometry of the SPH simulation. The use of emission cones combined with ViPs gives us the freedom to choose emission directions independently of the spatial clustering of the neighbours. This allows us to model any angular dependence of the source emissivity, within the bounds of the chosen angular resolution.

In summary, source particles transfer photon packets to their neighbouring gas particles using a set of randomly oriented, tessellating cones. Each cone defines a direction of transport, i.e. the emission direction, associated with the packets. The random orientation applied to the cone tessellation ensures that photon packets are not transferred along a fixed set of directions only. Virtual particles (ViPs) are placed in emission cones not containing any neighbours, to which the photon packets are then transferred to. The combination of emission cones and ViPs makes the radiation transport independent of the spatial distribution of the neighbours.

Photon transmission by gas particles and ViPs

In the last section we described how a source particle distributes photon packets amongst the gas particles in its neighbourhood. For each packet we defined an emission direction, independently of the spatial distribution of the neighbouring gas particles by employing a randomly oriented set of emission cones. In this section we describe how the packets are propagated through the simulation box along their emission directions, by employing directed particle-to-

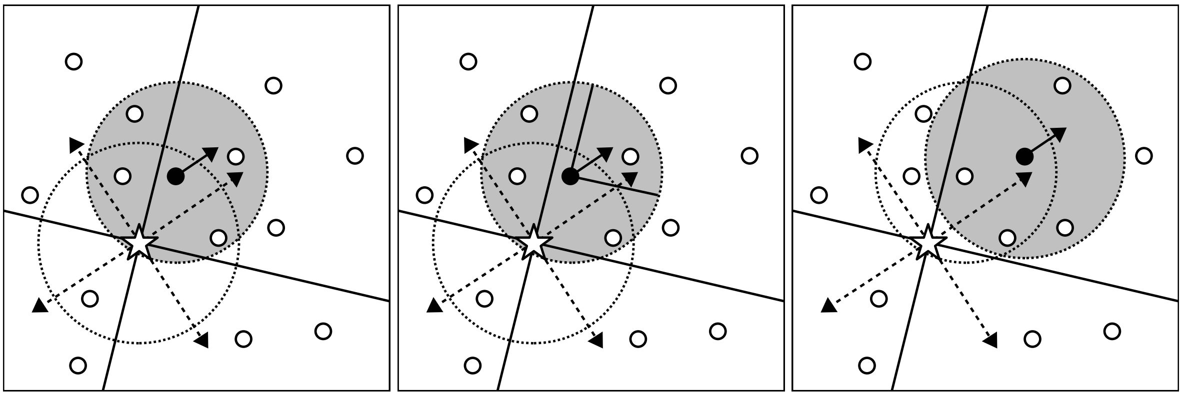

Figure 4.2: Transmission of photon packets by gas and virtual particles. The particle positions shown are the same as in Fig. 4.1, as are the neighbourhood (dashed circle) and emission cone tessellation of the source particle (white star). The transmission of photons is illustrated for one of the neighbours that received radiation from the star in Fig. 4.1. *Left-hand panel:* The neighbourhood (big grey disc) of the transmitting gas particle (black disc) is defined. As in Fig. 4.1, $\tilde{N}_{\rm ngb} = 4$. The emission direction associated with the photon packet to be transmitted is shown as the short solid arrow. *Middle panel:* The transmission cone is shown, centred on the emission direction of the photon packet that is to be transmitted. In this cone one downstream neighbour is found. *Right-hand panel:* The photon packet is transmitted to the downstream neighbour, turning it into a transmitting particle. The cycle repeats with defining the neighbourhood for this particle. As a result, the photon packet is propagated downstream, radially away from the source particle.

neighbour transport, a process which we refer to as transmission.

Consider a gas particle i, which receives a photon packet. Recall that the neighbours of particle i are the $\tilde{N}_{\rm ngb}$ nearest gas particles located in the sphere with radius $\tilde{h}_i$, centred on particle i (Fig. 4.2, left-hand panel). Analogous to the case of emission, particle i re-distributes the photons contained in the packet amongst its neighbours. In contrast to emission, photons are only distributed amongst the subset of neighbours $\tilde{N}_{\rm t,ngb} \leq \tilde{N}_{\rm ngb}$ located *downstream*. These are the neighbours residing in a *regular*[2] cone centred on the direction of propagation of the packet (see the middle panel of Fig. 4.2). We refer to this cone as transmission cone.

The apex of the transmission cone is located at the position of gas particle i. The solid angle of the cone is set by the angular resolution[3], $\Omega_{\rm t} = 4\pi/N_{\rm c} \equiv \langle\Omega\rangle$, and determines the apex angle ω through the standard relation

$$\omega = 2 \arccos\left(1 - \frac{\Omega_{\rm t}}{2\pi}\right) \times \frac{180}{\pi}. \tag{4.9}$$

We show this relation in Fig. 4.3. By definition, a neighbour j with position $\mathbf{r_j}$ is interior to the transmission cone with apex at the position $\mathbf{r}_i$ of the transmitting particle i if the inner angle between the transmission cone axis and the vector $\mathbf{r_j} - \mathbf{r}_i$ is less than $\omega/2$.

The received photon packet is split into $\tilde{N}_{\rm t,ngb}$ packets, each of which is transferred to one of the downstream neighbours j of particle i. The number of photons contained in each packet is set by the weights w_i^j, such that each neighbour j receives a photon fraction $w_i^j / \sum_k w_i^k$ of

---

[2] A regular cone is a pyramid with a circular cross-section.

[3] In principle it is possible to chose the solid angle of the transmission cones independently of the angular resolution $4\pi/N_{\rm c}$ implied by the reception cone tessellation. However, here we do not explore this option.

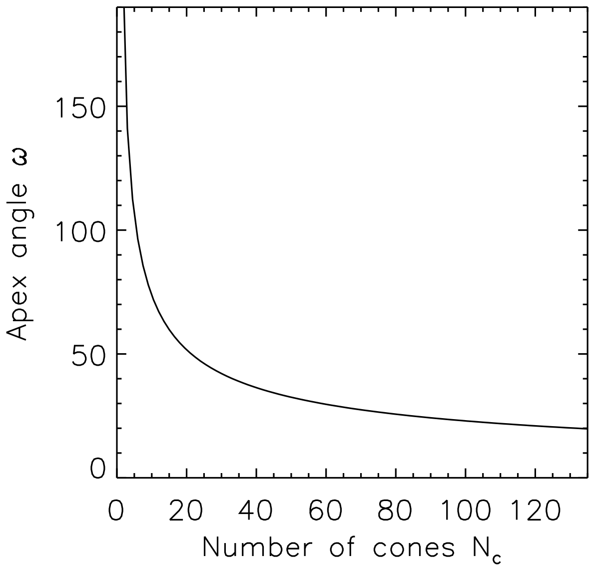

Figure 4.3: The apex angle ω of the transmission cones as a function of the angular resolution $N_{\rm c}$ (see Eq. 4.9).

the parent photon packet, where the sum is over all downstream neighbours $k = 1, ..., \tilde{N}_{\rm t,ngb}$. Here we assume $w_i^j = 1$, giving equal weight to each neighbour. If there are no downstream neighbours, i.e. if the transmission cone is empty, we simply create a neighbour as in the case of empty emission cones described in the previous section. That is, we place a virtual particle (ViP) along the emission direction of the photon packet, a random (in volume) radial distance $< \tilde{h}_i$ away from the transmitting gas particle. The properties of the ViP are determined by SPH interpolation from its neighbours, and the photon packet is transferred.

Each photon packet inherits the emission direction from its parent packet (Fig. 4.2, right-hand panel). After all packets have been transferred to the downstream neighbours, the transmission is finished. Subsequently, the transmission procedure can be applied again. The transmission process thus generally splits each photon packet into multiple packets, propagating with the same emission direction. With each subsequent transmission individual photon packets are confined to a smaller fraction of the solid angle traced out by the emission cone they were emitted into (see Fig. 4.2, middle panel). This is similar to the technique of ray splitting employed in ray-tracing codes. Hence, in TRAPHIC the photon transport takes place adaptively in angle.

The transmission procedure specified above for gas particles is also applied for ViPs. Again, the transmission cone of the ViP can either contain gas neighbours or be empty. If it is empty, the ViP creates another ViP, as in the case of transmission by gas particles. After the ViP has performed the transmission, it is deleted. ViPs are therefore temporary constructs. For $N_{\rm c} \gg \tilde{N}_{\rm ngb}$ the total number of ViPs in the simulation is proportional to $N_{\rm c}$, whereas for $\tilde{N}_{\rm ngb} \gg N_{\rm c}$ the total number of ViPs approaches zero.

The main purpose of the transmission cones is to confine the downstream propagation of photons to the solid angles into which they were emitted by the source particles, which is the main challenge for schemes using particle-to-neighbour transport. Just as emission cones were introduced to make the emission of photons by source particles independent of the geometry of the SPH particle distribution, transmission cones are introduced to further propagate the photons downstream, independently of the geometry of the SPH particle distribution. As a

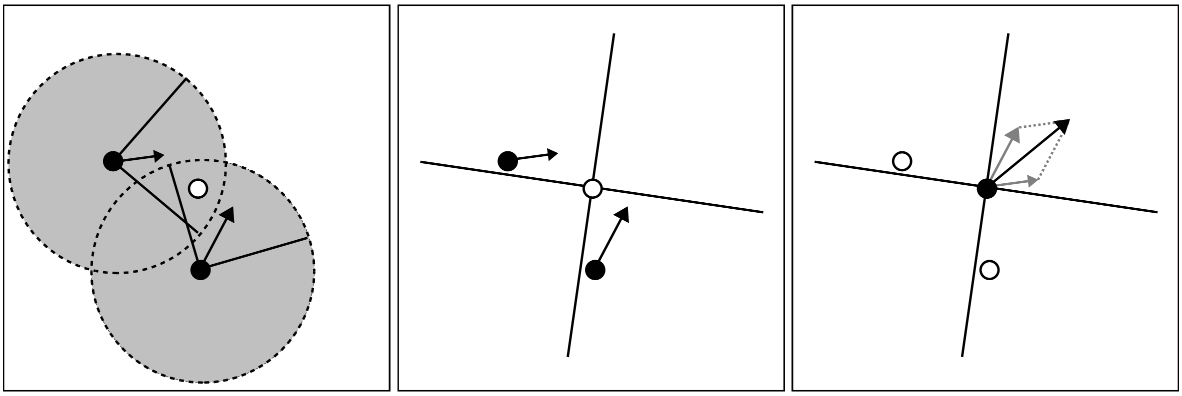

Figure 4.4: Merging of photon packets by gas particles. *Left-hand panel:* A gas particle (white disc) is receiving photon packets simultaneously from two transmitting gas particles (black discs). The emission direction associated with each photon packet is indicated by an arrow, whose length is given by the number of photons contained in the packet. The big grey discs indicate the neighbourhoods of the transmitting gas particles, the solid lines are the transmission cones (we assume $N_{\mathrm{c}} = 4$). For clarity, we do not show particles and photon packets that are not directly involved in the merging event. *Middle panel:* A randomly oriented reception cone tessellation is defined for the receiving gas particle. We omitted the transmission cones and the neighbourhoods of the transmitting particles. *Right-hand panel:* The photon packets have been transferred to the receiving gas particle, turning it into a transmitter. Their emission vectors (grey arrows), after translation to the position of the receiver, are both found to fall into the upper-right reception cone. Note that the particles itself fall into different reception cones. Their positions are irrelevant for the merging, since transmitted photon packets rather than transmitting particles are merged. The emission vectors are merged through a weighted average as described in Section 4.4.2, resulting in a single photon packet (black arrow).

consequence, shadows will be thrown behind opaque obstacles, and their sharpness will be in agreement with the chosen angular resolution. In fact, as we will see in Chapter 5, the shadows are much sharper than implied by the formal angular resolution.

The cones making up the emission tessellation will generally be irregular - in three dimensions there exists no tessellation of space with regular cones. The use of regular cones for the downstream propagation of photon packets emitted into a certain irregular emission cone is therefore an approximation. In principle, each photon packet could be transmitted into a cone having the shape of the emission cone it originates from. However, tracing photons within irregular cones is computationally more demanding. Furthermore, in the next section we will see the necessity for combining multiple photon packets propagating along different directions into a single photon packet that propagates along a correspondingly averaged direction. Since there is no unique way of defining the shape of a transmission cone associated with this average direction, we use a regular shape.

Photon merging by gas particles

In the previous section we described the transmission of a *single* photon packet arriving at a gas particle. In principle, each gas[4] particle can simultaneously receive *multiple* photon packets, possibly emitted by different sources at different times, propagating along different emission directions, a situation which is depicted schematically in the left-hand panel of Fig. 4.4. Ac-

---

[4] We do not consider ViPs here, since by construction each ViP can receive only a single photon packet.

complishing the transmission would then require executing a loop over all received packets for each transmitting gas particle. Clearly, for each gas particle this would imply a linear scaling of the computation effort with the number of packets that need to be transmitted, or in other words, with the total number of source particles present in the simulation.

In cosmological simulations of structure formation, for instance, where a significant number of star particles can usually be found already at high redshift, the simultaneous reception of multiple photon packets will be the rule rather than the exception. Even without taking into account the diffuse radiation of the intergalactic gas resulting from radiative de-excitations, recombinations and scatterings, a linear scaling with the number of sources would quickly turn the radiation transport into a computational task that would be too expensive to be carried out even with the most advanced supercomputer available today.

A few radiation tracing schemes have attempted to tackle this scaling problem by replacing sources that are close to each other with a single point source (e.g. Cen 2002; Razoumov & Sommer-Larsen 2006; Gnedin & Abel 2001). Here we introduce a photon packet merging procedure that strictly limits the number of packets that need to be transmitted per particle to at most $N_{\rm c}$, without restricting the number of directions along which each individual packet can propagate.

For each gas particle i receiving a photon packet we define a so-called reception cone tessellation, as shown in the middle panel of Fig. 4.4. A reception cone tessellation is a tessellating set of $N_{\rm c}$ cones attached to a gas particle. It is identical to the set of $N_{\rm c}$ cones employed for the emission of photons by source particles, but generally has a different orientation. As their name indicates, and in contrast to the emission cones, reception cones are used to collect photons. Whenever a photon packet p is transferred to gas particle i, the packet is binned into one of the reception cones by examining into which reception cone its emission direction $\mathbf{n}_p$ falls, after translation to the location of the gas particle. Photon packets whose emission directions fall in one and the same cone are merged, leaving only a single packet for transmission (Fig. 4.4, right-hand panel). The reception cone tessellation is given a random orientation to prevent artefacts.

A merged photon packet created in cone k is assigned the new, merged emission direction $\mathbf{n}_{m,k}$. This new emission direction is defined as the weighted sum[5] $\mathbf{n}_{m,k} = \sum w_p \mathbf{n}_p / |\sum w_p \mathbf{n}_p|$, where the sum is over all photon packets received in emission cone k ($k = 1, 2, ..., N_{\rm c}$), and the weights w_p are the number of photons per packet p that are to be transmitted into direction $\mathbf{n}_p$ to the downstream neighbours of particle i (Fig. 4.4, right-hand panel). Similarly, the merged photon packet is associated a merged clock $t^\star_{m,k}$ by averaging over the individual clock times $t^\star_p$ in reception cone k, i.e. $t^\star_{m,k} = \sum w_p t^\star_p / \sum w_p$.

As a result of the photon packet (resp. source) merging at most $N_{\rm c}$ packets have to be transmitted per gas particle, fully consistent with the angular resolution of our transport scheme. The computation effort required to perform radiative transfer simulations with TRAPHIC can therefore be readily controlled: In the most demanding situation, i.e. in the optically thin limit, when the whole box is filled with radiation, it merely scales with the product of spatial and angular resolution, $N \times \tilde{N}_{\rm ngb} \times N_{\rm c}$, where N is the total number of particles (SPH + stars). The merged photon packets are not associated with any existing source particle in the simulation. They should be thought of as emerging from an imaginary source, whose properties are implicitly defined by our merging prescription. The merged photon packets are traced further downstream, radially away from this imaginary source, into the merged emission direction,

---

[5] We note that this expression contains a typo in the original publication, i.e. in Pawlik & Schaye (2008). The sum used in that publication does not result in a unit vector, which is inconsistent with the employed notation.

exactly as was described for non-merged emission directions in the previous section.

4.4.3 Photon interactions with gas particles

Photons are propagated radially away from each source until they interact with the matter represented by the SPH particles. Here we distinguish between absorptions and scattering interactions and describe how they are accounted for in TRAPHIC. We remind the reader that in this chapter we do not discuss the effect of interactions on the thermodynamical and hydrodynamical evolution of the SPH particles.

Absorption

Absorptions remove photons from the beam emitted by the source. This process is described in terms of the mass absorption coefficient κ_ν. From the formal solution of the radiative transfer equation it can easily be seen (e.g. Mihalas & Weibel Mihalas 1984) that the fraction of photons of frequency ν that is absorbed while travelling along the straight line connecting the positions $\mathbf{r}_1$ and $\mathbf{r}_2$ is given by $1 - \exp(-\tau)$, where

$$\tau = \int_{\mathbf{r}_1}^{\mathbf{r}_2} dr\ \kappa_\nu(r)\rho(r), \tag{4.10}$$

is the optical depth over the distance $d = |\mathbf{r}_1 - \mathbf{r}_2|$.

In TRAPHIC, absorptions are accounted for by removing the photon fraction $1 - \exp(-\tau_{ij})$ from photon packets propagating between particle i and its neighbouring particles j. For the calculation of the optical depth τ_{ij} between these two particles we need to numerically evaluate the integral Eq. 4.10. This is computationally expensive, since it involves the calculation of the density ρ (and the absorption coefficient κ_ν) at a large number of points along the photon path using the SPH formulation. Similar to the approach of Kessel-Deynet & Burkert (2000), we therefore approximate the density field near a gas or virtual particle i by the SPH density ρ_i evaluated at its position.

Since photon packets are propagated between particle i, located at $\mathbf{r}_i$, and particle j, located at $\mathbf{r}_j$, along their emission direction, i.e. in the direction of the unit vector $\mathbf{n}$, the distance d they cover is generally not equal to the distance between the particles. Instead, we set $d = |\mathbf{n} \cdot (\mathbf{r}_i - \mathbf{r}_j)|$, i.e., we employ the projection of the particle distance along the emission direction. This is the correct limit far away from the source from which the photon packets originate, but is not applicable close to it. Therefore, we only employ the projected distance when propagating photons between a transmitting particle and its neighbours. On the other hand, when propagating photons from a source particle to its neighbours, we use the particle distance, i.e. we set $d = |\mathbf{r}_j - \mathbf{r}_i|$, corresponding to radially outward propagation.

The distance d is used to obtain the optical depth τ_{ij} between particle i and particle j. We set $\tau_{ij} = \kappa_\nu \rho_j d$. This approximation neglects the existence of any substructure between particle i and its neighbouring particle j. However, this does not result in a loss of information if the radius $\tilde{h}_i$ of the neighbourhood of particle i is chosen such that $\tilde{h}_i \lesssim h_i$ (resp. $\tilde{N}_{\mathrm{ngb}} \lesssim N_{\mathrm{ngb}}$).

The distance d is furthermore used to advance the clock $t^\star$ of each photon packet according to the rule

$$t^\star \to t^\star + d/c. \tag{4.11}$$

By synchronising the clock $t^\star$ with the simulation time t_{r}, the clock can be employed to advance photon packets at the speed of light, as we discuss in Sec. 4.4.4. We note in passing that the clock $t^\star$ can also be used to implement the cosmological redshifting of photons.

The number of absorbed and transmitted photons is now calculated as follows. From the photon packet emitted or transmitted by particle i to particle j, a fraction $1 - \exp(-\tau_{ij})$ is absorbed by particle j. The photon packet is subsequently transmitted by particle j containing a fraction $\exp(-\tau_{ij})$ of the original number of photons. By construction, this procedure explicitly conserves photons, since

$$1 - e^{-\tau_{ij}} + e^{-\tau_{ij}} = 1. \tag{4.12}$$

Photons absorbed by ViPs are distributed amongst all neighbours of the ViP using photon-conserving SPH interpolation. This is necessary, because ViPs are a temporary construct employed for the transport of photons; permanent information is only stored at the particles in the SPH simulation. For further reference, we denote the total number of photons impinging on and the total number of photons absorbed by particle i over a single time step Δt_{r} with $\Delta\mathcal{N}_{\mathrm{in},i}$ and $\Delta\mathcal{N}_{\mathrm{abs},i}$, resp.

Scattering

In contrast to absorptions, scatterings change the direction and possibly the frequency of the interacting photons. A scattering event can be thought of as an absorption event followed by an immediate re-emission. Scatterings can hence be described by Eq. 4.7 after adapting the absorption coefficient κ_ν and the emissivity ϵ_ν. The re-emission re-distributes the photons in angle (and possibly frequency). For this reason the scattered photons are sometimes referred to as diffuse. Adapting the emissivity for scatterings requires evaluating an integral over the angular dependence of the intensity. Therefore, scatterings turn the radiative transfer equation (Eq. 4.7) into an integro-differential equation.

In TRAPHIC, scatterings, that is the transport of diffuse photons, are modelled by a combination of absorption and re-emission events. Photons to be scattered travelling between two particles are first removed from the photon packet as described in the last section. For a true absorption event, the photon energy would be lost to the thermal bath provided by the matter. In contrast, in case of scattering, a gas particle that absorbed photons re-emits them, closely following the description for source particles in Sec.4.4.2.

In particular, we employ randomly oriented emission cones in combination with Eq. 4.8 to re-emit the absorbed photons. Since modelling the scattering process means following photons emitted earlier by a source, the clock of the photon packets that are to be re-emitted is not set to the simulation time t_{r}, as was the case for the intrinsic emission of photons by source particles. Instead, it is determined by the clock of the photon packets that are scattered and the details of the scattering interactions (e.g. there could be a time delay between absorption and re-emission, or photons could have travelled a distance greater than the (projected) particle distance d when inferring the properties of the scattering process from a sub-resolution model). If the scattering details are taken into account by correspondingly adjusting d, Eq. 4.11 can be employed to find the new clock time. Note that it is crucial for the modelling of scatterings to employ a radiative transfer scheme which does not scale with the number of sources, since every gas particle will soon re-emit photons.

4.4.4 Solving the radiative transfer equation

TRAPHIC solves the radiative transfer equation (Eq. 4.7) in discrete time steps Δt_{r}, the size of which depends on the details of the problem under study and has to be decided on a case by case basis. Hence, we defer its discussion to chapter 5, where we present an implementation of

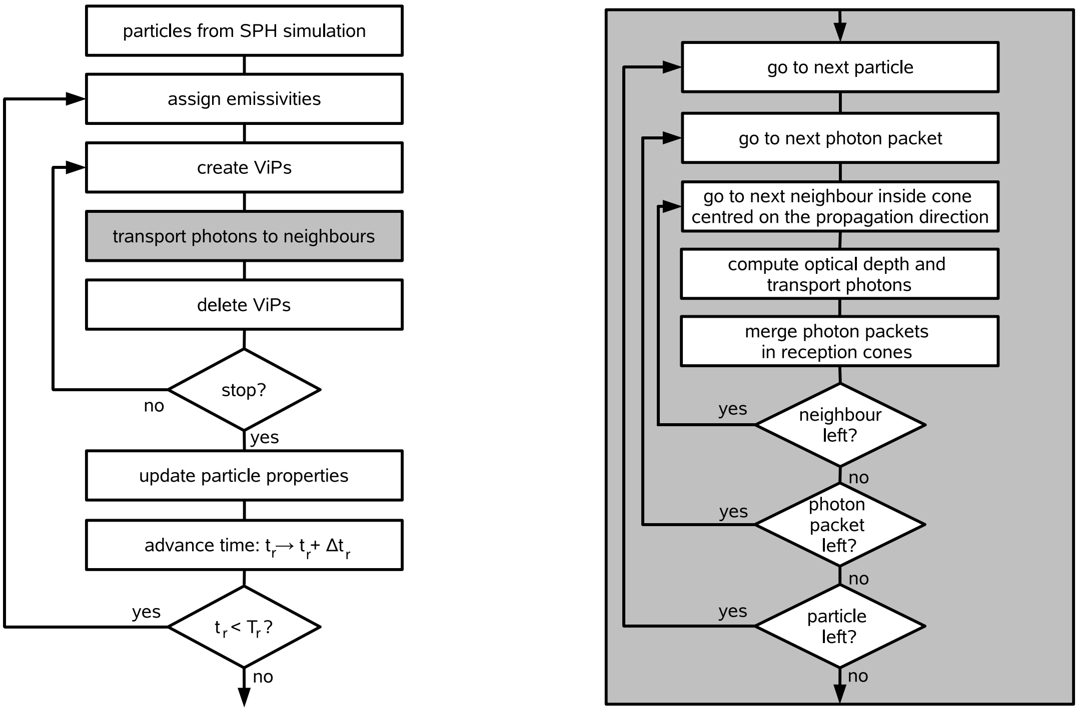

Figure 4.5: Flow charts. *Left-hand chart:* Overview of the radiation transport with TRAPHIC. The radiative transfer simulation starts with the assignment of emissivities to source particles. Thereafter, photon packets are transported from all particles to their neighbours (see right-hand chart for details). ViPs, if needed, are created in advance of the transport and are deleted immediately afterwards. The transport cycle continues until the user-defined stopping criterion is satisfied. Then, the properties of the particles are updated according to the photon-matter interactions that occurred. Finally, the radiative transfer time step is advanced. The radiative transfer simulation ends at time T_r. *Right-hand chart:* Details of the transport of photons to neighbours (grey box in the left-hand panel). Each particle holds at most N_c photon packets. The photons in these packets are distribute amongst the $\tilde{N}_\mathrm{ngb}$ neighbouring particles inside (tessellating) emission or (regular) transmission cones centred on the corresponding propagation directions. The optical depth to each neighbour is computed and the fraction of transmitted and absorbed/scattered photons is determined. Multiple photon packets received by individual neighbors are merged in (tessellating) reception cones, which limits the number of photon packets held by each particle to at most N_c.

our method to solve specific problems. In this section we briefly review the concepts described in the previous sections used to obtain the solution to the radiative transfer equation over a single time step before discussing how this solution is advanced in time. A schematic summary is provided by the flow chart in Fig. 4.5.

Starting at simulation time $t_{\rm r}$, the size of the radiative transfer time step $\Delta t_{\rm r}$ is determined. Source particles emit photon packets to their $\tilde{N}_{\rm ngb}$ neighbouring gas particles employing $N_{\rm c}$ cones. The total number of photons contained in the packets is determined by the number of photons $\dot{\mathcal{N}}_{\nu,i}$ to be emitted per unit time in frequency bin ν and by the size of the time step $\Delta t_{\rm r}$. For each neighbouring gas particle the optical depth to the source particle is evaluated and the number of photons interacting with the matter on their way from the source particle is inferred. Some photons may be absorbed, some may be scattered; the remaining photons are left unimpeded for transmission.

For the subsequent transmission of photons by the gas particles, photons associated to sources that are seen as close (in angle) to each other are merged, limiting the number of directions into which photons have to be transmitted to at most $N_{\rm c}$. Next, for each transmitting and scattering gas particle the $\tilde{N}_{\rm ngb}$ neighbours are found. Photons to be transmitted are distributed amongst the subset $\tilde{N}_{\rm t,ngb}$ of neighbours that are located downstream, as determined by the corresponding (merged) emission directions. Photons to be scattered are distributed amongst all $\tilde{N}_{\rm ngb}$ neighbours following the prescription in Sec.4.4.3. Virtual particles (ViPs), which are placed in cones that do not contain any neighbours, are deleted after having transmitted or scattered their photons. Photons that were absorbed by a ViP are distributed amongst the neighbours of the ViP using photon-conserving SPH interpolation.

The cycle described in the previous paragraph repeats until a stopping criterion is satisfied. The form of the stopping criterion depends on whether one solves the time-*independent* or the time-*dependent* radiative transfer equation. When solving the time-independent radiative transfer equation, i.e. when neglecting the first term on the left hand side of Eq. 4.7, one formally assumes $c \to \infty$. Accordingly, the stopping criterion becomes independent of the speed of light. The cycle can then for example be repeated until all photons have been absorbed or have left the simulation box. In contrast, when solving the time-dependent radiative transfer equation, the stopping criterion is directly tied to the speed of light c: the cycle is repeated until all photons have propagated a distance $c\Delta t_{\rm r}$.

To decide whether or not a photon packet has travelled over the distance $c\Delta t_{\rm r}$, we employ its clock $t^\star$. For further illustration it is convenient to explicitly follow the clock of a photon packet as it is propagated through the simulation box. Upon emission, the clock of the photon packet is initialised with the simulation time $t_{\rm r}$, as already mentioned in Sec. 4.4.2. After the emission, when the photon packet has been transferred from the source to one of the neighbouring SPH particles (or to a ViP), its clock is advanced according to Eq. 4.11. It is then checked whether the clock has reached or crossed the threshold value

$$t^\star_{\rm thr} = t_{\rm r} + \Delta t_{\rm r}. \tag{4.13}$$

If not, the photon packet is transmitted further downstream. As before, its clock is advanced according to Eq. 4.11. The photon packet is repeatedly transmitted and its clock is advanced until it has reached or crossed the threshold value defined in Eq. 4.13. At this point, the value displayed by its clock can in full generality be expressed as $t^\star = t^\star_{\rm thr} + \epsilon_0$, with $\epsilon_0 \geq 0$.

The propagation error, ϵ_0, is typically larger than zero because the set of particles on which the photon packets are propagated is discrete, with the particle-to-neighbour distances generally not related to $c\Delta t_{\rm r}$. Employing Eq. 4.13 to stop photon packets therefore results in the photon packets typically being propagated too far. Due to the Lagrangian nature of the SPH simulation, ϵ_0 is individual for each photon packet. If d is the particle-to-neighbour distance corresponding to the emission or transmission event after which the photon packet was stopped, then $\epsilon_0 < d/c$. The propagation error ϵ_0 is therefore strictly limited, $\epsilon_0 < \max_i \tilde{h}_i/c$, where the maximum is over all emitting and transmitting particles. Note that ϵ_0 becomes smaller with higher spatial resolution.

Once stopped, a photon packet is held (and hence its clock stands still) until the simulation time progresses to a value $t_\mathrm{r} + \Delta t_\mathrm{r} > t^\star$, at which point the packet is transmitted and its clock is advanced again. The clocks of photon packets are thus kept in synchronisation with the current simulation time, which effectively matches their propagation speed to become the speed of light[6]. Photon packets may be held over several radiative transfer time steps, as ϵ_0 may be (several times) larger than Δt_r. While the photon packet is held, its propagation error with respect to the current simulation time steadily decreases with each passing radiative transfer time step. Since $t^\star$ is fixed while t_r is increasing in steps of Δt_r, the current propagation error decreases according to $\epsilon_n = \epsilon_{n-1} - \Delta t_\mathrm{r}$, where n indicates the number of radiative transfer time steps that have passed since the photon packet was stopped. Immediately before the photon packet is propagated again, its propagation error is strictly limited by the size of the time step, $-\Delta t_\mathrm{r} \leq \epsilon_n < 0$. The photon packet is then propagated such as to again bring the clock into synchronisation with the simulation time, as described above.

When multiple photon packets are merged into a single packet, the clock of the merged packet is determined by the averaging procedure described in Sec.4.4.2. As a result, photons may be propagated over distances that differ somewhat from the case without merging. We have seen above that, due to the synchronisation of the photon packet propagation with the current simulation time t_r, clocks display only values in the interval $t_\mathrm{r} \leq t^\star \leq t_\mathrm{r} + \Delta t_\mathrm{r} + \epsilon_0$. The difference in the clocks of different photon packets and hence the photon propagation error introduced by the merging procedure can therefore be controlled to become arbitrarily small by increasing the temporal (i.e. decreasing Δt_r) and spatial (leading to smaller ϵ_0) resolution.

After the stopping criterion (time-independent or time-dependent) has been fulfilled for all photon packets, the properties of gas particles are updated according to the radiative interactions that occurred. We emphasise that the properties of the gas particles (e.g. the ionization state) are therefore only updated at the end of each time step. Within each time step the order in which photon packets from different sources arrive at gas particles is therefore irrelevant. After updating the particle properties, the simulation time is advanced, $t_\mathrm{r} \rightarrow t_\mathrm{r} + \Delta t_\mathrm{r}$. Finally, the size of the next time step is determined and the radiation is transported as described above.

In summary, we have presented a radiative transfer scheme for use in SPH simulations that works directly on the unstructured grid formed by the discrete set of irregularly distributed SPH particles. TRAPHIC thus employs the full spatial resolution of the SPH simulation. It achieves directed transport of radiation by adaptively tracing photon packets in cones. TRAPHIC can be used to solve both the time-independent and the time-dependent radiative transfer equation in an explicitly photon-conserving way. Our scheme is by construction parallel on distributed memory machines if the SPH simulation itself is parallel on distributed memory machines. Furthermore, the computation time necessary to accomplish the radiation transport does not scale linearly with the number of sources. Instead, it merely scales with the product of spatial and angular resolution, making our scheme suitable for simulations contain-

---

[6] We note that the clocks can also be employed to propagate photon packets at speeds $\tilde{c}$ different from the speed of light (cp. the reduced speed of light approximation suggested in Gnedin & Abel 2001), by simply making the replacement $c \rightarrow \tilde{c}$.

ing a large number of sources as well as for taking into account a diffuse radiation component.

4.4.5 Reduction of particle noise

The radiative transfer equation describes the propagation of photons within a continuum. In our scheme, however, photons are propagated on the discrete set of SPH particles, localised at irregular positions dictated by the SPH simulation. Consequently, numerical noise may arise from the discreteness and irregularity of the spatial distribution of SPH particles and this could influence the numerical solution of the radiative transfer equation obtained with TRAPHIC.

To see how this *particle noise* can be reduced, it is helpful to employ a formal analogy (e.g. Monaghan 2005) between estimating the density in SPH simulations and estimating a probability density from sample points: We can consider the positions of the SPH particles as a random[7] sample drawn from a probability density function proportional to the mass density. We can therefore Monte Carlo resample[8] the density field without sacrificing its information content. Periodically assigning new positions to the SPH particles during the radiation transport by resampling the density field should lead to a better representation of the continuum physics by the discrete set of SPH particles and hence lead to a reduction of particle noise.

To employ the resampling, we think of particle i at position $\mathbf{r_i}$ in the simulation box as being de-localised within its sphere of influence of radius h_i centred on $\mathbf{r_i}$ and assume that the probability of finding it in the volume d^3r around a particular point $\mathbf{r}$ in that sphere is given by the value of the interpolation kernel at that point (cp. the scattering approach of Sec.4.2). For the radiative transfer on a static set of particles with positions $\mathbf{r}_i$ we then periodically Monte Carlo re-distribute the particles within their sphere of influence according to this probability. We note that while we change the positions of the SPH particles, we keep all their other properties (e.g. density) fixed in order to avoid introducing scatter in the physical variables. In the tests performed in Chapter 5 we will demonstrate that the application of this recipe leads to a significant reduction of particle noise. There we will, however, also see that for most applications the noise is small. We therefore do not employ the resampling technique in our simulations, unless explicitly stated.

Since the resampling randomly offsets the SPH particles from their positions provided by the hydrodynamical simulation, the apexes of the transmission cones attached to them are randomly offset, too. The resampling procedure may therefore lead to a slight diffusion of photons out of the emission cone they were emitted into, effectively decreasing the angular resolution. Note that a similar diffusion of photons could occur when solving the radiative transfer equation coupled to the hydrodynamics (on which we will report in a future publication), because of the physical particle motion. We will study this diffusion in our numerical implementation of TRAPHIC that we present in Chapter 5, but note already that it does not lead to any noticeable degradation of the effective angular resolution and hence leaves TRAPHIC's shadowing properties unaffected.

---

[7] We stress that SPH itself is not a Monte Carlo method, as first noted in Gingold & Monaghan (1978). We only appeal to the Monte Carlo picture for use with the radiative transfer, not for the hydrodynamic evolution of the particles in the SPH simulation.

[8] We explicitly note that the resampling does not affect the hydrodynamical simulation, for which the original positions are used.

4.5 SUMMARY

In this chapter we have presented TRAPHIC (TRAnsport of PHotons In Cones), a novel radiative transfer scheme for SPH simulations. TRAPHIC has been designed for use in radiation-hydrodynamical simulations exhibiting a wide dynamic range and containing a large number of light sources, as for instance encountered in cosmological simulations. The requirements for this are high: Due to the limits on the computational power available today, radiative transfer simulations at the resolution of state-of-the-art hydrodynamical simulations need to be adaptive both in space and in angle and parallel on distributed memory machines.

TRAPHIC meets these requirements. The radiative transfer equation is solved by transporting photons in an explicitly photon-conserving manner directly on the discrete set of SPH particles. Photons are transported globally by propagating them locally, between a particle and its neighbours. For a fixed number of SPH particles, the number of neighbours employed for the transport, the parameter $\tilde{N}_{\rm ngb}$, sets the adaptive spatial resolution. The conceptual similarity between the photon transport and the calculation of particle properties in SPH simulations allows a straightforward numerical implementation of TRAPHIC in SPH simulations for application on distributed memory machines.

In TRAPHIC photon packets are transported inside cones. Because source particles emit into a set of cones that tessellates the simulation box, the angular dependence of the emission can be modelled independently of the spatial distribution of the neighbouring SPH particles. The number of cones, $N_{\rm c}$, is the second parameter employed in TRAPHIC and determines the formal angular resolution of the radiative transfer simulation.

After their emission, the photon packets are transported downstream from SPH particle to SPH particle. They are confined to the solid angle they were originally emitted into by regular cones of solid angle $4\pi/N_{\rm c}$. Mimicking the ray-splitting technique used in ray-tracing schemes, the photon transport is adaptive in angle. The effective angular resolution is therefore much higher than the formal one. As we will demonstrate in the next chapter, Chapter 5, radiative transfer simulations employing TRAPHIC can thus be performed using only a relatively small number of cones.

The propagation of photons inside cones that do not contain a neighbour requires the introduction of so-called virtual particles (ViPs). It is the concept of cones combined with ViPs that enables the directed transport of photons on the unstructured grid defined by the discrete set of irregularly distributed SPH particles.

A practical problem often encountered when solving the radiative transfer equation is the linear scaling of the computational effort with the number of sources. Such a scaling limits the application of most of the existing radiative transfer schemes to simulations containing only a few sources. In TRAPHIC this problem is circumvented by introducing a source merging procedure. Photon packets emitted by different sources are merged in accordance with the angular resolution employed, such that at any point in space at most $N_{\rm c}$ photon packets need to be propagated. This renders the photon transport effectively independent of the number of sources in the simulation and makes it feasible to include a diffuse radiation component emitted by the SPH particles. In the most extreme case of radiation from an arbitrary number of sources completely filling the simulation box, the computational effort required by TRAPHIC merely scales as the product of spatial and angular resolution, $N \times \tilde{N}_{\rm ngb} \times N_{\rm c}$, where N is the total number of particles (SPH + stars).

Applications of TRAPHIC include the solution of both the time-independent and time-dependent radiative transfer equation in large-scale simulations of cosmological reionisation. In the next chapter, Chapter 5, we will show that TRAPHIC is able to accurately reproduce the expected growth of the ionised sphere around a single ionising point source, both in a homogeneous and in a centrally peaked medium, and to cast sharp shadows behind opaque obstacles. Furthermore, we will test our scheme in a physical setting of complex geometry, simulating the growth of ionised regions around multiple point sources in a cosmological density field. We will find that the results obtained with our implementation of TRAPHIC are in excellent agreement with results obtained with other radiative transfer codes for the same test problem.

ACKNOWLEDGEMENTS

We thank Claudio Dalla Vecchia for stimulating discussions and Huub Röttgering for his valuable advice. We are grateful to Craig Booth and Benedetta Ciardi for a thorough reading of the draft version of Pawlik & Schaye (2008). This work was supported by Marie Curie Excellence Grant MEXT-CT-2004-014112.

REFERENCES

Abel T., Norman M. L., Madau P., 1999, ApJ, 523, 66

Abel T., Wandelt B. D., 2002, MNRAS, 330, L53

Altay G., Croft R. A. C., Pelupessy I., 2008, MNRAS, 386, 1931

Alvarez M. A., Bromm V., Shapiro P. R., 2006, ApJ, 639, 621

Barkana R., Loeb A., 2004, ApJ, 609, 474

Brookshaw L., 1994, MmSAI, 65, 1033

Cen R., 2002, ApJS, 141, 211

Ciardi B., Ferrara A., Marri S., Raimondo G., 2001, MNRAS, 324, 381

Croft R. A. C., Altay G., 2007, arXiv, 709, arXiv:0709.2362

Dale J. E., Ercolano B., Clarke C. J., 2007, MNRAS, 1056

Dale J. E., Bonnell I. A., Whitworth A. P., 2007, MNRAS, 375, 1291

Dopita M. A., Sutherland R. S., 2003, Astrophysics of the diffuse universe, Springer

Finlator K., Özel F., Davé R., 2009, MNRAS, 393, 1090

Fryer C. L., Rockefeller G., Warren M. S., 2006, ApJ, 643, 292

Gingold R. A., Monaghan J. J., 1977, MNRAS, 181, 375

Gingold R. A., Monaghan J. J., 1978, MNRAS, 184, 481

Gingold R. A., Monaghan J. J., 1982, J. Comput. Phys., 46, 429

Gnedin N. Y., Abel T., 2001, NewA, 6, 437

Gritschneder M., Naab T., Heitsch F., Burkert A., 2007, IAUS, 237, 246

Herant M., Benz W., Hix W. R., Fryer C. L., Colgate S. A., 1994, ApJ, 435, 339

Hernquist L., Katz N., 1989, ApJS, 70, 419

Hockney R. W., Eastwood J. W., 1988, Computer Simulations Using Particles, Taylor & Francis

Iliev I. T., Mellema G., Pen U.-L., Merz H., Shapiro P. R., Alvarez M. A., 2006, MNRAS, 369, 1625

Iliev I. T., et al., 2006, MNRAS, 371, 1057

Johnson J. L., Greif T. H., Bromm V., 2007, ApJ, 665, 85

Kessel-Deynet O., Burkert A., 2000, MNRAS, 315, 713

Kohler K., Gnedin N. Y., Hamilton A. J. S., 2007, ApJ, 657, 15

Lucy L. B., 1977, AJ, 82, 1013

Maselli A., Ferrara A., Ciardi B., 2003, MNRAS, 345, 379

Mayer L., Lufkin G., Quinn T., Wadsley J., 2007, ApJ, 661, L77

Shampine L. F., Gear C. W., 1979, SIAM Review, Vol. 21, No.1, pp. 1-17

Mellema G., Iliev I. T., Alvarez M. A., Shapiro P. R., 2006, NewA, 11, 374

Mihalas D., Weibel Mihalas B., 1984, Foundations of radiation hydrodynamics, Oxford University Press, New York

Monaghan J. J., 1992, ARA&A, 30, 543

Monaghan J. J., Rep. Prog. Phys., 68, 1703 (2005)

Okabe A., Boots B., Sugihara K., Chiu S. N., 2000, Spatial Tessellations, Second edition, Wiley

Osterbrock D. E., 1989, Astrophysics of gaseous nebulae and active galactic nuclei, Palgrave Macmillan

Oxley S., Woolfson M. M., 2003, MNRAS, 343, 900

Paschos P., Norman M. L., Bordner J. O., Harkness R., 2007, arXiv, 711, arXiv:0711.1904

Pawlik A. H., Schaye J., 2008, MNRAS, 389, 651

Petkova M., Springel V., submitted

Price D., 2005, astro, arXiv:astro-ph/0507472

Razoumov A. O., Cardall C. Y., 2005, MNRAS, 362, 1413

Razoumov A. O., Sommer-Larsen J., 2006, ApJ, 651, L89

Ritzerveld J., Icke V., 2006, PhRvE, 74, 026704

Semelin B., Combes F., Baek S., 2007, arXiv, 707, arXiv:0707.2483

Soneira R. M., Peebles P. J. E., 1978, AJ, 83, 845

Springel V., Hernquist L., 2002, MNRAS, 333, 649

Springel V., 2005, MNRAS, 364, 1105

Stamatellos D., Whitworth A. P., 2005, A&A, 439, 153

Susa H., 2006, PASJ, 58, 445

Susa H., Umemura M., 2006, ApJ, 645, L93

Trac H., Cen R., 2006, astro, arXiv:astro-ph/0612406

Viau S., Bastien P., Cha S.-H., 2006, ApJ, 639, 559

Whalen D., Norman M. L., 2007, arXiv, 708, arXiv:0708.2444

Wise J. H., Abel T., 2007, arXiv, 710, arXiv:0710.3160

White S. D. M., 1996, Cosmology and large scale structure, Proceedings of the "Les Houches Ecole d'Ete de Physique Theorique" (Les Houches Summer School), p. 349, Elsevier Scientific Publishing Company, Amsterdam

Whitehouse S. C., Bate M. R., 2006, MNRAS, 367, 32

Yoshida N., Oh S. P., Kitayama T., Hernquist L., 2007, ApJ, 663, 687

4.A THE ANISOTROPY OF PARTICLE-TO-NEIGHBOR TRANSPORT

In Sec.4.4.2 we introduced an emission cone tessellation to accomplish the emission of photons by a source particle to its neighboring gas particles. Then we also mentioned that the cones are required to emit in agreement with the angular dependence of the emissivity of the source, independently of the spatial distribution of the neighbors. In this appendix we explain why this is the case. In particular, assuming that particles have equal mass, we show that when transporting photons (or more generally, any extensive quantity) in particle simulations from a particle to its neighbors, the net transport direction is generally correlated with the direction towards the centre of mass of the neighbouring particles. As a result, the transport is partly governed by the geometry of the simulation, in addition to the intrinsic emissivity of the source.

Consider a particle located at the origin O of a 3-dimensional coordinate system (the emitter frame). The particle emits photons to its $\tilde{N}_{\rm ngb}$ nearest neighbours, residing in the sphere of radius $\tilde{h}$ centred on the emitting particle. Throughout this section we assume that all particles have equal mass, $m = 1$. The emission is performed by transferring the fraction $w_i / \sum_{j=1}^{\tilde{N}_{\rm ngb}} w_j$ of the total number of photons to neighbour i ($i = 1, 2, ..., \tilde{N}_{\rm ngb}$), where the $w_i \geq 0$ are weights to be specified. The emission properties will depend both on the weights and on the spatial distribution of the neighbours.

To study the angular dependence of the emission process, we introduce the vector sum $\mathbf{s} = \sum_i w_i \mathbf{u}_i / \sum_i w_i$ over all unit vectors $\mathbf{u}_i \equiv \mathbf{r}_i / |\mathbf{r}_i|$, where $\mathbf{r}_i$ is the position of neighbour i. This vector sum can be interpreted as the net direction of the emission. Let us denote the angle enclosed by s and the vector to the centre of mass $\mathbf{r}_{\rm cm}$ of the neighbours, $\mathbf{r}_{\rm cm} = \sum_i \mathbf{r}_i / \tilde{N}_{\rm ngb}$, with α. We ask for the probability density function (pdf) $p(\cos\alpha)$ of the cosine of α, where

$$\cos\alpha = \frac{\mathbf{s} \cdot \mathbf{r}_{\rm cm}}{|\mathbf{s}|\,|\mathbf{r}_{\rm cm}|} = \frac{\sum_i w_i \mathbf{u}_i \cdot \sum_j \mathbf{r}_j}{|\sum_i w_i \mathbf{u}_i| |\sum_j \mathbf{r}_j|}. \tag{4.14}$$

The meaning of the pdf can be understood by looking at its extremes. If $p(\cos\alpha)$ is strongly peaked around $\cos\alpha \approx 1$, the emission has a net direction biased towards the centre of mass direction, and photons will be preferentially transported into the high (particle) density regions. On the other hand, if $p(\cos\alpha)$ is strongly peaked around $\cos\alpha \approx -1$, photons will be preferentially transported into the direction opposite to the centre of mass. Finally, a flat pdf $p(\cos\alpha) = 1/2$ indicates that the net emission direction and the direction towards the centre of mass are uncorrelated.

As an illustration, assume that all neighbours have identical weights $w_i = 1$ and that their positions $\mathbf{r}_i$ are drawn from a probability distribution that uniformly samples the surface of the sphere of radius $\tilde{h}$ surrounding the emitter at O. To obtain $p(\cos\alpha)$, we note that our assumptions imply that the centre of mass vector $\mathbf{r}_{\rm cm}$ and the vector sum s point in the same direction, so that $p(\cos\alpha) = 2\delta_{\rm D}(\cos\alpha - 1)$, where $\delta_{\rm D}(x)$ is the Dirac δ -function. Hence, there is a perfect correlation between s and $\mathbf{r}_{\rm cm}$.

Another example is given by assuming that the particles of unit mass are distributed randomly within the sphere of radius $\tilde{h}$ around the emitter. The resulting pdf $p(\cos\alpha)$ as obtained through a Monte Carlo simulation is shown in its cumulative form $F(\cos\alpha) = \int_{-1}^{\cos\alpha} dx\ p(x)$ in Fig. 4.6 for two choices of the number of neighbours, $\tilde{N}_{\rm ngb} = 16$ (thin dotted curve) and $\tilde{N}_{\rm ngb} = 64$ (thick dotted curve; falling nearly on top of the thin dotted curve). Clearly, there is a very strong correlation between the net direction of emission and the direction towards the centre of mass of the neighbour distribution.

For the important case of isotropic sources of photons the net emission direction should not be correlated with the direction towards the centre of mass, i.e. $p(\cos\alpha) = 1/2$, independent of $\cos\alpha$, and thus $F(\cos\alpha) = (1 + \cos\alpha)/2$. From here on, we will refer to this case as isotropic emission of radiation. We emphasize the statistical character of this statement. An individual particle may still emit anisotropically, which could be revealed by studying the amplitude $|\mathbf{s}|$. For emission that is isotropic for individual particles, $|\mathbf{s}| = 0$. Consider the neighbour distribution of the last example, for which we showed the emission pattern to be far from isotropic. Can the emission be isotropized by tuning the weights?

For instance, consider solid angle weighting, defined as follows. We project all neighbours radially onto the unit sphere. To each neighbour we attach a weight proportional to its area of influence, which we define by the collection of all points on the unit sphere which are closer to the projected neighbour for which we calculate the weight than to all other projected neighbours. Hereby, the distance of two points on the sphere is given by the arclength of the connecting geodesic (great circle). This definition of the area of influence results in a specific tessellation of the surface of the sphere, the so-called Voronoi tessellation (e.g. Okabe et al. 2000), and provides us with well-defined non-overlapping solid angles.

The resulting cumulative distribution $F(\cos\alpha)$ is shown in Fig. 4.6 (dashed curves). Although the weighted emission has weakened the correlation between s and $\mathbf{r}_{\rm cm}$ as compared to the case of equal weights, the net emission direction is still markedly peaked towards the direction to the centre of mass. We note that weighting by solid angle is the most natural choice and its inability to isotropize the transport might be surprising. Alternatively, one could introduce *ad hoc* weights $\hat{w}_i = w_i^r$, where $r > 1$ is some exponent and the w_i are solid angle weights, to re-shape the distribution $p(\cos\alpha)$ to become less and less peaked around $\cos\alpha \sim 1$.

However, the reason why the solid angle weights fail to isotropize the transport is not that the weights are inappropriate, but that the directions to the neighbours are fixed and thus cannot be freely chosen along with the weights, as mentioned in Sec.4.4.2. This strongly limits one's ability to influence the shape of $p(\cos\alpha)$. For illustration, consider an emitter having all its neighbours located in one hemisphere. The net emission direction s will then necessarily lie in that hemisphere, too, *regardless* of the chosen weights. For a statistical ensemble of emitters, s will then necessarily be correlated with the direction towards the centre of mass.

This also explains the dependence of $p(\cos\alpha)$ on the number of neighbours. The larger $\tilde{N}_{\rm ngb}$, the greater the probability of finding a neighbour in any chosen solid angle. Through this increase in directional sampling, $p(\cos\alpha)$ can be expected to approach the uncorrelated case. This behaviour can indeed be observed in Fig. 4.6.

We also compute the statistic $p(\cos\alpha)$ for the case of neighbours clustered in space, which is more typical for cosmological simulations of structure formation. We did this both using a toy clustering model (Soneira & Peebles 1978) and for a cosmological density field obtained from a ΛCDM hydrodynamical simulation (the same field that is used in Sec.5.4.5, Chapter 5). For the weighting schemes we investigated the dependence of the shape of $p(\cos\alpha)$ on the chosen weights is qualitatively very similar to that in the case of the random distribution of neighbours discussed earlier.

We emphasize that our discussion is not limited to the transport of photons. Indeed, particle-to-neighbour transport is for example routinely employed in SPH simulations of galaxy formation, where a star particle distributes its metals and energy amongst its neighbours. Different recipes for distributing metals and energy can be found in the literature. Most of these apply a weighting related to the SPH formalism. As an example, to each neighbour i we associate the weight

$$w_i = \frac{\frac{m_i}{\rho_i} W(r_i, \tilde{h})}{\sum_j \frac{m_j}{\rho_j} W(r_j, \tilde{h})}. \tag{4.15}$$

Here, $\tilde{h}$ is the radius of the neighbourhood of the emitting particle (at O), $r_i = |\mathbf{r}_i|$ and W is the spline kernel Eq. 4.4. Performing the transport on the same random neighbour distribution as before, we obtain the distribution $p(\cos\alpha)$. As can be seen in Fig. 4.6 (solid curves), the direction of net transport and the direction to the centre of mass are found to be almost uncorrelated. We note that this result, the reason of which at the moment is not clear to us, is only a statistical statement. We calculated $|\mathbf{s}|$ and found that the emission of individual particles is still not close to isotropic. We arrive at qualitatively similar results for different definitions of

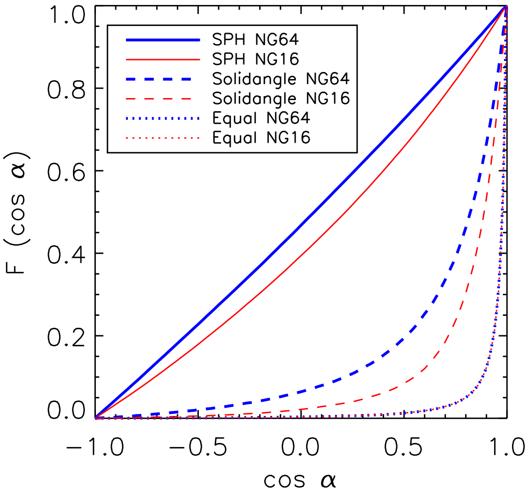

Figure 4.6: Monte Carlo simulation of particle-to-neighbour transport. We show the cumulative probability distribution of $\cos\alpha$, where α is the angle between the net emission direction s and the direction towards the centre of mass $\mathbf{r}_{\rm cm}$ of the neighbours. The curves correspond to the following weighting schemes, with the number of neighbours indicated in brackets (from top to bottom): SPH (64), SPH (16), Solidangle (64), Solidangle (16), Equal (64), Equal (16). The last two curves are nearly on top of each other.

the SPH weights, both for random and clustered neighbour distributions. A more quantitative statement, however, must depend on both the specific properties of the spatial distribution of the neighbours, and the precise form of the adopted SPH weights.

In summary, in this appendix we have shown that when transporting a quantity from a particle to its neighbours, the net transport direction is generally governed by the spatial distribution of the neighbours, in addition to the the intrinsic properties of the emitting particle. We emphasize that our observations apply to the particle-to-neighbour transport of arbitrary quantities in *any* particle simulation. We would like to remind the reader that in Sec.4.4 we presented a specifically designed particle-based transport scheme, TRAPHIC, that overcomes the problems of particle-to-neighbour based transport discussed in this appendix, not just statistically, but also on a particle by particle basis. We achieved this by employing cones to confine photons to the solid angle into which they are emitted, making the transport independent of the geometry of the SPH simulation, on the scale of the chosen angular resolution.

> Cuius rei demonstrationem mirabilem sane detexi. Hanc marginis exiguitas non caperet.
>
> Fermat, margin note in his copy of Arithmetica of Diophantus

CHAPTER 5

TRAPHIC in GADGET
implementation and tests

Andreas H. Pawlik & Joop Schaye

This chapter contains material that has been published together with the material presented in the previous chapter, Chapter 4, in MNRAS 389 (2008), 651-677. It provides an updated and significantly extended version of Section 5 in that publication.

We present and test a parallel numerical implementation of our radiative transfer scheme TRAPHIC, specified for the transport of monochromatic hydrogen-ionising radiation, in the smoothed particle hydrodynamics code GADGET-2. The tests comprise several radiative transfer problems of increasing complexity. Some of these tests have been specifically designed to investigate TRAPHIC's ability to solve the radiative transfer problem in the large cosmological reionisation simulations that it was developed for, while others have been designed to demonstrate that TRAPHIC can also be employed in more general contexts. The results of all tests are in excellent agreement with both analytic solutions and numerical reference results obtained with state-of-the-art radiative transfer codes.

5.1 INTRODUCTION

Ionising radiation is thought to play a key role in determining the ionisation state and shaping the spatial distribution of the baryonic matter in our Universe on both small and large scales. Examples include the triggering and quenching of star formation through radiative feedback from nearby ionising stellar sources both in the early (e.g. Yoshida et al. 2007; Wise & Abel 2007; Johnson, Greif, & Bromm 2007; Alvarez, Bromm, & Shapiro 2006; Susa & Umemura 2006) and present-day universe (e.g. Gritschneder et al. 2007; Dale, Bonnell, & Whitworth 2007), the thin shell instability (for a recent simulation see Whalen & Norman 2007) and the growth and percolation of ionised regions generated by the first stars and quasars during the so-called Epoch of Reionisation (for recent simulations see e.g. Iliev et al. 2006a; Trac & Cen 2007; Kohler, Gnedin, & Hamilton 2007; Paschos et al. 2007). Accomplishing the transport of ionising radiation in hydrodynamical simulations of our Universe, both on large and small scales, in an efficient, computationally feasible manner has therefore become one of the primary goals in numerical astrophysics.

TRAPHIC is a novel radiative transfer scheme that we have developed to solve the radiative transfer problem in Smoothed Particle Hydrodynamics (SPH) simulations (Chapter 4). Its design has been guided by the wish to transport radiation in an adaptive manner directly on the unstructured grid traced out by the particles in SPH simulations, in parallel on distributed memory and with a computation time that does not scale with the number of radiation sources. This is done by transporting photon packets subject to absorption and scattering on a particle-by-particle basis with a well-defined spatial and angular resolution. In this chapter we apply TRAPHIC to the transport of ionising radiation.

It is helpful to briefly recall some basic concepts and notations that we have used in our description of TRAPHIC in Chapter 4 and that will be frequently employed here. The transport process can be decomposed into the emission of photon packets by source particles followed by their directed transport on the irregular set of SPH particles. Photon packets are emitted from source particles to their $\tilde{N}_{\rm ngb}$ neighbouring SPH particles (residing in a sphere of radius $\tilde{h}$ centred on the source) using a tessellating set of $N_{\rm c}$ emission cones. The number of cones is a parameter that determines the angular resolution of the radiative transfer. The number of neighbours $\tilde{N}_{\rm ngb}$ is a parameter that determines the spatial resolution and is usually matched to the number of neighbours $N_{\rm ngb}$ (residing in the sphere of radius h) used in the computation of the SPH particle properties, $\tilde{N}_{\rm ngb} \lesssim N_{\rm ngb}$.

To each of the emitted photon packets we associate a propagation direction that is parallel to the central axis of the corresponding emission cone. After emission, the photon packets are traced downstream along their propagation direction. The packets thereby remain confined to the solid angle they were originally emitted into thanks to the use of transmission cones with solid angle $4\pi/N_{\rm c}$. Virtual particles (ViPs) are introduced to accomplish the photon transport along directions for which no neighbouring SPH particle could be found in the associated cones. Finally, the photon transport is supplemented with a photon packet (or, equivalently, source) merging procedure that respects the chosen angular resolution to strictly limit the required computation time.

The photon transport is performed using (radiative transfer) time steps $\Delta t_{\rm r}$. During each such time step, photons are propagated and their interactions with the gas are computed until a certain stopping criterion is satisfied. The form of this criterion depends on whether one aims to solve the time-independent or the time-dependent radiative transfer equation. In the first case, photons are propagated until they are absorbed or have left the computational domain. In the second case, photon clocks associated with each photon packet are used to synchronise the packet's travel time with the simulation time such that the photon packet travels at the speed of light. After each time step, the state of the SPH particles is updated according to the interactions (absorptions, scatterings) with photon packets they experienced. Finally, the radiative transfer time is advanced, which concludes the algorithm. The reader is referred to Chapter 4 for more details.

This chapter is organised as follows. We start by briefly reviewing the physics of photo-ionisation (Sec. 5.2). We will then describe a numerical implementation of TRAPHIC specified for the transport of mono-chromatic hydrogen-ionising radiation in the SPH code GADGET-2 (Springel 2005) (Sec. 5.3). We will verify our implementation in several tests that are set up to allow comparisons to accurate reference solutions, obtained either analytically or numerically with state-of-the-art radiative transfer codes (Sec. 5.4). Finally, we will present our conclusions (Sec. 5.5).

5.2 PHOTO-IONISATION RATE EQUATION

Here we briefly recall the principles of the photo-ionisation and recombination process occurring for a hydrogen-only gas parcel of mass density ρ exposed to hydrogen-ionising radiation. We will employ the equations derived in this section in the description of the numerical implementation of TRAPHIC.

Hydrogen-ionising photons can be absorbed by neutral hydrogen. The absorption strength is typically expressed using the frequency-dependent mass absorption coefficient κ_ν for hydrogen-ionising radiation (e.g. Osterbrock 1989). For the demonstrational purpose of this chapter it will be sufficient to approximate the frequency-dependence of κ_ν by (see, e.g., Fig. 7.1 in Chapter 7)

$$\kappa_\nu \equiv \frac{\sigma_\nu n_{\rm HI}}{\rho} \tag{5.1}$$

$$\sigma_\nu = \sigma_0 \left(\frac{\nu}{\nu_0}\right)^{-3} \Theta(\nu-\nu_0), \tag{5.2}$$

with $n_{\rm HI} = (1-\chi)\rho/m_{\rm H}$ the neutral hydrogen number density, ν_0 the Lyman-limit frequency of energy $h_{\rm p}\nu_0 = 13.6$ eV, $\sigma_0 = 6.3 \times 10^{-18}$ cm^2 the absorption cross-section for photons at the Lyman-limit, $m_{\rm H}$ the mass of a hydrogen atom and $\Theta(x)$ the Heaviside step function; the ionised fraction is $\chi \equiv n_{\rm HII}/n_{\rm H}$. The number of photo-ionisations per unit time per neutral hydrogen atom at a certain point in space is determined by the photo-ionisation rate Γ,

$$\Gamma = \int_0^\infty d\nu\, \frac{4\pi J_\nu(\nu)}{h_{\rm p}\nu}\sigma_\nu, \tag{5.3}$$

where $J_\nu \equiv \int d\Omega\ I_\nu/(4\pi)$ is the mean ionising intensity. The rate of change of the neutral fraction $\eta \equiv 1-\chi$ at this point is then

$$\frac{d}{dt}\eta = \alpha(T)n_{\rm e}\chi - \Gamma\eta \equiv \frac{\chi}{\tau_{\rm rec}} - \frac{\eta}{\tau_{\rm ion}}. \tag{5.4}$$

In the last equation, $\alpha(T)n_{\rm e}$ is the number of recombinations occurring per unit time per ionised hydrogen atom, $\tau_{\rm rec} \equiv 1/(\alpha n_{\rm e})$ is the recombination time scale and $\tau_{\rm ion} \equiv 1/\gamma$ is the photo-ionisation time scale.[1]

---

[1] Note that in Eq. 5.4 collisional ionisations can easily be taken into account by replacing Γ with $(\Gamma + C(T)n_{\rm e})$,

With the definition $\tilde{\chi} \equiv \tau_{\rm rec}/(\tau_{\rm ion} + \tau_{\rm rec})$ we can rewrite Eq. 5.4 to read

$$\frac{d\chi}{dt} = -\frac{\chi - \tilde{\chi}}{\tau_{\rm ion}\tilde{\chi}}. \tag{5.5}$$

Setting $d\chi/dt = 0$ yields the equilibrium ionised fraction $\chi_{\rm eq} = \tau_{rec,eq}/(\tau_{\rm ion} + \tau_{rec,eq})$. Over time scales that are short compared with $\tau_{\rm rec}/|d\tau_{\rm rec}/dt|$ and $n_{\rm e}/|dn_{\rm e}/dt|$, Eq. 5.5 constitutes a first order linear homogeneous differential equation in $\chi - \tilde{\chi}$ with constant coefficients, whose solution reads

$$\begin{aligned} \chi(t) - \chi_{\rm eq} &= (\chi(t_0) - \chi_{\rm eq})e^{-\frac{t-t_0}{\tau_{\rm eq}}} && (5.6) \\ \tau_{\rm eq} &\equiv \frac{\tau_{\rm ion}\tau_{\rm rec}}{\tau_{\rm ion} + \tau_{\rm rec}}. && (5.7) \end{aligned}$$

From Eq. 5.6 we see that the equilibrium ionised fraction is exponentially approached on the instantaneous ionisation equilibrium time scale $\tau_{\rm eq}$. We will employ this time scale later on for the numerical integration of the rate equation.

We emphasise that our derivation of Eq. 5.6 was based on the assumption that the electron density does not change significantly. We have adopted this assumption in order to point out the characteristic time scales involved. In Sec. 5.4.1 we will present an alternative derivation of the solution of the photo-ionisation rate equation (Eq. 5.4) that is also valid for the case of an evolving electron density.

5.3 NUMERICAL IMPLEMENTATION

We have adapted the description of TRAPHIC that we have presented in Chapter 4 for the transport of hydrogen-ionising radiation according to the physics of photo-ionisation as reviewed in Sec. 5.2. We implemented it using a single frequency bin in the parallel N-body-Tree-SPH code GADGET-2 (Springel 2005). The description of (important aspects of) this implementation is the subject of this section.

5.3.1 Transport of ionising photons and computation of the photo-ionisation rate

The transport of ionising photons is performed in finite radiative transfer time steps of size $\Delta t_{\rm r}$, during which photon packets emitted by ionising sources are propagated through the SPH density field guided by cones as we have described in Chapter 4. This propagation starts with the emission of photons using a set of tessellating emission cones with random orientation. For definiteness, we present our choice of the emission cone tessellation in App. 5.B.1 and our implementation of the random rotations applied to it in App. 5.B.2.

During each time step the number of photons that are absorbed by neutral hydrogen is computed using the absorption coefficient κ_ν, given by Eqs. 5.1 and 5.2, together with the expression for the optical depth in Chapter 4 (Eq. 4.10). At the end of the time step, i.e. at time $t_{\rm r} + \Delta t_{\rm r}$, where $t_{\rm r}$ is the simulation time, the number of ionising photons $\Delta\mathcal{N}_{{\rm in},i}$ impinging on and the number of ionising photons $\Delta\mathcal{N}_{{\rm abs},i}$ absorbed by particle i over the time interval $\Delta t_{\rm r}$

---

where $C(T)n_{\rm e}$ describes the number of collisional ionisations per unit time per neutral hydrogen atom. In this chapter, however, we assume that collisional ionisations are unimportant, setting $C \equiv 0$ throughout. We will extend our description to include collisional ionisations in Chapter 7.

are then known. The photo-ionisation rate Γ_i is obtained directly from the number of absorbed photons using

$$\eta_i^{t_r} \mathcal{N}_{\mathrm{H},i} \Gamma_i^{t_r} \Delta t_r \quad = \quad \Delta \mathcal{N}_{\mathrm{in},i} \left[1 - \exp(-\tau_i^{t_r})\right] , \tag{5.8}$$

where $\mathcal{N}_{\mathrm{H},i} \equiv m_i^{t_r} X_i^{t_r} / m_{\mathrm{H}}$ is the number of hydrogen atoms associated with particle i (X_i is the hydrogen mass fraction) and superscripts indicate the time at which quantities are evaluated. Thereby

$$\tau_i^{t_r} \equiv - \ln \left(1 - \frac{\Delta \mathcal{N}_{\mathrm{abs},i}}{\Delta \mathcal{N}_{\mathrm{in},i}}\right) \tag{5.9}$$

is the a posteriori optical depth[2] that relates the number of impinging photons $\Delta \mathcal{N}_{\mathrm{in},i}$ to the number of absorbed photons $\Delta \mathcal{N}_{\mathrm{abs},i}$. In the next section we describe how the photo-ionisation rate is used to update the neutral fraction of particle i.

5.3.2 Solving the rate equation

The photo-ionisation rate equation, i.e. the differential equation Eq. 5.4, belongs to a class of problems that are referred to as stiff (for useful introductions to stiff problems see, e.g., Shampine & Gear 1979; Press et al. 1992). There is no universally accepted definition of stiffness. Often, the classification of a problem as stiff is based on examinations of the stability of numerical integrators applied to solve this problem.

As an example, consider the equation (cp. Press et al. 1992)

$$\frac{d}{dt} y = - \frac{y}{\tau} \tag{5.10}$$

with solution

$$y(t) = y(t_0) e^{-(t-t_0)/\tau} \tag{5.11}$$

Hereby, τ is a constant with dimensions of time. Accordingly, the equilibrium solution obtained considering the limit $t \to \infty$ is $y \to 0$. The explicit (or forward) Euler scheme for integrating this equation with step size Δt is (Press et al. 1992)

$$y^{t+\Delta t} = y^t + \Delta t \frac{d}{dt} y^t = y^t (1 - \frac{\Delta t}{\tau}), \tag{5.12}$$

where we used Eq. 5.10 in the last step. The method is unstable for $\Delta t / \tau > 2$ as then $|y| \to \infty$ for $t \to \infty$. Its stable integration requires steps $\Delta t < 2\tau$, which become prohibitively small for $\tau \to 0$. Observe that this limit on the integration step is independent of the value of the solution y. Small integration steps are therefore needed even when simulating the equilibrium solution, despite the fact that this solution is not changing at all.

Applied to the integration of the photo-ionisation rate equation (Eq. 5.4), the explicit Euler scheme reads

$$\frac{\eta_i^{t_r + \Delta t_r} - \eta_i^{t_r}}{\Delta t_r} = \alpha_i^{t_r} n_{\mathrm{e},i}^{t_r} \chi_i^{t_r} - \Gamma_i^{t_r} \eta_i^{t_r} \tag{5.13}$$

In Appendix 5.A we demonstrate that in order not to violate the physical bound $0 \le \eta_i \le 1$, the integration in the explicit Euler discretisation would require time steps $\Delta t_r < \tau_{\mathrm{eq}}$, where τ_{eq}

---

[2] We use the expression *a posteriori* since this optical depth is computed *after* finishing the transport of photons over the radiative transfer time step Δt_r, using the *total* number of photons $\Delta \mathcal{N}_{\mathrm{in},i}$ and $\Delta \mathcal{N}_{\mathrm{abs},i}$ that were, respectively, impinging on and absorbed by particle i over that time step.

is the characteristic time scale over which the neutral fraction changes (see Eq. 5.7). We would like to choose the radiative transfer time step Δt_r independently of the time scale τ_eq because the latter can be prohibitively small to allow efficient radiative transfer computations. In the following, we discuss two approaches to accomplish this.

Implicit integration

The first approach to decouple the radiative transfer time step Δt_r from the time scale τ_eq we consider is the use of implicit integrators. These integrators, which advance the solution based on the advanced solution itself, are in fact commonly employed to deal with stiff problems like the problem at hand. As an example, consider the so-called implicit or (backward) Euler integration of Eq. 5.10 (Press et al. 1992),

$$y^{t+\Delta t} = y^t + \Delta t \frac{d}{dt} y^{t+\Delta t} = y_t + \Delta t(-\frac{y^{t+\Delta t}}{\tau}), \tag{5.14}$$

or,

$$y^{t+\Delta t} = \frac{y^t}{1+\Delta t/\tau}. \tag{5.15}$$

This integrator is stable: even for $\Delta t \to \infty$ it yields $y \to 0$ as $t \to \infty$, which is the correct equilibrium solution. Note, however, that this gain in stability typically comes along with a loss in accuracy in following the approach to equilibrium (Press et al. 1992).

Applied to the integration of the photo-ionisation rate equation, Eq. 5.4, the backwards Euler scheme reads

$$\frac{\eta_i^{t_\mathrm{r}+\Delta t_\mathrm{r}} - \eta_i^{t_\mathrm{r}}}{\Delta t_\mathrm{r}} = \alpha_i^{t_\mathrm{r}+\Delta t_\mathrm{r}} n_{\mathrm{e},i}^{t_\mathrm{r}+\Delta t_\mathrm{r}} \chi_i^{t_\mathrm{r}+\Delta t_\mathrm{r}} - \Gamma_i^{t_\mathrm{r}+\Delta t_\mathrm{r}} \eta_i^{t_\mathrm{r}+\Delta t_\mathrm{r}}. \tag{5.16}$$

To proceed, we need to evaluate the photo-ionisation rate $\Gamma_i^{t_\mathrm{r}+\Delta t_\mathrm{r}}$ at time $t_\mathrm{r}+\Delta t_\mathrm{r}$. Because of the discretisation of the photon transport using times steps Δt_r, the flux $d\mathcal{N}_{\mathrm{in},i}/dt$ of ionising photons impinging on particle i may be considered as constant over the time step Δt_r, i.e. $d\mathcal{N}_{\mathrm{in},i}/dt = \Delta\mathcal{N}_{\mathrm{in},i}/\Delta t_\mathrm{r}$. Employing the last equality in Eq. 5.8 yields the following, instantaneous scaling of the photo-ionisation rate,

$$\Gamma(\eta) \propto (1 - e^{-\tau(\eta)})\eta^{-1}. \tag{5.17}$$

A similar derivation of this scaling can be found in Mellema et al. (2006). Hence,

$$\Gamma_i^{t_\mathrm{r}+\Delta t_\mathrm{r}} = \Gamma_i^{t_\mathrm{r}} \left[\frac{1-\exp(-\tau_i^{t_\mathrm{r}+\Delta t_\mathrm{r}})}{1-\exp(-\tau_i^{t_\mathrm{r}})}\right] \frac{\eta_i^{t_\mathrm{r}}}{\eta_i^{t_\mathrm{r}+\Delta t_\mathrm{r}}}, \tag{5.18}$$

where $\Gamma_i^{t_\mathrm{r}}$ and $\tau_i^{t_\mathrm{r}}$ are the photo-ionisation rate and the optical depth at the beginning of the step, given by Eqs. 5.8 and 5.9, and $\tau_i^{t_\mathrm{r}+\Delta t_\mathrm{r}} = \tau_i^{t_\mathrm{r}} \eta_i^{t_\mathrm{r}+\Delta t_\mathrm{r}}/\eta_i^{t_\mathrm{r}}$ is the optical depth at time $t_\mathrm{r}+\Delta t_\mathrm{r}$.

In general, Eq. 5.16 needs to be solved iteratively[3]. This may be done by finding the zero of the function

$$f(\chi_i^{t_\mathrm{r}+\Delta t_\mathrm{r}}) = \frac{\chi_i^{t_\mathrm{r}+\Delta t_\mathrm{r}} - \chi_i^{t_\mathrm{r}}}{\Delta t_\mathrm{r}} + \alpha_i^{t_\mathrm{r}+\Delta t_\mathrm{r}} n_{\mathrm{e},i}^{t_\mathrm{r}+\Delta t_\mathrm{r}} \chi_i^{t_\mathrm{r}+\Delta t_\mathrm{r}} - \Gamma_i^{t_\mathrm{r}+\Delta t_\mathrm{r}}(1-\chi_i^{t_\mathrm{r}+\Delta t_\mathrm{r}}) \tag{5.19}$$

---

[3] For the special case $\eta = 1-\chi$ and a non-evolving photo-ionisation rate $\Gamma(\eta) = const$, Eq. 5.16 yields a quadratic equation that can be directly solved (Petkova & Springel 2008).

using a combination of bracketing (Press et al. 1992; to set the interval within which to look for the zero) and bisection (Press et al. 1992; to locate the zero).

Because the neutral fraction changes continuously within the time step (although this is hidden behind the implicit integrator), the number of ionisations $\Delta\mathcal{N}_{\mathrm{impl},i}$ that have been used to advance it may be less than the number of photons $\Delta\mathcal{N}_{\mathrm{abs},i}$ that have been removed due to absorptions during the radiation transport over the time step Δt_{r} based on the assumption of a non-evolving neutral fraction. Photon conservation requires reinserting the number of absorbed photons that have not been used to advance the ionised fraction, $\Delta\mathcal{N}^{t_{\mathrm{r}}}_{\mathrm{abs},i} - \Delta\mathcal{N}^{t_{\mathrm{r}}}_{\mathrm{impl},i}$, into the photon transport (in the next radiative transfer time step). This number is, however, not well-defined, because the decomposition of the change in the ionised fraction as being due to ionisations or recombinations is ambiguous.

A possible interpretation of Eq. 5.16 is that the first term on the right-hand side determines the number of recombinations, while the second term determines the number of ionisations that have led to the change $\eta_i^{t_{\mathrm{r}}+\Delta t_{\mathrm{r}}} - \eta_i^{t_{\mathrm{r}}}$ of the neutral fraction over the time step Δt_{r}. If we follow this interpretation, we find that the number of ionising photons that have been used to advance the neutral fraction is

$$\Delta\mathcal{N}^{t_{\mathrm{r}}}_{\mathrm{impl},i} = \mathcal{N}^{t_{\mathrm{r}}}_{\mathrm{H},i}\Gamma_i^{t_{\mathrm{r}}+\Delta t_{\mathrm{r}}}\eta_i^{t_{\mathrm{r}}+\Delta t_{\mathrm{r}}}\Delta t_{\mathrm{r}}. \tag{5.20}$$

Note, however, that this interpretation of Eq. 5.16 is only one of (infinitely) many interpretations. This ambiguity makes it generally impossible to strictly conserve photons when employing the implicit Euler integrator.

The loss of accuracy during the approach to equilibrium and the impossibility of a strictly photon-conserving formulation lead us to consider a more direct integration method that does not suffer from these problems.

Explicit integration: Sub-cycling

To decouple the radiative transfer time step Δt_{r} from the time scale τ_{eq} in a strictly photon-conserving manner, we employ the following sub-cycling procedure. We explicitly follow the evolution of the neutral fraction during the time interval $t_{\mathrm{r}} \le t_i < t_{\mathrm{r}} + \Delta t_{\mathrm{r}}$ on sub-cycle steps $\delta t_i \le \Delta t_{\mathrm{r}}$,

$$\eta_i^{t_i+\delta t_i} - \eta_i^{t_i} = \alpha_i^{t_i} n_{\mathrm{e},i}^{t_i}\chi_i^{t_i}\delta t_i - \Gamma_i^{t_i}\eta_i^{t_i}\delta t_i. \tag{5.21}$$

As noted above (Eq. 5.17), the photo-ionisation rate $\Gamma(\eta) \propto (1 - e^{-\tau(\eta)})\eta^{-1}$. Hence, a change in the neutral fraction implies a change in the photo-ionisation rate $\Gamma_i^{t_i}$,

$$\Gamma_i^{t_i} = \Gamma_i^{t_{\mathrm{r}}}\left[\frac{1-\exp(-\tau_i^{t_i})}{1-\exp(-\tau_i^{t_{\mathrm{r}}})}\right]\frac{\eta_i^{t_{\mathrm{r}}}}{\eta_i^{t_i}}, \tag{5.22}$$

where $\Gamma_i^{t_{\mathrm{r}}}$ and $\tau_i^{t_{\mathrm{r}}}$ are the photo-ionisation rate and the optical depth at the beginning of the sub-cycling, given by Eqs. 5.8 and 5.9, and $\tau_i^{t_i} = \tau_i^{t_{\mathrm{r}}}\eta_i^{t_i}/\eta_i^{t_{\mathrm{r}}}$ is the optical depth at time t_i.

The number of ionisations $\Delta\mathcal{N}_{\mathrm{sub},i}$ occurring over the radiative transfer time step Δt_{r} is then $\Delta\mathcal{N}_{\mathrm{sub},i} = \mathcal{N}_{\mathrm{H},i}\sum\Gamma_i^{t_i}\eta_i^{t_i}\delta t_i$, where the sum is over all sub-steps δt_i in $(t_{\mathrm{r}}, t_{\mathrm{r}} + \Delta t_{\mathrm{r}})$. We set $\delta t_i \equiv \min(f\tau^{t_i}_{\mathrm{eq},i}, t_{\mathrm{r}} + \Delta t_{\mathrm{r}} - t_i)$, where $f < 1$ is a dimensionless factor. That is, we follow the evolution of the neutral fraction using an integration step that ensures its accurate integration (see Appendix 5.A). If $\Delta\mathcal{N}_{\mathrm{sub},i} = \Delta\mathcal{N}_{\mathrm{abs},i}$ for $t_i < t_{\mathrm{r}} + \Delta t_{\mathrm{r}}$, we set $\Gamma_i^{t_i} = 0$ for the remaining sub-cycles[4]. If at the end of the sub-cycling $\Delta\mathcal{N}_{\mathrm{sub},i} < \Delta\mathcal{N}_{\mathrm{abs},i}$, we explicitly conserve photons by adding $\Delta\mathcal{N}_{\mathrm{abs},i} - \Delta\mathcal{N}_{\mathrm{sub},i}$ photons to the photon transport in the next radiative transfer step.

When either the photo-ionisation rate or the recombination rate is high, τ_{eq} and hence δt will be very small (dropping the particle index i for simplicity). For $\delta t \ll \Delta t_{\mathrm{r}}$ the sub-cycling would become computationally very expensive. We could set a lower limit to the sub-cycling step δt to speed up the numerical integration of the rate equation. Of course, this would imply a loss of accuracy, and until the physical problem would re-adjust to match the condition $\delta t < \tau_{\mathrm{eq}}$, the numerical integration could even lead to a neutral fraction outside the physical range $0 \leq \eta \leq 1$. For instance, the number of ionisations $\Delta\mathcal{N}_{\mathrm{sub}}$ occurring for a particle during the sub-cycling over the time step Δt_{r} could then be larger than the number of neutral atoms $\eta^{t_{\mathrm{r}}}\mathcal{N}_{\mathrm{H}}^{t_{\mathrm{r}}}$ it represents at the beginning of the time step. In this case we could set $\eta = 0$ and add $\Delta\mathcal{N}_{\mathrm{sub}} - \eta^{t_{\mathrm{r}}}\mathcal{N}_{\mathrm{H}}^{t_{\mathrm{r}}}$ photons to the photon transport in the next radiative transfer time step.

We find, however, that photo-ionisation equilibrium is typically reached after only a few sub-cycles. Once photo-ionisation equilibrium is reached, integration of the rate equation is no longer necessary, since the solution does not change anymore. Instead of imposing a minimum size on the sub-cycle step, we therefore take the following short-cut to speed up the computation. We integrate the rate equation over the few sub-cycles required to reach equilibrium. Thereafter, we stop and simply keep the neutral fraction fixed. As opposed to imposing a minimum size on the sub-cycle step, this approach gives the exact solution. At the same time, it is very fast. For a photon-conserving transport we still need to know the number of photo-ionisations and recombinations occurring during the equilibrium phase. Both can, however, be obtained in a stroke, based on the number of photo-ionisations and recombinations that occurred during the last sub-cycle step over which the rate equation was integrated explicitly.

An evolving photo-ionisation rate

In the above presentation of our numerical implementation of the integration of the photo-ionisation rate equation we have changed the photo-ionisation rate according to the changes in the neutral fraction during that integration (Eq. 5.22). The importance[5] of properly following the evolution of the photo-ionisation rate in the presence of an evolving neutral fraction has been pointed out by Mellema et al. (2006). There, a time-averaged photo-ionisation rate obtained from an iterative (implicit) procedure was employed. While the derivation of the Mellema et al. (2006) procedure assumes a vanishing recombination rate (see the discussion in their Sec. 2.2), the sub-cycling procedure (Eq. 5.22) presented here does not suffer from this limitation.

If one is only interested in obtaining the equilibrium neutral fraction, the detailed handling of the photo-ionisation rate is, however, rather unimportant. This is because ionisation equilibrium implies that the number of photo-ionisations $d\mathcal{N}_{\mathrm{in}}/dt(1 - e^{-\tau})\Delta t_{\mathrm{r}}$ over the time interval Δt_{r} exactly equals the number of recombinations $(1-\eta)\mathcal{N}_{\mathrm{H}} n_{\mathrm{e}} \alpha \Delta t_{\mathrm{r}}$ over that same time interval.

---

[4] The particle then only recombines. This situation essentially occurs because the radiative transfer is discretized using finite time steps. In reality (i.e. for time steps $\Delta t_{\mathrm{r}} \rightarrow 0$), the ionisation rate will be constant. One may therefore also consider not to change the photo-ionisation rate, even though all photons that have been absorbed over the time step have already been used up in the integration of the photo-ionisation rate equation, to prevent the particle from artificially recombining.

[5] As already pointed out by Mellema et al. (2006), it actually is only important for large optical depths. For $\tau \ll 1$, Eq. 5.22 implies that the photo-ionisation rate is constant, $\Gamma_i^{t_i} = \Gamma_i^{t_r}$. In the optically thick regime, the assumption of $\Gamma = const$ would, however, generally lead to an underestimate of the true photo-ionisation rate, since $\Gamma(\eta) \propto (1 - e^{-\tau(\eta)})\eta^{-1}$ is a monotonically increasing function of decreasing neutral fraction (see Fig. 1 in Mellema et al. 2006).

This balance, however, has a unique (and stable; see Eq. 5.6) solution for the neutral fraction[6]. The equilibrium neutral fraction then also implies the correct photo-ionisation rate, via Eq. 5.8. When one is interested in following the details of the evolution of the neutral fraction towards photo-ionisation equilibrium, on the other hand, the dependence of the photo-ionisation rate on the neutral fraction needs to be taken into account, as presented above.

5.3.3 The time step $\Delta t_{\rm r}$

Our main consideration when choosing the size of the radiative transfer time step for the simulations we are presenting in this work, is that we wish to accurately reproduce the analytical and numerical reference results we are comparing with. These results include the time-dependence of the size of ionised regions around ionising sources. At early times, just after the sources start to emit ionising photons, the ionised regions expand quickly into the neutral hydrogen field surrounding the sources. To accurately reproduce this early phase of rapid growth, we necessarily have to employ time steps $\Delta t_{\rm r}$ that are relatively small. The phase of rapid growth is, however, only of relatively short duration. The subsequent evolutionary stages of modest resp. slow growth, which account for most of the (simulation) time, are often more interesting. We show in Sec. 5.4.2 that whenever we are not interested in the very early phase of rapid growth we can, thanks to the photon-conserving nature of TRAPHIC, choose substantially larger time steps without affecting the final outcome of our simulations.

For all but one of the simulations we present in this work, we will be concerned with solving the time-independent radiative transfer equation (see Sec. 4.4.4 in Chapter 4). In these simulations, we choose to propagate photon packets downstream from their location of emission only over a single inter-particle distance per radiative transfer time step, unless stated otherwise. This approach is equivalent to solving the time-independent radiative transfer equation in the limit of small radiative transfer time steps[7], $\Delta t_{\rm r} \to 0$. We have explicitly checked for all our simulations that the time step was chosen sufficiently small to be in agreement with this limit.

Our treatment of the time-independent radiation transport reduces the computational effort for the simulation of problems for which the time step has been fixed to a small value, e.g. by considerations like those presented in the beginning of this section. In the limit that radiation completely fills the simulation box, the computational effort required to solve the time-independent radiative transfer equation over the time interval T by propagating photon packets only over a single inter-particle distance per radiative transfer time step $\Delta t_{\rm r}$ is proportional to (cp. Sec. 4.4.2) $N_{\rm SPH} \times \tilde{N}_{\rm ngb} \times N_{\rm c} \times T/\Delta t_{\rm r}$. This has to be compared to the computational effort required to follow all photon packets over each time step until they leave the simulation box, which is proportional to $N_{\rm SPH} \times \tilde{N}_{\rm ngb} \times N_{\rm c} \times N_{\rm SPH}^{1/3} \times T/\Delta t_{\rm r}$. This is larger by a factor of $N_{\rm SPH}^{1/3}$, which for typical simulations reaches values of the order of 100.

In Sec. 5.4.5 we will present one simulation in which we solve the time-dependent radiative transfer equation. In this simulation we will employ the photon clock (see Chapter 4) to accurately control the distance over which photon packets are propagated over each time step $\Delta t_{\rm r}$ to match the light crossing distance $c\Delta t_{\rm r}$. In this context it is interesting to note that in the case of small time steps, i.e. $c\Delta t_{\rm r} < L_{\rm box}$, it is less expensive to solve the time-

---

[6] Note that this balance does not depend on the size of the time step $\Delta t_{\rm r}$, since it appears on both sides of the equation describing it.

[7] In the limit of small time steps $\Delta t_{\rm r} \to 0$, the time it takes for photons to travel to the simulation box boundaries by only propagating a single inter-particle distance per time step goes to zero. Hence, in this limit photons immediately leave the simulation box, as required for solving the time-independent radiative transfer equation.

dependent than the time-independent radiative transfer equation. This is because the computational effort to solve the time-dependent equation (again in the limit that radiation completely fills the simulation box and assuming that its boundaries are photon-absorbing) scales as $N_{\rm SPH} \times \tilde{N}_{\rm ngb} \times N_{\rm c} \times c\Delta t_{\rm r}/L_{\rm box} \times N_{\rm SPH}^{1/3} \times T/\Delta t_{\rm r}$, which is smaller than the computational effort for obtaining the time-independent solution (assuming that over each radiative transfer time step photon packets are transported until they leave the box) by the factor[8] $c\Delta t_{\rm r}/L_{\rm box}$.

5.3.4 Resampling

For some of the simulations that we present in Secs. 5.4.2 - 5.4.5 we employ the resampling technique described in Chapter 4 to reduce numerical artefacts that arise from the representation of the continuous density field with a discrete set of particles. The resampling requires the sampling of the SPH kernel used in GADGET-2, which is the spline given in Chapter 4, Eq. 4.4. We approximate this kernel by a Gaussian,

$$W_\sigma(r) = \frac{1}{(2\pi)^{3/2}\sigma^3}\exp(-r^2/2\sigma^2). \tag{5.23}$$

We find that with a standard deviation of $\sigma \sim 0.29 \times h$, the Gaussian provides a reasonable fit to the spline. A similar relation was employed in Alvarez, Bromm, & Shapiro (2006). When we resample the SPH density field, all SPH particles are redistributed by randomly displacing them from the positions given by the hydrodynamical simulation, with the probability to find a given particle displaced by the distance r given by Eq. 5.23. The (rare) displacements larger than h are discarded; in this case the original particle positions as determined by the hydrodynamical simulation are used.

5.3.5 Effective multi-frequency description - grey approximation

In our current implementation we use only a single frequency. Thus, we either assume that the ionising radiation is mono-chromatic, or we assume ionising radiation with a frequency spectrum J_ν and provide an effective multi-frequency description using only a single frequency bin. This is called the grey approximation (for a textbook discussion on the numerical treatment of multi-frequency radiation and the grey approximation see, e.g., Mihalas & Weibel Mihalas 1984).

For the latter case, we define a frequency-independent (grey) photo-ionisation cross-section $\bar{\sigma}$ such that the total photo-ionisation rate (Eq. 5.3) is conserved,

$$\Gamma = \int_0^\infty d\nu\,\frac{4\pi J_\nu(\nu)}{h_{\rm p}\nu}\sigma_\nu \equiv \bar{\sigma}\int_{\nu_0}^\infty d\nu\,\frac{4\pi J_\nu(\nu)}{h_{\rm p}\nu}, \tag{5.24}$$

with

$$\bar{\sigma} = \int_0^\infty d\nu\,\frac{4\pi J_\nu(\nu)}{h_{\rm p}\nu}\sigma_\nu \times \left[\int_{\nu_0}^\infty d\nu\,\frac{4\pi J_\nu(\nu)}{h_{\rm p}\nu}\right]^{-1}. \tag{5.25}$$

---

[8] Observe that for larger time steps, i.e. $\Delta t_{\rm r} \geq L_{\rm box}/c$, and assuming photon-absorbing boundaries, the computational effort for solving the time-dependent radiative transfer equation equals the computational effort for solving the time-independent radiative transfer equation. It exceeds the computational effort for solving the time-independent radiative transfer equation with photon packets propagating only a single inter-particle distance per radiative transfer time step if $c\Delta t_{\rm r} > L_{\rm box}/N_{\rm SPH}^{1/3}$.

We note that for the purpose of computing the photo-ionisation rate the grey approximation provides an exact description of the multi-frequency problem if the radiation spectrum $J_\nu(\nu)$ is known. If instead the radiation spectrum is also computed in the grey approximation, i.e. by performing radiative transfer simulations using only a single frequency bin, then this approximation will provide an exact description of the multi-frequency problem only in the optically thin regime. In the optically thick regime, the frequency dependence of the photo-ionisation cross-section results in a deformation of the radiation field spectral shape that favours high-energy photons, because low-frequency photons are more likely to be absorbed (Eq. 5.2). This *spectral hardening* can only be accounted for by performing true multi-frequency radiative transfer, i.e. by using sufficiently many frequency bins (see Sec. 7.6.2 in Chapter 7 for a discussion of spectral hardening).

In the following we will be interested in the special case where the mean intensity obeys a black-body spectrum with temperature $T_{\rm bb} = 10^5$ K. That is, $J_\nu(\nu) \propto B_\nu(\nu)$, where

$$B_\nu(\nu, T_{\rm bb}) = \frac{2h_{\rm p}}{c^2} \frac{\nu^3}{\exp\left(\frac{h_{\rm p}\nu}{kT_{\rm bb}}\right) - 1}, \tag{5.26}$$

is the Planck function. Eq. 5.25 then implies a value

$$\bar{\sigma} = 1.49 \times 10^{-18}\ {\rm cm}^{-2} \tag{5.27}$$

for the grey photo-ionisation cross-section.

5.4 TESTS

In this section we report the performance of the implementation of TRAPHIC that we have presented in the previous section in well-defined tests. We will demonstrate that TRAPHIC can be used to accurately solve the radiative transfer equation for hydrogen-ionising radiation in arbitrary geometries and arbitrary optical depth regimes.

We start by verifying the accuracy of our sub-cycling approach in computing the non-equilibrium neutral fraction (Sec. 5.4.1). We then perform several three-dimensional radiative transfer simulations of increasing complexity. These simulations comprise the evolution of the ionised region around a single star in a homogeneous density field (Sec. 5.4.2), the casting of a shadow behind an opaque obstacle (Sec. 5.4.1), the propagation of an ionisation front around a star in a centrally peaked density profile (Sec. 5.4.4) and the propagation of ionisation fronts driven by the ionising radiation of multiple stars in an inhomogeneous density field obtained from a cosmological simulation (Sec. 5.4.5).

We compare the results obtained with TRAPHIC with analytic solutions, where available. For all but the simplest test problems, however, no analytic solution is known, mainly due to the complex geometries involved. We have therefore designed the test problems in Secs. 5.4.1, 5.4.2 and 5.4.5 to closely follow the description given in the Cosmological Radiative Transfer Codes Comparison Project (Iliev et al. 2006b), which provides a useful set of numerical reference solutions to compare with. We have designed the test problems in Sec. 5.4.3 and 5.4.4 to resemble the corresponding test problems presented in Mellema et al. (2006). In addition, we have developed a radiative transfer code that solves the radiative transfer equation for spherically symmetric problems on a one-dimensional regular mesh. We refer to this code as TT1D (TestTraphic1D). We will use TT1D to obtain reference solutions for the spherically symmetric test problems in Secs. 5.4.2 and 5.4.4. We will refer to these reference solutions as the exact solutions to the corresponding radiative transfer problems.

Throughout we will assume that the density field is static. We defer a discussion of radiative transfer simulations on dynamically evolving density fields to Chapter 6. To facilitate a direct comparison with Iliev et al. (2006b), we present results after mapping physical quantities defined on the SPH particles to a regular grid, unless stated otherwise. This is done using a mass-conserving SPH interpolation similar to the one described in Alvarez, Bromm, & Shapiro (2006) that we have implemented for this purpose. We opted for the SPH interpolation since it is consistent with the SPH simulation we are employing. For comparison, we repeated our analysis using TSC mass-conserving interpolation (Hockney & Eastwood 1988) but found no significant differences.

For all tests reported in this section we employ the on-the-spot approximation (e.g. Osterbrock 1989) in order to allow a direct comparison with Iliev et al. (2006b). In the on-the-spot approximation diffuse photons emitted during recombinations to the hydrogen ground energy level are assumed to be immediately re-absorbed by neutral hydrogen atoms close to the location of emission. The effect of recombination radiation can then be simply taken into account by setting the recombination coefficient α to the so-called case B value $\alpha_{\rm B}$, which can be well approximated by (see, e.g., Fig. 7.3 in Chapter 7)

$$\alpha_{\rm B}(T) = 2.59 \times 10^{-13} \left(\frac{T}{10^4 \ {\rm K}}\right)^{-0.7} \ {\rm cm}^3 \ {\rm s}^{-1}, \tag{5.28}$$

where $T \approx 10^4$ K is the gas temperature. We will report on the study of diffuse radiation in which we will explicitly follow the scattering of recombination photons instead of employing the on-the-spot approximation in future work.

To keep the tests problems clean, we furthermore assume that the gas temperature T is constant, taking $T = 10^4$ K for the ionised gas. In Chapter 7 we will extend our implementation of TRAPHIC to also compute the temperature of the gas, in a self-consistent manner in step with the evolution of its ionisation state, and repeat some of the test problems discussed here.

In their simulations, Iliev et al. (2006b) and Mellema et al. (2006) assumed that the speed of light is infinite, i.e. they solved the time-independent radiative transfer equation. For the comparison with these simulations we will therefore make the same assumption (recall Sec. 5.3.3 for the discussion of how we solve the time-independent radiative transfer equation). From now on, when referring to the radiative transfer equation, we therefore assume it to be of the time-independent form, unless stated otherwise. We will repeat one of the simulations presented in Sec. 5.4.5 to solve the time-dependent radiative transfer equation by employing the photon packet clocks as described in Sec. 4.4.4 in Chapter 4.

Since its publication in Pawlik & Schaye (2008), TRAPHIC has been continuously improved. An important change with respect to the description in Pawlik & Schaye (2008) is a new treatment of how virtual particles (ViPs) distribute the photons they absorbed amongst their $\tilde{N}_{\rm ngb}$ neighbouring SPH particles that have been used to compute the ViPs' neutral density. Previously, this was done by giving, to each of the neighbours, a fraction of the absorbed photons that is proportional to the value of the ViPs' SPH kernel at their position. In the current version, the distribution is done by giving, to each of the neighbours, a fraction of the absorbed photons that is proportional to the neutral mass with which they contributed to the SPH estimate of the neutral density of the given ViP. The new way of distributing the absorptions is more consistent, since each of the SPH neighbours contributed to the ViP's absorptions coefficient (that is then used to compute the number of photons it absorbs and distributes amongst its

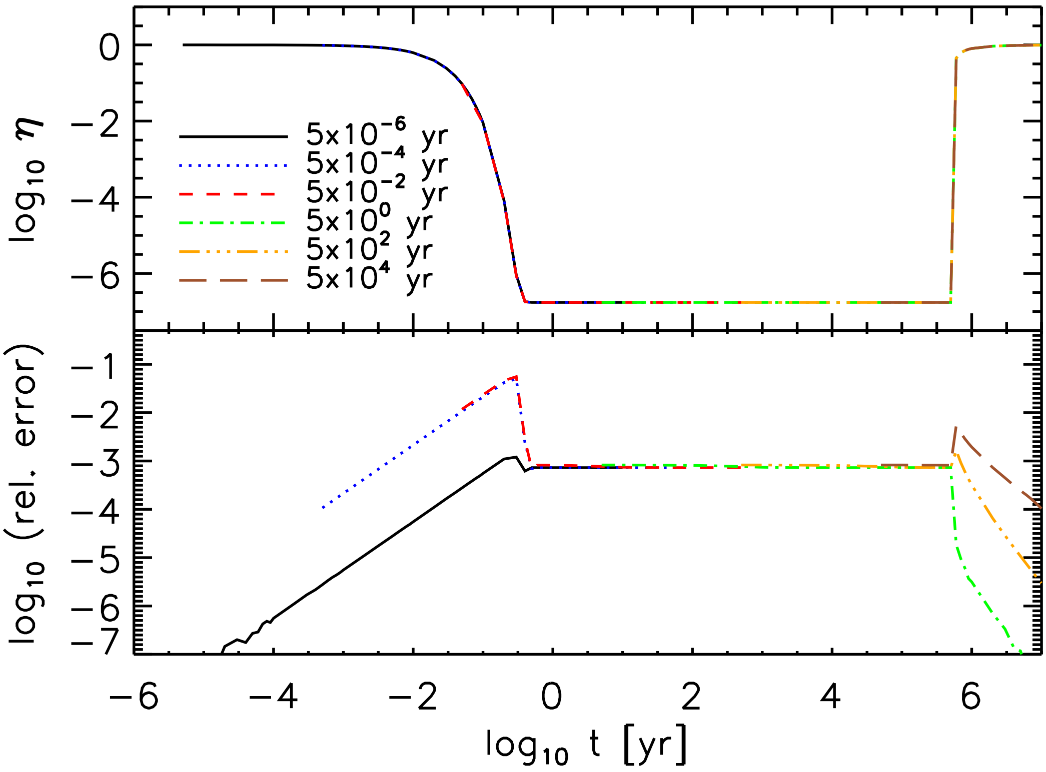

Figure 5.1: Test 0. Optically thin gas particle ionising up and recombining. *Top panel:* evolution of the neutral fraction obtained from the numerical integration (using Euler sub-cycling) of the photo-ionisation rate equation (Eq. 5.29). The curves show the neutral fraction evolution obtained using the integration steps $\Delta t_{\rm r}$ indicated in the legend. *Bottom panel:* relative difference between the numerically computed evolution shown in the top panel and the exact result, Eq. 5.35. Thanks to the sub-cycling, the numerical integration accurately reproduces the exact evolution of the neutral fraction for all sizes of the radiative transfer time step. Note that the simulations with time step $\Delta t_{\rm r} \leq 10^{-2}$ yr have been stopped before $t_{\rm end} = 5$ Myr because they are computationally very expensive.

neighbours) in proportion to its neutral fraction. Unless noted otherwise, the results presented in the following have been obtained with this new version of TRAPHIC. They may therefore differ slightly from those presented in Pawlik & Schaye (2008). We discuss these differences in detail in App. 5.C, to which the reader is referred.

5.4.1 Test 0: Sub-cycling the photo-ionisation rate equation

We start by testing the sub-cycling approach to the computation of the non-equilibrium neutral fraction of gas exposed to ionising radiation that we have introduced in Sec. 5.3.2. Our aim is to demonstrate that, given a flux impinging on a gas parcel (or, equivalently, a photo-ionisation rate experienced by this parcel), the sub-cycling allows for an accurate computation of the evolution of its ionisation state, independent of the size of the radiative transfer time step $\Delta t_{\rm r}$.

In close analogy to Test 0 in Iliev et al. (2006b) we simulate the evolution of the ionisation state of an optically thin gas parcel with hydrogen number density $n_{\rm H} = 1 \ {\rm cm}^{-3}$. The simulation starts with a fully neutral parcel at time t = 0. We then apply a flux of $F = 10^{12} \ {\rm s}^{-1}\,{\rm cm}^{-2}$ hydrogen-ionising photons with a black-body spectrum $B_\nu(\nu, T_{\rm bb})$ of characteristic temperature $T_{\rm bb} = 10^5$ K. Consequently, the parcel becomes highly ionised. After $t = 0.5$ Myr we switch off the ionising flux and the parcel only recombines. The simulation ends at $t_{\rm end} =$ 5 Myr. Throughout the simulation we assume a constant gas temperature $T = 10^4$ K (note that this is in contrast to the test described in Iliev et al. 2006b, where the temperature evolution was followed self-consistently). This simplification will allow us to analytically derive the evolution of the neutral fraction with which our numerical results will then be compared. We will consider the combined evolution of the neutral fraction and the temperature of an optically thin gas parcel exposed to ionising radiation in Chapter 7.

We simulate the evolution of the gas parcel's neutral fraction $\eta = 1 - \chi$ by numerically integrating the photo-ionisation rate equation (see Eq. 5.4),

$$\frac{d}{dt}\eta = \alpha(T) n_{\rm e} \chi - \Gamma\eta, \tag{5.29}$$

employing the sub-cycling procedure described in Sec. 5.3.2. Recall that the sub-cycling integrates Eq. 5.29 explicitly using sub-cycle steps $\delta t \equiv f\tau_{\rm eq} \leq \Delta t_{\rm r}$. The dimensionless parameter f controls the accuracy of the integration. The recombination coefficient $\alpha(T)$ is given by Eq. 5.28 and the photo-ionisation rate Γ is (see Eq. 5.24)

$$\Gamma = \bar\sigma \int_{\nu_0}^{\infty} d\nu \, \frac{4\pi J_\nu(\nu)}{h_{\rm p}\nu}. \tag{5.30}$$

Using $\bar\sigma = 1.49 \times 10^{-18}$ cm^{-2} appropriate for the black body-spectrum $B_\nu(\nu, T_{\rm bb})$ under consideration (cp. Eq. 5.27) and $4\pi J_\nu(\nu)/(h_{\rm p}\nu) = F B_\nu(\nu, T_{\rm bb}) / \int_{\nu_0} d\nu \ B_\nu(\nu, T_{\rm bb})$, the photo-ionisation rate becomes $\Gamma = 1.49 \times 10^{-6}$ s^{-1}.

Eq. 5.29 can also be integrated analytically[9]. To see this, we write it in the form

$$\frac{d\chi}{dt} = -b(\chi - \chi_+)(\chi - \chi_-), \tag{5.31}$$

where

$$\chi_\pm \equiv \frac{a}{2b}\left(-1 \pm \sqrt{1 + \frac{4b}{a}}\right), \tag{5.32}$$

$$a \equiv \Gamma^{-1}, \tag{5.33}$$

$$b \equiv n_{\rm H}\alpha. \tag{5.34}$$

Eq. 5.31 is a differential equation of Riccati type. Its integration by separation of variables yields

$$\chi(t) = \frac{\chi_+ - \chi_- \exp[(-bt + C)(\chi_+ - \chi_-)]}{1 - \exp[(-bt + C)(\chi_+ - \chi_-)]}. \tag{5.35}$$

The integration constant C is fixed by the initial condition $\chi(t_0) = \chi_0$,

$$C = (\chi_+ - \chi_-)^{-1} \ln \frac{\chi_0 - \chi_+}{\chi_0 - \chi_-} + bt_0. \tag{5.36}$$

---

[9] This is a standard result from kinetic theory. For a discussion in the astrophysical literature see, e.g., Dove & Shull (1994).

In Fig. 5.1 we show the result of the simulation and compare it to the analytical result, which we will refer to as the exact result. The top panel shows the evolution of the neutral fraction for simulations using time steps $\Delta t_{\rm r} = 5 \times (10^{-6}$,$10^{-4}$, 10^{-2}, 10^{0}, 10^{2}, 10^{4} yr), which span 10 orders in magnitude. Note that the photo-ionisation rate implies a photo-ionisation time of only $\tau_{\rm ion} \equiv \Gamma^{-1} \approx 0.02$ yr and that the recombination time is $(\alpha n_{\rm H})^{-1} \approx 0.1$ Myr. The bottom panel shows the relative difference between the numerically computed evolutions shown in the top panel and the exact result. The agreement is excellent, with the numerical evolution never deviating by more than 10% from the exact result. This small deviation can be further reduced by lowering the value of the parameter f that controls the size of the sub-cycle steps[10]. The calculation presented here employed $f = 0.01$.

In conclusion, we have shown that with our sub-cycling approach we are able to accurately follow the evolution of the ionisation state of a gas parcel, regardless of the size of the radiative transfer time step $\Delta t_{\rm r}$ (assuming that the impinging flux is correctly computed over this time step), which was our main motivation to introduce the sub-cycling. It allows us to perform the radiative transfer and correctly compute the neutral fractions using radiative transfer time steps whose sizes are independent (and generally much larger) of the occurring photo-ionisation and recombination times, which are often impractically small.

Having established our method to solve the photo-ionisation rate equation, which comprises an important building block of our numerical implementation of TRAPHIC, we can now confidently turn to testing TRAPHIC's performance in radiative transfer problems. This will be the subject of Secs. 5.4.2 to 5.4.5.

5.4.2 Test 1: HII region expansion in a uniform medium

In this section we consider the problem of a steady ionising source emitting $\dot{\mathcal{N}}_\gamma$ mono-chromatic photons of frequency $h_{\rm p}\nu = 13.6$ eV per unit time, which is turned on in a static, initially neutral, uniform medium of constant hydrogen number density $n_{\rm H}$. This is a standard test problem, for which there exists a well-known analytical solution (for a text book discussion see Dopita & Sutherland 2003).

In equilibrium, the number of photons emitted by the source has to compensate the number of recombinations within the surrounding, stationary, ionised region, the so-called Strömgren sphere. Assuming that the Strömgren sphere is fully ionised, i.e. $\chi \equiv 1$, its radius $r_{\rm s}$ is therefore given by the balance equation

$$\dot{\mathcal{N}}_\gamma = \frac{4}{3}\pi r_{\rm s}^3 \alpha_{\rm B}(T) n_{\rm H}^2. \tag{5.37}$$

The evolution of the spherical, fully ionised region towards the equilibrium Strömgren sphere is described by the following equation for its radius $r_{\rm I}$, the ionisation front,

$$4\pi r_{\rm I}^2 n_{\rm H} \frac{dr_{\rm I}}{dt} = \dot{\mathcal{N}}_\gamma - 4\pi \int_0^{r_{\rm I}} dr\ r^2 \alpha_{\rm B}(T) n_{\rm H}^2(r), \tag{5.38}$$

which, for the case of constant density $n_{\rm H}(r) = n_{\rm H}$ that is of interest here, reads

$$4\pi r_{\rm I}^2 n_{\rm H} \frac{dr_{\rm I}}{dt} = \dot{\mathcal{N}}_\gamma - \frac{4}{3}\pi r_{\rm I}^3 \alpha_{\rm B}(T) n_{\rm H}^2. \tag{5.39}$$

---

[10] In the simulations with time step $\Delta t_{\rm r} < f \times \Gamma^{-1}$ (here: in the simulations using $\Delta t_{\rm r} = 5 \times 10^{-6}$ yr) the integration accuracy is controlled by the size of $\Delta t_{\rm r}$. This is the reason why the relative error for the simulation with time step $\Delta t_{\rm r} = 5 \times 10^{-6}$ yr is smaller than that for the simulation with time step $\Delta t_{\rm r} = 5 \times 10^{-4}$ yr.

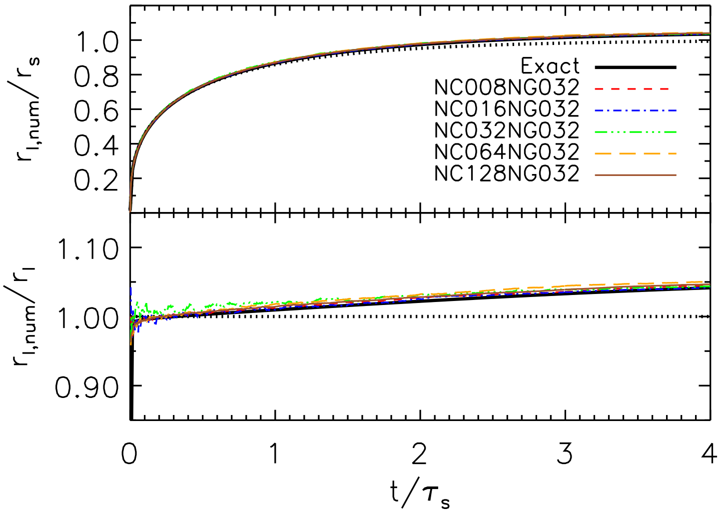

Figure 5.2: Test 1. The evolution of the ionisation front for the angular resolutions $N_{\rm c} = 8, 16, 32, 64$ and 128, as indicated in the legend. The spatial resolution is fixed ($N_{\rm SPH} = 64^3$, $\tilde{N}_{\rm ngb} = 32$). The top panel shows the position of the ionisation front $r_{\rm I,num}$ normalised by the Strömgren radius $r_{\rm s}$ as a function of time. The thick black solid curve shows a numerical reference solution obtained with a one-dimensional, grid-based radiative transfer code (see text). The black dotted curve shows the analytic reference solution, Eq. 5.41, which has been obtained by assuming $\chi \equiv 1$ throughout the ionised region. The results from the numerical simulations employing TRAPHIC closely match the numerical reference solution. The bottom panel shows the position of the ionisation fronts of the top panel divided by the analytic reference solution. Note that the analytic reference solution slightly differs from the numerical reference solution, due to the simplifying assumptions inherent to the analytic approach (see also the discussion of Eq. 5.43).

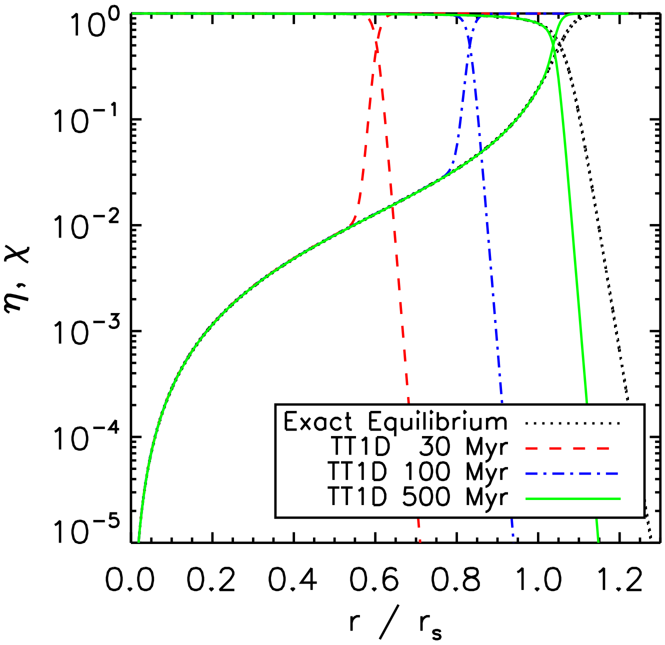

Figure 5.3: Test 1. Neutral and ionised fractions obtained from Eq. 5.43 (dotted black curves), which is the exact equilibrium solution, and from simulations with our reference code TT1D at times $t = 30$ Myr (red dashed curves), 100 Myr (blue dot-dashed curves) and 500 Myr (green solid curves). The simulations with TT1D yield results that are identical to the exact equilibrium solution at all radii for which photo-ionisation equilibrium has been reached, i.e. for radii well inside the ionised region. This excellent agreement justifies the use of TT1D for obtaining accurate reference solutions. Note that, for the chosen parameters, the equilibrium position of the ionisation front is at $r = 1.05 r_{\rm s}$ and thus at a slightly larger radius than implied by the commonly employed analytical approximation Eq. 5.41.

Introducing the new variables $\xi \equiv r_{\rm I}/r_{\rm s}$ and $\tau \equiv t/\tau_{\rm s}$, where the Strömgren time scale $\tau_{\rm s} = 1/(\alpha_{\rm B} n_{\rm H})$ is the recombination time in a fully ionised gas, we arrive at the differential equation

$$\frac{d\xi}{d\tau} = \frac{1-\xi^3}{3\xi^2}, \tag{5.40}$$

the solution of which reads

$$r_{\rm I}(t) = r_{\rm s}(1 - e^{-t/\tau_{\rm s}})^{1/3}. \tag{5.41}$$

Hence, the ionisation front reaches the Strömgren sphere after a few Strömgren times $\tau_{\rm s}$ and stays static thereafter.

In reality the neutral fraction inside the ionised region is, however, not zero, but varies smoothly with the distance to the ionising source. We therefore invoke the commonly employed definition of the ionisation front as the radius at which the neutral fraction equals 50 per cent, i.e. $\eta = 0.5$. The equilibrium neutral fraction $\eta_{\rm eq}(r) = \lim_{t\to\infty} \eta(r)$ can be obtained from (e.g. Osterbrock 1989)

$$\frac{\eta_{\rm eq}(r) n_{\rm H}}{4\pi r^2} \int d\nu\, \dot{\mathcal{N}}_\gamma(\nu) e^{-\tau_\nu} \sigma_\nu = \chi^2_{\rm eq}(r) n^2_{\rm H} \alpha_{\rm B}, \tag{5.42}$$

which can be rewritten to give the quadratic equation

$$\eta^2_{\rm eq}(r) - \left(\int d\nu\, \frac{\dot{\mathcal{N}}_\gamma(\nu) e^{-\tau_\nu}}{4\pi r^2 n_{\rm H} \alpha_{\rm B}} \sigma_\nu + 2 \right) \eta_{\rm eq}(r) + 1 = 0, \tag{5.43}$$

where the optical depth $\tau_\nu(r)$ is given by

$$\tau_\nu(r) = n_{\rm H} \sigma_\nu \int_0^r dr'\, \eta_{\rm eq}(r'). \tag{5.44}$$

We refer to the neutral fraction $\eta_{\rm eq}(r)$ obtained by direct numerical integration of Eq. 5.43 as the exact equilibrium neutral fraction profile and to $\chi_{\rm eq}(r) = 1 - \eta_{\rm eq}(r)$ as the exact equilibrium ionised fraction profile.

In the following we present a suite of radiative transfer simulations demonstrating that TRAPHIC is able to accurately follow the evolution of the ionisation front around a single ionising point source. For the setup of the numerical simulations we closely follow the description of Test 1 presented in Iliev et al. (2006b). The only differences are that we employ a different spatial resolution and that we start from ionised fractions [11] $\chi = 0$ instead of $\chi = 1.2 \times 10^{-3}$. This close matching of the setup allows us to directly compare our results to the results presented in the code comparison project. In particular, we choose a number density $n_{\rm H} = 10^{-3}$ cm^{-3} and an ionising luminosity of $\dot{\mathcal{N}}_\gamma = 5 \times 10^{48}$ photons s^{-1}. The gas is assumed to have a constant temperature $T = 10^4$ K. With these values, $r_{\rm s} = 5.4$ kpc and $\tau_{\rm s} = 122.4$ Myr.

The exact equilibrium neutral and ionised fraction profiles computed using Eq. 5.43 are shown as black dotted curves in Fig. 5.3. Note that for our choice of parameters, $r_{\rm I,eq} = 1.05\ r_{\rm s}$. The ionisation front obtained from the solution to Eq. 5.43 is thus at a slightly larger radius than the equilibrium ionisation front obtained assuming the Strömgren sphere is fully ionised (Eq. 5.41).

---

[11] Iliev et al. (2006b) motivated their choice of a nonzero initial ionised fraction with the presence of collisional ionisations, which we do not consider here.

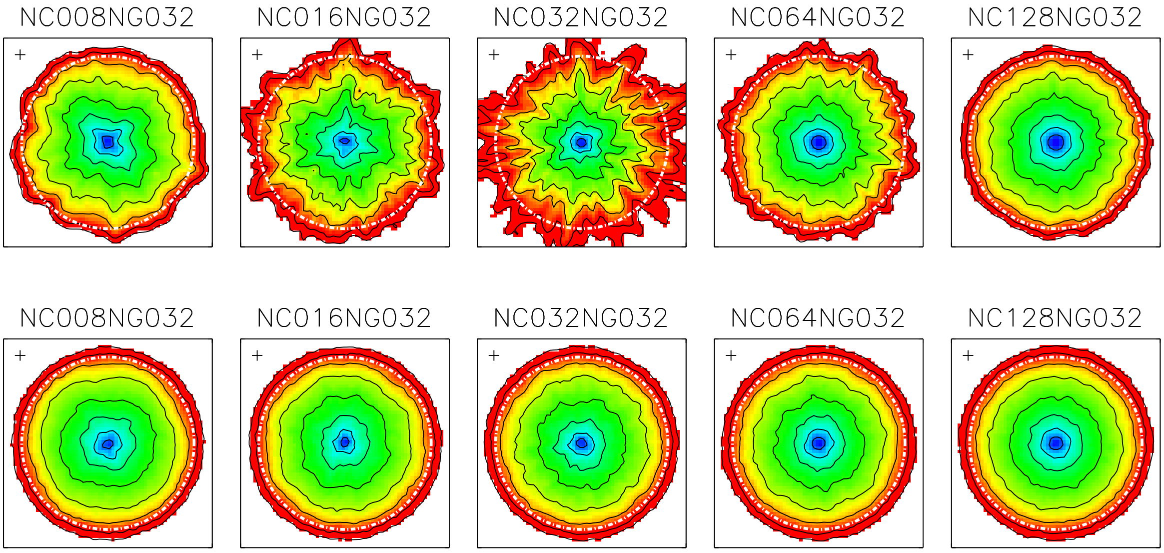

Figure 5.4: Test 1. Slice through the simulation box at $z = L_{\rm box}/2$ showing the neutral fraction at the end of the simulation ($t_{\rm r} = 500$ Myr) for simulations with (bottom row) and without (top row) resampling of the density field. The angular resolution increases from $N_{\rm c} = 8$ in the left-most to $N_{\rm c} = 128$ in the right-most column, as indicated in the panel titles. The spatial resolution is fixed to $N_{\rm SPH} = 64^3$, $\tilde{N}_{\rm ngb} = 32$ and is indicated by the cross of length $2\langle\tilde{h}\rangle$ in the upper left corner of each panel. Black contours show neutral fractions of $\eta = 0.9, 0.5, \log\eta = -1, -1.5, -2, -2.5, -3, -3.5$, going from the outside in. The white dot-dashed circle indicates the Strömgren sphere, which should be, and is, just inside to the $\eta = 0.5$ contour. The colour scale is logarithmic and has a lower cut-off of $\log\eta = -5$ (see Fig. 7.14 in Chapter 7 for a colour bar). Note that the resampling strongly suppresses the particle noise seen in the top-row panels.

The last observation indicates that the analytic solution given by Eq. 5.41 generally fails to provide an accurate reference solution that can be used to judge the validity of the numerical results obtained with a new radiative transfer scheme like TRAPHIC, due to its simplification of the problem. We therefore additionally employ the numerical solution obtained with our spherically symmetric mesh-based radiative transfer code TT1D, that we have mentioned in Sec. 5.4, in our comparisons below. In Fig. 5.3 we compare the neutral (ionised) fraction profiles obtained in simulations with TT1D to the exact equilibrium solution. The spatial resolution and the size of the time step employed in these simulations have been chosen such as to achieve numerical convergence. At radii where photo-ionisation equilibrium has been reached, the results obtained with TT1D are in excellent agreement with the exact equilibrium solution. At $t = 500$ Myr, i.e. after about 4 recombination times, equilibrium has been reached for most of (but not all of) the final ionised volume, as expected.

With accurate reference solutions at hand, we now turn to discuss the performance of TRAPHIC in the present test problem. We have set up the initial conditions described above in a simulation box of length $L_{\rm box} = 13.2$ kpc containing $N_{\rm SPH} = 64^3$ SPH particles[12]. The ionising source is located in the centre. The box boundary is photon-transmissive. We assign

---

[12] We note that Iliev et al. (2006b) employed $N_{\rm cell} = 128^3$ cells, with the ionising source located in one of the corners of the box.

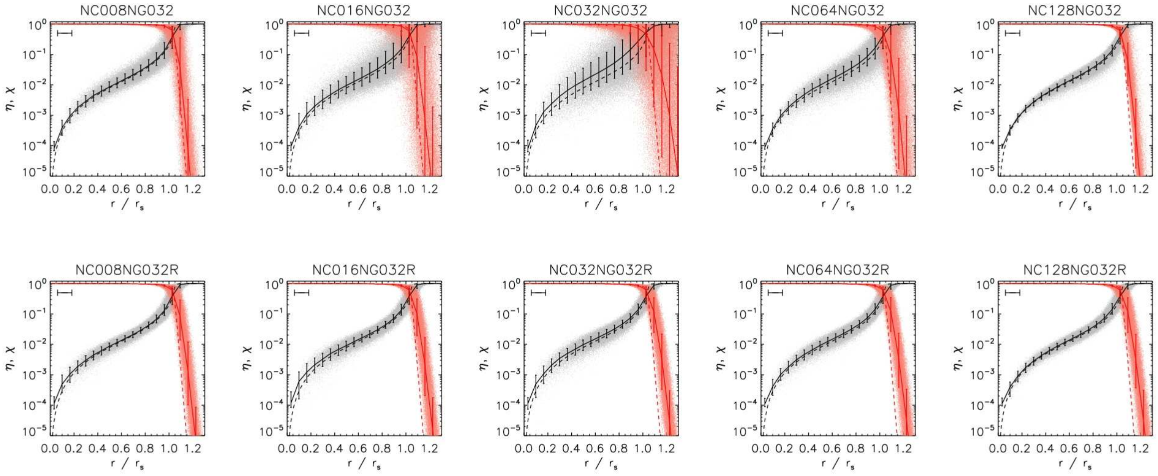

Figure 5.5: Test 1. Profiles of neutral and ionised fraction at the end of the simulation ($t_{\mathrm{r}} = 500$ Myr) for simulations with (bottom row) and without (top row) resampling of the density field. The spatial resolution is fixed to $N_{\mathrm{SPH}} = 64^3$, $\tilde{N}_{\mathrm{ngb}} = 32$ and is indicated by the horizontal error bars in the upper left corner of each panel. The angular resolution increases from $N_{\mathrm{c}} = 8$ in the left-most to $N_{\mathrm{c}} = 128$ in the right-most column, as indicated in the panel titles. The panels therefore directly correspond to those shown in Fig. 5.4. The grey (light red) points show the neutral (ionised) fraction of each particle. The solid black (red) curve shows the median neutral (ionised) fraction in spherical bins and the error bars show the corresponding 68.3% confidence intervals. The dashed black (red) curves show the exact solution, obtained with TT1D.

each SPH particle a mass $m = n_{\mathrm{H}} m_{\mathrm{H}} L_{\mathrm{box}}^3 / N_{\mathrm{SPH}}$. The positions of the SPH particles are chosen to be glass-like (White 1996). Glass-like initial conditions yield a more regular distribution of the particles within the box as compared to Monte Carlo sampling of the density field and are thus more suitable for the simulation of the current problem (see also our discussion in App. 5.D). The SPH smoothing kernel is computed and the SPH densities are found using the SPH formalism implemented in GADGET-2, with $N_{\mathrm{ngb}} = 48$.

We perform 5 simulations, increasing the angular resolution by factors of two from $N_{\mathrm{c}} = 8$ to $N_{\mathrm{c}} = 128$. The number of neighbours employed for the transport of radiation is fixed to $\tilde{N}_{\mathrm{ngb}} = 32$. Hence all 5 simulations employ the same spatial resolution. The time step is set to $\Delta t_{\mathrm{r}} = 10^{-2}$ Myr. In Fig. 5.2 we show the evolution of the ionisation front radius, which we determined by taking the average over the positions of all particles that have a neutral fraction $0.4 < \eta < 0.6$. For all 5 simulations, the position of the ionisation front never deviates more than 5 per cent from the analytic solution, Eq. 5.41, comparable to what has been found with other codes as reported in the Cosmological Radiative Transfer Code Comparison Project (Iliev et al. 2006b). Note that the deviations from the analytic solution can mainly be attributed to the fact that the analytic approach provides only an approximate expression for the radius of the ionisation front, because it erroneously assumes $\chi \equiv 1$. In fact, all simulations nearly perfectly follow the numerical reference solution and approach the proper asymptotic limit $r_{\mathrm{I,eq}} = 1.05\, r_{\mathrm{S}}$.

The top row of Fig. 5.4 shows the neutral fraction in a slice through the centre of the simulation box at $t_{\mathrm{r}} = 500$ Myr, which marks the end of the simulation, for each of the 5 simulations. As we already noted, the ionisation front is at the expected position. As is true for all other

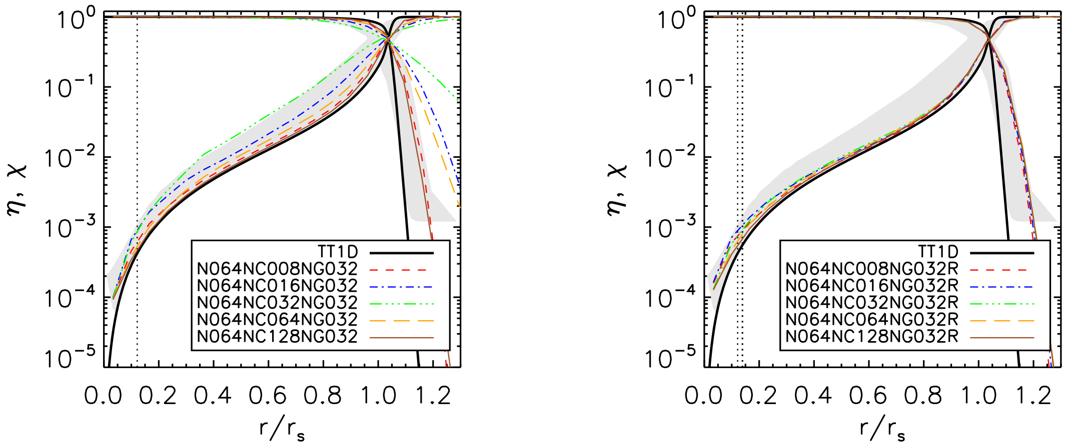

Figure 5.6: Test 1. Comparison to Iliev et al. (2006b). Spherically averaged neutral and ionised fractions within the Strömgren sphere at $t_\mathrm{r} = 500$ Myr for different angular resolutions, as indicated in the legend. The profiles in the left-hand (right-hand) panel correspond to simulations without (with) resampling the density field. The spatial resolution is fixed ($N_\mathrm{SPH} = 64^3$, $\tilde{N}_\mathrm{ngb} = 32$). The thick black solid curves correspond to the exact profile obtained with our reference code TT1D. The vertical dotted line marks the radius r = $2\langle\tilde{h}\rangle$, corresponding to the spatial resolution employed. In the right-hand panel, the additional (right-most) vertical dotted line indicates the radius corresponding to the spatial resolution $2\langle h\rangle$ of the SPH simulations, which is the scale on which particle positions are randomly displaced during the resampling. The grey bands show the range of neutral and ionised fractions found by other codes as reported in Iliev et al. (2006b). There, the simulations were initialised with an ionised fraction $\chi = 1.2 \times 10^{-3}$, which explains the cut-off exhibited by the grey band at large distances $r/r_\mathrm{s} \gtrsim 1.2$.

surfaces of constant neutral fraction shown, the ionisation front clearly exhibits the expected spherically symmetric shape, although it is noisy in some of the simulations. The amount of noise depends on the ratio of the angular and spatial resolutions employed. For $N_\mathrm{c} = 8$ (left-most panel in the top row), the average number of neighbours per emission or transmission cone is high, $\tilde{N}_\mathrm{ngb}/N_\mathrm{c} = 4$ and, as a result, numerical noise arising from the representation of the continuous density field with discrete SPH particles is suppressed. With increasing angular resolution the average number of neighbours per cone decreases and the contours become more noisy. The noise level reaches a maximum for $N_\mathrm{c} = \tilde{N}_\mathrm{ngb}$ (middle panel in the top row). For higher angular resolutions, the probability of finding no neighbours inside an emission or transmission cone becomes high and a large number of ViPs are created. The ratio of the number of ViPs to the number of SPH particles enclosed by the ionisation front for the simulation with angular resolution $N_\mathrm{c} = 8, 16, 32, 64$ and 128 is $\approx 0, 0.003, 0.06, 0.5$ and 0.9, resp. The ViPs placed in empty cones regularise the neutral fraction of the ionised density field by distributing the photons they absorb amongst their $\tilde{N}_\mathrm{ngb}$ SPH neighbours using (photon-conserving) SPH interpolation.

The panels in the top row of Fig. 5.5 show profiles of the neutral and ionised fraction around the ionising source at $t = 500$ Myr. Each grey (light red) dot represents the neutral (ionised) fraction of an individual particle, and the solid black (red) curves with error bars show the median neutral (ionised) fraction in spherical bins. They are compared to the dashed black (red) curves that indicate the exact results obtained with TT1D. The agreement between the results obtained with TRAPHIC and the exact result is generally very good. We note that this good

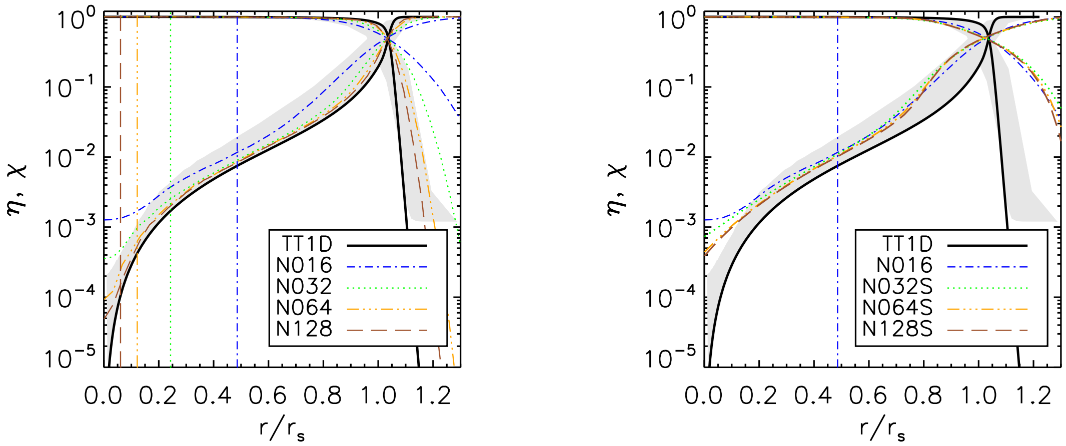

Figure 5.7: Test 1. Spherically averaged neutral and ionised fractions within the Strömgren sphere at $t_\mathrm{r} = 500$ Myr. The simulations all have the same angular resolution ($N_\mathrm{c} = 8$) and employ the same number of neighbours ($\tilde{N}_\mathrm{ngb} = 32$), but use a different number of SPH particles, increasing from $N_\mathrm{SPH} = 16^3$ to $N_\mathrm{SPH} = 128^3$ in factors of 2^3. The black solid curves correspond to the exact profiles, obtained with our reference code TT1D. The grey bands show the range of neutral and ionised fractions found by other codes as reported in Iliev et al. (2006b). Left-hand panel: For each simulation the spatial resolution is marked by a vertical line (in colour and line-style identical to the corresponding profile) at radius $2\langle\tilde{h}\rangle$. The higher the spatial resolution, the more closely the exact profile is approached. Right-hand panel: The profile corresponding to the lowest spatial resolution simulation ($N_\mathrm{SPH} = 16^3$, blue dot-dashed line) is repeated from the left-hand panel. The profiles of all other simulations have been smoothed over the spatial resolution element $2\langle\tilde{h}\rangle$ of the lowest spatial resolution simulation, corresponding to the radius marked by the vertical line. The profiles become nearly identical after smoothing them to the same resolution.

agreement also holds at earlier times, when the ionised sphere is still rapidly expanding, which we explicitly demonstrate for the high angular resolution simulation ($N_\mathrm{c} = 128$) in App. 5.C. Small deviations from the exact result occur for the simulations with $N_\mathrm{c} = 16, 32$ and 64 due to the noise they exhibit that we have already discussed above. The panels shown here illustrate this discussions in a more quantitative manner.

In the left-hand panel of Fig. 5.6 we plot the neutral and ionised fraction averaged in spherical shells as a function of distance to the star, for all 5 simulations, to perform a comparison with the results obtained with other radiative transfer codes as reported in the cosmological radiative transfer code comparison project (Iliev et al. 2006b). The range of neutral and ionised fraction found in the code comparison project simulations are indicated by the grey bands. Except for the $N_\mathrm{c} = 32$ run, for which the neutral contours were most noisy (see Fig. 5.4), all our simulations agree very well with the results published in the comparison project. The deviations of the results obtained with TRAPHIC from the exact neutral fraction profile obtained with TT1D, that were also visible in the top row panels of Fig. 5.5, can be explained by the particle noise seen in Fig. 5.4. Due to the fuzzy structure exhibited by the neutral fraction contours, a range of neutral fractions can simultaneously be found within each spherical shell. The profiles obtained from the numerical simulation with TRAPHIC should therefore not be directly compared to the exact profile, i.e. the solution of Eq. 5.43, but to the profile that results after locally averaging the exact profile along the radial direction. The fact that the deviations from the exact result exhibited by the results published in the comparison project are relatively large illustrates the computational difficulties in obtaining accurate three-dimensional solutions of the radiative transfer equation even in a simple test problem like the one presented here.

To investigate the effect of particle noise on the neutral fraction profile we apply the resampling technique introduced in Sec. 4.4.5, Chapter 4. We perform a series of 5 simulations that are identical to the simulations presented above, except that every 10th radiative transfer time step the particle positions are randomly perturbed within their SPH spheres of influence. The densities are not recalculated after the positions have been changed due to the resampling, because this would generate fluctuations in the neutral hydrogen density which would increase the recombination rate due to an increased gas clumping factor and lead to a smaller Strömgren sphere. The resulting neutral fraction profiles are shown in the right-hand panel of Fig. 5.6. All profiles are now in close agreement with each other and with the exact result. The panels in the bottom row of Fig. 5.4 show the neutral fraction in a slice through the centre of the simulation box from the simulations with resampling. Clearly, resampling strongly suppresses the particle noise visible in the panels in the top row of Fig. 5.4, yielding nearly spherical neutral fraction contours. This effect of resampling is further confirmed by the panels in the bottom row of Fig. 5.5, which show the median neutral and ionised fractions in spherical bins as well as the neutral and ionised fraction of each particle in the simulations that employed the resampling recipe.

We now investigate the dependence of the equilibrium neutral and ionised fraction profile on the spatial resolution by varying N_{SPH}, the number of particles employed in the simulation. Because TRAPHIC is explicitly photon-conserving, we expect that the radiative transfer in a homogeneous medium is essentially independent of the spatial resolution (see e.g. the discussion in Mellema et al. 2006), except for a trivial smoothing. For each of the simulations with angular resolution $N_{\mathrm{c}} = 8, 32$ and 128 and $\tilde{N}_{\mathrm{ngb}} = 32$ presented above, we performed three additional simulations, at lower ($N_{\mathrm{SPH}} = 16^3, 32^3$) and higher ($N_{\mathrm{SPH}} = 128^3$) spatial resolutions, but otherwise identical to the fiducial ($N_{\mathrm{SPH}} = 64^3$) case. We will focus on the $N_{\mathrm{c}} = 8$ runs[13], but note that the $N_{\mathrm{c}} = 32$ and $N_{\mathrm{c}} = 128$ series show a similar behaviour.

The equilibrium neutral and ionised fraction profiles are shown in the left-hand panel of Fig. 5.7. For all spatial resolutions the ionisation front is at nearly the same radius. It can furthermore be seen that when the spatial resolution is increased, the equilibrium neutral fraction follows the exact result more closely. The simulation employing the fiducial spatial resolution ($N_{\mathrm{SPH}} = 64^3$) is almost converged. The differences in the neutral fraction profiles between the simulations using different numbers of particles are fully consistent with the corresponding spatial resolutions, as is demonstrated in the right-hand panel of Fig. 5.7. There, we smooth the neutral fraction profiles obtained in the simulations employing $N_{\mathrm{SPH}} = 32^3, 64^3$ and 128^3 particles over the spatial resolution element of the lowest resolution simulation ($N_{\mathrm{SPH}} = 16^3$), the size of which is indicated by the vertical line. The smoothed profiles match the neutral fraction profile obtained in the low spatial resolution simulation almost exactly. This shows that decreasing the spatial resolution does not introduce any artefacts. The solution obtained by TRAPHIC is the converged solution smoothed over the adopted spatial resolution.

Finally, we show how the size of the time step Δt_{r} affects the outcome of our simulations. We again concentrate on the simulation[14] with angular resolution $N_{\mathrm{c}} = 8$ (and $N_{\mathrm{SPH}} = 64^3$, $\tilde{N}_{\mathrm{ngb}} = 32$), noting that the simulations of higher angular resolution exhibit a similar behaviour. In Fig. 5.8 we show the evolution of the ionisation front for four different choices for the size

---

[13] These runs have been performed with the version of TRAPHIC described in Pawlik & Schaye (2008). We have not repeated them with the current code version, since this version only differs in the manner virtual particles are treated. For the low angular resolution employed here, however, no virtual particles are created.

[14] See footnote 13

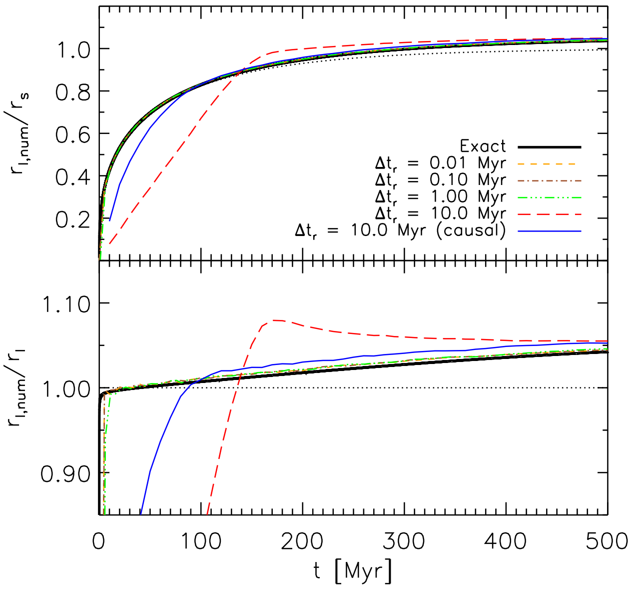

Figure 5.8: Test 1. Effect of the size of the time step. We show the evolution of the ionisation fronts for four simulations with $N_{\rm c} = 8$, $N_{\rm SPH} = 64^3$, $\tilde{N}_{\rm ngb} = 32$ and time steps $\Delta t_{\rm r} = 0.01, 0.1, 1$ and 10 Myr, resp, as indicated in the legend. After an initial phase, the evolution of the ionisation fronts becomes independent of the size of the radiative transfer time step. The duration of this initial phase can be shortened by applying the causal correction explained in the text, as we explicitly demonstrate for the simulation with time step $\Delta t_{\rm r} =$ 10 Myr.

of the radiative transfer time step, $\Delta t_{\rm r} = 0.01, 0.1, 1$ and 10 Myr. In order to keep the angular sampling the same, at each radiative transfer step we split the emission of photons over 10, 100 and 1000 random orientations of the emission cone tessellation of the ionising source for the simulations employing $\Delta t_{\rm r} = 0.1, 1$ and 10 Myr, resp. Differently from what is done for all other simulations described in this section, photon packets that are emitted by the source in a certain orientation are transmitted further downstream and can propagate over multiple inter-particle distances during a single time step. We follow each photon packet until it has either been absorbed or left the simulation box, to properly solve the time-independent radiative transfer equation for the large time steps under consideration.

From Fig. 5.8 we see that the evolution of the ionisation front for the simulations with time step $\Delta t_{\rm r} = 0.1, 1$ and 10 Myr is delayed with respect to the evolution of the ionisation front for the simulation with time step $\Delta t_{\rm r} = 0.01$ Myr. This delay increases with the size of the time step, being barely visible for the simulation using $\Delta t_{\rm r} = 0.1$ Myr. The delay arises because the neutral fraction is only updated at the end of each radiative transfer time step. Photons that have been absorbed during the transport over a single time step but that have not been used to advance the neutral fraction during the subsequent sub-cycling of the rate equation are therefore only re-inserted in the transport process at the beginning of the next time step and are thus delayed. From Fig. 5.8 it can, however, be seen that after a few time steps, the ionisation front catches up to agree with the ionisation front obtained in the simulation using $\Delta t_{\rm r} = 0.01$ Myr. We note that we have also tried to re-insert these photons immediately after they have been absorbed, by integrating the rate equation already at the end of each transport cycle (without updating the neutral fraction) to obtain the number of photons that have been erroneously counted as being absorbed (because of the assumption of a constant neutral fraction). We refer to this manner of transporting photons as causal, because of its similarity with the causal transport employed in Mellema et al. (2006). The causal correction, i.e. the re-insertion of these photons in the transport process within the same radiative transfer time step over which they have been absorbed, indeed reduces the observed delay of the ionisation front (see the blue

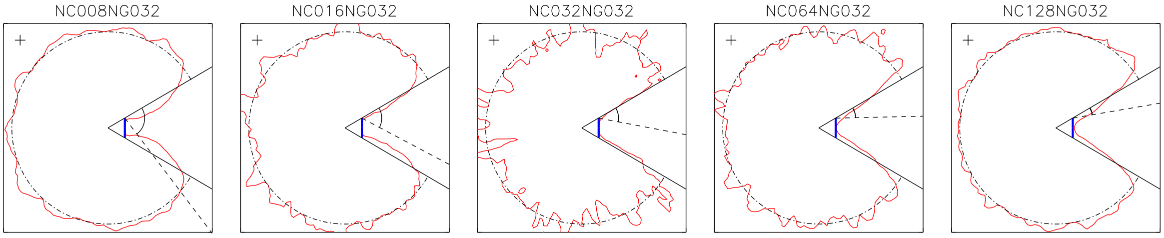

Figure 5.9: Test 2. Slice through the simulation box at $z = L_{\mathrm{box}}/2$ showing the ionisation front (red solid line) at time $t_{\mathrm{r}} = 80$ Myr around an ionising source sitting in the centre of the simulation box. The black dot-dashed circle shows the expected ionisation front position. The thick blue vertical line indicates an obstacle opaque to ionising photons and the black solid lines trace out the boundaries of the shadow this obstacle is expected to throw. The cross and the black dashed line indicate the spatial and angular resolution, respectively, as described in the text. The spatial resolution is fixed to $N_{\mathrm{SPH}} = 64^3$, $\tilde{N}_{\mathrm{ngb}} = 32$. The angular resolution increases from $N_{\mathrm{c}} = 8$ in the left-most panel to $N_{\mathrm{c}} = 128$ in the right-most panel, in factors of 2.

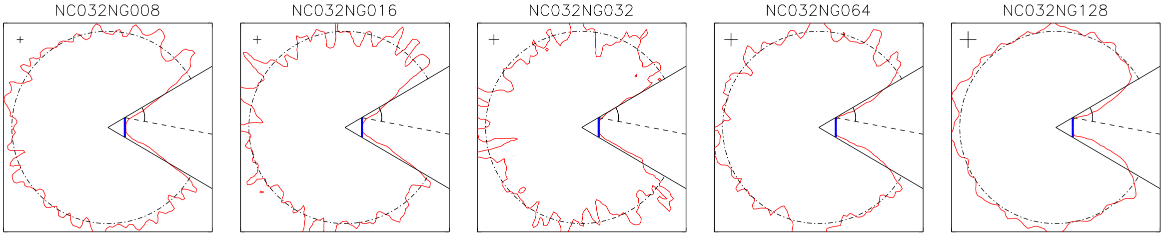

Figure 5.10: Test 2. Same as Fig. 5.9, but with the angular resolution fixed to $N_{\mathrm{c}} = 32$ and the spatial resolution decreasing, from $N_{\mathrm{SPH}} = 64^3$, $\tilde{N}_{\mathrm{ngb}} = 8$ in the left-most panel to $N_{\mathrm{SPH}} = 64^3$, $\tilde{N}_{\mathrm{ngb}} = 128$ in the right-most panel, increasing the number of neighbours $\tilde{N}_{\mathrm{ngb}}$ in factors of 2.

thin solid line in Fig. 5.8).

In summary, in this section we showed that TRAPHIC is able to reproduce the expected equilibrium neutral fraction around an ionising source embedded in a homogeneous medium, as well as the dynamical evolution towards it. Because the radiative transfer is explicitly photon-conserving, the spatial resolution only determines the scale over which the converged solution is smoothed. We have furthermore seen that the performance of TRAPHIC is stable with respect to variations in the size of the time step. Particle noise due to the discrete nature of SPH simulations is small except for the choice of parameters $N_{\mathrm{c}} \approx \tilde{N}_{\mathrm{ngb}}$. The noise can be successfully suppressed by applying a resampling technique that periodically perturbs the positions of the SPH particles within their spatial resolution element.

5.4.3 Test 2: Ionisation front shadowing by an opaque obstacle

In the absence of scattering interactions, photons propagate along straight lines into the direction set at the time of their emission. Consequently, opaque obstacles throw sharply defined shadows. In this section we are mainly interested in studying the properties of the shadow thrown by an opaque obstacle exposed to ionising radiation from a single point source, as obtained with TRAPHIC. At the same time, we will extend the study of particle noise presented in Sec. 5.4.2 to include other choices for the parameter $\tilde{N}_{\rm ngb}$. All of the simulations presented in this section have been performed with the original version of TRAPHIC presented in Pawlik & Schaye 2008. We have verified for a few individual simulations that our current, improved version, in which the distribution of photons absorbed by virtual particles amongst the neighbouring SPH particles is done using a more self-consistent weighting scheme than the one that was used in the original publication (see our discussion in Sec. 5.4), produces nearly identical results.

The geometry of our test problem closely follows the description of the shadow test in Mellema et al. (2006). We consider a source emitting $\dot{\mathcal{N}}_\gamma = 10^{54}$ photons $\rm s^{-1}$, each of hydrogen-ionising energy $h_{\rm p}\nu = 13.6$ eV, residing in an initially neutral, static hydrogen-only field of constant number density $n_{\rm H} = 1.87 \times 10^{-4}$ $\rm cm^{-3}$ and temperature $T = 10^4$ K. The Strömgren radius (Eq. 5.37) corresponding to this set of parameters is $r_{\rm s} = 0.965$ Mpc and the Strömgren time is $\tau_{\rm s} = 654.3$ Myr. For the numerical simulation a star particle is placed in the centre of a box of size $L_{\rm box} = 1$ Mpc. The boundaries of the box are photon-transmissive. The density field is sampled using $N_{\rm SPH} = 64^3$ gas particles with mass $m = n_{\rm H} m_{\rm H} L_{\rm box}^3 / N_{\rm SPH}$ at glass-like positions. The particle densities are found using the SPH interpolation implemented in GADGET-2, with $N_{\rm ngb} = 48$. We furthermore place an infinitely thin opaque disc perpendicular to the x-axis at a distance of 0.08 Mpc along the x-axis from the star (thick blue vertical lines in Figs. 5.9-5.13). The y and z coordinates of the disc centre are identical to those coordinates of the star. Photons that cross the disc are removed.

We performed a series of radiative transfer simulations (with time step $\Delta t_{\rm r} = 10^4$ yr), using different choices for the parameters $\tilde{N}_{\rm ngb}$, which sets the spatial resolution if the total number of SPH particles is fixed, and $N_{\rm c}$, which sets the angular resolution. The results are shown in Figs. 5.9 - 5.13, displaying a slice through the simulation box at $z = L_{\rm box}/2$. In each panel, the black dash-dotted circle shows the expected position of the ionisation front (Eq. 5.41) at time $t_{\rm r} = 80$ Myr, which marks the end of the simulation. The black solid lines emerging from the star at the centre of the slice show the boundaries of the shadow expected to be thrown by the opaque disc (thick blue vertical line). In the top-left corner of each panel we indicate the spatial resolution by a cross of length $2\langle\tilde{h}\rangle$ corresponding to the average diameter of the sphere containing $\tilde{N}_{\rm ngb}$ neighbours. The angular resolution is indicated by the angle ω enclosed by the black dashed line and the upper shadow boundary, where ω is determined using Eq. 4.9. It indicates the *maximum* angle photons can theoretically diverge from the shadow boundary into the shadow region, given the chosen angular resolution $N_{\rm c}$.

The position of the ionisation front (the iso-surface for which the neutral fraction $\eta = 0.5$) at time $t_{\rm r} = 80$ Myr as obtained with TRAPHIC is shown by the red solid line. In all panels, that is for all spatial and angular resolutions, the ionisation front is found at the proper position, in agreement with our findings of Sec. 5.4.2. The shadow thrown by the opaque disc is always sharp. We now discuss the dependence of the results on the chosen spatial and angular resolutions.

In Fig. 5.9 we show the ionisation front obtained in simulations employing a fixed spatial resolution, $\tilde{N}_{\rm ngb} = 32$, but varying angular resolution, ranging from $N_{\rm c} = 8$ in the left-most to $N_{\rm c} = 128$ in the right-most panel. The most prominent difference between the results of the different simulations is the noisiness of the contour tracing out the ionisation front. The angular resolution study presented here is very similar to the one in the last section. For the lowest

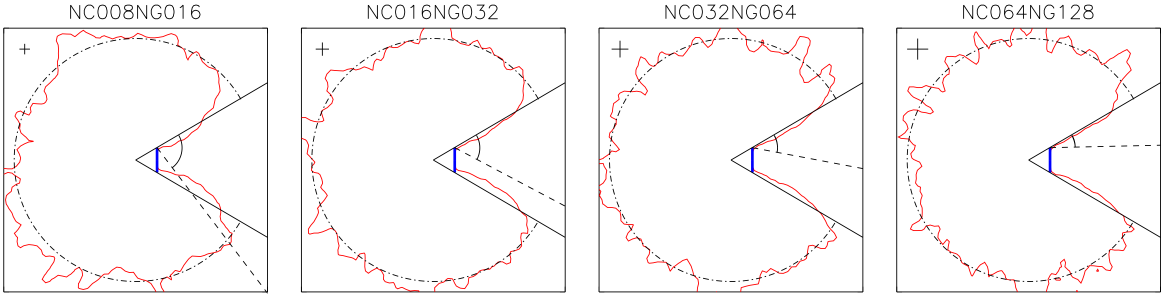

Figure 5.11: Test 2. Same as Fig. 5.9, but fixing the ratio between spatial and angular resolution to $\tilde{N}_{\rm ngb}/N_{\rm c} = 2$ ($N_{\rm SPH} = 64^3$).

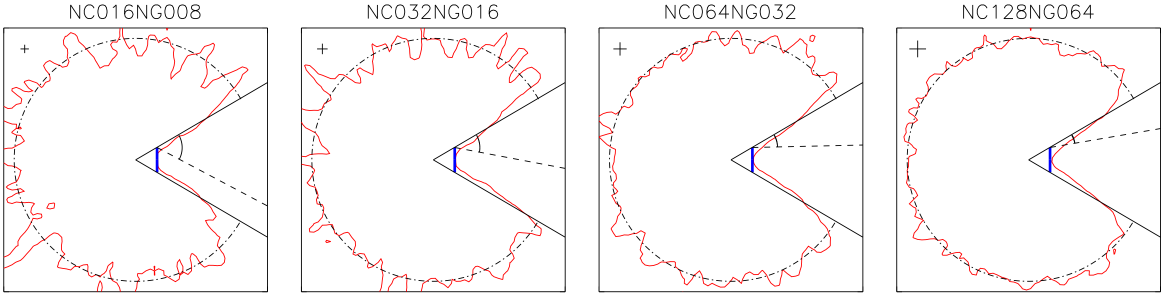

Figure 5.12: Test 2. Same as Fig. 5.9, but fixing the ratio between spatial and angular resolution to $\tilde{N}_{\rm ngb}/N_{\rm c} = 1/2$ ($N_{\rm SPH} = 64^3$).

angular resolution, $N_{\rm c} = 8$, the ionisation front is very smooth due to the large number of neighbours within each emission and transmission cone. The noise increases with the angular resolution until it reaches a maximum for $N_{\rm c} = \tilde{N}_{\rm ngb}$. For higher angular resolutions, particle noise is efficiently suppressed due to the large number of ViPs that are placed in empty cones and that distribute the photons they absorb amongst their $\tilde{N}_{\rm ngb}$ SPH neighbours using (photon-conserving) SPH interpolation.

From Fig. 5.9 it can furthermore be seen how the sharpness of the shadow thrown by the opaque disc depends on the angular resolution. For the lowest angular resolution, the shadow is somewhat blurred, though not nearly as much as the angular resolution would imply. Increasing the angular resolution yields slightly sharper shadows. However, if the angular resolution is increased beyond $N_{\rm c} = \tilde{N}_{\rm ngb}$, the shadows become slightly less sharp. This is because the photons absorbed by ViPs are distributed amongst the neighbouring gas particles using SPH interpolation and the interpolation procedure does not know about the shadow region. The slight diffusion of photons across the shadow boundary is in this case consistent with the spatial resolution.

In Fig. 5.10 we show the results of the simulations where we fixed the angular resolution to $N_{\rm c} = 32$, but varied the spatial resolution by changing $\tilde{N}_{\rm ngb}$. The trends visible in Fig. 5.9

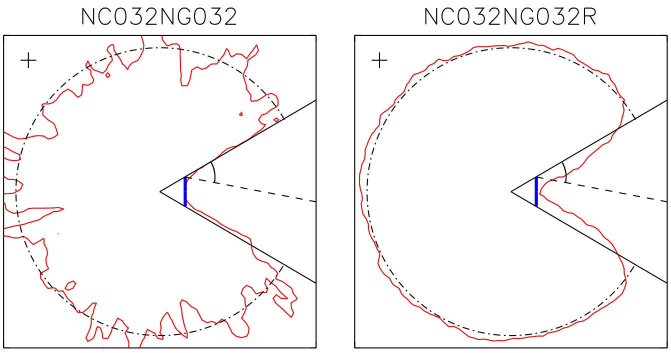

Figure 5.13: Test 2. *Left-hand panel:* Identical to the middle panels of Figs. 5.9 and 5.10. *Right-hand panel:* Same as left-hand panel, except for the fact that in the simulation we periodically re-sampled the density field, resulting in a strong suppression of the particle noise seen in the left-hand panel. Note the (small amount of) diffusion of photons across the shadow boundary due to the motion of the transmission cone apexes.

can also be observed here. The ionisation front is most noisy and the shadow is sharpest for $N_c = \tilde{N}_{ngb}$. For $\tilde{N}_{ngb} > N_c$, noise due to the discreteness of the particles employed for the transport of photons is suppressed by the large number of neighbours per cone, but the shadow is slightly blurred. The shadow becomes sharper for a smaller number of neighbours, since generally not all of the solid angle will be covered by the neighbours, an effect that becomes more important for smaller numbers of neighbours. For $\tilde{N}_{ngb} < N_c$ the ionisation front becomes smoother due to the regularising effect of the SPH interpolation from ViPs, which also leads to a small diffusion of photons across the shadow boundary, consistent with the spatial resolution.

In Figs. 5.11 and 5.12 we keep the ratio $\tilde{N}_{ngb}/N_c$ fixed at $\tilde{N}_{ngb}/N_c = 2$ and $\tilde{N}_{ngb}/N_c = 1/2$, resp. In the first case there are on average 2 neighbours per cone, whereas in the second case there is on average one neighbour in every second cone. From Fig. 5.11 it is clear that the shadow does get sharper when the angular resolution is increased, although the effect is small, since the shadow is always very sharp. Because we keep the ratio $\tilde{N}_{ngb}/N_c$ fixed at 2, the number of ViPs employed in the simulation stays low for all angular resolutions and the shadows are not visibly diffused by the SPH interpolation of absorbed photons from the ViPs. Furthermore, the noisiness of the ionisation front remains constant throughout the parameter range. This is because the noise is primarily set by the ratio $\tilde{N}_{ngb}/N_c$ if $\tilde{N}_{ngb} > N_c$. In Fig. 5.12, on the other hand, there is a substantial probability for creating a ViP per cone. Since the absolute number of ViPs present in the simulation increases with increasing angular resolution N_c, the noise decreases with N_c.

In the last section (see bottom row of Fig. 5.4) we employed a resampling technique to decrease the noise exhibited by the neutral fraction contours. Recall from Section 4.4.2 that the apexes of the transmission cones are attached to the positions of the SPH particles. Hence, resampling results in slight shifts in the position of each transmission cone apex, on the scale of the spatial resolution employed in the SPH simulation. This shifting is expected to lead to a small diffusion of photons across the expected shadow boundary. Such a diffusion due to particle resp. apex motion will also occur in radiation-hydrodynamical simulations because of the movement of the SPH particles. It is therefore interesting to study the properties of the shadow thrown by an opaque obstacle in the case of resampling.

In Fig. 5.13 we show the results of a simulation which employs the same parameters as used for the simulation presented in the middle panels of Fig. 5.9 and 5.10, but with an additional resampling of the hydrogen density field every 10th radiative transfer time step. As in the last section, the resampling is performed without changing the hydrogen density, since this would lead to an enhanced recombination rate. Numerical noise is successfully suppressed by the random perturbations given to the positions of the SPH particles. Consequently, the ionisation front appears significantly smoother. The degree of photon diffusion into the shadow region is small and does not significantly degrade the angular resolution of the radiative transfer. This is because the diffusion scale is set by the spatial resolution employed in the SPH simulation. Therefore, well-defined shadows will be thrown as long as the obstacle is spatially resolved. The effect of resampling on the properties of shadows will be further discussed in Sec. 5.4.5.

In summary, in this section we showed that TRAPHIC is able to produce a well-defined shadow behind an opaque obstacle, with the shadow sharpness in full agreement with the chosen spatial and angular resolutions. In fact, the shadows are much sharper than implied by the formal angular resolution, thanks to the angular adaptivity inherent to TRAPHIC. For a fixed angular resolution, the shadows are sharpest for $N_{\rm c} = \tilde{N}_{\rm ngb}$. They are slightly broadened by photon diffusion for both $N_{\rm c} < \tilde{N}_{\rm ngb}$ and $N_{\rm c} > \tilde{N}_{\rm ngb}$, due to the increased coverage of the solid angles traced out by the transmission cones with SPH particles for an increasing number of neighbours $\tilde{N}_{\rm ngb}$ and the SPH interpolation of the photons absorbed by ViPs, resp. We confirmed our finding of the last section that unless $\tilde{N}_{\rm ngb} = N_{\rm c}$, noise due to the discreteness of the particles on which the transport of photons takes place is small, since it is suppressed by either the large number of neighbours per cone (if $N_{\rm c} < \tilde{N}_{\rm ngb}$) or the large number of ViPs employed (if $N_{\rm c} > \tilde{N}_{\rm ngb}$). The resampling technique that we have already used in Sec. 5.4.2 is confirmed to be very effective at suppressing particle noise. We have seen that resampling the density field does not severely degrade the angular resolution, even though it leads to a small shift of the cone apexes. As long as the opaque obstacle is spatially resolved by the SPH simulation, a well-defined shadow will still be thrown.

The ability to produce sharp shadows is one of the main requirements a radiative transfer code has to pass. The results of this section, together with the results of Test 1, which showed that TRAPHIC is able to reproduce the expected neutral fraction within a spherically symmetric HII region, indicate that TRAPHIC can be used to perform the transport of ionising photons in arbitrarily complex geometries. This will be the subject of Test 4 presented below. Before that, however, we will discuss the performance of TRAPHIC in the important problem of the spherically symmetric expansion of an HII-region in a centrally peaked density field.

5.4.4 Test 3: HII region expansion in a centrally peaked density field

The spherically averaged gas density profile in the dense central regions of star-forming galaxies can often be described by a simple power-law relation between gas density and distance from the galaxy centre. For example, the central parts of galaxies embedded in a Navarro, Frenk, & White (1997) dark matter halo will obey a spherically averaged gas density profile that is inversely proportional to the distance from the halo centre (assuming that the gas distribution follows that of the dark matter). Dark matter simulations (e.g., Springel et al. 2008) and first-principle considerations (He 2009) suggest that the Navarro, Frenk, & White (1997) profile provides a universal description of the distribution of matter in galaxy halos. It is thus important to verify that our radiative transfer scheme is able to accurately compute the propagation of ionisation fronts in such a centrally peaked density field. In this section we therefore study the propagation of an ionisation front in the singular density profile

$$n_{\rm H}(r) = n_0 \frac{r_0}{r}, \tag{5.45}$$

where n_0 is the density at radius $r = r_0$.

An analytic solution to the ionisation front evolution in such a density profile was derived by Mellema et al. (2006), as follows. Assuming a fully ionised sphere, the position of the ionisation front driven by a source with constant ionising luminosity $\dot{\mathcal{N}}_\gamma$ is given by Eq. (5.38). Making use of the density profile Eq. 5.45, this equation reads

$$\frac{dr_{\rm I}}{dt} = \frac{\dot{\mathcal{N}}_\gamma}{4\pi n_0 r_0} r_{\rm I}^{-1} - n_0 r_0 \alpha_{\rm B}(T). \tag{5.46}$$

Substituting $u \equiv r_{\rm I}^{-1}$, the last equation transforms into

$$\frac{du}{dt} = u^2 \left(-\frac{\dot{\mathcal{N}}_\gamma}{4\pi n_0 r_0} u + n_0 r_0 \alpha_{\rm B}(T) \right). \tag{5.47}$$

Introducing the notation

$$\tilde{u} \equiv \frac{\dot{\mathcal{N}}_\gamma}{4\pi n_0^2 r_0^2 \alpha_{\rm B}} u \tag{5.48}$$

$$\tilde{t} \equiv \frac{4\pi n_0^3 r_0^3 \alpha_{\rm B}^2}{\dot{\mathcal{N}}_\gamma} t, \tag{5.49}$$

the ionisation front evolution is described by

$$\frac{d\tilde{u}}{d\tilde{t}} = \tilde{u}^2 (1 - \tilde{u}). \tag{5.50}$$

The solution to Eq. (5.50) can be expressed in terms of Lambert's W function (e.g., Corless et al. 1996),

$$\tilde{u}(\tilde{t}) = \frac{1}{1 + W\left(z e^{z - \tilde{t}}\right)} \tag{5.51}$$

$$z = \frac{1}{\tilde{u}(0)} - 1. \tag{5.52}$$

Imposing the initial condition $r_{\rm I}(0) = 0$ and transforming back to the original variables,

$$r_{\rm I}(t) = r_{\rm s} \left\{ 1 + W \left[-\exp\left(-\frac{r_0}{r_{\rm s} \tau_{\rm s}} t - 1 \right) \right] \right\} \tag{5.53}$$

$$\tag{5.54}$$

Hereby, $r_{\rm s} = \dot{\mathcal{N}}_\gamma / (4\pi n_0^2 r_0^2 \alpha_{\rm B})$ is the (generalised) Strömgren radius and $\tau_{\rm s} = (n_0 \alpha_{\rm B})^{-1}$ is the (generalised) Strömgren time, i.e. the characteristic time on which equilibrium is approached.

We will employ Eq. 5.54 as a reference solution and refer to it as an analytic approximation. In Sec. 5.4.2 we have, however, seen that the assumption of a fully ionised sphere may not yield a sufficiently accurate expression for the evolution of the ionisation front. As in Sec. 5.4.2, we will therefore additionally compare the results of our simulations obtained with TRAPHIC to the solution derived numerically using our spherically symmetric radiative transfer code TT1D, to which we refer as the exact solution.

We set up the density profile Eq. 5.45 around an ionising source located at the centre of a simulation box with side length 7.5 kpc. We use the parameters $n_0 = 0.015$ cm^{-3}, $r_0 = 5$ kpc which are identical to those used in the corresponding test problem by Mellema et al.

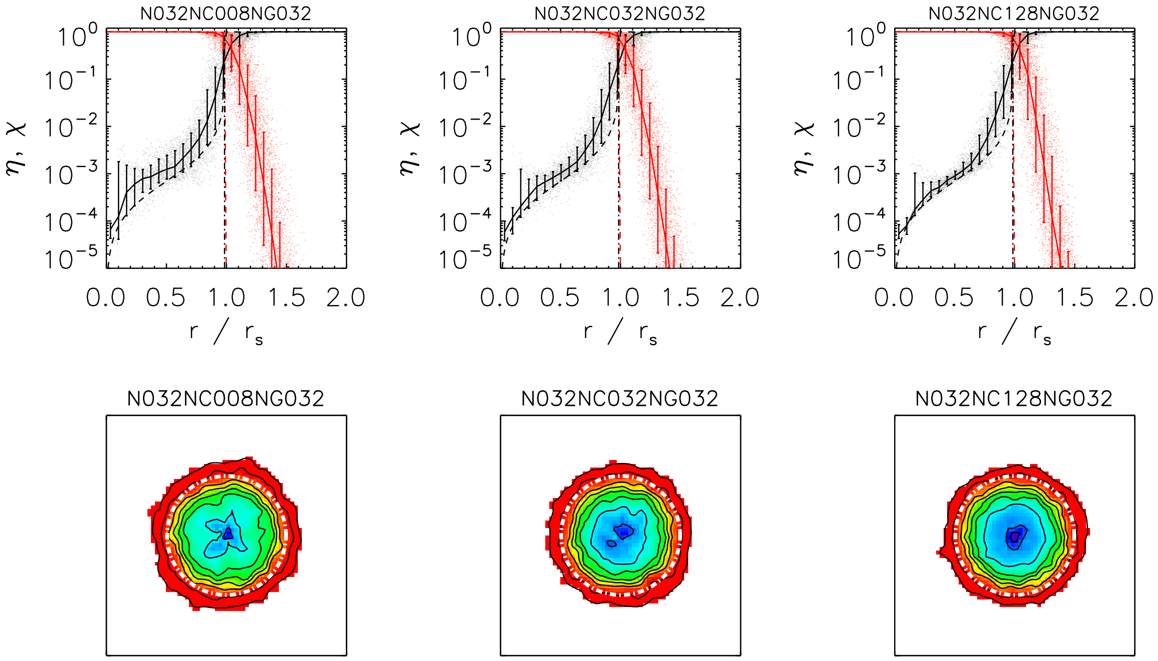

Figure 5.14: Test 3. *Top row:* Profiles of the neutral and ionised fraction at $t = 10$ Myr. The angular resolution increases from $N_c = 8$ in the left-most panel and $N_c = 32$ in the middle panel to $N_c = 128$ in the right-most panel. The grey (light red) points show the neutral (ionised) fraction of each particle. The solid black (red) curve shows the median neutral (ionised) fraction in spherical bins, the error bars the corresponding 68.3% confidence intervals. The dashed black (red) curves show the exact solution and the vertical dot-dashed black line indicates the ionisation front position from Eq. 5.54. The dashed red curve and the black dot-dashed curve are nearly on top of each other. *Bottom row:* neutral fraction in a slice through the simulation box at $z = L_{\rm box}/2$, corresponding to the panels shown in the top row. Black contours show neutral fractions of $\eta = 0.9, 0.5, \log\eta = -1, -1.5, -2, -2.5, -3, -3.5, -4$, going from the outside in. The white dot-dashed circle indicates the ionisation front position from Eq. 5.54. The colour scale is logarithmic and has a lower cut-off of $\log\eta = -5$ (see Fig. 7.14 in Chapter 7 for a colour bar). See text for discussion.

(2006). The central source has a luminosity of $L_\gamma = 10^{51}$ s^{-1} hydrogen-ionising photons. Our parameter choices imply a Strömgren radius $r_{\rm s} \sim 1.86$ kpc and a Strömgren time $\tau_{\rm s} \sim 8.16$ Myr.

The density profile is obtained by applying a coordinate transformation to particles that are initially uniformly distributed (at glass-like positions), which is described in App. 5.D. In short, particles are moved radially away from their original (glass-like) positions to stretch the local mean particle distance such that the SPH volume the particles occupy becomes proportional to their distance from the source. After the particles have been placed, their densities are calculated using the SPH formalism of GADGET-2, with $N_{\rm ngb} = 48$. All simulations presented in this section are initialised with 32^3 particles at glass-like positions, which results in ≈ 10000 (≈ 2000) SPH particles within the central sphere of radius 3 kpc (2 kpc). We employ this relatively small number of particles (and hence a correspondingly low spatial resolution) in order to more closely resemble simulated halos in cosmological simulations. We note that (for the angular resolution $N_c = 8$) we have performed simulations of both lower and higher spatial resolution to convince ourself that these simulations show the expected behaviour.

The boundaries of the simulation box are assumed to be transmissive, i.e. photons leaving the box are lost from the computational domain. We use $\tilde{N}_{\rm ngb} = 32$ radiative transfer neighbours. In Secs. 5.4.2 and 5.4.3 we have seen that the resampling procedure introduced in Chapter 4 strongly reduces artefacts caused by the particular realization of particle positions. In all the simulations presented here we therefore resample the density field every 10th time step. The radiative transfer time step is set to $\Delta t_{\rm r} = 10^{-3}$ Myr. We furthermore split, during each radiative transfer time step, the emission of photons by the source over 32 random orientations of its emission cone tessellation. We found that this increase in angular sampling is required in order to to obtain sufficiently accurate results (see also the discussion on the related effect of angular resolution below). We have made no attempt to optimise this number.

In Fig. 5.14 we show profiles of the neutral fraction η and ionised fraction χ and images of the neutral fraction η in a slice through the box centre at $t = 10$ Myr for three simulations that have increasing angular resolutions: $N_{\rm c} = 8$ (left-most panel), $N_{\rm c} = 32$ (middle panel) and $N_{\rm c} = 128$ (right-most panel). For all three simulations the median neutral (ionised) fraction, as indicated by the solid black (red) curve with error bars (which are the 68.3% confidence intervals) in the top panels of Fig. 5.14, closely agrees with the exact solution. Inside the ionised region, away from the ionisation front, the agreement is best for the simulation with the highest angular resolution. This is because a higher angular resolution implies a larger number of cones into which the source simultaneously emits photon packets, which implies an increased angular sampling.

At low angular resolutions, fewer SPH particles receive radiation during a time step. These particles then only recombine. As a result, their neutral fraction temporarily drifts away from its expected value, introducing scatter. Such a behaviour is commonly encountered in Monte Carlo radiative transfer schemes (for discussions see, e.g., Maselli, Ciardi, & Kanekar 2009; Altay, Croft, & Pelupessy 2008). It illustrates the Monte Carlo aspect of TRAPHIC. For the angular resolution $N_{\rm c} = 128$, the median neutral fraction inside the ionisation front is nearly indistinguishable from the exact solution[15]. The remaining difference with respect to the exact solution as well as the small deviation of the median from the exact solution close to the ionisation front is due to the employed low spatial resolution, which implies an effective smoothing of the exact solution (which corresponds to infinitely high spatial resolution), as we already discussed in Sec. 5.4.2.

In conclusion, we have shown that TRAPHIC is able to accurately reproduce the expected growth of ionised regions in centrally peaked density fields. This is important since such density fields are typical for the first sites of star formation in the cosmological simulations we wish to employ TRAPHIC. The results also illustrated the Monte-Carlo aspect of TRAPHIC: although the spherically symmetric problem is formally independent of angular resolution, we found that the agreement with the exact solution increases with angular resolution. This is because of the increased number of cones into which photon packets are simultaneously emitted, which increases the angular sampling of the computational domain. The same result can, however, be obtained by distributing the photons to be emitted during a given time step over an increased number of random orientations of the emission cone tessellation (or, alternatively, by decreasing the time step).

---

[15] Note, however, that there are still a few particles (around $r \approx 0.2 r_{\rm s}$) that due to a lack of angular sampling are not sufficiently frequently updated with ionising radiation and therefore have a neutral fraction that is too high.

5.4.5 Test 4: Expansion of multiple HII regions in a cosmological density field

Until now we have considered highly idealised test problems. We studied the performance of TRAPHIC in simulations of the growth of spherically symmetric ionised regions in a uniform medium and a centrally peaked density profile, and we analysed its capability to produce shadows behind opaque obstacles. In this section we will consider a more complex test that combines all the difficulties posed by the problems discussed so far: we test the propagation of ionisation fronts around multiple sources in a static cosmological density field. The test is designed to resemble important aspects of state-of-the-art simulations of the epoch of reionisation. Its parameters are taken from Test 4 of the Cosmological Radiative Transfer Code Comparison Project (Iliev et al. 2006b). The simulations presented there were limited to solving the time-independent radiative transfer equation. To allow an accurate comparison, we will therefore focus on solving the time-independent radiative transfer equation, but we will briefly discuss the differences to a corresponding time-dependent simulation.

The initial conditions are provided by a snapshot (at redshift $z \approx 8.85$) from a cosmological N-body and gas-dynamical simulation performed using the cosmological (uniform-mesh) PM+TVD code of Ryu et al. (1993). The simulation box is $L_{\rm box} = 0.5\ h^{-1}$ comoving Mpc on a side, uniformly divided into $N_{\rm cell} = 128^3$ cells. The initial temperature is fixed at $T = 100$ K everywhere. The halos in the simulation box were found using a friends-of-friends halo finder with a linking length of 0.25. The ionising sources are chosen to correspond to the 16 most massive halos in the box. We assume that these have a black-body spectrum $B_\nu(\nu, T)$ with temperature $T = 10^5$ K. The ionising photon production rate is assumed to be constant and assigned assuming that each source lives for $t_{\rm s} = 3$ Myr and emits $f_\gamma = 250$ photons per atom during its lifetime. Hence, the number of ionising photons emitted per unit time is

$$\dot{\mathcal{N}}_\gamma = f_\gamma \frac{M\Omega_{\rm b}}{\Omega_0 m_{\rm H} t_{\rm s}}, \tag{5.55}$$

where M is the total halo mass, $\Omega_0 = 0.27$, $\Omega_b = 0.043$ and $h = 0.7$. For simplicity, all sources are assumed to switch on at the same time. The boundary conditions are photon-transmissive. Outputs are produced at $t = 0.05, 0.1, 0.2, 0.3$ and 0.4 Myr.

With respect to the original test setup described above, we require three changes. First, since our code does not yet solve for the temperature of the gas, we assume a constant temperature of $T = 10^4$ K for the ionised gas. Second, since our code currently treats only a single frequency (bin), we treat the multi-frequency problem in the grey approximation, assuming the grey photo-ionisation cross-section Eq. 5.27. The third change concerns the input density field. Since our code works directly on the set of particles used in SPH simulations, we have to Monte Carlo sample the original input density field in order to place particles in the box. We replace every grid cell i by $N_{\rm SPH}^i = M_i/m$ SPH particles (randomly distributed within the volume of the grid cell), where $M_i = \rho_i L_{\rm box}^3/N_{\rm cell}$ is the mass of the cell and m is the mass of an SPH particle. If $N_{\rm SPH}^i$ is not an integer, we draw a random number from a uniform distribution on the interval (0,1) and place an additional particle if this number is smaller than the difference between $N_{\rm SPH}^i$ and the nearest lower integer. We use $N_{\rm SPH} = N_{\rm cell} = 128^3$. Since the Monte Carlo sampling only results in the approximate equality $\sum_i N_{\rm SPH}^i \approx N_{\rm SPH}$, we adjust the particle masses a posteriori to conserve mass, i.e. $m \rightarrow m \times N_{\rm SPH}/\sum_i N_{\rm SPH}^i$. After the particles have been placed, we calculate their densities using the SPH formalism of GADGET-2, with $N_{\rm ngb} = 48$.

Note that Monte Carlo sampling the density field with $N_{\rm SPH} \simeq N_{\rm cell}$ particles yields a smaller effective resolution than that of the grid input field in low density regions (many grid

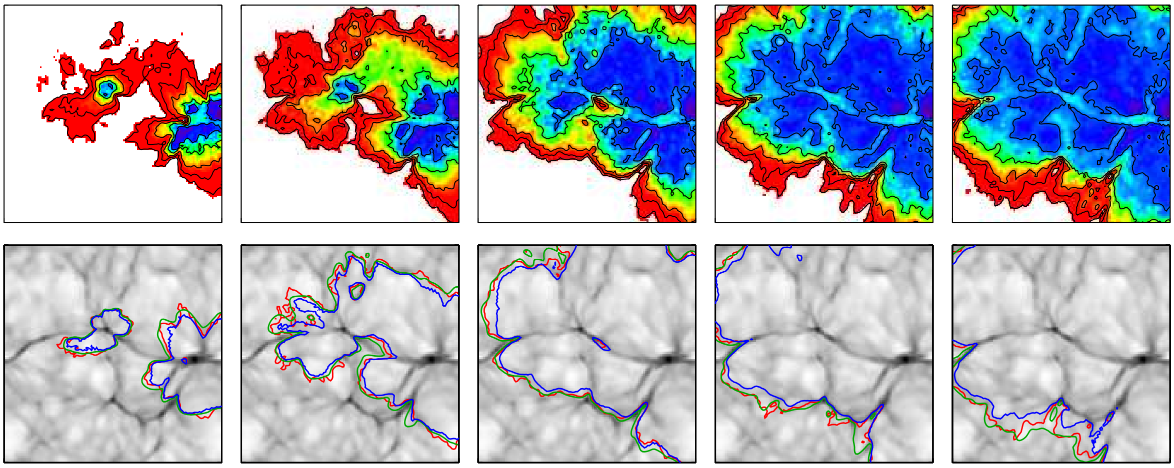

Figure 5.15: Test 4: *Top row:* neutral fraction in a slice through $z = L_{\rm box}/2$ at times $t = 0.05, 0.1, 0.2, 0.3, 0.4$ Myr (from left to right). Contours show neutral fractions $\eta = 0.9, 0.5, \log \eta = -1, -3$ and -5, from the outside in. The colour scale is logarithmic and has a lower cut-off of $\eta = 10^{-7}$. It is identical to the colour scale used and shown in Fig. 7.19 of the corresponding test 7 in Chapter 7. *Bottom row:* Density field in the slices shown in the top panels. Contours show ionisation fronts (neutral fraction of $\eta = 0.5$). Red contours show the results of our fiducial ($N_{\rm c} = 32, \tilde{N}_{\rm ngb} = 32$) simulation. For comparison, we show the results of C^2-RAY (green) and CRASH (blue), as reported in Iliev et al. (2006b). The agreement is excellent. *See Fig. 3 in the appendix at the end of this thesis for a coloured version.*

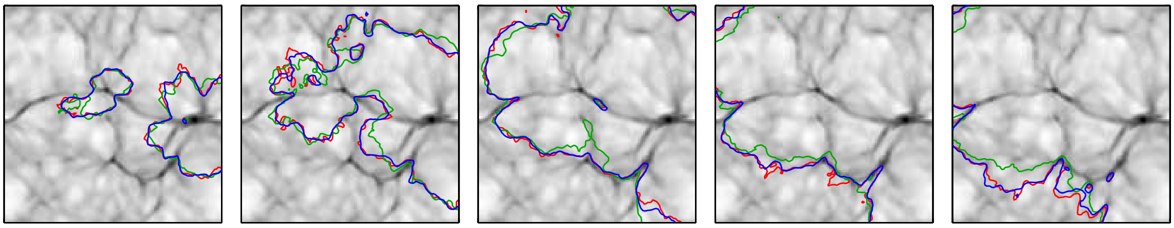

Figure 5.16: Test 4: Effect of angular resolution. The same slice as shown in Fig. 5.15, bottom row. Contours show ionisation fronts (neutral fraction $\eta = 0.5$) at times $t = 0.05, 0.1, 0.2, 0.3$ and 0.4 Myr (from left to right). Green, red and blue lines correspond to the low ($N_{\rm c} = 8$), fiducial ($N_{\rm c} = 32$) and high ($N_{\rm c} = 128$) angular resolution simulations, respectively. The fiducial simulation is already converged, even though its angular resolution $N_{\rm c} = 32$ corresponds to a relatively large cone opening angle of $\omega \approx 41$ degrees.

cells will be left empty of particles), and to a spurious higher resolution in high density regions (cells are sampled with many particles, even though there is no substructure on the scale of a single cell in the input field). Note also that because the initial conditions were specified on a uniform grid, we do not benefit from the intrinsic spatial adaptivity of TRAPHIC, effectively wasting computational resources.

We performed a set of three radiative transfer simulations with angular resolutions $N_{\rm c} = 8, 32$ and 128, which we refer to as the low angular resolution, fiducial and high angular resolution simulations, resp. Every simulation used $\tilde{N}_{\rm ngb} = 32$ neighbours. The time step was set to $\Delta t_{\rm r} = 10^{-4}$ Myr.

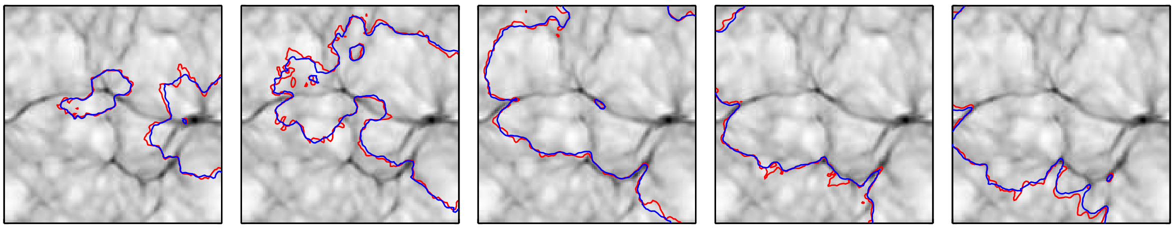

Figure 5.17: Test 4: Effect of resampling. The same slice as shown in Fig. 5.15, bottom row. Contours show ionisation fronts (neutral fraction $\eta = 0.5$) at times $t = 0.05, 0.1, 0.2, 0.3$ and 0.4 Myr (from left to right). The red contours correspond to the fiducial angular resolution simulation. The blue contours correspond to a simulation identical to the simulation employing the fiducial angular resolution, except for the fact that in this simulation we periodically (every 10th radiative transfer time step) re-sampled the density field to suppress the particle noise. Note that resampling does not visibly decrease the effective angular resolution.

In Fig. 5.15 we show the result of our fiducial simulation at times $t = 0.05, 0.1, 0.2, 0.3$ and 0.4 Myr (from left to right). The panels in the top row show images of the neutral fraction in a slice through the centre of the simulation box. Contours of neutral fraction $\eta = 0.9, 0.5$, $\log_{10} \eta = -1, -3$ and -5 have be superimposed. The panels in the bottom row repeat the $\eta = 0.5$ contour, i.e. the ionisation front, showing it on top of the input density field. It can be clearly seen that the ionisation front is delayed by the dense filaments, leading to the characteristic "butterfly" shapes of the ionised regions.

For comparison, we also show the results obtained with two other codes, the ray-tracing scheme C^2-RAY (Mellema et al. 2006; green contours) and the Monte Carlo code CRASH (Maselli, Ferrara, & Ciardi 2003; Ciardi et al. 2001; blue contours), as published in the cosmological radiative transfer code comparison project (Iliev et al. 2006b)[16]. Both C^2-RAY and CRASH are mesh codes, working directly on the uniform mesh input density field provided by the PM+TVD code of Ryu et al. (1993).

The agreement between the results of TRAPHIC and C^2-RAY resp. CRASH is very good. We have explicitly verified that this good agreement is also true for contours of lower neutral fraction (see Pawlik & Schaye 2008 and the result of Test 7 in Chapter 7). The contours from TRAPHIC are slightly noisier than those from C^2-RAY, which is expected since in addition to the particle noise affecting the radiative transfer, the Monte-Carlo sampling noise imprinted on the density field affects our simulations, particularly in the under-sampled low density regions, as already noted earlier. The noise level is, however, substantially lower than one would anticipate based on the tests presented in Secs. 5.4.2 and 5.4.3. The most likely explanation for this welcome surprise is that the presence of multiple ionising sources leads to a regularisation in the distribution of the neutral fraction (a fact that has been noted also by other authors, e.g. Trac & Cen 2007). Numerical noise arising from the representation of the continuous density field by a discrete set of particles is therefore reduced.

Differences between our results and those of C^2-RAY resp. CRASH also arise through the different treatment of the photon spectrum. Since the photo-ionisation cross-section depends

---

[16] The performance of two more codes was reported in Iliev et al. (2006b): FTTE (Razoumov & Cardall 2005) and SIMPLEX (Ritzerveld & Icke 2006). For clarity and since they are very similar to the results obtained with C^2-RAY and CRASH, we do not show the results obtained with FTTE (but see Test 7 in Chapter 7). We do not include the results of SIMPLEX in our comparison, since they differ considerably from those obtained with all other codes.

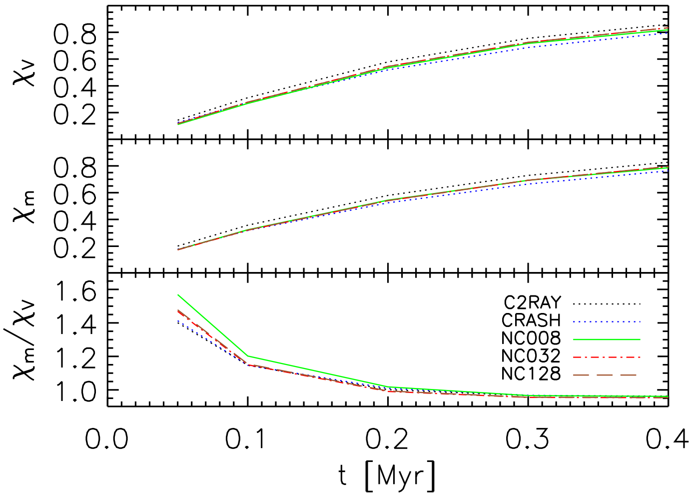

Figure 5.18: Test 4: The volume- and mass-weighted mean ionised fractions, χ_V and χ_m, resp., averaged over the whole simulation box as a function of time, for the low, fiducial and high angular resolution simulation, as indicated in the legend. All results fall nearly on top of each other. Differences in χ_m/χ_V are only noticeable when χ_V is small. For comparison, we also show the results obtained with C^2-RAY and CRASH as reported in Iliev et al. (2006b).

on frequency (Eq. 5.2), the thickness of finite ionisation fronts (e.g. defined as $0.9 < \eta < 0.1$) and hence the position of the particular contour $\eta = 0.5$ will in part be determined by the details of the numerical implementation of the multi-frequency transport. Finally, while both C^2-RAY and CRASH follow the thermal evolution of the gas, our simulations assume a fixed gas temperature, which provides another source for the observed differences.

In Fig. 5.16 we show the ionisation fronts at times $t = 0.05, 0.1, 0.2, 0.3$ and 0.4 Myr (from left to right) for the low (green contours) and the high (blue contours) angular resolution simulations. For comparison, the contours obtained in the fiducial simulation are also shown (red). We note that the high angular resolution simulation yields neutral fraction contours that are almost identical to those obtained in our fiducial simulation, indicating numerical convergence. The low angular resolution simulation, although still in good agreement with the high angular resolution simulation, fails to properly reproduce the expected neutral fraction contours when scrutinised in detail. In the low angular resolution simulation we noticed that neutral fraction contours are sometimes slightly advanced instead of delayed by the dense filaments. The effect is small, but it becomes apparent when the contours are compared to the corresponding contours of the high angular resolution simulation (although it is barely visible in the images presented here).

Our observation agrees with the discussion of anisotropies in particle-to-neighbour transport schemes presented in Chapter 4 (see in particular its App. 4.A). There we demonstrated that when photons are transported from a given particle to its neighbours, the net transport direction is generally strongly correlated with the direction towards the centre of mass of the neighbouring particles. As a result, the transport is partly governed by the spatial distribution of the SPH particles. For cosmological simulations this implies that photons are preferentially transported along dense filaments. TRAPHIC propagates photons in cones to overcome this problem. The cones confine the photons to the solid angles they were emitted into, ensuring a correct transport of radiation on the scale of the chosen angular resolution. If the angular resolution is chosen too low to properly resolve the structures in the SPH density field, the transport is no longer independent of the geometry of the SPH simulation and artefacts may occur. In the present case, even with an angular resolution as low as $N_c = 8$, the artefacts are small. Nevertheless, it is clear that in order to properly solve the radiative transfer equation, the angular resolution must be chosen high enough to establish numerical convergence.

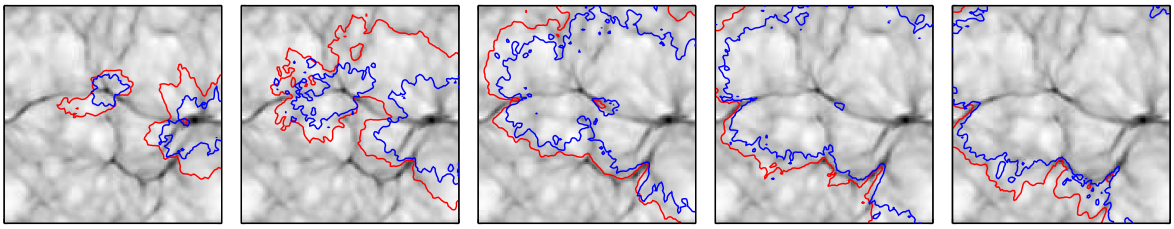

Figure 5.19: Test 4: Slice through the density field at $z = L_{\rm box}/2$. Contours show a neutral fraction of $\eta = 0.5$ at times $t = 0.05, 0.1, 0.2, 0.3$ and 0.4 Myr (from left to right). Red contours show the results of our fiducial ($N_{\rm c} = 32, \tilde{N}_{\rm ngb} = 32$) simulation (and are thus identical to the red contours shown in Fig. 5.15). Blue contours show the result of a simulation employing the same resolution ($N_{\rm c} = 32, \tilde{N}_{\rm ngb} = 32$), but using the clock of the photon packets to solve the time-dependent radiative transfer equation. Note that in the simulation solving the time-independent radiative transfer equation the ionised regions are too large, since in this simulation the ionisation fronts are initially propagating at speeds larger than the speed of light. The fact that the ionisation fronts are more noisy in the simulation that employed the clocks than in the one which did not is due to the fact that the former simulation was performed with the original (slightly noisier, see App. 5.C) version of TRAPHIC, while the latter (as all other simulations presented in this section) made use of our current version.

Fig. 5.16 shows that an angular resolution of $N_{\rm c} = 32$, which corresponds to a relatively large opening angle of $\omega \approx 41$ degrees (Eq. 4.9 in Chapter 4), is already converged. The reason why a relatively poor formal angular resolution suffices, is, as already noted in the discussion of the sharpness of shadows thrown by opaque obstacles in Sec. 5.4.3, that the photon transport with TRAPHIC is intrinsically adaptive in angle.

In Fig. 5.17 we present results for a simulation that used the resampling technique presented in Sec. 5.3.4, but which was otherwise identical to the fiducial simulation presented above. The neutral hydrogen densities of the SPH particles were not re-calculated according to the perturbed positions resulting from the resampling, but kept constant to avoid additional scatter in the density. The resampling leads to a reduction in the particle noise. The improvement is not dramatic since the noise is already very low, as noted above. Observe that the resampling does not noticeable degrade the angular resolution - shadows remain sharp.

In Fig. 5.18 we show the evolution of the mean (over all particles i) ionised fraction, both volume-weighted, i.e. $\chi_{\rm V} = \sum_i h_i^3 \chi_i / \sum_i h_i^3$, where h_i is the radius of the SPH kernel of particle i, and mass-weighted, i.e. $\chi_{\rm m} = \sum_i m_i \chi_i / \sum_i m_i$. Again, the results obtained with TRAPHIC are in excellent agreement with the results obtained with C^2-RAY and CRASH. For the latter two we obtained the mean ionised fraction by averaging the ionised fraction reported in the cosmological radiative transfer code comparison project (Iliev et al. 2006b) over all grid cells i, i.e. $\chi_{\rm V} = \sum_i \chi_i / \sum_i 1$ and $\chi_{\rm m} = \sum_i \rho_i \chi_i / \sum_i \rho_i$.

The ratio of mass-weighted and volume-weighted mean ionised fractions is at early times slightly larger for the low angular resolution simulation than for the high angular resolution simulation, as can be seen in the bottom panel of Fig. 5.18. This is another manifestation of the fact that particle-to-neighbour transport is generally not independent of the geometry of the SPH simulation, resulting in photons being preferentially transported into high (particle) density regions. It once more underlines the importance of the concept of emission and transmission cones (with sufficiently small solid angles) which TRAPHIC uses to accomplish the transport of radiation independently of the spatial distribution of the SPH particles.

Finally, we show that for the present radiative transfer problem, simulations solving the time-dependent radiative transfer equation give a significantly different result than the simulations solving the time-independent radiative transfer equation discussed above. We carried out a simulation using $N_{\rm c} = 32, \tilde{N}_{\rm ngb} = 32$ and additionally employed the photon packet clocks to limit the distance over which photon packets can propagate during each time step. The size of the radiative transfer time step was set to $\Delta t_{\rm r} = 10^{-3}$ Myr. This time step is a factor 10 larger than the time step used for solving the time-independent radiative transfer equation in the simulations presented above, which required a smaller time step because of our particular treatment of the time-independent radiative transfer equation (see Sec. 5.3.3). The locations of the ionisation fronts (i.e. $\eta = 0.5$) obtained in this simulation are shown in Fig. 5.19 (blue curves), together with those obtained in the corresponding simulation solving the time-independent radiative transfer equation (red curves, which are identical to those in Fig. 5.15), at times $t = 0.05, 0.1, 0.2, 0.3$ and 0.4 Myr.

It is clear from Fig. 5.19 that the simulation solving the time-independent radiative transfer equation produces ionised spheres that are unphysically large. This is due to the well-known fact (see, e.g., the discussion in Abel, Norman, & Madau 1999) that ionisation fronts may propagate at speeds larger than the speed of light, if the time-independent radiative transfer equation is solved. The difference between the two simulations is larger at early times than at late times, which is expected, since in equilibrium, i.e. $t_{\rm r} \rightarrow \infty$, the results of both simulations must agree.

In summary, in this section we studied the propagation of ionisation fronts around multiple sources in a static cosmological density field. We demonstrated the importance of the concept of cones which underlies the photon transport in TRAPHIC. Without the confinement by transmission cones of sufficiently small solid angle, particle-to-neighbour transport is governed in part by the spatial distribution of the particles, resulting in the preferential transport of photons into high (particle) density regions. Thanks to the fact that TRAPHIC is adaptive in angle, a relatively modest formal angular resolution of $N_{\rm c} = 32$ is already sufficient to obtain a converged solution. Since the setup of our simulations followed the description of the corresponding test in the cosmological radiative transfer code comparison project (Iliev et al. 2006b), we were able to benchmark our radiative transfer scheme by comparing with the results obtained by the ray-tracing scheme C^2-RAY (Mellema et al. 2006) and the Monte Carlo code CRASH (Maselli, Ferrara, & Ciardi 2003; Ciardi et al. 2001). We found excellent agreement in the positions of neutral fraction contours as well as the mass and volume-weighted mean ionised fractions.

We have furthermore seen that for the test problem presented in this section, simulations solving the time-independent radiative transfer equation lead to ionised regions that are unphysically large during their early evolution. This illustrates the importance of correctly accounting for the finite speed of light when performing radiative transfer simulations to study the morphology of ionised regions that are strongly out of equilibrium.

5.5 CONCLUSIONS

We have presented an implementation of our radiative transfer scheme TRAPHIC, that we have described in Chapter 4, in the smoothed particle hydrodynamics code GADGET-2 to accomplish the transport of (mono-chromatic) hydrogen-ionising radiation in hydrodynamical simulations.

As part of this implementation we have introduced a numerical method that allows us to accurately compute the evolution of the ionised fraction of a gas parcel exposed to ionising radiation, independently of the size of the radiative transfer time step $\Delta t_{\rm r}$ employed. This decoupling of the radiative transfer time step from the time scales that govern the evolution of the neutral fraction, i.e. from the photo-ionisation time scale τ_{ion} and the recombination time scale τ_{rec}, is an important pre-requisite for performing efficient radiative transfer simulations. The alternative, a radiative transfer time step limited by the values for the photo-ionisation or recombination time scales, would generally be computationally infeasible, since these time scales may become very small. The method consists of sub-cycling the evolution of the neutral fraction over the radiative transfer time step in an explicitly photon-conserving manner. We have verified it by comparing results of numerical simulations of an optically thin gas parcel ionising up and recombining with the analytical solution to this problem.

We have then ran several radiative transfer simulations on static density fields and solved the radiative transfer equation, in both its time-independent and time-dependent form, in problems of increasing complexity. Throughout we have employed both analytical and numerical reference solutions to quantify TRAPHIC's performance in these problems. For the latter we have developed a spherically symmetric mesh-based radiative transfer code (TT1D). We also employed results reported in the literature (Mellema et al. 2006; Iliev et al. 2006b) that have been obtained by other radiative transfer codes in identical test problems for our comparison.

We first showed that TRAPHIC is able to accurately reproduce the expected growth of the ionised sphere around a single point source in a homogeneous medium. There we found that in addition to the number of cones N_{c} and the number of SPH neighbours $\tilde{N}_{\mathrm{ngb}}$, it is the ratio $N_{\mathrm{c}}/\tilde{N}_{\mathrm{ngb}}$ that directly influences the performance of TRAPHIC. It controls the amount of noise introduced by the representation of the underlying continuum physics with a discrete set of particles. This particle noise is small for both $N_{\mathrm{c}} < \tilde{N}_{\mathrm{ngb}}$ and $N_{\mathrm{c}} > \tilde{N}_{\mathrm{ngb}}$ due to the large number of neighbours per cone and the large number of ViPs, resp. For the choice of parameters $N_{\mathrm{c}} = \tilde{N}_{\mathrm{ngb}}$ the particle noise can be substantial. It can, however, be efficiently suppressed by employing the density field resampling strategy that we have suggested in Chapter 4.

We have furthermore verified that TRAPHIC is able to cast sharp shadows behind opaque obstacles, which is a main requirement for radiative transfer schemes to pass. We have shown that the sharpness of the shadows is controlled by and in agreement with the formal angular resolutions employed. In fact, we found that the shadows are much sharper than implied by that formal angular resolution. We have demonstrated that transmission cone apex motions implied by a moving set of SPH particles do not noticeably degrade the effective angular resolution and hence TRAPHIC's shadowing characteristics. TRAPHIC can therefore also be applied in dynamical simulations, in step with the hydrodynamical evolution of the SPH particles, and we will present such dynamical simulations in Chapter 6.

We also computed the growth of an ionised region in a centrally peaked density profile. The setup of this problem is characteristic for star-forming regions in cosmological structure formation simulations. This test problem clearly revealed the Monte-Carlo aspect of TRAPHIC. The numerical results obtained in simulations of this problem converged towards the exact solution with increasing number of cones N_{c} used, which can be explained by noting that the number of cones determines the number of directions that are simultaneously sampled.

Finally, we tested our scheme in a scaled-down version of a typical epoch-of-reionisation simulation: we studied the growth of ionised regions around multiple point sources in a cosmological density field at high redshift. Comparisons to the results obtained by other radiative transfer codes showed excellent agreement. These codes were limited to solving the time-independent radiative transfer problem. Thanks to the use of photon packet clocks, TRAPHIC may also be used to solve the time-dependent radiative transfer problem. We have repeated the simulation and performed such a time-dependent computation. We have confirmed the well-known fact that time-independent radiative transfer simulations, because they assume an infinite speed of light, may predict too fast a growth of the ionised regions.

The fact that the results of all tests performed in this chapter are in excellent agreement with both analytically and numerically computed reference solutions confirms the validity of the concepts underlying our radiative transfer scheme TRAPHIC. The radiative transfer test problems performed in this chapter have been set up in a somewhat idealised manner to facilitate the evaluation of their results and the comparison with reference solutions. Their simplified design is, unfortunately, not suited to demonstrate the advantages of TRAPHIC over conventional radiative transfer schemes - that it is spatially adaptive, that it is implemented for use in parallel on distributed memory machines and that its computation time is independent of the number of radiation sources. TRAPHIC will unfold its true strength only in the large hydrodynamical simulations it has been developed for. We will perform such simulations in the next chapter, Chapter 6.

ACKNOWLEDGEMENTS

We thank Claudio Dalla Vecchia for stimulating discussions and help with the setup of simulations. We are grateful to Craig Booth and Benedetta Ciardi for a thorough reading of the draft version of Pawlik & Schaye (2008). A.H.P. thanks the University of Potsdam and the Max Planck Institut für Astrophysik for their hospitality where part of the work presented in this chapter has been done. He is indebted to Prof. Arkardi Pikovsky and Volker Springel for their cordiality during these stays. Some of the simulations presented here were run on the Cosmology Machine at the Institute for Computational Cosmology in Durham as part of the Virgo Consortium research programme and on Stella, the LOFAR BlueGene/L system in Groningen. This work was supported by Marie Curie Excellence Grant MEXT-CT-2004-014112.

REFERENCES

Abel T., Norman M. L., Madau P., 1999, ApJ, 523, 66

Alvarez M. A., Bromm V., Shapiro P. R., 2006, ApJ, 639, 621

Altay G., Croft R. A. C., Pelupessy I., 2008, MNRAS, 386, 1931

Ciardi B., Ferrara A., Marri S., Raimondo G., 2001, MNRAS, 324, 381

Corless, R. M.; Gonnet, G. H.; Hare, D. E. G.; Jeffrey, D. J.; and Knuth, D. E., Adv. Comput. Math. 5, 329-359

Dale J. E., Bonnell I. A., Whitworth A. P., 2007, MNRAS, 375, 1291

Dopita M. A., Sutherland R. S., 2003, Astrophysics of the diffuse universe, Springer

Dove J. B., Shull J. M., 1994, ApJ, 430, 222

Gnedin N. Y., Abel T., 2001, NewA, 6, 437

Goldstein H., 1980, Classical Mechanics, Addison-Wesley Publ. Co

Gritschneder M., Naab T., Heitsch F., Burkert A., 2007, IAUS, 237, 246

He P., 2009, arXiv, arXiv:0903.2208

Hockney R. W., Eastwood J. W., 1988, Computer Simulations Using Particles, Taylor & Francis

Iliev I. T., Mellema G., Pen U.-L., Merz H., Shapiro P. R., Alvarez M. A., 2006, MNRAS, 369, 1625

Iliev I. T., et al., 2006, MNRAS, 371, 1057

Johnson J. L., Greif T. H., Bromm V., 2007, ApJ, 665, 85

Kohler K., Gnedin N. Y., Hamilton A. J. S., 2007, ApJ, 657, 15

Maselli A., Ferrara A., Ciardi B., 2003, MNRAS, 345, 379

Petkova M., Springel V., submitted

Shampine L. F., Gear C. W., 1979, SIAM Review, Vol. 21, No. 1., pp. 1-17, Jstor.

Maselli A., Ciardi B., Kanekar A., 2009, MNRAS, 393, 171

Mellema G., Iliev I. T., Alvarez M. A., Shapiro P. R., 2006, NewA, 11, 374

Mihalas D., Weibel Mihalas B., 1984, Foundations of radiation hydrodynamics, Oxford University Press, New York

Miles R. E., 1965, Biometrika, Vol. 52, No. 3/4, pp. 636

Navarro J. F., Frenk C. S., White S. D. M., 1997, ApJ, 490, 493

Osterbrock D. E., 1989, Astrophysics of gaseous nebulae and active galactic nuclei, Palgrave Macmillan

Paschos P., Norman M. L., Bordner J. O., Harkness R., 2007, arXiv, 711, arXiv:0711.1904

Pawlik A. H., Schaye J., 2008, MNRAS, 389, 651

Press W. H., Teukolsky S. A., Vetterling W. T., Flannery B. P., 1992, Numerical recipes in C. The art of scientific computing, Cambridge University Press, 2nd ed.

Razoumov A. O., Cardall C. Y., 2005, MNRAS, 362, 1413

Ritzerveld J., Icke V., 2006, PhRvE, 74, 026704

Ryu D., Ostriker J. P., Kang H., Cen R., 1993, ApJ, 414, 1

Springel V., 2005, MNRAS, 364, 1105

Springel V., et al., 2008, MNRAS, 391, 1685

Stewart G. W., 1980, SIAM Journal on Numerical Analysis, Vol. 17, No. 3, 403

Trac H., Cen R., 2007, ApJ, 671, 1

Susa H., Umemura M., 2006, ApJ, 645, L93

White S. D. M., 1996, Cosmology and large scale structure, Proceedings of the "Les Houches Ecole d'Ete de Physique Theorique" (Les Houches Summer School), p. 349, Elsevier Scientific Publishing Company, Amsterdam

Whalen D., Norman M. L., 2007, arXiv, 708, arXiv:0708.2444

Wise J. H., Abel T., 2007, arXiv, 710, arXiv:0710.3160

Yoshida N., Oh S. P., Kitayama T., Hernquist L., 2007, ApJ, 663, 687

5.A CONSTRAINTS ON THE INTEGRATION STEP SIZE IN THE EULER DISCRETIZATION

In this section we show that when advancing the neutral fraction over a single time step $\Delta t_{\rm r}$ according to Eq. 5.21, that is using the Euler discretization, this time step has to satisfy $0 \leq \Delta t_{\rm r} \leq f\tau_{\rm eq}$ in order for the neutral fraction to obey its physical bounds. Hereby, $\tau_{\rm eq}$ is the time scale on which photo-ionisation equilibrium is approached (Sec. 5.2, Eq. 5.7) and $f < 1$ is a dimensionless parameter that will be defined below.

In the Euler discretization, the new neutral fraction $\eta(t+\Delta t_{\rm r})$ is related to the current neutral fraction $\eta(t)$ via

$$\begin{aligned}\eta(t+\Delta t_{\rm r}) &= \eta(t) + \beta n_{\rm e}(1-\eta(t))\Delta t_{\rm r} - \Gamma\eta(t)\Delta t_{\rm r} && (5.56)\\ &= \eta(t)\left(1 - \frac{\Delta t_{\rm r}}{\tau_{\rm eq}}\right) + \frac{\Delta t_{\rm r}}{\tau_{\rm rec}}. && (5.57)\end{aligned}$$

In the following we understand all quantities to be evaluated at time t and hence will not explicitly indicate the time dependence.

By definition the neutral fraction must satisfy $0 \leq \eta \leq 1$. Satisfying the lower bound means

$$\eta\left(1-\frac{\Delta t_{\mathrm{r}}}{\tau_{\mathrm{eq}}}\right)+\frac{\Delta t_{\mathrm{r}}}{\tau_{\mathrm{rec}}} \geq 0, \tag{5.58}$$

which poses the conditions

$$\Delta t_{\mathrm{r}} \leq \frac{-\eta}{\tau_{\mathrm{rec}}^{-1}-\eta\tau_{\mathrm{eq}}^{-1}} \quad \text{for } \tau_{\mathrm{rec}}^{-1}-\eta\tau_{\mathrm{eq}}^{-1}<0 \tag{5.59}$$

and

$$\Delta t_{\mathrm{r}} \geq \frac{-\eta}{\tau_{\mathrm{rec}}^{-1}-\eta\tau_{\mathrm{eq}}^{-1}} \quad \text{for } \tau_{\mathrm{rec}}^{-1}-\eta\tau_{\mathrm{eq}}^{-1}>0 \tag{5.60}$$

on the size of the time step Δt_{r}. Satisfying the upper bound means, on the other hand,

$$\eta\left(1-\frac{\Delta t_{\mathrm{r}}}{\tau_{\mathrm{eq}}}\right)+\frac{\Delta t_{\mathrm{r}}}{\tau_{\mathrm{rec}}} \leq 1, \tag{5.61}$$

which poses the conditions

$$\Delta t_{\mathrm{r}} \geq \frac{1-\eta}{\tau_{\mathrm{rec}}^{-1}-\eta\tau_{\mathrm{eq}}^{-1}} \quad \text{for } \tau_{\mathrm{rec}}^{-1}-\eta\tau_{\mathrm{eq}}^{-1}<0, \tag{5.62}$$

and

$$\Delta t_{\mathrm{r}} \leq \frac{1-\eta}{\tau_{\mathrm{rec}}^{-1}-\eta\tau_{\mathrm{eq}}^{-1}} \quad \text{for } \tau_{\mathrm{rec}}^{-1}-\eta\tau_{\mathrm{eq}}^{-1}>0 \tag{5.63}$$

on the size of the time step Δt_{r}. Let us consider the two limiting cases of fully neutral and fully ionised gas, since these are the ionisation states for which a violation of the physical bound $0 \leq \eta \leq 1$ due to an inaccurate integration is most likely. For the former, we find from Eq. 5.59 (using $\tau_{\mathrm{eq}} \rightarrow \tau_{\mathrm{ion}}$ for $\tau_{\mathrm{rec}} \rightarrow \infty$)

$$0 \leq \Delta t_{\mathrm{r}} \leq \tau_{\mathrm{ion}}, \tag{5.64}$$

while for the latter we find from Eq. 5.63

$$0 \leq \Delta t_{\mathrm{r}} \leq \tau_{\mathrm{rec}}. \tag{5.65}$$

In order for the neutral fraction to satisfy $0 \leq \eta \leq 1$, the time step Δt_{r} must be chosen such that it simultaneously satisfies the bounds Eqs. 5.64 and 5.65. Since $\tau_{\mathrm{eq}} \rightarrow \tau_{\mathrm{ion}}$ for $\tau_{\mathrm{ion}} \ll \tau_{\mathrm{rec}}$ whereas $\tau_{\mathrm{eq}} \rightarrow \tau_{\mathrm{rec}}$ for $\tau_{\mathrm{rec}} \ll \tau_{\mathrm{ion}}$ we may conveniently summarise the derived bounds by writing

$$0 \leq \Delta t_{\mathrm{r}} \leq f\tau_{\mathrm{eq}}, \tag{5.66}$$

where $f \leq 1$ is a dimensionless factor.

Finally, we note that the case of photo-ionisation equilibrium, i.e. $\eta_{\mathrm{eq}} = \tau_{\mathrm{ion}}/(\tau_{\mathrm{ion}}+\tau_{rec,eq})$, is formally excluded from our analysis, since then $\tau_{\mathrm{rec}}^{-1}-\eta\tau_{\mathrm{eq}}^{-1}=0$ and Eqs. 5.59-5.62 become undefined. This simply means that in photo-ionisation equilibrium the time step can be chosen arbitrarily large[17].

---

[17] This statement only applies to considerations of discretization accuracy. As explained in Sec. 5.3.2, the numerically stable explicit integration of stiff equations like the photo-ionization rate equation puts an additional constraint on the size of the integration time step.

5.B CONES

5.B.1 Cone tessellation

In this section we describe the numerical implementation of the cones employed for the emission and reception of photon packets in TRAPHIC. For the emission (Sec. 4.4.2 in Chapter 4), each source particle divides its neighbourhood using a set of tessellating emission cones. The same tessellation is also employed for the reception of photon packets by gas particles (Sec. 4.4.2 in Chapter 4). In the following, we employ spherical coordinates (r, ϕ, θ), which are related to the Cartesian components (r_x, r_y, r_z) of an arbitrary vector $\mathbf{r}$ through

$$r_x = r\cos\phi\sin\theta \tag{5.67}$$

$$r_y = r\sin\phi\sin\theta \tag{5.68}$$

$$r_z = r\cos\theta. \tag{5.69}$$

In our implementation, the emission (reception) cones sample the volume around each particle isotropically. Since the surface element of the unit sphere is given by $ds = d(\cos\theta)d\phi$, this is achieved by distributing the cone boundaries[18] uniformly (i.e. on a regular lattice with indices i, j) in $(\cos\theta, \phi)$. Thus, the boundaries of cone (i, j) are described by the four arcs of constant

$$\phi_1^{ij} = i\frac{2\pi}{N_\phi}, \quad 0 \le i < N_\phi, \tag{5.70}$$

$$\phi_2^{ij} = (i+1)\frac{2\pi}{N_\phi}, \quad 0 \le i < N_\phi, \tag{5.71}$$

$$\theta_1^{ij} = \arccos(1 - 2\frac{j}{N_\theta}), \quad 0 \le j < N_\theta, \tag{5.72}$$

$$\theta_2^{ij} = \arccos(1 - 2\frac{j+1}{N_\theta}), \quad 0 \le j < N_\theta. \tag{5.73}$$

Correspondingly, we define the emission (reception) cone axes by

$$\phi^{ij} = \frac{\phi_1^{ij} + \phi_2^{ij}}{2}, \tag{5.74}$$

$$\theta^{ij} = \frac{\theta_1^{ij} + \theta_2^{ij}}{2}, \tag{5.75}$$

Note that each of the $N_\mathrm{c} = N_\phi \times N_\theta$ emission (reception) cones has the same solid angle $\Omega = 4\pi/N_\mathrm{c}$, as can be seen from integrating over the surface element of the unit sphere within the boundaries (Eqs. 5.70-5.73). We also implemented the tessellation used in Abel, Norman, & Madau (1999), which leads to cones that are more similar in shape. We could not find any systematic differences in the test problems described in Secs. 5.4.2 - 5.4.5 using either of the two types of tessellations. This is not surprising because any artefacts due to the shape of the cones will be suppressed by the random rotations of the emission (reception) cones we perform before each emission (reception). Our implementation of these rotations is described in the next section.

---

[18] Strictly speaking, one should distribute the cone *axes* uniformly in $(\cos\theta, \phi)$, but this implies asymmetric cones.

5.B.2 Random rotations

Recall from Sections 4.4.2 and 4.4.2 (Chapter 4) that we apply a random rotation to each cone tessellation. Consequently, each cone tessellation has a random orientation. The primary motivation for randomly rotating cones is to increase the angular sampling. Furthermore, randomly rotating the emission and reception cones leads to a reduction of artefacts arising from the particular definition we employ to construct the cone tessellation, as noted in the last section. Here we describe our numerical implementation of the random rotations.

We can think of the set of cones that comprises a particular cone tessellation as a rigid body, to which we can attach a local Cartesian coordinate system with axes $\{e'_x, e'_y, e'_z\}$. The orientation of this coordinate system with respect to the canonical Cartesian coordinate system, e.g. the simulation box axes $\{e_x, e_y, e_z\}$, is fully described by three variables, the Eulerian angles (e.g. Goldstein 1980).

Eulerian angles are defined as the three successive angles of rotations that map the axes $\{e_x, e_y, e_z\}$ onto the axes $\{e'_x, e'_y, e'_z\}$. There exist several conventions. In the zxz convention we employ here, the initial system of axes $\{e_x, e_y, e_z\}$ is first rotated counter-clockwise by an angle ϕ around the z-axis, with the resulting coordinate system labelled $\{e_\xi, e_\eta, e_\zeta\}$. Second, the coordinate system $\{e_\xi, e_\eta, e_\zeta\}$ is rotated by an angle θ counter-clockwise about the ξ-axis, leaving the new coordinate system $\{e'_\xi, e'_\eta, e'_\zeta\}$. The third and last rotation is carried out counter-clockwise by an angle ψ around the ζ'-axis, giving the desired $\{e'_x, e'_y, e'_z\}$ coordinate system.

To obtain random Eulerian angles, we note that the invariant measure μ (the "volume element") on $\mathrm{SO}(3)$, the group of proper rotations in $\mathbb{R}^3$, in the zxz Eulerian angle parametrisation reads (e.g. Miles 1965),

$$\mu(\phi, \theta, \psi) d\phi d\theta d\psi = \frac{1}{8\pi} \sin\theta d\phi d\theta d\psi. \tag{5.76}$$

Random Eulerian angles are therefore obtained by drawing random variables u_1, u_2, u_3 from a uniform distribution on the interval $[0, 1]$ and applying the usual transformation (cp. Press et al. 1992),

$$\phi = 2\pi u_1 \tag{5.77}$$
$$\theta = \arccos(1 - 2u_2) \tag{5.78}$$
$$\psi = 2\pi u_3. \tag{5.79}$$

We implement random rotations using rotation matrices, which are obtained from the random Eulerian angles. The matrix elements of a matrix R representing a rotation $\mathbf{r}' = \mathbf{R}\mathbf{r}$ associated with a given set of Eulerian angles can be readily calculated (e.g. Goldstein 1980):

$$R = \begin{pmatrix} \cos\psi\cos\phi - \cos\theta\sin\phi\sin\psi & \cos\psi\sin\phi + \cos\theta\cos\phi\sin\psi & \sin\psi\sin\theta \\ -\sin\psi\cos\phi - \cos\theta\sin\phi\cos\psi & -\sin\psi\sin\phi + \cos\theta\cos\phi\cos\psi & \cos\psi\sin\theta \\ \sin\theta\sin\phi & -\sin\theta\cos\phi & \cos\theta \end{pmatrix}. \tag{5.80}$$

In principle, random rotation matrices can be obtained directly, without drawing random Eulerian angles (e.g. Stewart 1980). We find, however, that it is faster to generate random Eulerian angles, and then calculate the corresponding rotation matrices. Moreover, storing the three Eulerian angles instead of the nine rotation matrix elements reduces the memory cost.

5.C A NEW TREATMENT OF ABSORPTIONS BY VIRTUAL PARTICLES

In this appendix we show that the treatment of virtual particles (ViPs) in the implementation of TRAPHIC that we have used to perform the simulations published in Pawlik & Schaye (2008), and that we will refer to as the old implementation, results in a temporary underestimate of the neutral fraction just behind evolving ionisation fronts in simulations that use a high angular resolution. We will show that this underestimate is absent in simulations that employ our current implementation of TRAPHIC. Moreover, in simulations that employ this new implementation, the numerical scatter in the neutral fraction is significantly reduced.

The difference between the treatments of ViPs in the old and current implementations of TRAPHIC has already been explained in Sec. 5.4. The old and current implementation only differ in the manner in which photons that have been absorbed by ViPs are distributed amongst their neighboring SPH particles. We remind the reader that this distribution of absorptions is necessary, because ViPs are temporary constructs that are just invoked to transport photons inside cones that do not contain SPH particles (see Chapter 4). Permanent information is only stored at the SPH particles in the simulation.

The number of ionising photons a ViP absorbs depends on its neutral density. As explained in Chapter 4, the computation of this number is performed in exactly the same manner as for SPH particles. The only difference between the treatment of photons absorbed by SPH particles and ViPs is that the latter distribute the absorbed photons amongst their SPH neighbors. For this distribution of absorptions one must specify the fraction of the total that is given to each of the SPH neighbors. In the old implementation of TRAPHIC this fraction was taken to be proportional to the value of the SPH kernel of the distributing ViP at the position of the SPH neighbor. In the new version this fraction is taken to be proportional to the neutral mass with which the SPH neighbor contributed to the SPH estimate of the ViP's neutral density.

The old treatment of ViPs results in an underestimate in the simulated non-equilibrium neutral fractions. Fig. 5.20 serves to demonstrate this. Its panels show the neutral and ionised fractions around a single ionising source in a homogeneous hydrogen-only medium at times $t = 30, 100$ and 500 Myr (from left to right) obtained with the old (first and third rows) and current (second and fourth rows) implementation. The setup and parameters for the simulations presented here are identical to the setup and parameters used for the $N_{\rm SPH} = 64^3$, $N_{\rm c} = 128$ simulation presented in Test 1 in Sec. 5.4.2. In addition to the neutral (grey dots) and ionised (light red dots) fractions of each particle, Fig. 5.20 shows the median neutral (black solid curves) and ionised (red solid curves) fractions in spherical bins, which are compared to the exact solution obtained with TT1D (dashed curves of the corresponding color). The error bars indicate the 68.3% confidence intervals in each bin. For each implementation we have performed simulations both with and without resampling the density field, as indicated by the presence or absence of the letter 'R' in the panel titles. Note that the right-most panels in the second and fourth row are identical (except for the bin size) to the right-most panels in the top and bottom row of Fig. 5.5 in Sec. 5.4.2.

In the simulations employing the old implementation of TRAPHIC the neutral fraction at times $t = 30$ and 100 Myr is underestimated at radii slightly smaller than the radius of the ionisation front. In the simulations that employ the current implementation this underestimate, thanks to the new manner in which the ViPs' absorptions are distributed, is no longer present. At $t = 500$ Myr, i.e. when the ionised region has (nearly) reached its equilibrium size, the underestimate is also absent in the simulations that employ the old implementation. However, at this time these simulations still exhibit an increased scatter around the median when compared to the corresponding snapshots from the simulations that employ the current implementation.

The underestimate of the neutral fraction just behind evolving ionisation fronts in simulations employing the old implementation is caused by the fact that in this implementation the distribution of the photons absorbed by ViPs does not respect the spatial distribution of the neutral gas in their surroundings. It mainly affects the neutral fraction of particles close to evolving ionisation fronts, because the number of photons absorbed and subsequently distributed by ViPs near the ionisation front is significantly larger than the number of photons that are absorbed by the SPH particles behind the ionisation front that have already reached photo-ionisation equilibrium and because the ViPs distribute the absorbed photons irrespective of the neutral mass with which the corresponding SPH particles contributed to the computation of its neutral density. The absorptions that SPH particles behind evolving ionisation fronts receive from ViPs in addition to the number of photons they have already absorbed according to their own optical depth therefore results in an overestimate of the photo-ionisation rate and hence an underestimate of the neutral fraction. Once the ionisation front becomes stationary the underestimate of the neutral fraction practically disappears, because the number of photons absorbed and distributed by ViPs in the ionisation front is consistent with the expectations from photo-ionisation equilibrium.

We did not notice the described temporary underestimate of the neutral fraction just behind non-equilibrium ionisation fronts in the simulations that we have presented in our original publication, i.e. in Pawlik & Schaye (2008), since there we only discussed profiles of the neutral fraction at $t = 500$ Myr. The reason why we limited ourselves to discussion of equilibrium results in that publication was mainly that we were at that time still lacking accurate non-equilibrium reference solutions: our one-dimensional reference radiative transfer code TT1D was still under development. The discovery of the underestimate of the neutral fraction was triggered by scatter plots of the neutral and ionised fractions like those presented in Fig. 5.20 that we have performed more recently.

5.D POWER-LAW INITIAL CONDITIONS FOR SMOOTHED PARTICLE HYDRODYNAMICS SIMULATIONS

In this appendix we describe the procedure that was used to generate the centrally peaked density field with spherically averaged profile $\rho(r) \propto r^{-1}$ employed in Test 3 in Sec. 5.4.4. We will explain more generally how to generate power-law density profiles

$$\hat{\rho}(r) \propto r^{-n}, \tag{5.81}$$

and then consider the special case $n = 1$.

The gas density at a given position is proportional to the probability of finding a gas particle at this position (assuming that the particle mass is the same for all gas particles). Arbitrary Smoothed Particle Hydrodynamics (SPH) density fields can therefore be generated using Monte Carlo methods. We have employed such a method in Sec. 5.4.5. Monte Carlo methods yield, however, particle distributions that are subject to Poisson noise. Alternative methods of generating density fields that avoid this noise are therefore often more desirable.

The uniform density fields used to initialise cosmological SPH simulations, for example, are obtained by placing particles at glass-like instead of Monte Carlo positions. Glass-like positions may be considered as regularised Monte Carlo positions. They are produced by first placing particles randomly in the simulation box and thereafter letting them freely evolve under the influence of a reversed-sign (i.e. repelling) gravitational force until they settle down into an

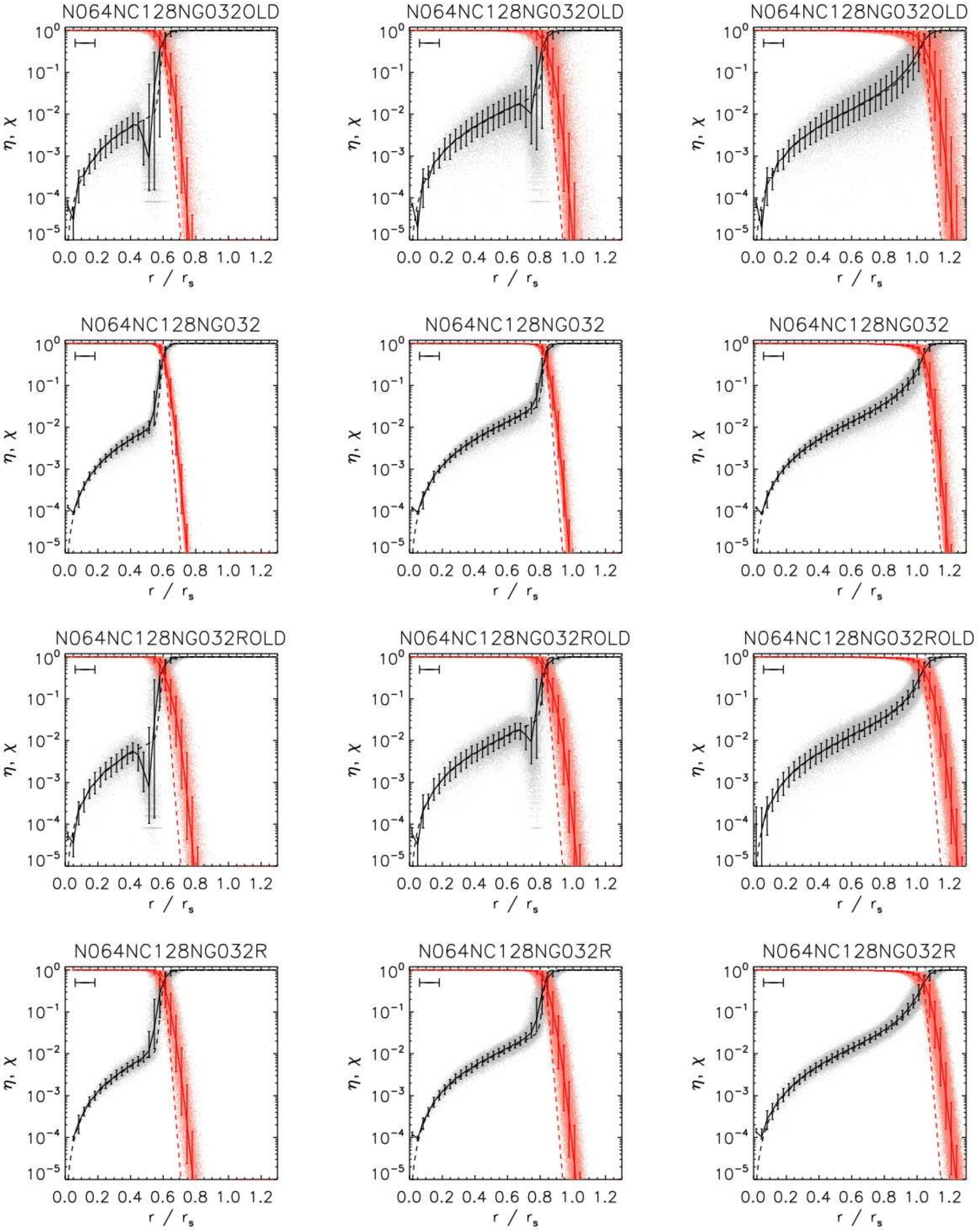

Figure 5.20: Test 1. Neutral and ionised fractions obtained in simulations with the old (first and third row) (Pawlik & Schaye 2008) and current (second and fourth row) implementations of TRAPHIC. Shown are profiles of neutral and ionised fraction at times $t = 30$ (left-hand panel), 100 (middle panel) and 500 Myr (right-hand panel), for simulations with (second and fourth row) and without (first and third row) resampling of the density field. The spatial resolution is fixed to $N_{\rm SPH} = 64^3$, $\tilde{N}_{\rm ngb} = 32$ and is indicated by the horizontal error bar in the upper left corner of each panel. The angular resolution is $N_{\rm c} = 128$. The grey (light red) points show the neutral (ionised) fraction of each SPH particle. The solid black (red) curve shows the median neutral (ionised) fraction in spherical bins and the error bars show the corresponding 68.3% confidence intervals. The dashed black (red) curves show the exact solution, obtained with our reference code TT1D. The non-equilibrium underestimate of the neutral fraction exhibited in simulations with the old implementation of TRAPHIC is absent in the simulations that employ our current implementation, thanks to a new self-consistent manner of distributing photons absorbed by ViPs. The new implementation also reduces the scatter in the ionisation balance.

equilibrium configuration (see White 1996). This regularisation leads to a significant reduction of small-scale fluctuations in the (random) inter-particle distances.

These glass-like density fields can also be used to set up centrally peaked power-law density fields of the desired form, Eq. 5.81 (Volker Springel, Claudio Dalla Vecchia, private communication). The idea is to deform the (unstructured) grid traced out by the set of uniformly distributed particles at glass-like positions such as to locally stretch the mean inter-particle distance in the radial direction. Assume that the uniform, glass-like particle distribution has density ρ_0 and express this stretching by a coordinate transformation in spherical coordinates, $(r, \theta, \phi) \rightarrow (\hat{r}, \theta, \phi)$. Mass conservation requires the new particle positions to satisfy

$$\hat{\rho}(\hat{r})\hat{r}^2 \sin\theta d\hat{r} d\theta d\phi = \rho_0 r^2 \sin\theta dr d\theta d\phi, \tag{5.82}$$

Substituting the desired density profile Eq. 5.81, the coordinate transformation reads

$$\hat{r}^{2-n} d\hat{r} \propto r^2 dr, \tag{5.83}$$

which can be easily integrated,

$$\hat{r} \propto r^{3/(3-n)}. \tag{5.84}$$

To set up the density field used in Test 3 in Sec. 5.4.3 we are interested in producing a centrally peaked density field with power-law index $n = 1$. In this case, the last expression gives $\hat{r} \propto r^{3/2}$.

> Чтобы достичь совершенства, надо прежде многого не понимать. А слишком скоро поймем, так, пожалуй, и не хорошо поймем.
>
> Достоевский, Идиот

CHAPTER 6

Radiative transfer simulations of cosmic reionisation

Andreas H. Pawlik & Joop Schaye

In preparation.

RADIATIVE transfer (RT) simulations coupled to cosmological hydrodynamical simulations are one of the most promising tools to study reionisation, a key epoch in the high-redshift Universe. Current generations of RT schemes are, however, often limited for use with uniform and relatively coarse grids that imply a spatial resolution far below that of state-of-the-art spatially adaptive hydrodynamical simulations. Small-scale structure in the cosmic gas is then, at best, only statistically accounted for. Here we use the spatially adaptive RT scheme TRAPHIC (Chapter 4) to investigate the implications of this approximate approach. We contrast RT simulations performed on spatially adaptive smoothed particle hydrodynamics density fields with RT simulations performed on density fields that are defined on a uniform grid. Comparisons of the evolution of the mean ionised fraction, of the dependence of the ionised fraction on the local gas density and of power spectra of the 21 cm signal from neutral hydrogen reveal substantial differences caused by the difference in the dynamic range employed by the two types of RT simulations. Our results underpin earlier suggestions that ignoring the inhomogeneous distribution of gas on small scales, as is typically done in current RT simulations of reionisation, can give rise to misleading conclusions about the spatial distribution of the ionised gas and hence affect the interpretation of current and the predictions of future observations of reionisation.

6.1 INTRODUCTION

The first stars and galaxies are thought to have formed a few hundred million years after the Big Bang, when the Universe had only a small fraction of its present age. Their radiation transformed the previously cold and neutral hydrogen that filled intergalactic space into the hot and ionised plasma that is observed today. This milestone in the history of the Universe is called the epoch of reionisation (e.g., Barkana & Loeb 2001; Ciardi & Ferrara 2005; Loeb, Ferrara, & Ellis 2008; Choudhury 2009).

Much about reionisation is still unknown. When did reionisation occur? Was it a (nearly) instantaneous event or a complex process of extended duration? How did it proceed? What were the properties of the stars and galaxies that reionised the Universe? Theoretical studies of the epoch of reionisation are currently particularly timely because of the wealth of observational data of unparallelled quality that will soon be provided by a new generation of observatories.

Radio interferometers like LOFAR[1], MWA[2] and SKA[3] will open a previously unexplored observational window by surveying the Universe at very low frequencies with unprecedented high resolution and sensitivity. By mapping the redshifted 21 cm signal from the neutral hydrogen, these interferometers will provide a three-dimensional tomographic view on the intergalactic gas in the distant Universe and offer one of the most direct probes of its evolution during reionisation to date. The infrared space-based observatory JWST[4] and the optical ground-based adaptive optics telescope ELT[5] will even enable the direct imaging of the sources responsible for the reionisation process.

If the Universe was indeed reionised by the first stars, then the high-density gas in and around the halos in which these stars formed must have been ionised first (e.g., Barkana & Loeb 2001). Consequently, reionisation started from the inside out. The low-density gas far away from the first sites of star formation would only be reionised once the ionising radiation was channelled into the large-scale voids (Ciardi, Stoehr, & White 2003). Towards the end, reionisation would, on the other hand, proceed from the outside in (Miralda-Escudé, Haehnelt, & Rees 2000), with the ionising radiation slowly carving its way from the highly ionised voids into the remaining dense pockets of neutral gas.

The depicted scenario is supported by the results of early radiative transfer (RT) simulations (e.g., Sokasian et al. 2003; Gnedin 2000; Nakamoto, Umemura, & Susa 2001) and detections of Lyman-limit systems in the observed spectra of distant ($z \lesssim 6$) quasars (e.g., Fan, Carilli, & Keating 2006). It gave rise to the construction of semi-analytic models of reionisation targeted to investigate the epoch of reionisation in either of the two limiting topological regimes (e.g., Miralda-Escudé, Haehnelt, & Rees 2000; Furlanetto, Zaldarriaga, & Hernquist 2004). More recent RT simulations and semi-analytical models draw a more complex picture. While some works (e.g., Lee et al. 2008) confirm the traditional view of reionisation proceeding inside-out with a reversal to outside-in, others (e.g. Iliev et al. 2006; McQuinn et al. 2007; Zahn et al. 2007) predict that reionisation occurs in a strictly inside-out manner.

The different conclusions may be the result of the fact that many of even the most advanced reionisation simulations lack adequate spatial resolution. To keep the computations feasible, many state-of-the-art RT schemes require the use of uniform grids with relatively few grid points. Combined with the fact that large simulation boxes are necessary to model representa-

---

[1] http://www.lofar.org

[2] http://www.haystack.mit.edu/ast/arrays/mwa/

[3] http://www.skatelescope.org

[4] http://www.jwst.nasa.gov/

[5] http://www.eso.org/sci/facilities/eelt/

tive volumes of the Universe (Barkana & Loeb 2004; Iliev et al. 2006), this means that the spatial resolution of state-of-the-art RT simulations is typically far below that of routine hydrodynamical simulations of galaxy formation. Small-scale clumpiness of the cosmic gas is therefore, if at all, only statistically accounted for. Many RT simulations ignore hydrodynamical effects altogether and assume the gas to trace the dark matter.

Some works (e.g., Furlanetto & Oh 2005; Choudhury, Haehnelt, & Regan 2009; Finlator, Özel, & Davé 2009) have argued that a proper modelling of the inhomogeneous distribution of gas on small scales could, however, play a critical role in determining the topology of the ionised gas, because it strongly affects the computation of recombination rates (e.g., Gnedin & Ostriker 1997; Miralda-Escudé, Haehnelt, & Rees 2000; Kohler, Gnedin, & Hamilton 2007; Pawlik, Schaye, & van Scherpenzeel 2009a). In fact, Choudhury, Haehnelt, & Regan (2009) showed that due to the inhomogeneous nature of recombinations, the ionised fraction shows a non-trivial dependence on the local gas density.

Here we present preliminary results from an ongoing project to study the progress, topology and observability of reionisation using accurate, spatially adaptive RT simulations in combination with high-resolution hydrodynamical simulations of the high-redshift Universe. We will employ our RT scheme TRAPHIC (Chapter 4) on top of cosmological hydrodynamical simulations performed with the N-body/Tree-PM/SPH code P-GADGET3-BG, an enhanced version of GADGET-2 (Springel 2005), to follow the propagation of ionising photons emitted by the first galaxies and to compute their interaction with the cosmic gas. TRAPHIC has been specifically designed for use with large, spatially adaptive simulations of reionisation and hence is well-suited for the current project. Its distinguishing properties that enable these types of simulations are that it is spatially adaptive, that its computation time does not directly scale with the number of radiation sources and that it operates in parallel on distributed memory machines.

We will use TRAPHIC to carry out spatially adaptive RT simulations of reionisation by post-processing static density fields provided by the spatially adaptive SPH simulation we perform. Although the current version of TRAPHIC can also be employed to perform RT simulations in step with the hydrodynamical evolution, we have chosen the commonly employed post-processing technique and the static approximation to facilitate a comparison with previous works. The RT simulations are performed directly on top of the SPH particle distribution and hence fully exploit the available dynamic range. We will also carry out RT simulations on top of density fields obtained by first mapping the SPH particles onto a uniform grid and then Monte-Carlo sampling it for use with TRAPHIC. These simulations hence do not employ the full dynamic range exhibited by the SPH simulation. The analysis of the results obtained in these two types of RT simulations and their comparison will allow us to judge the importance of performing RT simulations that exploit the full dynamic range inherent to the underlying hydrodynamical simulation.

This chapter is organised as follows. We describe our SPH simulation method and explain our approach to accomplish the transport of ionising radiation in Sec. 6.2. We present our results in Sec. 6.3, where we employ various statistics to discuss the differences between the spatially adaptive RT simulations performed on density fields obtained directly from the SPH simulation and the RT simulations that are performed on density fields obtained by interpolating the densities from the SPH simulation to a uniform grid. We summarise our conclusions and discuss the limitations of the present work in Sec. 6.4. Throughout we assume a flat ΛCDM universe and employ the set of cosmological parameters $\Omega_{\rm m} = 0.258$, $\Omega_{\rm b} = 0.0441$, $\Omega_\Lambda = 0.742$, $\sigma_8 = 0.796$, $n_{\rm s} = 0.963$, $h = 0.719$, in agreement with the WMAP 5-year observations (Komatsu et al. 2008).

6.2 SIMULATIONS

In this section we describe the RT simulations that we employ for the present study. The RT is carried out by post-processing static SPH density fields obtained from a cosmological hydrodynamical simulation. The hydrodynamical simulation is performed using a modified version of the SPH code GADGET-2 (Springel 2005). We describe it in Sec. 6.2.1. The RT simulations make use of the spatially adaptive RT scheme TRAPHIC (Chapter 4) and are described in Sec. 6.2.2.

We perform the RT both on top of the density fields obtained directly from the spatially adaptive hydrodynamical simulation and on top of density fields generated by mapping the SPH particles from the hydrodynamical simulation to a uniform grid. We briefly illustrate the difference in dynamic range exhibited by the two types of density fields used in the RT simulations in Sec. 6.2.3.

6.2.1 Cosmological N-body/SPH simulations

We use P-GADGET3-BG, a modified version of the SPH code GADGET-2 (Springel 2005). The initial dark matter (DM) and SPH particle positions and velocities are obtained from glass-like initial conditions using CMBFAST (version 4.1; Seljak & Zaldarriaga 1996) and employing the Zeldovich approximation to evolve the particles down to the initial simulation redshift $z = 127$.

The gas is of primordial composition, with a hydrogen mass fraction $X = 0.752$ and a helium mass fraction $Y = 1 - X$. It is allowed to cool by collisional ionisation and excitation, emission of free-free and recombination radiation and Compton cooling off the cosmic microwave background. Molecular hydrogen is kept photo-dissociated at all times by the inclusion of a soft UV background. The implementation of the cooling is described in Wiersma, Schaye, & Smith (2009).

We employ the star formation recipe of Schaye & Dalla Vecchia (2008) to convert SPH particles into star particles. Briefly, gas with densities exceeding the critical density for the onset of the thermo-gravitational instability (hydrogen number densities $n_{\rm H} = 10^{-2} - 10^{-1}$ cm^{-3}) is expected to be multiphase and star-forming (Schaye 2004). We therefore impose an effective equation of state (EoS) with pressure $P \propto \rho^{\gamma_{\rm eff}}$ for densities $n_{\rm H} > n_{\rm H}^*$, where $n_{\rm H}^* \equiv 10^{-1}$ cm^{-3}, normalised to $P/k = 10^3$ cm^{-3} K at the critical density $n_{\rm H}^*$. We use $\gamma_{\rm eff} = 4/3$ for which both the Jeans mass and the ratio of the Jeans length and the SPH kernel are independent of the density, thus preventing spurious fragmentation due to a lack of numerical resolution. Gas on the effective EoS is allowed to form stars using a pressure-dependent rate that reproduces the observed Kennicutt-Schmidt law (Kennicutt 1998), renormalised by a factor of $1/1.65$ to account for the fact that it assumes a Salpeter IMF whereas we are using a Chabrier IMF (Chapter 2).

We perform a single simulation, using $N_{\rm DM} = 64^3$ equal-mass DM particles and $N_{\rm SPH} = 64^3$ equal-mass SPH particles in a box of comoving size $L_{\rm box} = 1.5625\ h^{-1}$ Mpc. The number of SPH particles decreases during the simulation as SPH particles are transformed into star particles. The gravitational forces are softened over a length of $1/25$ of the mean DM interparticle distance, and we employ $N_{\rm ngb} = 48$ SPH neighbours for computing the SPH properties of the SPH particles. Our choice for the particle number and the box size results in DM and SPH particle masses of $8.3 \times 10^5\ h^{-1}$ M$_\odot$ and $1.8 \times 10^5\ h^{-1}$ M$_\odot$, respectively, and hence a relatively high mass resolution: atomic coolers, i.e. halos with virial temperature $T_{\rm vir} \sim 10^4$ K, corresponding to masses $M_{\rm DM} \sim 10^8\ h^{-1}$ M$_\odot$, which in the absence of molecular hydrogen and metal line cooling constitute the first sites of star formation (for a review see, e.g., Barkana & Loeb 2001), are resolved with more than 100 particles. Note that our choice for box size and mass resolution implies a spatial resolution that is high compared with that encountered in typical cosmological RT simulations.

The simulation box employed in the present study is, however, comparatively small. Representative models of the Universe during reionisation require simulation boxes of at least 30 h^{-1} Mpc (Barkana & Loeb 2004; Iliev et al. 2006). Simulating the field of view of future epoch-of-reionisation observatories (see Sec. 6.3.3) will require even larger simulation boxes (e.g., Mellema et al. 2006). Our choice for the simulation box is a direct consequence of our choice for the particle number, which we wish to keep low to allow for a quick exploration of the parameter space in this *pilot* study. Simulations that employ the same particle number but use a significantly larger box would lack the resolution to form (a sufficient number of) star particles required for the RT simulations performed here. We note that for the present choice of box size and particle number, the number of star particles formed until redshift 6.0 (8.8) is 815 (49), which is still very low.

Simulation snapshots are generated at 100 equally spaced redshifts between $z = 20$ and $z = 6$. The SPH densities from these snapshots are processed to generate gas density fields on a uniform grid with $N_{\rm g} = 64^3$ points using mass-conserving SPH interpolation (e.g., Alvarez, Bromm, & Shapiro 2006). We will perform RT simulations on top of both the original, spatially adaptive and the uniformly gridded SPH density fields. Note that, as a result of the relatively small simulation box, the physical (proper) size of individual grid cells is only $\approx 2\,h^{-1}$ kpc $((1+z)/10)^{-1}$ and hence small compared to the sizes of grid cells employed in typical cosmological RT simulations. The spatial resolution employed in the RT simulations that are performed on the uniformly gridded density fields is therefore still comparatively high, which will likely lead us to strongly underestimate the importance of performing spatially adaptive RT simulations to study reionisation.

6.2.2 Radiative transfer

The RT simulations employ the RT scheme TRAPHIC presented in Chapter 4. Before describing the set-ups of the simulations, we briefly recall the main characteristics of TRAPHIC and explain the parameters that control its performance.

TRAPHIC is a RT scheme for use with SPH simulations that solves the RT equation in a spatially adaptive manner by tracing photons from radiation sources directly on the unstructured grid comprised by the SPH particles. Hence, it is ideally suited for the present study which aims to investigate the difference between RT simulations of reionisation that exploit the full dynamic range of the underlying cosmological hydrodynamical simulation and those that do not. Photons are traced by propagating photon packets from particles to their $\tilde{N}_{\rm ngb}$ neighbours inside cones. The introduction of cones is necessary to accomplish the transport of radiation in a directed manner on the generally highly irregular distribution of the SPH particles. The opening angle Ω of the cones determines the formal angular resolution of the RT. It is conveniently expressed in terms of a cone number, $N_{\rm c} \equiv 4\pi/\Omega$.

The photon transport proceeds in two parts. First, source particles emit photon packets to their $\tilde{N}_{\rm ngb}$ neighbouring SPH particles by means of a set of $N_{\rm c}$ tessellating emission cones. The number of neighbours $\tilde{N}_{\rm ngb}$ is a parameter that is usually matched to the number of neighbours $N_{\rm ngb}$, residing in a sphere of radius h (the SPH *kernel*), that is used in the computation of the particle's SPH properties, $\tilde{N}_{\rm ngb} \lesssim N_{\rm ngb}$. The use of a fixed number of neighbours $\tilde{N}_{\rm ngb}$ renders the RT spatially adaptive, and the choice $\tilde{N}_{\rm ngb} \lesssim N_{\rm ngb}$ exploits the full dynamic range inherent to the underlying hydrodynamical simulation. Second, the photon packets received by the neighbouring SPH particles are propagated further downstream. They are confined to the emission cones into which they were originally emitted through the use of transmission cones of solid angle $4\pi/N_{\rm c}$. The transport is performed using RT time steps of size $\Delta t_{\rm r}$. After each such time step, the properties of the SPH particles are updated according to their interactions (absorptions, scatterings) with the photon packets. We refer the reader to Chapter 4 for a more detailed description of TRAPHIC.

The RT simulations are performed by post-processing the (static) density fields obtained from the cosmological SPH simulation described above. We mention that TRAPHIC can already be employed for RT simulations performed in step[6] with the hydrodynamical evolution of the gas in simulations with P-GADGET3-BG. We opted for the post-processing approach because it enables a more direct comparison between the results obtained in RT simulations performed on top of the original SPH density fields and those performed on top of the associated uniformly gridded density fields. The RT simulations start at redshift $z = 8.94$ (with the formation of the first stars), using the density fields at redshifts $z_i = 8.94 - 0.14i$, where $i = 1, ..20$. For each density field, the RT simulations are performed over the redshift interval $\Delta z = 0.14$, corresponding to the time between two consecutive snapshots.

We assume that all star particles that were formed up to the redshift of the current density field are ionising sources, each of which emits 10^{51} ionising photons per second. The ionising luminosities were roughly chosen such as to achieve reionisation in the simulations that are performed on top of the SPH density fields from the hydrodynamical simulation by the final simulation redshift $z = 6$. We verified that with the employed luminosities, the reionisation histories in our simulations are in (1-sigma) agreement with current constraints on the electron scattering optical depth (Komatsu et al. 2008). We have adopted this simplified approach to facilitate the comparison between the different simulations we perform. We note that we have already coupled TRAPHIC to the population synthesis models of Bruzual & Charlot (2003) that allow the determination of ionising luminosities as a function of the stellar mass, the age and the metalicity of star particles. We will employ this feature in future work in order to consider more realistic source populations.

We refer to the RT simulation that is performed directly on top of the snapshots from the hydrodynamical simulation as *rt-sph*. This simulation fully exploits the available dynamic range of the underlying hydrodynamical simulation. The simulation that is performed using SPH particle positions obtained by Monte-Carlo sampling the associated uniformly gridded density fields is referred to as *rt-grid*. The Monte Carlo sampling is performed by replacing every grid cell i by $N^i_{\rm SPH} = M_i/m$ SPH particles (randomly distributed within the volume of the grid cell) of equal mass, where M_i is the mass of the cell and m is the SPH particle mass. If $N^i_{\rm SPH}$ is not an integer, we draw a random number from a uniform distribution on the interval (0,1) and place an additional particle if this number is smaller than the difference between $N^i_{\rm SPH}$ and the nearest lower integer. We target a total of $N_{\rm SPH} = 64^3$ SPH particles (i.e. the same number of particles as for the original SPH simulation). Since the Monte Carlo sampling only results in the approximate equality $\sum_i N^i_{\rm SPH} \approx N_{\rm SPH}$, we adjust the particle masses a posteriori to conserve mass, i.e. $m \to m \times N_{\rm SPH}/\sum_i N^i_{\rm SPH}$. After the particles have been placed, we calculate their densities using the SPH formalism of P-GADGET3-BG, with $N_{\rm ngb} = 48$.

In this work we solve the time-independent RT equation. We will contrast our results to results obtained from solving the time-dependent RT equation in future work. We use a fixed RT time step $\Delta t_{\rm r} = 10^{-1}$ Myr, during which photons are propagated over a single inter-particle

---

[6] The current implementation still ignores, however, the radiation-hydrodynamical feedback. The radiation-hydrodynamical coupling of TRAPHIC will be presented in a future work.

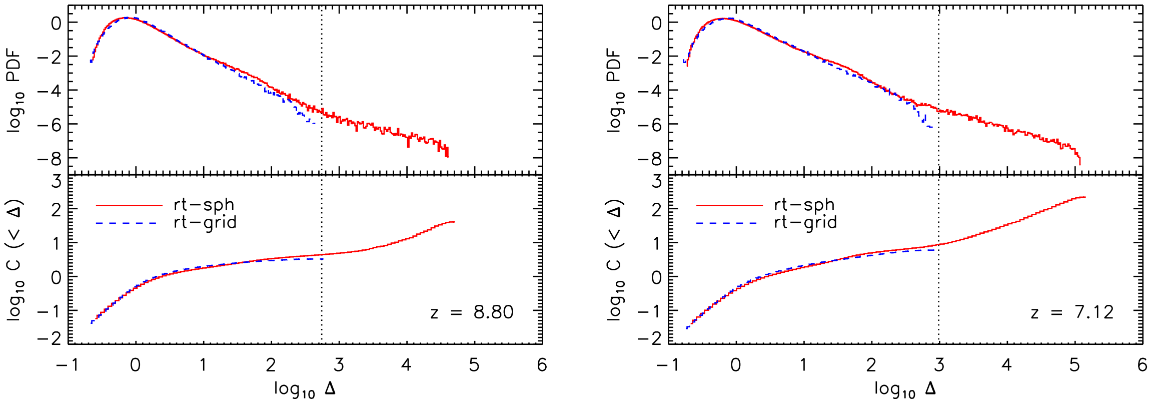

Figure 6.1: *Top panels:* volume-weighted PDF of the gas overdensity Δ per unit $\log_{10}\Delta$ for simulations *rt-sph* (solid red histogram) and *rt-grid* (blue dashed histogram) at redshifts $z = 8.80$ (left) and $z = 7.12$ (right). *Bottom panels:* volume-weighted clumping factor $C(< \Delta)$ of gas with overdensity $< \Delta$ corresponding to the PDFs shown in the top panel. The vertical dotted lines indicate the (redshift-dependent) overdensity corresponding to the (physical) star formation threshold hydrogen density $n_{\rm H}^* \equiv 10^{-1}$ cm^{-3} (Sec. 6.2.1). Note that the dynamic range exhibited by the spatially adaptive *rt-sph* simulation is more than two orders of magnitude larger than the dynamic range exhibited by the *rt-grid* simulation.

distance only, as explained in Sec. 5.3.3 of Chapter 5. We demonstrate in App. 6.A that the RT time step is sufficiently small to obtain converged results. We furthermore use an angular resolution of $N_{\rm c} = 32$, which we show to be sufficiently high to obtain converged results in App. 6.A, and set $\tilde{N}_{\rm ngb} = 32$. We do not employ the density field resampling technique introduced in Chapter 5.

In performing the RT we assume that the gas consists purely of hydrogen, i.e. we set $X = 1$, despite that fact that the SPH simulation employed primordial abundances. This is because we have not yet implemented helium in TRAPHIC. Photons are transported using a single frequency bin in the grey approximation (Sec. 5.3.5 in Chapter 5). We employ a grey photoionisation cross-section $\sigma_{\rm HI} = 6.3 \times 10^{-18}$ cm^2, corresponding to a black-body spectrum of temperature $T = 10^5$ K for the ionising sources (Chapter 7). We assume a constant temperature of $T = 10^4$ K for the ionised gas and compute recombinations in the case B approximation, using a recombination coefficient $\alpha_{\rm B} = 2.59 \times 10^{-13}$ cm^3 s^{-1} (appropriate for the assumed gas temperature). The ionised fraction of the SPH particles is initially set to zero and is appropriately transferred between the density fields during each simulation. The boundaries of the simulation box are transmissive, i.e. photons leaving the box are lost from the computational domain.

6.2.3 Density field comparison

Before we present our results, we briefly illustrate the difference in the dynamic ranges between the *rt-sph* and the *rt-grid* simulation (Fig. 6.1).

The top panels in Fig. 6.1 show the redshift $z = 8.80$ (left) and the redshift $z = 7.12$ (right) volume-weighted probability density function (PDF) of the gas overdensity $\Delta \equiv \rho/\langle\rho\rangle$, where ρ is the SPH particle gas density and $\langle\rho\rangle$ is the cosmic average gas density. The minimum particle overdensity present is similar in both simulations, but the *rt-sph* simulation contains particles with overdensities more than two orders of magnitude larger than the largest particle overdensities in the *rt-grid* simulation.

The bottom panels of Fig. 6.1 show the volume-weighted gas clumping factor

$$C(<\Delta) \equiv \langle\rho^2\rangle_{<\Delta}/\langle\rho\rangle^2, \tag{6.1}$$

where the brackets $\langle\rangle_{<\Delta}$ indicate an average over all gas particles with overdensities $<\Delta$. The (overdensity-dependent) clumping factor $C(<\Delta)$ is a convenient measure for the average recombination rate of gas with overdensities $<\Delta$ (Miralda-Escudé, Haehnelt, & Rees 2000). We computed it by performing a volume-weighted summation over all SPH particles with overdensities $<\Delta$ (cp. Chapter 2),

$$C(<\Delta) = \frac{\sum_{\Delta_i<\Delta} V_i \Delta_i^2}{\sum_{\Delta_i<\Delta} V_i}, \tag{6.2}$$

where $V_i \equiv h_i^3$ is the characteristic volume of SPH particle i, h_i is the radius of its SPH smoothing kernel and Δ_i is its gas overdensity.

For overdensities $\log_{10}\Delta \lesssim 2$ the clumping factors obtained from the two simulations largely agree. For overdensities $\log_{10}\Delta \gtrsim 2$ the clumping factor obtained from the simulation *rt-sph* is, however, significantly larger than that obtained from the simulation *rt-grid*. Averaged over all SPH particles, the clumping factor obtained from *rt-sph* is more than an order of magnitude larger than the clumping factor obtained from *rt-grid*. We may therefore expect that recombinations are more important in the *rt-sph* than in the *rt-grid* simulation, in particular close to the ionising sources, i.e. for densities $n_{\rm H} \gtrsim n_{\rm H}^*$, where $n_{\rm H}^* \equiv 10^{-1}$ cm^{-3} is the star formation threshold density (Sec. 6.2.1). We have indicated the star formation threshold density with the vertical dotted line in Fig. 6.1.

6.3 RESULTS

In this sections we present and discuss our results. We investigate the differences between the *rt-sph* simulation (which exploits the full dynamic range of the underlying spatially adaptive hydrodynamical simulation) and the *rt-grid* simulation (which employs only a fraction of the dynamic range of the hydrodynamical simulation by sampling the densities on a uniform grid) by comparing several key quantities.

We start by explaining differences in the evolution of the mean ionised fraction (Sec. 6.3.1). We then discuss differences in the morphologies of the ionised regions and in the topologies of reionisation as traced by the spatial distribution of the ionised gas and correlations between the ionised fraction and the gas density (Sec. 6.3.2). The product of neutral fraction and gas density determines the 21 cm brightness temperature of the hydrogen gas, one of the most important potential observables of reionisation. We will discuss differences in the statistical properties of this observable between the *rt-sph* and the *rt-grid* simulation by computing the power spectrum of the 21 cm brightness temperature fluctuations (Sec. 6.3.3).

In each of our comparisons we discuss similarities and differences between the results obtained in the *rt-sph* and the *rt-grid* simulation at fixed times or, equivalently, at fixed redshifts. In addition, we compare the results from the two simulations at fixed (volume-weighted) mean ionised fractions. In both simulations, the mean ionised fraction is a monotonically increasing function of time (Fig. 6.2). It therefore provides another unambiguous parametrisation of the

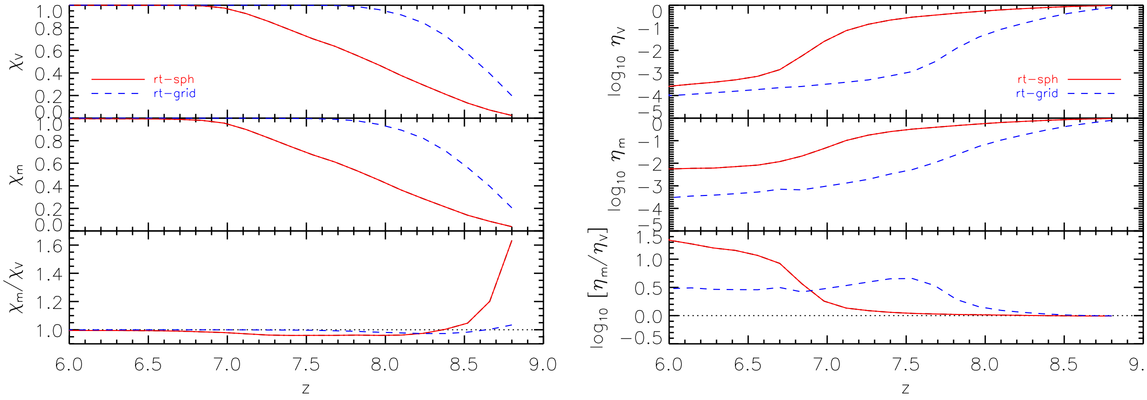

Figure 6.2: *Left-hand panel:* Evolution of the mean ionised fraction in the simulations *rt-sph* (red solid curves) and *rt-grid* (blue dashed curves). The panels show the volume-weighted (top) and mass-weighted (middle) means and their ratio (bottom). The RT simulations start at redshift $z = 8.94$ and the first data is saved at $z = 8.80$. At this point, the volume-weighted mean ionised fraction in *rt-grid* is already $\chi_V \approx 0.2$. In both simulations, reionisation starts inside-out ($\chi_m/\chi_V > 1$) and reverses to outside-in ($\chi_m/\chi_V < 1$). *Right-hand panel:* Same as left-hand panel, but for the mean neutral fraction to illustrate differences between *rt-sph* and *rt-grid* when $\chi_V \approx 1$.

reionisation history. We will point out that the two simulations should, however, really be compared at *both* fixed times *and* fixed ionised fractions. Although we leave such a comparison to future work, we will briefly explain how it could be accomplished.

6.3.1 Mean ionised fraction

Fig. 6.2 shows the evolution of the mean ionised (left) and neutral fraction (right) in the simulations *rt-sph* (red solid curves) and *rt-grid* (blue dashed curves). The individual panels show the volume-weighted means (top)

$$\chi_V \equiv \sum_i V_i \chi_i / \sum_i V_i \tag{6.3}$$

$$\eta_V \equiv \sum_i V_i \eta_i / \sum_i V_i, \tag{6.4}$$

the mass-weighted means (middle)

$$\chi_m \equiv \sum_i m_i \chi_i / \sum_i m_i \tag{6.5}$$

$$\eta_m \equiv \sum_i m_i \eta_i / \sum_i m_i \tag{6.6}$$

and their ratios (bottom). Here, $\chi_i \equiv n_{HII}/n_H$ is the ionised fraction of SPH particle i, $\eta_i \equiv n_{HI}/n_H$ is its neutral fraction, m_i is its mass and $V_i \equiv h_i^3$ is its characterstic volume.

At the end of the simulation, i.e. at redshift $z = 6$, the gas is highly ionised in both the *rt-sph* simulation and the *rt-grid* simulation, i.e. $\chi_m \approx \chi_V \approx 1$. The evolution of the mean ionised fractions from $z \approx 9$ to $z = 6$ in these two simulations is, however, very different. The transition from the initial, fully neutral to the final, highly ionised regime occurs much more rapidly in the *rt-grid* than in the *rt-sph* simulation. The reason for this difference in the evolutions of the mean ionised fraction is that the number of recombinations that need to be overcome to keep the gas ionised is much larger in the *rt-sph* simulation than in the *rt-grid* simulation, a result of the increased small-scale clumpiness for high-density ($\log_{10}\Delta \gtrsim 2$) gas (see Fig. 6.1).

The ratio $\chi_{\rm m}/\chi_{\rm V}$ characterises the distribution of the ionised gas. To see this, let us assume for the moment that gas particles can either be fully ionised, i.e. $\chi_i = 1$, or fully neutral, ie. $\chi_i = 0$. Then (e.g., Iliev et al. 2006)

$$\begin{aligned}\frac{\chi_{\rm m}}{\chi_{\rm V}} &\equiv \frac{\sum m_i\chi_i/\sum m_i}{\sum V_i\chi_i/\sum V_i} && (6.7)\\ &= \frac{\sum_{\rm ionised\ particles} m_i/\sum_{\rm all\ particles} m_i}{\sum_{\rm ionised\ particles} V_i/\sum_{\rm all\ particles} V_i} && (6.8)\\ &= \frac{1}{\langle\rho\rangle}\frac{M_{\rm ionised}}{V_{\rm ionised}}, && (6.9)\end{aligned}$$

and the ratio $\chi_{\rm m}/\chi_{\rm V}$ is thus equal[7] to the mean density of the ionised gas in units of the mean gas density $\langle\rho\rangle$. Consequently, if $\chi_{\rm m}/\chi_{\rm V} > 1$, then overdense regions are preferentially ionised, and if $\chi_{\rm m}/\chi_{\rm V} < 1$, then underdense regions are preferentially ionised. The ratio $\chi_{\rm m}/\chi_{\rm V}$ is therefore commonly employed to characterise the topology of reionisation: if $\chi_{\rm m}/\chi_{\rm V} > 1$, then reionisation is said to proceed inside-out while it is said to proceed outside-in if $\chi_{\rm m}/\chi_{\rm V} < 1$.

In both the *rt-sph* simulation and the *rt-grid* simulation, $\chi_{\rm m}/\chi_{\rm V}$ decreases from $\chi_{\rm m}/\chi_{\rm V} > 1$ at early times to $\chi_{\rm m}/\chi_{\rm V} < 1$ at intermediate times and converges to $\chi_{\rm m}/\chi_{\rm V} \approx 1$ at late times. There are, however, clear difference in the evolution of $\chi_{\rm m}/\chi_{\rm V}$ predicted by the two simulations. The ratio of the mass-weighted to volume-weighted mean ionised fraction obtained from the *rt-sph* simulation is initially substantially larger than the one obtained from the *rt-grid* simulation. Moreover, the transition from $\chi_{\rm m}/\chi_{\rm V} > 1$ to $\chi_{\rm m}/\chi_{\rm V} < 1$ occurs significantly later in the *rt-sph* simulation than in the *rt-grid* simulation. Finally, at low redshifts ($z \lesssim 8.2$) the values for $\chi_{\rm m}/\chi_{\rm V}$ obtained from the *rt-sph* simulation remain systematically below the values for $\chi_{\rm m}/\chi_{\rm V}$ obtained from the *rt-grid* simulation.

We have compared the ratio $\chi_{\rm m}/\chi_{\rm V}$ obtained from the *rt-sph* simulation with the one obtained from the *rt-grid* simulation as a function of redshift. It is, however, also interesting to perform this comparison as a function of the mean ionised fraction. Indeed, a simple delay in the ionisation history due to an increased number of recombinations may in principle be compensated by an increase in the luminosities of the ionising sources, which are, both from a theoretical and from an observational point of view, still poorly constrained. Moreover, the hydrodynamical simulations employed here still lack the resolution (and large-scale dynamics) and physics to properly compute the fraction of ionising photons that are not used up by recombinations within the star-forming regions and hence manage to escape and ionise the intergalactic gas. Uncertainties in this *escape fraction* (e.g., Inoue, Iwata, & Deharveng 2006; Razoumov & Sommer-Larsen 2006; Gnedin, Kravtsov, & Chen 2008) are degenerate with the uncertainties in the source luminosities and hence may also be employed to compensate for a delay in the reionisation history.

In the left-hand panel of Fig. 6.3 we therefore compare the ratio $\chi_{\rm m}/\chi_{\rm V}$ obtained from the *rt-sph* simulation with the one obtained from the *rt-grid* simulation as a function of the volume-

---

[7] This equality is only approximate, because the SPH particle volumes do not tessellate space, i.e. $\sum_i V_i \neq L_{\rm box}^3$.

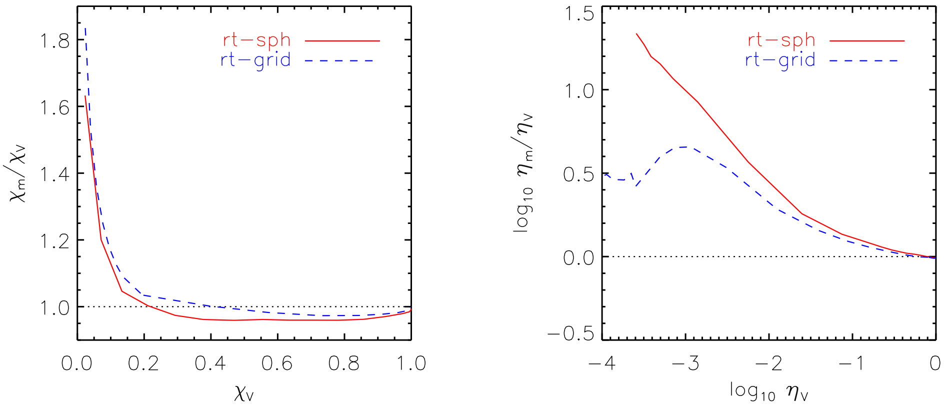

Figure 6.3: *Left-hand panel:* The ratio of mass-weighted to volume-weighted mean ionised fraction obtained from the *rt-sph* simulation (red solid curve) and the *rt-grid* simulation (blue dashed curve) as a function of the volume-weighted mean ionised fraction. The *rt-sph* simulation predicts a consistently lower ratio and hence a more marked outside-in reionisation topology than the *rt-grid* simulation. *Right-hand panel:* Same as left-hand panel, but for the mean neutral fractions to illustrate differences between *rt-sph* and *rt-grid* when $\chi_V \approx 1$.

weighted mean ionised fraction[8]. The *rt-sph* simulation predicts a reionisation history that is significantly more outside-in than the one predicted by the *rt-grid* simulation. This is likely due to the increased role of recombinations (and partly self-shielding / shadowing, see the next section) that keep the high-density gas in that simulation at larger neutral fractions. To illustrate the differences between the simulations for volume-weighted mean ionised fractions $\chi_V \approx 1$, we also show the ratio η_m/η_V of the mass-weighted mean neutral fraction $\eta_m = 1 - \chi_m$ and the volume-weighted mean neutral fraction $\eta_V = 1 - \chi_V$ as a function of η_V (right-hand panel of Fig. 6.3).

We caution the reader of the qualitative nature of our conclusions and that we only aim at highlighting differences between (the reionisation topologies obtained from) RT simulations that exploit the full dynamic range of the underlying hydrodynamical simulation (*rt-sph*) and those that do not (*rt-grid*). The simulations presented here use too small a box and too simplistic prescriptions for the ionising sources to be employed for predictions of the topology of reionisation. We will come back to this and other short-comings inherent to the present approach in our discussion in Sec. 6.4.

We finally note that reionisation simulations should ideally be compared at both fixed ionised fraction *and* fixed redshift (e.g., Lidz et al. 2008). Such a comparison would be particular preferable over comparisons performed at fixed redshift *or* fixed ionised fraction when studying the distribution of the ionised mass with respect to the total mass (Sec. 6.3.2) or when computing quantities that depend on both density and neutral fraction (Sec. 6.3.3). The comparison could be accomplished by tuning the luminosities of the ionising sources such as to yield a certain ionised fraction at a given redshift. Alternatively, one could perform RT simu-

---

[8] The volume-weighted mean ionised fraction at the first output of the *rt-grid* simulation is $\chi_V \approx 0.2$ (Fig. 6.2). To extend the ratio of mass-weighted to volume-weighted mean ionised fraction shown in the left-hand panel of Fig. 6.3 down to lower mean volume-weighted ionised fractions, we have resimulated part of the *rt-grid* simulation with more frequent outputs. We have, however, not included the results from this resimulation in Fig. 6.2.

lations on top of a single static snapshot at fixed redshift. Such simulations would clearly not be appropriate for studying the reionisation process as a whole, but they would facilitate the exposition of differences between corresponding RT simulations.

6.3.2 The morphology and the topology of ionised regions

In this section we discuss the morphology and the topology of the ionised regions predicted by the simulations *rt-sph* and *rt-grid*. We describe how the shapes of ionised regions and the spatial distribution of the ionised hydrogen mass evolve with time and we also point out differences in the evolution obtained from the two simulations. We present our results both as a function of redshift and as a function of mean volume-weighted ionised fraction.

Slices through the simulation box of the *rt-sph* and the *rt-grid* simulations are shown in the panels of the left-hand (*rt-sph*) and middle (*rt-grid*) columns of Figs. 6.4 and 6.5. While the panels in Fig. 6.4 show neutral fraction contours (and densities) at fixed redshift ($z = 8.80$, 8.38, 7.96, 7.54, 7.12 from top to bottom), the panels in Fig. 6.5 show neutral fraction contours (and densities) at fixed volume-weighted mean ionised fraction ($\chi_{\rm V} = 0.2$, 0.4, 0.6, 0.8, 0.95 from top to bottom[9]). The slices were generated by mapping the SPH particles densities and neutral fractions to a uniform grid with $\tilde{N}_{\rm g} = 128$ points per dimension using mass-conserving SPH interpolation. The contours show neutral fractions of $\eta = 0.5$ (blue), 0.05 (red) and 0.005 (green). When speaking of the morphology of ionised regions, we refer to the shape of the $\eta = 0.5$ contours. The grey-scale background image shows the gas overdensity Δ.

In both the *rt-sph* and the *rt-grid* simulation the first ionised regions appear around the densest structures, which correspond to the most massive halos hosting the first stellar sources of ionising radiation. The ionised regions quickly grow and combine to form a single ionised region that pervades the simulation box. The rapid formation of a single large ionised bubble is mostly a consequence of the relatively few ionising sources the simulations contain (Sec. 6.2.1). Inside the ionised bubble, there are regions where the gas is still substantially neutral. These are regions of very high density, where recombinations (partially) offset the ionisations due to the stellar radiation. In the densest regions, one may also expect to find the gas (partially) neutral because it is self-shielded (see the discussion below).

At fixed redshift (Fig. 6.4), the ionised regions in the *rt-grid* simulation are always larger than the ionised regions in the *rt-sph* simulation, which is simply a reflection of the different evolution of the mean ionised fraction in these simulations (Fig. 6.2). Likewise, when compared at fixed redshift, the simulations predict different topologies for the ionised gas: the *rt-sph* simulation displays substantially more substructure in the neutral fraction than the *rt-grid* simulation. To remove the large dependence of the results on the mean ionisation history, we compare the *rt-sph* and *rt-grid* simulations at fixed mean ionised fraction (Fig. 6.5). This is justified by the fact that a simple delay in the reionisation history is degenerate with uncertainties in the ionising luminosities and other quantities (see our discussion in Sec. 6.3.1).

The comparison at fixed mean ionised fraction paints a rather different picture. Both simulation now predict very similar shapes for the ionised regions, a finding that is in agreement with expectations from previous work (e.g., McQuinn et al. 2007). In the present case this can be understood by noting that the properties of the density fields employed in the *rt-sph* and the *rt-grid* simulation differ mainly at high densities, which correspond to regions that occupy only a small volume. The *rt-sph* simulation still predicts, however, substantially more substructure

---

[9] The actual values of the volume-weighted mean ionised fraction may fluctuate around the quoted values (within $\lesssim 5\%$), because the data was saved only at a finite number of redshifts.

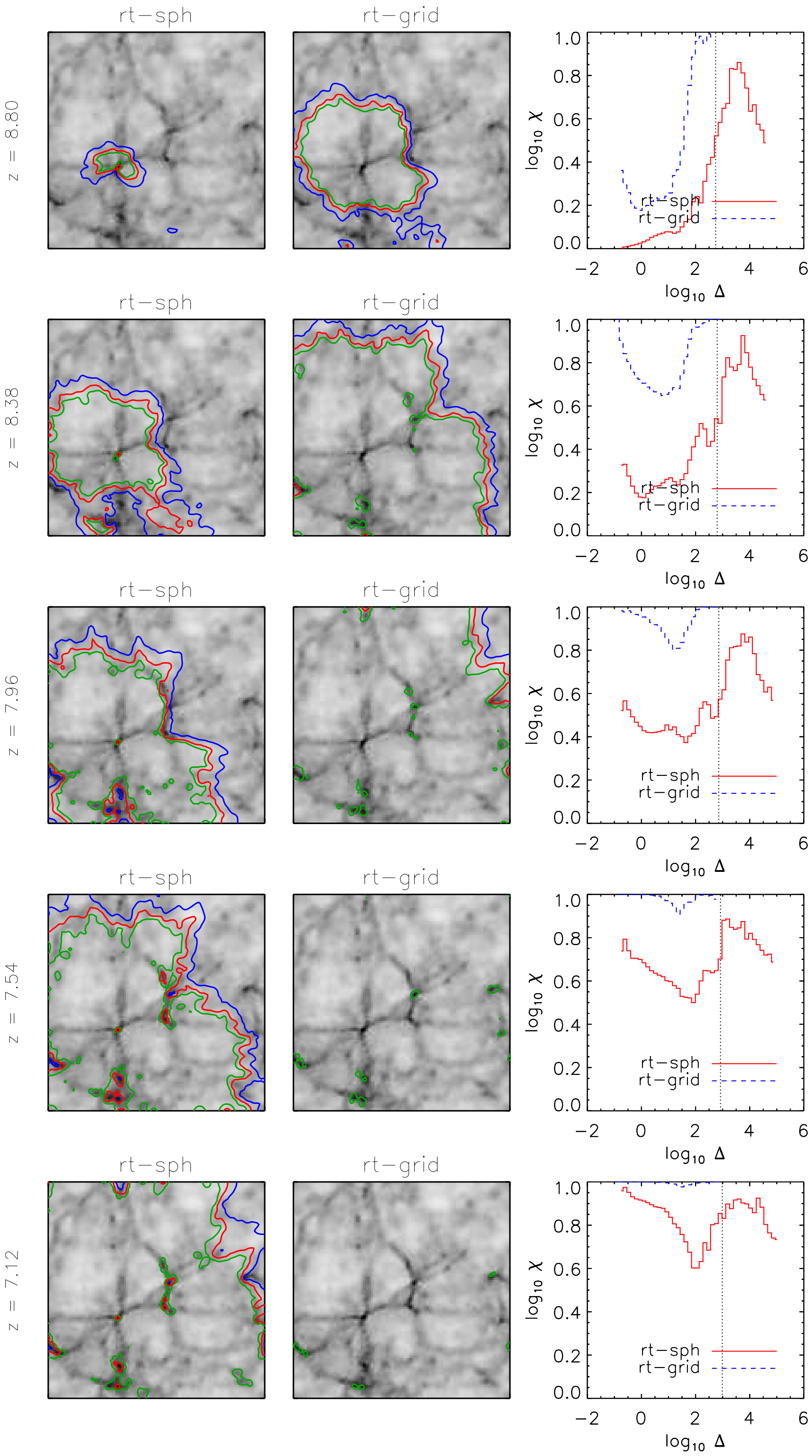

Figure 6.4: Morphology of ionised regions and topology of reionisation: evolution with redshift z. In each column, panels correspond to $z = 8.80, 8.38, 7.96, 7.54$, and 7.12 (from top to bottom). *Left-hand and middle column:* Slices through the centre of the *rt-sph* (left-hand column) and the *rt-grid* (middle column) simulation, as indicated in the panel titles. Contours show neutral fractions of $\eta = 0.5$ (blue), 0.05 (red) and 0.005 (green). *Right-hand column:* average (in logarithmic overdensity bins) ionised fraction for both the *rt-sph* (solid red histogram) and the *rt-grid* (dashed blue histogram) simulation. The vertical dotted lines indicate the (redshift-dependent) overdensity that corresponds to the (physical) star formation threshold hydrogen density $n_{\mathrm{H}}^{*} \equiv 10^{-1}\ \mathrm{cm}^{-3}$ (Sec. 6.2.1). See text for a discussion.

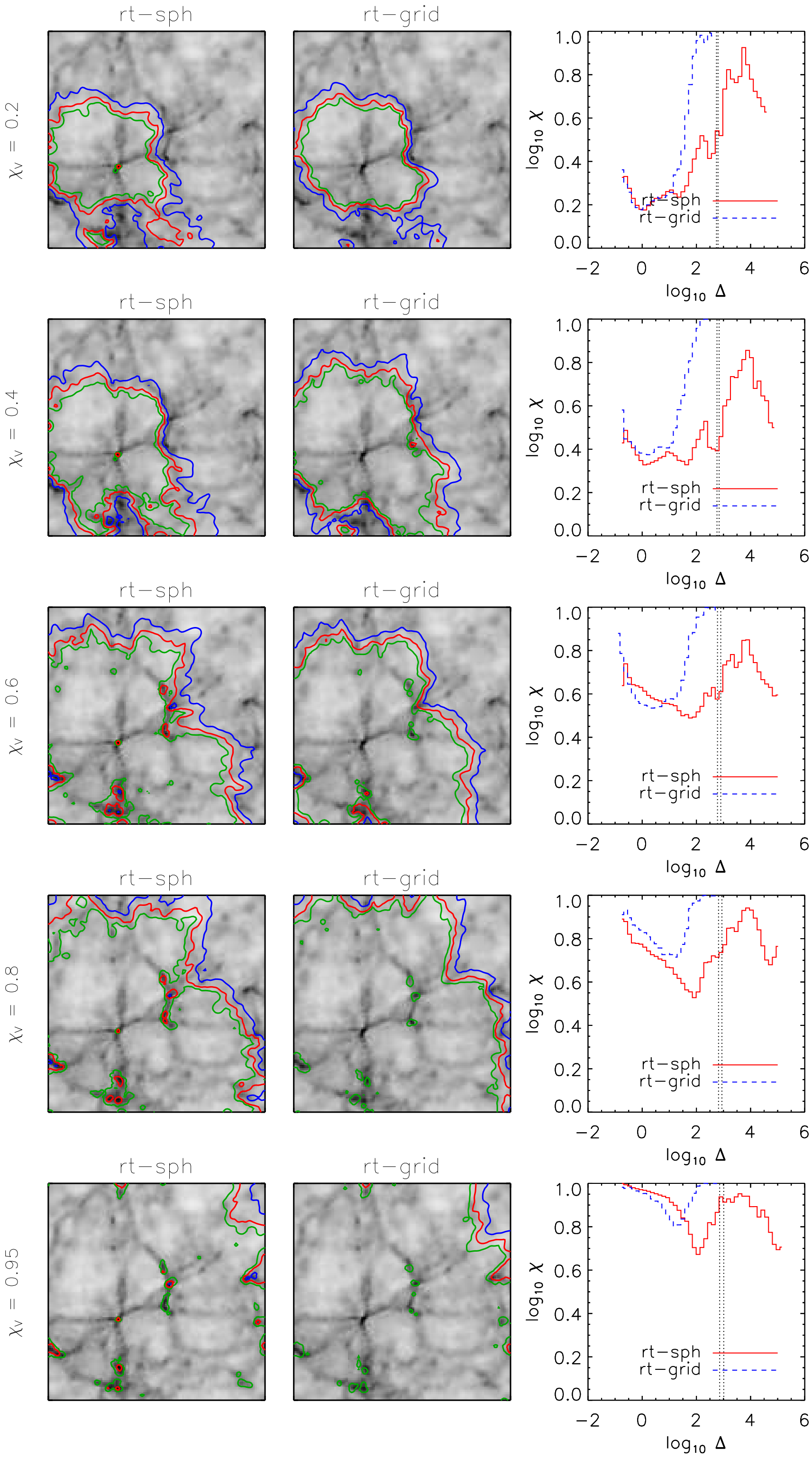

Figure 6.5: Morphology of ionised region and topology of reionisation: evolution with the volume-weighted mean ionised fraction $\chi_{\rm V}$. In each column, panels correspond to $\chi_{\rm V} = 0.2$, 0.4, 0.6, 0.8 and 0.95 (from top to bottom). The left-most (right-most) vertical dotted lines indicate the (redshift-dependent) overdensity that corresponds to the (physical) star formation threshold hydrogen density $n_{\rm H}^{*} \equiv 10^{-1}\ {\rm cm}^{-3}$ (Sec. 6.2.1) in the simulation *rt-grid* (*rt-sph*). Otherwise, the figure is identical to Fig. 6.4.

in the distribution of the ionised mass than the *rt-grid* simulation. It is clear that the difference in substructure is due to the difference in the dynamic range. Its interpretation is, however, impeded by the fact that the same mean ionised fraction corresponds to different redshifts in the two simulations. Some of the differences may therefore just be due to difference in the gravitational growth of structure, as discussed in the previous section.

We now compare the reionisation topologies predicted by the simulations *rt-sph* and *rt-grid* in a more quantitative manner. The panels in the right-hand columns of Figs. 6.4 and 6.5 show the mean ionised fraction in logarithmic bins of overdensity, both for the *rt-sph* simulation (red solid histogram) and the *rt-grid* simulation (blue dashed histogram). It is immediately apparent that in both simulations the ionised fraction shows a strong dependence on overdensity.

Let us first discuss the dependence of the ionised fraction on overdensity and its evolution for the *rt-grid* simulation. The first stars form in the regions of the highest densities. These regions are therefore expected to become ionised first. Indeed, gas at overdensities $\log_{10}\Delta \sim 2$, which correspond to the largest overdensities present in the *rt-grid* simulation, is almost fully ionised, even at a volume-weighted mean ionised fraction as low as $\chi_{\rm V} = 0.2$. The gas is also highly ionised in the most underdense regions, characterised by $\log_{10}\Delta \approx -1$.

For low volume-weighted mean ionised fractions, the particle ionised fractions at these low overdensities are on average somewhat smaller than those at overdensities $\log_{10}\Delta \sim 2$, because the ionised regions do not yet encompass a large fraction of the total volume of the underdense regions in the simulation. Instead, the ionisation fronts are still close to the dense regions that host the ionising sources. The ionised fractions at overdensities $\log_{10}\Delta \approx -1$ only become, on average, comparable to those at overdensities $\log_{10}\Delta \approx 2$ when the volume-weighted mean ionised fraction reaches $\chi_{\rm V} \gtrsim 0.6$. There is a distinct depression in the ionised fraction at overdensities $0 \lesssim \log_{10}\Delta \lesssim 2$. Note that this depression remains visible even at redshift $z = 7.12$, i.e. long after reaching a volume-weighted mean ionised fraction of $\chi_{\rm V} \approx 1$.

At fixed volume-weighted mean ionised fraction $\chi_{\rm V}$ (Fig. 6.5) and for overdensities $\log_{10}\Delta \lesssim 1$ the ionised fractions in the *rt-sph* simulations are on average similar to those in the *rt-grid* simulation. The distinct depression in the ionised fraction at overdensities $0 \lesssim \log_{10}\Delta \lesssim 2$ present in simulation *rt-grid* is also visible here, and extends to somewhat larger overdensities. Due to the larger dynamic range, recombinations can efficiently counteract photo-ionisations closer to the ionising sources (and hence out to denser regions) than in the *rt-grid* simulation.

Overdensities $\log_{10}\Delta > 3$ are only present in the *rt-sph* simulation. The gas in these regions shows a complex dependence of the ionised fraction on the overdensity. For overdensities $3 \lesssim \log_{10}\Delta \lesssim 4$, the ionised fraction generally increases with overdensity. This is probably because regions of larger overdensity will generally be located closer to ionising sources and hence experience a larger photo-ionisation rate. This general trend is, however, interrupted by several reversals. For overdensities $\log_{10}\Delta > 4$, i.e. for the largest overdensities in the simulation, the ionised fraction decreases with overdensity. Since regions of such high overdensities are almost certain to host (many) ionising sources, it is likely that this decrease is caused by the increased importance of recombinations at these overdensities.

Some of the high-density gas in the *rt-sph* simulation may also remain substantially neutral because it is (partly) self-shielded. The criterion for self-gravitating gas clouds to self-shield is (Schaye 2001) $n_{\rm H}^{\rm self} \gtrsim 10^{-1}~{\rm cm}^{-3}(\Gamma/10^{-12}~{\rm s}^{-1})$, where Γ is the hydrogen photo-ionisation rate. The critical hydrogen density $n_{\rm H}^{\rm self}$ above which self-shielding may become important corresponds to a critical gas overdensity $\Delta^{\rm self}$ of

$$\Delta^{\rm self} \gtrsim 10^3 \left(\frac{1+z}{7}\right)^{-3} \left(\frac{\Gamma}{10^{-12}~{\rm s}^{-1}}\right). \tag{6.10}$$

Unfortunately, we have not tracked the photo-ionisation rate in the current simulations. For now, lets simply assume that the photo-ionisation rate is roughly of the order of the photo-ionisation rate found in simulations reported by other authors, $\Gamma \sim 10^{-12}$ s^{-1} (e.g., Mesinger & Dijkstra 2008; Choudhury, Haehnelt, & Regan 2009). This assumption may be justified by noting that the *rt-sph* simulation shows a reionisation history whose duration is similar to that found there. Eq. 6.10 then suggests that self-shielding may be partly responsible for the depression in the ionised fraction in the densest regions. We note that Eq. 6.10 also implies that self-shielding is unimportant in the *rt-grid* simulation, where the overdensities do not exceed values of $\log_{10}\Delta = 3$.

A similar study of the density-dependence of the ionised fraction and the effects of recombinations was presented in the semi-analytical work of Choudhury, Haehnelt, & Regan (2009). Our general conclusions about the importance of recombinations are in qualitative agreement with theirs. There are, however, also differences. Most notably, in their simulations photo-ionisations always manage to overcome the effect of recombinations in the densest regions corresponding to the most massive halos, keeping the gas highly ionised. Note, however, that Choudhury, Haehnelt, & Regan (2009) only considered gas overdensities up to $\log_{10}\Delta = 1$. We mention that Choudhury, Haehnelt, & Regan (2009) used simulation boxes of size 100 h^{-1} Mpc, much larger than the one used here, and that they employed different prescriptions for obtaining the gas densities and placing the ionising sources. We will repeat our analysis using larger simulation boxes and different source prescriptions to allow for a more honest comparison to Choudhury, Haehnelt, & Regan (2009) in future work. We hope to improve on their work as our simulations not only employ a more accurate description of the gas distribution at small scales but also account for the effects of shadowing and self-shielding that their semi-analytical approach necessarily ignored.

The dependence of the ionised fraction on density was also studied by Iliev et al. (2006), who performed RT simulations on top of very high-resolution DM simulations. Their simulations were performed using box sizes up to 100 h^{-1} Mpc with a DM particle mass of 2.5×10^{7} $\mathrm{M}_{\odot}$ and constitute some of the largest and most accurate RT reionisation simulations carried out to date. However, the densities of the DM simulation, after translating them into gas densities using the cosmic baryon fraction, were interpolated to a grid with only 203^{3} points for their default RT simulations, which corresponds to a relatively low spatial resolution of ≈ 0.5 h^{-1} Mpc. The corresponding low dynamic range may explain why Iliev et al. (2006) find a much less pronounced effect of inhomogeneous recombinations (and self-shielding) than found in Choudhury, Haehnelt, & Regan (2009) and in the present study.

In summary, in this section we studied the morphology of ionised regions and the topology of reionisation in the *rt-sph* and the *rt-grid* simulations and compared them with each other. In agreement with previous work, when compared at fixed volume-weighted mean ionised fraction we found similar morphologies of the ionised regions in both simulations, despite the large difference in the dynamic range they exhibit. There are, however, large differences in the ionisation state of high-density ($\log_{10}\Delta \gtrsim 1$) gas, even when compared at fixed ionised fraction. In the (spatially adaptive) *rt-sph* simulation, recombinations are much more likely to overcome the effect of photo-ionisations than in the *rt-grid* simulation.

We emphasise that the current study should only be considered as preliminary, due to our use of a comparatively small simulation box and simplified prescriptions for the ionising sources. We will present simulations using larger box sizes and different source prescriptions in future work.

6.3.3 Statistical analysis - 21 cm power spectrum

The redshifted 21 cm signal emitted by neutral hydrogen atoms provides a potential probe of the epoch of reionisation and several radio telescopes are currently being planned and constructed to detect it. Radio surveys targeting the 21 cm signal promise to open a previously unexplored observational window onto reionisation by providing a three-dimensional tomographic view of the intergalactic gas in the high-redshift Universe.

Direct imaging of neutral regions during reionisation will require observatories like SKA and FTTE (Tegmark & Zaldarriaga 2009) which are still being developed and which will probably only become operational in one or two decades. Statistical probes of the high-redshift Universe in 21 cm will, however, already be possible within the next few years with radio interferometers like LOFAR, MWA and 21CMA[10] whose construction is nearly complete. One of the most promising statistical probes is provided by the 21 cm power spectrum, which we will therefore briefly discuss.

The 21 cm signal is formed by the spin-flip transition of neutral hydrogen. It may be detected by measuring the differential 21 cm brightness temperature T_{21} with respect to the Cosmic Microwave Background (CMB), which is determined by the density $n_{\mathrm{HI}} = \eta n_{\mathrm{H}}$ of neutral hydrogen and its spin temperature T_{s}. It is given by (e.g., Furlanetto, Oh, & Briggs 2006)

$$T_{21} = \frac{T_{\mathrm{s}} - T_{\mathrm{CMB}}}{1+z}\left(1 - e^{-\tau}\right), \tag{6.11}$$

where $T_{\mathrm{CMB}} = 2.73\ \mathrm{K}(1+z)$ is the temperature of the CMB at redshift z (Fixsen et al. 1996), and τ is the 21 cm optical depth. In the Gunn-Peterson approximation (Gunn & Peterson 1965; see, e.g., Furlanetto, Oh, & Briggs 2006 for its application to the 21 cm transition),

$$\tau(z) = \frac{3 h_{\mathrm{p}} c^3 A_{21} n_{\mathrm{HI}}(z)}{32\pi k_{\mathrm{B}} T_{\mathrm{s}}(z) H(z) \nu_{21}^2}, \tag{6.12}$$

where $\nu_{21} = 1420.4$ MHz is the rest-frame frequency of the spin-flip transition (corresponding to a wavelength of 21.1 cm), $A_{21} = 2.84 \times 10^{-15}\ \mathrm{s}^{-1}$ is the Einstein coefficient for spontaneous emission, k_{B} is the Boltzmann constant, h_{p} is the Planck constant, c is the speed of light and $H(z)$ is the Hubble constant at redshift z. Assuming $\tau \ll 1$, which is correct for the redshifts of interest here except for some lines of sight through mini-halos (Mellema et al. 2006; Iliev et al. 2002), Eqs. 6.11 and 6.12 yield

$$T_{21} \approx 28\ \mathrm{mK}\ \eta\Delta\left(1 - \frac{T_{\mathrm{CMB}}}{T_{\mathrm{s}}}\right)\left(\frac{1+z}{10}\right)^{1/2}, \tag{6.13}$$

where we have furthermore assumed that the hydrogen number density in units of the cosmic mean hydrogen number density is given by the gas overdensity, i.e. we have assumed that the hydrogen abundance X is constant, and we have employed the high-redshift approximation of the Hubble constant $H(z) \approx H_0 \Omega_{\mathrm{m}}^{1/2} (1+z)^{3/2}$.

The spin temperature, which characterises the population of the energy levels that correspond to the 21 cm transition, is determined by the statistical equilibrium of collisional excitations and de-excitations by hydrogen atoms and electrons and radiative excitations and de-excitations by cosmic microwave background and Lyman$-\alpha$ photons (Field 1959). For many applications it is a good approximation to assume that the spin temperature is much larger than

---

[10] http://21cma.bao.ac.cn

the CMB temperature, $T_{\mathrm{s}} \gg T_{\mathrm{CMB}}$ (e.g., Ciardi & Salvaterra 2007). The brightness temperature then becomes independent of T_{s},

$$T_{21} \approx 28\ \mathrm{mK}\ \eta\Delta \left(\frac{1+z}{10}\right)^{1/2}. \tag{6.14}$$

The 21 cm power spectrum $P_{21}(\mathbf{k})$ at wave vector $\mathbf{k}$ is defined as (e.g., Furlanetto, Oh, & Briggs 2006)

$$P_{21}(\mathbf{k}) = \langle|\hat{T}_{21}(\mathbf{k})|^2\rangle, \tag{6.15}$$

where the angular brackets denote an ensemble average and

$$\begin{aligned} \hat{T}_{21}(\mathbf{k}) &= \int d\mathbf{r}\ e^{-i\mathbf{kr}} T_{21}(\mathbf{r}) && (6.16) \\ &\approx 28\ \mathrm{mK} \left(\frac{1+z}{10}\right)^{1/2} \int d\mathbf{r}\ e^{-i\mathbf{kr}} \eta(\mathbf{r})\Delta(\mathbf{r}) && (6.17) \end{aligned}$$

is the Fourier transform of the differential brightness temperature T_{21}.

For the numerical estimation of the power spectrum we follow the description in Press et al. 1992, to which we refer the reader for details. Briefly, we start by assigning the neutral hydrogen masses of the SPH particles to a uniform grid with $\tilde{N}_{\mathrm{g}} = 128$ points per dimension using mass-conserving SPH interpolation. From the gridded densities and neutral fractions we obtain the 21 cm brightness temperature using Eq. 6.14. We use the FFTW library[11] to obtain the Fourier transform $\hat{T}_{21}(\mathbf{k})$ at discrete values of the wave vector $\mathbf{k} \equiv (k_x, k_y, k_z) = (i, j, k) k_{\mathrm{Ny}}/\tilde{N}_{\mathrm{g}}$, where i, j, k are integers that range from $-\tilde{N}_{\mathrm{g}}$ to $\tilde{N}_{\mathrm{g}}$ and $k_{\mathrm{Ny}} = \pi\tilde{N}_{\mathrm{g}}/L_{\mathrm{box}}$ the Nyquist frequency, which corresponds to the largest wave vector that is sampled by the employed grid. We then compute the periodogram estimate of the 21 cm power spectrum $P_{21}(\mathbf{k}) = |\hat{T}_{21}(\mathbf{k})|^2$. Finally, we average $P_{21}(\mathbf{k})$ in spherical bins to obtain the one-dimensional power spectrum estimate $P_{21}(k)$.

Fig. 6.6 shows the evolution of the 21 cm power spectra obtained from the *rt-sph* (left-hand panels) and the *rt-grid* (right-hand panels) simulation. The top and bottom panels show the evolution of the power spectra with redshift and ionised fraction, respectively. In each panel, the left and right solid vertical line indicates, respectively, the size of the simulation box L_{box} and the Nyquist scale $2\pi/k_{\mathrm{Ny}}$. The finite size of the simulation box, as well as the finite size of the grid employed to sample it, restricts our discussion to scales larger than the Nyquist scale[12] and smaller than the size of the simulation box.

The evolution of the 21 cm power spectrum depends on the details of the reionisation transition and hence is generally sensitive to the employed reionisation model. Some of its features are, however, generic to a large number of models (Lidz et al. 2008) and we summarise them here (see Furlanetto, Oh, & Briggs 2006 for an extensive review). Before reionisation, the 21 cm power spectrum of the neutral hydrogen gas is simply proportional to the power spectrum of the hydrogen density. At large scales, where linear theory is valid and the gaseous matter traces

---

[11] http://www.fftw.org/

[12] Due to the mass assignment onto the grid, the power spectrum may already be misrepresented at significantly larger scales and should therefore be deconvolved with an appropriate window function (Jing 2005) or computed using a mass assignment function that minimises artefacts (Cui et al. 2008). We have made no attempt to deconvolve the power spectrum to correct for the fact that the neutral hydrogen density field used in the computations is, due to our use of transmissive simulation box boundaries, not periodic, and hence constitutes only part of an infinitely large volume (e.g., Schlittgen & Streitberg 2001).

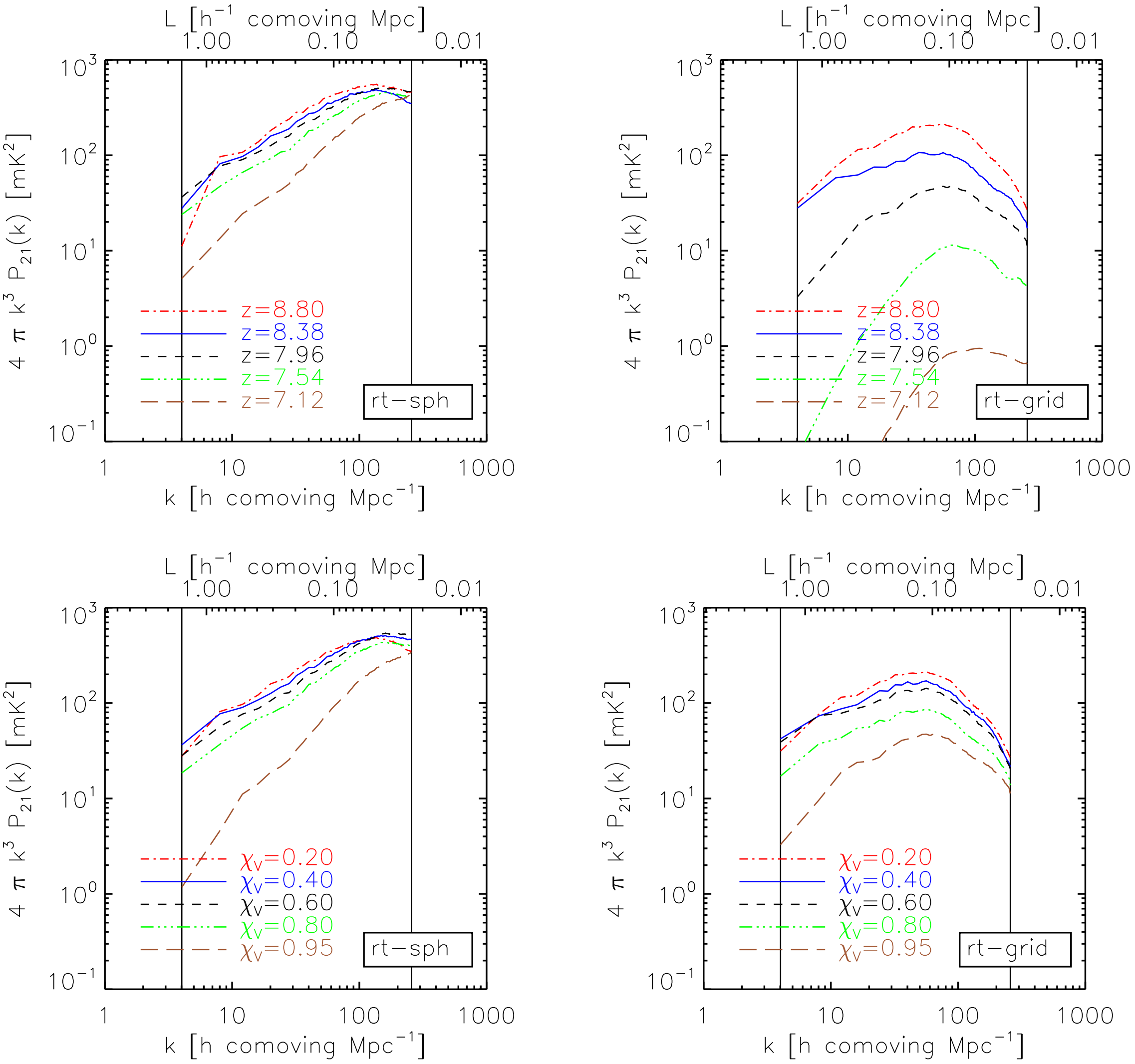

Figure 6.6: Evolution of the 21 cm power spectrum with redshift (top row) and ionised fraction (bottom row) for the simulations *rt-sph* (left-hand column) and *rt-grid* (right-hand column). In each panel, the right-hand solid vertical line indicates the Nyquist scale $2\pi/k_{\rm Ny}$ and the left-hand solid vertical line indicates the size of the simulation box $L_{\rm box}$.

the DM content of the Universe, the shape of the 21 cm power spectrum therefore resembles that of the well-known linear theory DM power spectrum at this time.

The growth of ionised regions during reionisation leads to a decrease in the 21 cm power spectrum amplitude at scales smaller than their typical size, where the gas is mostly ionised and hence the neutral fraction is very low, and an increase in the power spectrum on scales larger than that. Some models of stellar reionisation even predict a distinct bump in the 21 cm power spectrum at scales corresponding to the typical size of the ionised regions (e.g., Furlanetto, Zaldarriaga, & Hernquist 2004). The 21 cm power spectrum reaches its maximum amplitude at $\chi_{\rm V} \approx 0.5$, when the individual ionised regions start to overlap (Lidz et al. 2008). Towards the end of reionisation ($\chi_{\rm V} \gtrsim 0.9$) the amplitude of the 21 cm power spectrum rapidly decreases as the mean neutral fraction drops to zero. Despite this decrease in amplitude the 21 cm power spectrum may still be measurable at lower redshifts (Loeb & Wyithe 2008), since the contamination by galactic foreground signals, which poses the largest challenge for its detection, scales with redshift as $(1+z)^{2.6}$.

Both the simulations *rt-sph* and *rt-grid* predict qualitatively similar evolutions for the 21 cm power spectra, which are in close agreement with the discussion above. The overall amplitude of the power spectrum obtained from *rt-grid* evolves, however, much more rapidly with redshift than that obtained from *rt-sph*. This is mostly due to the fact that the mean ionised fraction evolves much more rapidly for *rt-grid* (Fig. 6.2), a direct consequence of the difference in the dynamic range exhibited by the two simulations (Sec. 6.2.3). Indeed, the overall amplitudes of the power spectra predicted by the *rt-sph* and the *rt-grid* simulation evolve on more similar time scales when compared as a function of mean (volume-weighted) ionised fraction, a fact that has also been noticed by other authors (e.g., Lidz et al. 2008).

On small scales, the amplitude of the power spectrum from the *rt-sph* simulation is much higher than the one from the *rt-grid* simulation. The difference in the power spectra at these scales is a direct consequence of the difference in the dynamic ranges probed by the simulations. Its interpretation is complicated by the fact that the 21 cm power spectrum is proportional to the product of the density and the neutral fraction (and also depends on redshift). It would therefore be helpful to compare the power spectra obtained from the *rt-sph* and the *rt-grid* simulation at *both* the same redshifts *and* the same mean ionised fractions. We have outlined earlier how such a comparison could be accomplished (Sec. 6.3.1). Moreover, it would be desirable to compare the differences between the 21 cm power spectra from the *rt-sph* and the *rt-grid* simulation to the differences between the corresponding hydrogen density and ionised fraction power spectra, to disentangle their contributions.

In summary, in this section we employed the *rt-sph* and the *rt-grid* simulation to compute the 21 cm power spectrum, one of the most promising future observational probes of reionisation. We found that the power spectra in both these simulations evolve in qualitative agreement with expectations from previous work. A direct comparison of the 21 cm power spectra obtained from the *rt-sph* and the *rt-grid* simulation, both at fixed redshifts and at fixed mean ionised fractions, revealed, however, significant differences, which we explained by the difference in the dynamic ranges probed. The presence of these differences illustrates the importance of performing spatially adaptive RT simulations that exploit the full dynamic range exhibited by state-of-the-art cosmological hydrodynamical simulations.

We acknowledge the preliminary character of the present work and emphasise the need to repeat the present analysis using a set of simulations that employ a range of box sizes and mass resolutions to enlarge the range of scales probed and to study the convergence of the results. Note that much larger simulation boxes are also required because interferometers observe the 21 cm signal through a beam that smoothes the power on angular scales of several arc minutes, corresponding to scales as large as several comoving Mpc over the redshift range of interest (e.g., Valdés et al. 2006; Mellema et al. 2006; Zaldarriaga, Furlanetto, & Hernquist 2004). Our results are also certainly affected by the small number of ionising sources and our simplified assumptions about their properties: in our simulations, the initial phase of reionisation that is characterised by the presence of many non-overlapping ionised regions, is largely skipped. By employing the Gunn-Peterson approximation to compute the 21 cm optical depth we have furthermore ignored the thermal broadening of the 21 cm spectral line and we also did not account for redshift space distortions (Kaiser 1987). We discuss more caveats of the present study in our conclusions, which we present next.

6.4 CONCLUSIONS

Radiative transfer (RT) simulations coupled to hydrodynamical models of the early Universe are one of the most promising techniques to study the epoch of reionisation, an important milestone in the history of our Universe. Simulating reionisation is a computationally demanding task that requires the hydrodynamical modelling of representative volumes of the Universe at very high resolution. Many RT simulations are, however, performed using relatively coarse, uniform grids. Many simulations also ignore the hydrodynamics and perform the RT on top of N-body simulations, assuming the gas to trace the dark matter.

It has, however, been pointed out that the modelling of the gas on small scales may crucially affect the predictions for the topology of reionisation. Because the first stars form in the densest regions, it is expected that reionisation starts from the inside out, with the gas in the halos that host the stars being ionised prior to the gas in the voids further away. The detection of Lyman-limit systems in the spectra of high redshift quasars, on the other hand, suggests that towards the end, reionisation proceeds outside-in, with the ionising radiation eating its way from the voids into remaining (partially) neutral regions of high density. The phase of outside-in reionisation is, however, not predicted by many of the current generations of RT simulations.

Here we performed spatially adaptive RT simulations on top of cosmological Smoothed Particle Hydrodynamics (SPH) simulations to study the epoch of reionisation. We compared these simulations with RT simulations that were performed on top of density fields obtained by mapping the SPH densities to a uniform grid. The two types of simulations were designed to investigate the importance of exploiting the full dynamic range available in the underlying hydrodynamical simulation.

Our RT simulations employed TRAPHIC (Chapter 4; Pawlik & Schaye 2008), a RT scheme that has been specifically designed for use with large SPH simulations. Its advantages are that it works directly on the SPH particles of the hydrodynamical simulation, that it is spatially adaptive and that its computation time does not scale with the number of sources. In addition, it is parallelised for use with distributed memory machines. TRAPHIC can be used to solve the time-dependent RT equation in step with the hydrodynamical evolution. Here we have, however, solved the time-independent RT equation by post-processing static density fields. We did this to facilitate the interpretation of our results and their comparison with previous work.

We first discussed the evolution of the mass- and volume-weighted mean ionised fractions obtained from our simulations. Due to the larger average recombination rate, the RT simulation performed on the original SPH density field predicted a much slower and more gradual evolution in the mean ionised fractions than the RT simulation that used the gridded density field. In both simulations the ratio of the mass-weighted and the volume-weighted mean ionised fractions evolved from values larger than one in the beginning of the simulation to values smaller than one towards its end. This shows that, at least globally, in both simulations reionisation first proceeds inside-out, with the ionising radiation propagating from the high-density star-forming regions into the low-density large-scale voids, before switching to outside-in, from the highly ionised voids into the remaining (partially) neutral regions of high density. The outside-in phase is, however, more marked in the RT simulation that was performed on the original spatially adaptive density field than in the one that was performed on the gridded density field (when compared at fixed mean ionised fraction).

We found that, in agreement with previous work, the morphology of ionised regions is, in contrast to their topology, largely unaffected when the dynamic range is increased. To further investigate the topology of reionisation, we studied the dependence of the ionised fraction on the density of the gas. We found that locally the evolution of the topology of the ionised gas cannot be characterised by a simple sequence of inside-out followed by outside-in reionisation. Instead, the ionised fraction is a complex function of the gas overdensity. For sufficiently high mean ionised fractions, the highest ionised fractions are generally found in the low-density voids and the high-density star-forming regions.

The ionised fraction shows a prominent depression at overdensities $\log_{10}\Delta \sim 2$ ($\log_{10}\Delta \sim 1$) in the simulations using the original (gridded) density fields. At both lower and higher densities, the recombination rate is too low to significantly overcome the ionising effect of the stellar radiation. The depression occurs at higher overdensities in the simulation employing the original gas density field, because the increased dynamic range increases the clumping factor and hence recombinations may overcome ionisations closer to the sources. In the simulations employing the gridded density fields the highest density gas ($\log_{10}\Delta \sim 3$) is always highly ionised. The dependence of the ionised fraction on density in the simulations employing the original density fields shows a more complex behaviour. For overdensities $3 \lesssim \log_{10}\Delta \sim 4$, the ionised fraction generally increases, but may exhibit several depressions similar to (but less pronounced than) that at overdensities $\log_{10}\Delta \sim 2$. For overdensities $\log_{10}\Delta > 4$, the ionised fraction generally decreases with overdensity.

Finally, we discussed the power spectrum of 21 cm brightness temperature fluctuations, which is one of the most important potential observables of the reionisation epoch. We found its general evolution to be consistent with expectations from previous work. The 21 cm power spectrum first traces the linear cold dark matter power spectrum with modifications on small scales due to the appearance of the first ionised regions. The power is shifting from small to large scales as the ionised regions grow and finally diminishes as most of the volume of the Universe becomes ionised. The simulation that was performed on the original SPH density field predicted significantly more power on small scales than the simulation that was performed on the gridded density field, as expected from the differences in the dynamic range. The interpretation of this enhanced small-scale power is, however, complicated by the fact that the 21 cm brightness temperature is proportional to the product of both density and neutral fraction and also depends on redshift.

We caution the reader that the hydrodynamical simulations that we have employed as part of the present pilot study have likely not yet converged. Although all of our simulations employ a sufficiently high resolution to resolve all halos with virial temperatures $T_{\rm vir} \gtrsim 10^4$ K with at least 100 particles, none of them has the resolution to predict the properties of the multiphase medium associated with the star-forming regions that these halos host. Furthermore, our use of a comparatively small box size leads us to underestimate the effects of large-scale structure formation on the small-scale clumpiness of the cosmic gas and biases the halo mass function away from its expected values. The mass of the most massive dark matter halos that the present simulations are able to host cannot exceed $\sim 10^{11}\ h^{-1}$ M$_\odot$, corresponding to the total mass in the simulation box. Simulations with box sizes of $30\ h^{-1}$ Mpc and larger will be required to obtain representative models of the Universe for use with RT simulations of reionisation (Barkana & Loeb 2004; Iliev et al. 2006).

As a result, the employed star formation rates have likely not converged. We have made no attempt to match observational constraints on the star formation rate (e.g., Hopkins & Beacom 2006). Instead, we have roughly rescaled the ionising luminosities of the stellar sources to accomplish reionisation in the *rt-sph* simulation by redshift $z = 6$. We expect that a convergence in the star formation rate is generally difficult to achieve, even when simulating representative volumes of the Universe at high-resolution. This is because the star formation rate depends on a number of physical processes that our analysis ignored, some of which are mentioned below.

Our simulations did not include the radiation-hydrodynamical feedback from photo-heating that is known to significantly affect the clumpiness of the gas in star-forming regions and the intergalactic medium (e.g., Haiman, Abel, & Madau 2001; Oh & Haiman 2003; Wise & Abel 2005; Pawlik, Schaye, & van Scherpenzeel 2009a). Photo-heating evaporates the gas out of low mass halos and decreases the average recombination rate in the intergalactic gas through Jeans filtering (e.g. Shapiro, Giroux, & Babul 1994; Gnedin & Hui 1998; Okamoto, Gao, & Theuns 2008). It moreover lowers the efficiency of gas to cool and hence impedes its accretion onto halos of all masses (Efstathiou 1992). The feedback from photo-heating may, moreover, be amplified by feedback from supernova explosions (Pawlik & Schaye 2009b), which we have also ignored.

Because we have assumed the presence of a photo-dissociating background, the formation of molecular hydrogen is suppressed in our simulations. In reality, the gas may contain a significant fraction of molecular hydrogen before reionisation (but see, e.g., Haiman, Rees, & Loeb 1997). Star formation and the associated kinetic feedback would then already be efficient in halos with virial temperatures much smaller than 10^4 K (e.g., Tegmark et al. 1997). We have also ignored the existence of atoms and ions heavier than helium. Supernova explosions may, however, quickly enrich the interstellar and intergalactic gas with metals (e.g., Bromm, Yoshida, & Hernquist 2003), which would increase its ability to cool. In our simulation the gas in halos with virial temperatures $< 10^4$ K is therefore biased to be ionised from the outside in.

These caveats are, however, unlikely to affect our qualitative conclusions derived from our comparisons of RT simulations that employ spatially adaptive density fields with RT simulations that employ density fields interpolated to a uniform grid. Our work therefore underlines the important role played by small-scale gas inhomogeneities in large-scale cosmological simulations of reionisation.

ACKNOWLEDGEMENTS

We thank Garrelt Mellema for useful discussions and we are grateful to Claudio Dalla Vecchia for help with the set-up of simulations. Some of the simulations presented here were run on Huygens, the Dutch national supercomputer. This work was supported by Marie Curie Excellence Grant MEXT-CT-2004-014112.

REFERENCES

Alvarez M. A., Bromm V., Shapiro P. R., 2006, ApJ, 639, 621

Barkana R., Loeb A., 2001, PhR, 349, 125

Barkana R., Loeb A., 2004, ApJ, 609, 474

Bromm V., Yoshida N., Hernquist L., 2003, ApJ, 596, L135

Bruzual G., Charlot S., 2003, MNRAS, 344, 1000

Choudhury T. R., 2009, arXiv, arXiv:0904.4596

Choudhury T. R., Haehnelt M. G., Regan J., 2009, MNRAS, 394, 960

Ciardi B., Stoehr F., White S. D. M., 2003, MNRAS, 343, 1101

Ciardi B., Ferrara A., 2005, SSRv, 116, 625

Ciardi B., Salvaterra R., 2007, MNRAS, 381, 1137

Cui W., Liu L., Yang X., Wang Y., Feng L., Springel V., 2008, ApJ, 687, 738

Efstathiou G., 1992, MNRAS, 256, 43P

Fan X., Carilli C. L., Keating B., 2006, ARA&A, 44, 415

Field G. B., 1959, ApJ, 129, 536

Finlator K., Özel F., Davé R., 2009, MNRAS, 393, 1090

Fixsen D. J., Cheng E. S., Gales J. M., Mather J. C., Shafer R. A., Wright E. L., 1996, ApJ, 473, 576

Furlanetto S. R., Zaldarriaga M., Hernquist L., 2004, ApJ, 613, 1

Furlanetto S. R., Oh S. P., 2005, MNRAS, 363, 1031

Furlanetto S. R., Oh S. P., Briggs F. H., 2006, PhR, 433, 181

Gnedin N. Y., Ostriker J. P., 1997, ApJ, 486, 581

Gnedin N. Y., Hui L., 1998, MNRAS, 296, 44

Gnedin N. Y., 2000, ApJ, 535, 530

Gnedin N. Y., Kravtsov A. V., Chen H.-W., 2008, ApJ, 672, 765

Gunn J. E., Peterson B. A., 1965, ApJ, 142, 1633

Haiman Z., Rees M. J., Loeb A., 1997, ApJ, 476, 458

Haiman Z., Abel T., Madau P., 2001, ApJ, 551, 599

Hopkins A. M., Beacom J. F., 2006, ApJ, 651, 142

Iliev I. T., Shapiro P. R., Ferrara A., Martel H., 2002, ApJ, 572, L123

Iliev I. T., Mellema G., Pen U.-L., Merz H., Shapiro P. R., Alvarez M. A., 2006, MNRAS, 369, 1625

Inoue A. K., Iwata I., Deharveng J.-M., 2006, MNRAS, 371, L1

Jing Y. P., 2005, ApJ, 620, 559

Kaiser N., 1987, MNRAS, 227, 1

Kennicutt R. C., Jr., 1998, ApJ, 498, 541

Kohler K., Gnedin N. Y., Hamilton A. J. S., 2007, ApJ, 657, 15

Komatsu E., et al., 2008, preprint (arXiv:0803.0547)

Lee K.-G., Cen R., Gott J. R. I., Trac H., 2008, ApJ, 675, 8

Lidz A., Zahn O., McQuinn M., Zaldarriaga M., Hernquist L., 2008, ApJ, 680, 962

Loeb A., Ferrara A., Ellis R. S., 2008, First Light in the Universe (Springer),

Loeb A., Wyithe J. S. B., 2008, PhRvL, 100, 161301

McQuinn M., Lidz A., Zahn O., Dutta S., Hernquist L., Zaldarriaga M., 2007, MNRAS, 377, 1043

Mellema G., Iliev I. T., Pen U.-L., Shapiro P. R., 2006, MNRAS, 372, 679

Mesinger A., Furlanetto S., 2007, ApJ, 669, 663

Mesinger A., Dijkstra M., 2008, MNRAS, 390, 1071

Miralda-Escudé J., Haehnelt M., Rees M. J., 2000, ApJ, 530, 1

Nakamoto T., Umemura M., Susa H., 2001, MNRAS, 321, 593

Oh S. P., Haiman Z., 2003, MNRAS, 346, 456

Okamoto T., Gao L., Theuns T., 2008, preprint (arXiv:0806.0378)

Pawlik A. H., Schaye J., 2008, MNRAS, 389, 651

Pawlik A. H., Schaye J., van Scherpenzeel E., 2009, MNRAS, 394, 1812

Pawlik A. H., Schaye J., 2009, MNRAS, L228

Press W. H., Teukolsky S. A., Vetterling W. T., Flannery B. P., 1992, Numerical recipes in C. The art of scientific computing, Cambridge University Press, 2nd ed.

Razoumov A. O., Sommer-Larsen J., 2006, ApJ, 651, L89

Schaye J., 2001, ApJ, 559, 507

Schaye J., 2004, ApJ, 609, 667

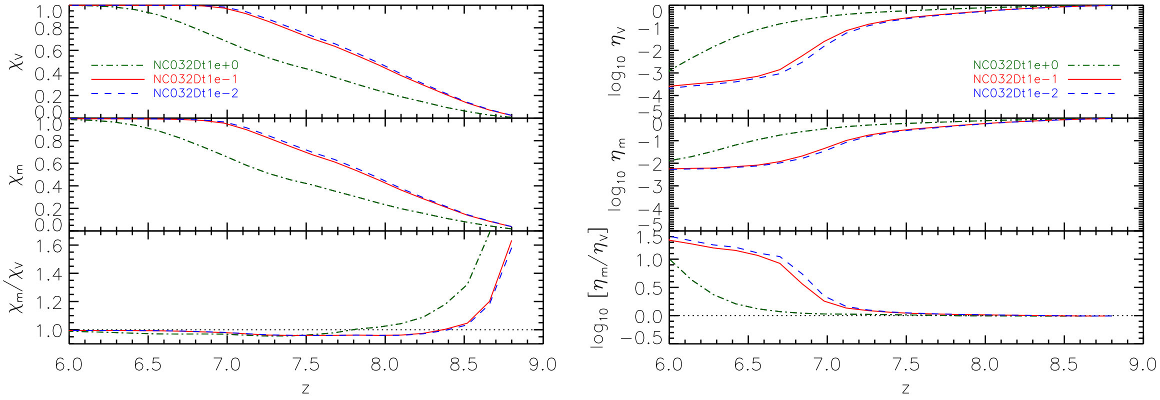

Figure 6.7: Numerical convergence study: RT time step. The evolution of the the mean ionised (left-hand panel) and the mean neutral (right-hand panel) fraction as obtained in the simulation *rt-sph* (red solid curves), which employed an angular resolution $N_\mathrm{c} = 32$ and a time step $\Delta t_\mathrm{r} = 10^{-1}$ Myr, is compared to those obtained from identical simulations but using time steps $\Delta t_\mathrm{r} = 1$ Myr (green dot-dashed curves) and $\Delta t_\mathrm{r} = 10^{-2}$ Myr (blue dashed curve). Both the evolution of the mean ionised fraction and the evolution of the mean neutral fraction obtained from the *rt-sph* simulation have converged.

Schaye J., Dalla Vecchia C., 2008, MNRAS, 383, 1210

Schlittgen R, Streitberg B. H. J., 2001, Zeitreihenanalyse (9. Auflage), Oldenburg Wissenschaftsverlag

Seljak U., Zaldarriaga M., 1996, ApJ, 469, 437

Shapiro P. R., Giroux M. L., Babul A., 1994, ApJ, 427, 25

Sokasian A., Abel T., Hernquist L., Springel V., 2003, MNRAS, 344, 607
Springel V., 2003, MNRAS, 344, 607

Springel V., 2005, MNRAS, 364, 1105

Tegmark M., Silk J., Rees M. J., Blanchard A., Abel T., Palla F., 1997, ApJ, 474, 1

Tegmark M., Zaldarriaga M., 2009, PhRvD, 79, 083530

Valdés M., Ciardi B., Ferrara A., Johnston-Hollitt M., Röttgering H., 2006, MNRAS, 369, L66

Wiersma R. P. C., Schaye J., Smith B. D., 2009, MNRAS, 393, 99

Wise J. H., Abel T., 2005, ApJ, 629, 615

Zahn O., Lidz A., McQuinn M., Dutta S., Hernquist L., Zaldarriaga M., Furlanetto S. R., 2007, ApJ, 654, 12

Zaldarriaga M., Furlanetto S. R., Hernquist L., 2004, ApJ, 608, 622

6.A CHOICE OF RADIATIVE TRANSFER PARAMETERS

In this section we demonstrate that the radiative transfer (RT) simulations that we described in Sec. 6.2.2 employ a sufficiently small RT time step Δt_r and a sufficiently high angular resolution N_c to obtain converged results.

The *rt-sph* simulation employs a time step $\Delta t_\mathrm{r} = 10^{-1}$ Myr and an angular resolution $N_\mathrm{c} = 32$. We have repeated this simulation at fixed angular resolution $N_\mathrm{c} = 32$ using both a larger ($\Delta t_\mathrm{r} = 1$ Myr) and a smaller ($\Delta t_\mathrm{r} = 10^{-2}$ Myr) time step. In addition, we have repeated this simulation at fixed time step $\Delta t_\mathrm{r} = 10^{-1}$ Myr using both a lower ($N_\mathrm{c} = 8$) and a higher ($N_\mathrm{c} = 128$) angular resolution. Figs. 6.7-6.10 show the results.

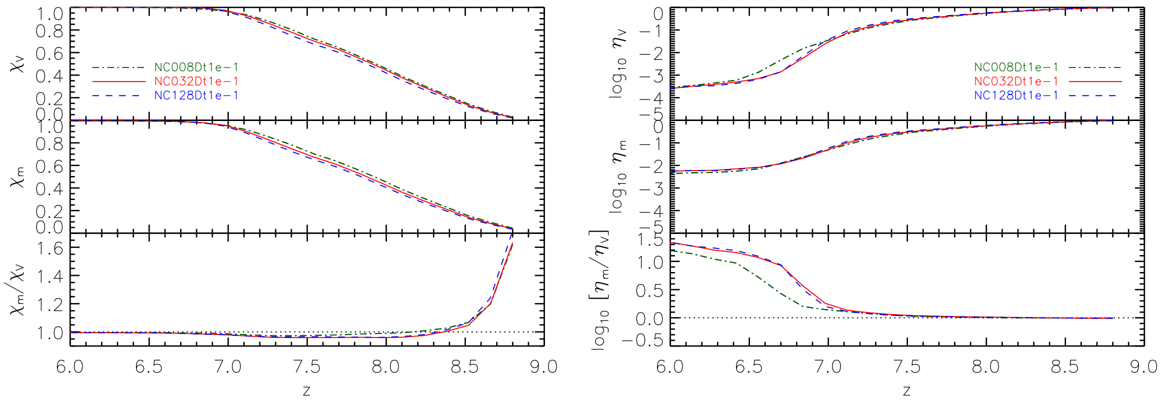

Figure 6.8: Numerical convergence study: angular resolution. The evolution of the the mean ionised (left-hand panel) and the mean neutral (right-hand panel) fraction as obtained in the simulation *rt-sph* (red solid curves), which employed an angular resolution $N_c = 32$ and a time step $\Delta t_r = 10^{-1}$ Myr, is compared to those obtained from identical simulations but using angular resolutions $N_c = 8$ (green dot-dashed curves) and $N_c = 32$ (blue dashed curve). Both the evolution of the mean ionised fraction and the evolution of the mean neutral fraction obtained from the *rt-sph* simulation have converged.

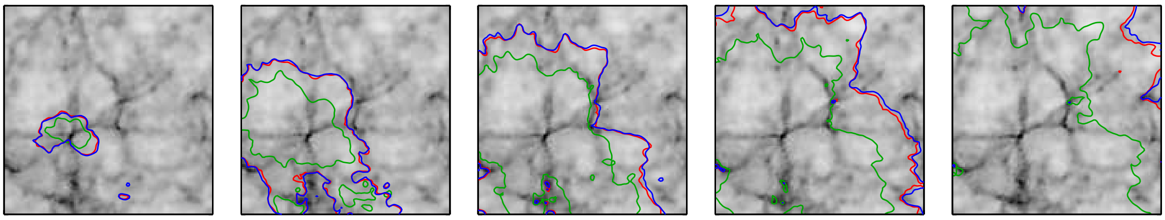

Figure 6.9: Numerical convergence study: RT time step. Slices through the center of the simulation box at redshifts $z = 8.80$, 8.38, 7.96, 7.54, and 7.12 (from left to right). Contours show neutral fractions $\eta = 0.5$ for simulations with fixed angular resolution $N_c = 32$ and radiative transfer time steps $\Delta t_r = 1$ Myr (green), 10^{-1} Myr (red, corresponding to the *rt-sph* simulation) and 10^{-2} Myr (blue). The *rt-sph* simulation has converged with respect to the chosen time step.

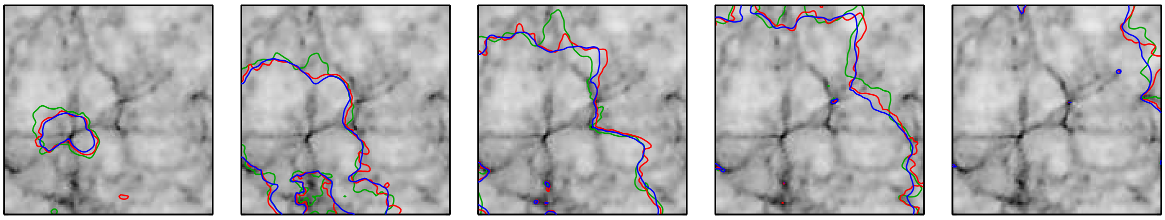

Figure 6.10: Numerical convergence study: angular resolution. Slices through the center of the simulation box at redshifts $z = 8.80$, 8.38, 7.96, 7.54, and 7.12 (from left to right). Contours show neutral fractions $\eta = 0.5$ for simulations with fixed RT time step $\Delta t_r = 10^{-1}$ Myr and angular resolutions $N_c = 8$ (green), $N_c = 32$ (red, corresponding to the *rt-sph* simulation) and $N_c = 128$ (blue). The *rt-sph* simulation has converged with respect to the chosen angular resolution.

Fig. 6.7 shows the evolution of the mean ionised (left-hand panel) and mean neutral (right-hand panel) fractions in the simulations using an angular resolution $N_{\rm c} = 32$ and time steps $\Delta t_{\rm r} = 1$ Myr (green dot-dashed curves), $\Delta t_{\rm r} = 10^{-1}$ Myr (red solid curves) and $\Delta t_{\rm r} = 10^{-2}$ Myr (blue dashed curves). Note that the red solid curves shown in the left-hand panel of this figure are identical to the red solid curves shown in Fig. 6.2, as they correspond to the same simulation. The results of the simulation with time-step $\Delta t_{\rm r} = 10^{-1}$ Myr are nearly on top of the results of the simulation with time-step $\Delta t_{\rm r} = 10^{-2}$ Myr, and hence are converged.

The convergence is confirmed by an inspection of the evolutions of the sizes of the ionised regions that are shown in Fig. 6.9. The figure shows a slice trough the center of the simulation box, generated by mapping the SPH particle densities and neutral fractions to a uniform grid with $\tilde{N}_g = 128$ points per dimension using mass-conserving SPH interpolation. Contours show neutral fractions of $\eta = 0.5$ for the simulations with time steps $\Delta t_{\rm r} = 1$ Myr (green), $\Delta t_{\rm r} = 10^{-1}$ Myr (red) and $\Delta t_{\rm r} = 10^{-2}$ Myr (blue). From left to right, the panels correspond to redshifts $z = 8.8$, 8.38, 7.96, 7.54, 7.12.

The results obtained in the simulation with the largest time step, i.e. with the time step $\Delta t_{\rm r} = 1$ Myr, are, however, not yet converged. The main reason why the mean ionised fraction and the sizes of the ionised regions predicted by this simulation are systematically smaller than those predicted by the simulations with smaller time steps is that for this simulation our approximate treatment of the time-indepedent RT equation, i.e. the fact that during each RT time step photons are only propagated over a single inter-particle distance (Sec. 5.3.3), becomes inadequate.

Fig. 6.8 shows the evolution of the mean ionised (left-hand panel) and mean neutral (right-hand panel) fractions in the simulations using a fixed time step $\Delta t_{\rm r} = 10^{-1}$ Myr but varying angular resolutions $N_{\rm c} = 8$ (green dot-dashed curves), $N_{\rm c} = 32$ (red solid curves) and $N_{\rm c} = 128$ (blue dashed curve). The red solid curves shown in the left-hand panel of this figure are identical to the red solid curves shown in Fig. 6.2. Clearly, the results of the simulation with angular resolution $N_{\rm c} = 32$ are converged, as they are nearly on top of the results of the simulation with the higher angular resolution $N_{\rm c} = 128$. This is confirmed by a look at the evolution of the sizes of the ionisation fronts shown in Fig. 6.10. The results obtained in the simulation with the lowest angular resolution, i.e. with the angular resolution $N_{\rm c} = 8$, are, on the other hand, not yet fully converged.

We have not yet discussed the convergence with respect to changes in the time step and the angular resolution for the *rt-grid* simulation. One may expect this simulation to be converged, because it exhibits a smaller dynamic range than the *rt-sph* simulation. We have explicitly verified this expectation by repeating the *rt-grid* simulation with smaller time steps and higher angular resolution (although only for part of the original simulation time).

Sed fugit interea, fugit irreparabile tempus.

Vergil, Georgica

CHAPTER 7

TRAPHIC - thermal coupling

Andreas H. Pawlik & Joop Schaye

In preparation.

THE temperature of the cosmic gas is a key astrophysical observable. The detailed modelling of its evolution with cosmological hydrodynamical simulations requires the use of radiative transfer methods to accurately compute the effects of photo-ionisation and photo-heating on the relevant cooling and heating rates. In Chapter 4 we presented TRAPHIC, a novel radiative transfer scheme for use with large Smoothed Particle Hydrodynamics (SPH) simulations. We described its implementation for the transport of hydrogen-ionising radiation in the SPH code GADGET-2 in Chapter 5. Here we extend our implementation to compute the non-equilibrium evolution of the temperature of gas exposed to hydrogen-ionising radiation. We verify this extension by comparing TRAPHIC's performance in thermally coupled radiative transfer test simulations with reference solutions obtained with other radiative transfer codes.

7.1 INTRODUCTION

A thorough understanding of the thermal history of the cosmic gas is crucial for the interpretation of many astrophysical observables that are employed to explore the physics of galaxy formation and evolution. The thermal history is, moreover, itself a powerful observable. It depends, for instance, strongly on the details of the reionisation of hydrogen (e.g. Miralda-Escudé & Rees 1994; Theuns et al. 2002; Hui & Haiman 2003; Tittley & Meiksin 2007), a key epoch in the history of the Universe (for a review see, e.g., Furlanetto, Oh, & Briggs 2006; Barkana & Loeb 2001). Knowledge of the thermal history therefore provides an important probe of the Universe during reionisation and beyond. In fact, constraints from the thermal evolution of the intergalactic medium were among the first to indicate that the Universe underwent another major transition after the reionisation of hydrogen: the reionisation of helium (e.g., Schaye et al. 2000; Ricotti, Gnedin, & Shull 2000; Bernardi et al. 2003; McQuinn et al. 2009).

The study of the formation and evolution of galaxies using cosmological gas-dynamical simulations therefore requires an accurate treatment of the evolution of the gas temperature. The gas temperature is determined by a manifold of cooling and heating processes. The most important (for cosmological applications) radiative cooling processes, i.e., collisional excitation, collisional ionisation, recombination, bremsstrahlung and Compton scattering off the cosmic microwave background, are nowadays included by default in almost all hydrodynamical cosmological simulations, although often under the assumption of primordial abundances and/or collisional ionisation equilibrium. The effects of photo-ionisation on the cooling rates are, if at all, only approximately accounted for (e.g., Wiersma, Schaye, & Smith 2009).

Photo-heating is one such, and, for the low densities that are of interest here, probably the most important, effect. The accurate computation of photo-heating rates requires the evaluation of complex radiative transfer effects (e.g., Abel & Haehnelt 1999; Bolton, Meiksin, & White 2004). Almost none of the cosmological simulations performed to date include, however, a sufficiently detailed treatment of the ionising radiation. In fact, the standard procedure is to compute photo-heating rates from an externally imposed, i.e. not self-consistently evolved, uniform UV background in the optically thin limit. We have performed simulations that employed this procedure in Chapters 2 and 3, where we have also discussed the main short-comings of this simplified approach, including its inability to account for the self-shielding of radiation in mini-halos (e.g., Kitayama & Ikeuchi 2000; Susa & Umemura 2004; Dijkstra et al. 2004; Shapiro, Iliev, & Raga 2004; Iliev, Shapiro, & Raga 2005).

In Chapter 4 we have presented a novel radiative transfer scheme, TRAPHIC, for use with cosmological smoothed particle hydrodynamics (SPH) simulations. TRAPHIC is one of the first of a new generation of radiative transfer schemes that have been specifically designed to overcome the enormous computational challenges posed by the desire to incorporate the accurate transport of radiation into simulations exhibiting a large dynamic range and containing many ionising sources (e.g., Ritzerveld & Icke 2006; Trac & Cen 2007; Petkova & Springel 2008). We have furthermore presented its numerical implementation for the transport of mono-chromatic (or grey), hydrogen-ionising radiation in the state-of-the-art SPH code GADGET-2 (Chapter 5) and one of its successors, P-GADGET3-BG (Chapter 6).

In this chapter we extend our implementation of TRAPHIC to compute, in addition to its ionisation state, the temperature of gas exposed to hydrogen-ionising radiation. This will allow us to accurately compute photo-heating rates in cosmological simulations. Here we limit ourselves to determining the thermal history of gas subject to photo-ionisation and will ignore the hydro-dynamical feedback associated with photo-heating (Chapters 2 and 3). We leave the radiation-hydrodynamical coupling of TRAPHIC for future work. For simplicity, we will furthermore ignore the contributions from metals and molecules to the gas cooling rates (e.g., Tegmark et al. 1997; Anninos et al. 1997; Bromm, Yoshida, & Hernquist 2003; Smith, Sigurdsson, & Abel 2008; Wiersma, Schaye, & Smith 2009; Choi & Nagamine 2009).

The structure of this chapter is as follows. The main subject of the chapter, the thermal coupling of TRAPHIC, will be presented in Sec. 7.6. The coupling requires some preparatory work, which we will present in Secs. 7.2 - 7.5. In Sec. 7.2 we will discuss the physics of ionisation and recombination. This section generalises the description of ionisation and recombination given in Chapter 5 to include also the contribution from helium and to account for collisional ionisations. In Sec. 7.3 we will discuss the thermodynamical relations that describe the evolution of the gas temperature and discuss (the physics of) the major cooling and heating processes relevant for cosmological simulations. The main outcome of Secs. 7.2 and 7.3 will be a compilation of references to (fits to) atomic data that we will employ to compute ionisation, recombination, heating and cooling rates in the simulations presented later on in this chapter. This reference set (Table 7.1) will be evaluated for the case of ionisation equilibrium and compared to the literature in Sec. 7.4. The final step before our presentation of the thermal coupling consists of describing our numerical method for evolving the gas temperature in Sec. 7.5.

Readers familiar with the physics of ionisation, recombination, heating and cooling may wish to skip Secs. 7.2-7.4 (and perhaps also Sec. 7.5) and directly start with Sec. 7.6, in which we present the thermal coupling of our radiative transfer scheme TRAPHIC. The same applies to readers who are less interested in the precise expressions for the atomic data than in their applications to thermally coupled radiative transfer problems. For those readers we have summarised the physical processes that we include in the computations of the ionisation and thermal state of gas in the radiative transfer simulations presented in this chapter - together with the references to the (fits to) atomic data sets employed for their numerical evaluation - in Table 7.1.

We end this introduction with some definitions that we will employ throughout the chapter. We consider an atomic gas of total number density $n = n_{\rm e} + \sum n_i$, where n_i is the number density of ion (or species) i and $n_{\rm e}$ is the number density of free electrons. The number density n_i is related to the total mass density ρ through $n_i = X_i \rho/(\mu_i m_{\rm H})$, where X_i is the mass fraction of ion i and $\mu_i = m_i/m_{\rm H}$ is its mass m_i in units of the hydrogen mass $m_{\rm H}$. We assume that the gas is of primordial composition, i.e. $i \in \{$HI, HeI, HeII, HeIII$\}$ and $X_{\rm H} + X_{\rm He} = 1$. We will set $X_{\rm H} = 0.25$ and $X_{\rm He} = 1 - X_{\rm H}$. We will make frequent use of the ion number density fractions with respect to hydrogen, $\eta_i \equiv n_i/n_{\rm H}$ and the electron fraction $\eta_{\rm e} = n_{\rm e}/n_{\rm H}$. Where required, we will assume cosmological parameters $[\Omega_{\rm m}, \Omega_{\rm b}, \Omega_\Lambda, \sigma_8, n_{\rm s}, h]$ given by $[0.258, 0.0441, 0.742, 0.796, 0.963, 0.719]$, which is consistent with the WMAP 5-year result (Komatsu et al. 2008).

7.2 IONISATION AND RECOMBINATION

The evolution of the ionisation state of primordial gas in the presence of a photo-ionising radiation background is determined by the set of rate equations

$$\frac{d\eta_{\rm HI}}{dt} = \alpha_{\rm HII} n_{\rm e} \eta_{\rm HII} - \eta_{\rm HI}(\Gamma_{\gamma {\rm HI}} + \Gamma_{\rm eHI} n_{\rm e}) \tag{7.1}$$

$$\frac{d\eta_{\rm HeI}}{dt} = \alpha_{\rm HeII} n_{\rm e} \eta_{\rm HeII} - \eta_{\rm HeI}(\Gamma_{\gamma {\rm HeI}} + \Gamma_{\rm eHeI} n_{\rm e}) \tag{7.2}$$

$$\frac{d\eta_{\rm HeIII}}{dt} = \eta_{\rm HeII}(\Gamma_{\gamma {\rm HeII}} + \Gamma_{\rm eHeII} n_{\rm e}) - \alpha_{\rm HeIII} n_{\rm e} \eta_{\rm HeIII}, \tag{7.3}$$

Table 7.1: Reference set of (fits to the) atomic data used to calculate photo-ionisation rates, collisional ionisation rates, recombination rates and cooling rates in the simulations presented in this chapter. We emphasise that our selection of physical processes is not intended to be exhaustive and that this table is not meant to establish a canonical set of references. In fact, our choices in favour of certain (fits to) atomic data sets partly reflects personal preferences.

Photo-ionisation	HI, HeI, HeII photo-ionisation cross-sections ($\sigma_{\rm HI}, \sigma_{\rm HeI}, \sigma_{\rm HeII}$)	Verner et al. (1996)
Collisional ionisation	HI, HeI, HeII collisional ionisation rate coefficients ($\Gamma_{\rm eHI}, \Gamma_{\rm eHeI}, \Gamma_{\rm eHeII}$)	Theuns et al. (1998)
Recombination	HII, HeIII recombination rate coefficients ($\alpha_{\rm HII}, \alpha_{\rm HeIII}$)	Hui & Gnedin (1997)
	HeII recombination rate coefficient ($\alpha_{\rm HeII}$)	Hummer & Storey (1998)
	HeII dielectronic recombination rate coefficient ($\alpha_{\rm di,HeII}$)	Aldrovandi & Pequignot (1973)
Collisional ionisation cooling	HI, HeI, HeIII collisional ionisation cooling rate	Shapiro & Kang (1987)
Collisional excitation cooling	HI, HeI, HeIII collisional excitation cooling rate	Cen (1992)
Recombination cooling	HII, HeIII recombination cooling rate	Hui & Gnedin (1997)
	HeII recombination cooling rate	Hummer & Storey (1998)
	HeII dielectronic recombination cooling rate	Black (1981)
Cooling by bremsstrahlung	Bremsstrahlung cooling rate	Theuns et al. (1998)
Compton cooling	Compton cooling rate	Theuns et al. (1998)

supplemented with the closure relations

$$\begin{aligned} \eta_{\rm HI} + \eta_{\rm HII} &= 1 \quad (7.4)\\ \eta_{\rm HeI} + \eta_{\rm HeII} + \eta_{\rm HeIII} &= \eta_{\rm He} \quad (7.5)\\ \eta_{\rm HII} + \eta_{\rm HeII} + 2\eta_{\rm HeIII} &= \eta_{\rm e}, \quad (7.6) \end{aligned}$$

where $\Gamma_{\gamma i}$ is the photo-ionisation rate and $\Gamma_{{\rm e}i}$ and α_i are the collisional ionisation and recombination rate coefficients for species i (the collisional ionisation rates are $n_{\rm e}\Gamma_{{\rm e}i}$ and the recombination rates are $n_{\rm e}\alpha_i$); $\eta_{\rm He} = n_{\rm He}/n_{\rm H} = X_{\rm He}(m_{\rm H}/m_{\rm He})/(1 - X_{\rm He})$ denotes the helium abundance (by number); $m_{\rm H}$ and $m_{\rm He}$ the masses of the hydrogen and helium atoms, respectively.

Hence, we have six equations (Eqs. 7.1-7.6) for six unknown variables ($\eta_{\rm HI}$, $\eta_{\rm HII}$, $\eta_{\rm HeI}$, $\eta_{\rm HeII}$, $\eta_{\rm HeIII}$, $\eta_{\rm e}$). In equilibrium ($d/dt = 0$) Eqs. 7.1 - 7.6 can be written as,

$$\begin{aligned} \eta_{\rm HI} &= \left(1 + \frac{\Gamma_{\gamma{\rm HI}} + n_{\rm e}\Gamma_{\rm eHI}}{\alpha_{\rm HII} n_{\rm e}}\right)^{-1}, \quad (7.7)\\ \eta_{\rm HII} &= 1 - \eta_{\rm HI}, \quad (7.8)\\ \eta_{\rm HeI} &= \eta_{\rm He}\left[1 + \frac{\Gamma_{\gamma{\rm HeI}} + n_{\rm e}\Gamma_{\rm eHeI}}{\alpha_{\rm HeII} n_{\rm e}}\right. \quad (7.9)\\ &\times \left.\left(1 + \frac{\Gamma_{\gamma{\rm HeII}} + n_{\rm e}\Gamma_{\rm eHeII}}{\alpha_{\rm HeIII} n_{\rm e}}\right)\right]^{-1}, \quad (7.10)\\ \eta_{\rm HeII} &= \eta_{\rm HeI}\frac{\Gamma_{\gamma{\rm HeI}} + n_{\rm e}\Gamma_{\rm eHeI}}{\alpha_{\rm HeII} n_{\rm e}}, \quad (7.11)\\ \eta_{\rm HeIII} &= \eta_{\rm HeII}\frac{\Gamma_{\gamma{\rm HeII}} + n_{\rm e}\Gamma_{\rm eHeII}}{\alpha_{\rm HeIII} n_{\rm e}}, \quad (7.12)\\ \eta_{\rm e} &= \eta_{\rm HII} + \eta_{\rm HeII} + 2\eta_{\rm HeIII}. \quad (7.13) \end{aligned}$$

It is worth noting the two important special cases of pure photo-ionisation equilibrium and pure collisional ionisation equilibrium, obtained by setting $\Gamma_{ei} = 0$ and $\Gamma_{\gamma i} = 0$, respectively. We will employ the corresponding equilibrium fractions in our computation of the equilibrium heating and cooling rates in Sec. 7.4 below.

In the following we briefly discuss the physics of photo-ionisation, collisional ionisation and recombination. Our description makes heavy use of the text books Osterbrock (1989), Spitzer (1978), Rybicki & Lightman (2004) and other excellent reviews of the subject that are referred to below. We will compare photo-ionisation cross-sections, collisional ionisation rates and recombination rates that are commonly employed in the literature. Our comparison will result in a reference set of photo-ionisation cross-sections, collisional ionisation rates and recombination rates that we will employ in the rest of this chapter. It is summarised in Table 7.1.

7.2.1 Photo-ionisation

The number of photo-ionisations of species i per unit time per unit volume is given by $\eta_i n_{\rm H}\Gamma_{\gamma i}$, where $\Gamma_{\gamma i}$ is the photo-ionisation rate,

$$\Gamma_{\gamma i} = \int_{\nu_i}^{\infty} d\nu \frac{4\pi J_\nu(\nu)}{h_{\rm p}\nu}\sigma_{\gamma i}(\nu), \quad (7.14)$$

where $i \in$ {HI, HeI, HeII}, $\sigma_{\gamma i}(\nu)$ is the photo-ionisation cross-section for species i and $h_{\rm p}\nu_i$ is the ionisation potential of species i. Note that $h_{\rm p}\nu_{\rm HI} = 13.6$ eV , $h_{\rm p}\nu_{\rm HeI} = 24.6$ eV and $h_{\rm p}\nu_{\rm HeII} = 54.4$ eV.

The cross-sections for photo-ionisation by photons with energies at the HI, HeI and HeII ionisation threshold are $\sigma_{\rm HI} = 6.3 \times 10^{-18}$ cm^2, $\sigma_{\rm HeI} = 7.83 \times 10^{-18}$ cm^2 and $\sigma_{\rm HeII} = 1.58 \times 10^{-18}$ cm^2 (Table 2.7 in Osterbrock 1989). The cross-sections are a decreasing function of photon energy. For hydrogenic ions, i.e. for HI and HeII, and not too far above the ionisation threshold, the dependence on energy can be well approximated by a single power-law,

$$\sigma_i = 6.3 \times 10^{-18}\ {\rm cm}^2 \frac{f_i}{A_i}\left(\frac{\nu}{\nu_i}\right)^{-3}, \tag{7.15}$$

where $f_{\rm HI} = 1$ and $f_{\rm HeII} = 1.21$ (Theuns et al. 1998) and A_i is the atomic number. The dependence of the HeI photo-ionisation cross-section is more difficult to approximate and requires the use of a combination of two power-laws (Osterbrock 1989). The (non-relativistic) high-energy scaling ($\nu \gg \nu_i$) is $\sigma_{\gamma i} \propto \nu^{-3.5}$ (e.g. Bethe & Salpeter 1957; Verner et al. 1996).

Fits to photo-ionisation cross-sections have, for example, been presented in Osterbrock (1989, their Eq. 2.31) and Verner et al. (1996). We show the cross-sections for photo-ionisation of HI, HeI and HeII using these fits in Fig. 7.1. In this work we employ the fits of Verner et al. (1996).

The photo-ionisation rates can be expressed in terms of the total number of ionising photons $\dot{\mathcal{N}_\gamma} = \int_{\nu_i}^{\infty} d\nu \frac{4\pi J_\nu(\nu)}{h_{\rm p}\nu}$,

$$\Gamma_{\gamma i} = \langle\sigma_{\gamma i}\rangle \dot{\mathcal{N}_\gamma}, \tag{7.16}$$

where $\langle\sigma_{\gamma i}\rangle$ is the average (or grey, cp. Sec. 5.3.5 in Chapter 5) photo-ionisation cross-section,

$$\langle\sigma_{\gamma i}\rangle \equiv \int_{\nu_i}^{\infty} d\nu \frac{4\pi J_\nu(\nu)}{h_{\rm p}\nu}\sigma_{\gamma i}(\nu) \times \left[\int_{\nu_i}^{\infty} d\nu \frac{4\pi J_\nu(\nu)}{h_{\rm p}\nu}\right]^{-1}. \tag{7.17}$$

The average photo-ionisation cross-section can only be calculated analytically for a few special cases, for instance, when both the spectrum and the cross-section can be expressed as power-laws of frequency. No analytic solution is available for the important case of a black-body spectrum,

$$J_\nu(\nu) \propto 2h_{\rm p}(\nu^3/c^2)/(\exp[h_{\rm p}\nu/(kT_{\rm bb})] - 1), \tag{7.18}$$

and the Verner et al. (1996) form of the photo-ionisation cross-sections referred to in Table 7.1. The numerically calculated average photo-ionisation cross-sections $\langle\sigma_{\gamma i}\rangle$ are shown in the left-hand panel of Fig. 7.1. The values for a black-body temperature $T_{\rm bb} = 10^5$ K are $\langle\sigma_{\gamma \rm HI}\rangle = 1.63 \times 10^{-18}$ cm^2, $\langle\sigma_{\gamma \rm HeI}\rangle = 4.13 \times 10^{-18}$ cm^2 and $\langle\sigma_{\gamma \rm HeII}\rangle = 1.06 \times 10^{-18}$ cm^2.

7.2.2 Collisional ionisation

The number of collisional ionisations per unit volume and unit time of species i by particle j, $n_j n_i \Gamma_{ji}$, can be written as $n_j n_i \langle v\sigma_{ji}\rangle$, where $\langle v\sigma_{ji}\rangle$ is the collisional ionisation cross-section averaged over the velocity distribution of the ionising particles j. We note that the inverse process, i.e. collisional recombination, is a three-body interaction (between the ion, the colliding particle and the recombining electron). For the low density plasmas of interest here we can therefore ignore this process. We only consider collisional ionisation of HI, HeI and HeII by electron impact (i.e. $i \in$ {HI, HeI, HeII} and $j =$ e), but note that collisional ionisation by other particles (e.g. cosmic rays) may also occur. The collisional ionisation rate coefficients we employ are derived using the coronal approximation (e.g. Osterbrock 1989), i.e. assuming that all ions are in their respective ground states. This is a valid assumption for the low densities of interest, but may be subject to reconsideration in the presence of a strong radiation background.

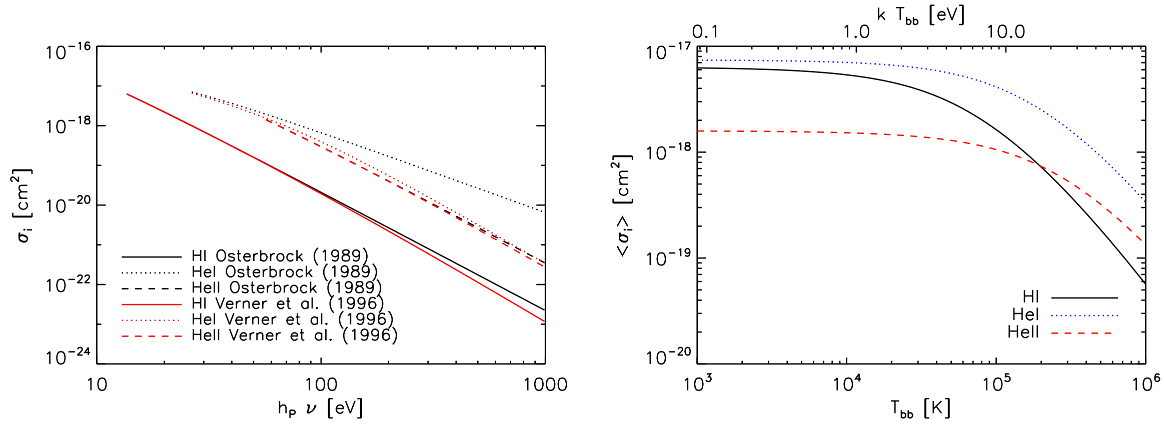

Figure 7.1: *Left-hand panel:* Cross-sections $\sigma_{\gamma i}$ for photo-ionisation of HI, HeI and HeII by photons of energy $h_{\rm p}\nu$. For each species, the cross-sections from Osterbrock (1989) are larger than those of Verner et al. (1996) for high photon energies, which obey the proper scaling for very high energies, $\sigma_{\gamma i} \sim \nu^{-3.5}$. The cross-section reported in (Osterbrock 1989, their Eq. 2.31), on the other hand, are approximations that are only good for photon energies within a few times the threshold energy. *Right-hand panel:* Average photo-ionisation cross-section $\langle\sigma_{\gamma i}\rangle$ (Eq. 7.16) for a range of temperatures of the incident black-body spectrum J_ν. We used the Verner et al. (1996) fits to the photo-ionisation cross-sections.

In Fig. 7.2 we show fits to the coefficients of collisional ionisation rates that are commonly employed in the literature. We briefly explain their origin and their range of validity below.

Lotz (1967) provided fits to experimental data on cross-sections for electron-impact collisional ionisation from the ground state for a large number of ions and tabulated collisional ionisation rate coefficients over the temperature range 10^3 K $\lesssim T \lesssim 10^7$ K, assuming a Maxwellian distribution for the electron velocities. These coefficients have been employed by Black (1981), who provided fits to the tabulated coefficients valid over the temperature range 10^4 K $\lesssim T \lesssim 2\times10^5$ K. Cen (1992) extended these fits to higher temperatures, multiplying them by[1] $(1 + (T/10^5\ \mathrm{K})^{1/2})^{-1}$. Theuns et al. (1998) multiplied the fits from Cen (1992) by a factor of two to improve the high temperature corrections, such that they are in better agreement with the Black (1981) fits in the low temperature regime. Hui & Gnedin (1997) used their own fits to the Lotz (1967) tabulated collisional ionisation coefficients, valid over the temperature range 10^4 K $\lesssim T \lesssim 10^9$ K. They agree very well with the fits used by Abel et al. (1997) for $T \gtrsim 10^4$ K.

In this work we employ the fits provided by Theuns et al. (1998). As can be seen from Fig. 7.2, for $T < 10^7$ K these fits show the least deviation from the Hui & Gnedin (1997) fits, which we consider to be the most accurate over this temperature interval (because they are direct fits to experimental data). We prefer them over the Hui & Gnedin (1997) fits, because they additionally obey the correct high temperature scaling ($\propto T^{-1/2}$).

7.2.3 Recombination

The number of radiative recombinations of ion i (with $i \in \{\mathrm{HII, HeII, HeIII}\}$) to energy level l occurring per unit time per unit volume $n_{\rm e} n_i \alpha_{il}$ may be written as $n_{\rm e} n_i \langle v\sigma_{il}\rangle$, where $\langle v\sigma_{il}\rangle$ is the recombination cross-section averaged over the velocity distribution of the recombining electrons. Radiative recombination is the inverse process of photo-ionisation. The cross-sections

---

[1] At high kinetic energies, $\sigma_{ji} \propto v^{-2}$, and hence $v\sigma_{ji} \propto T^{-1/2}$ (e.g. p. 16f of Osterbrock 1989).

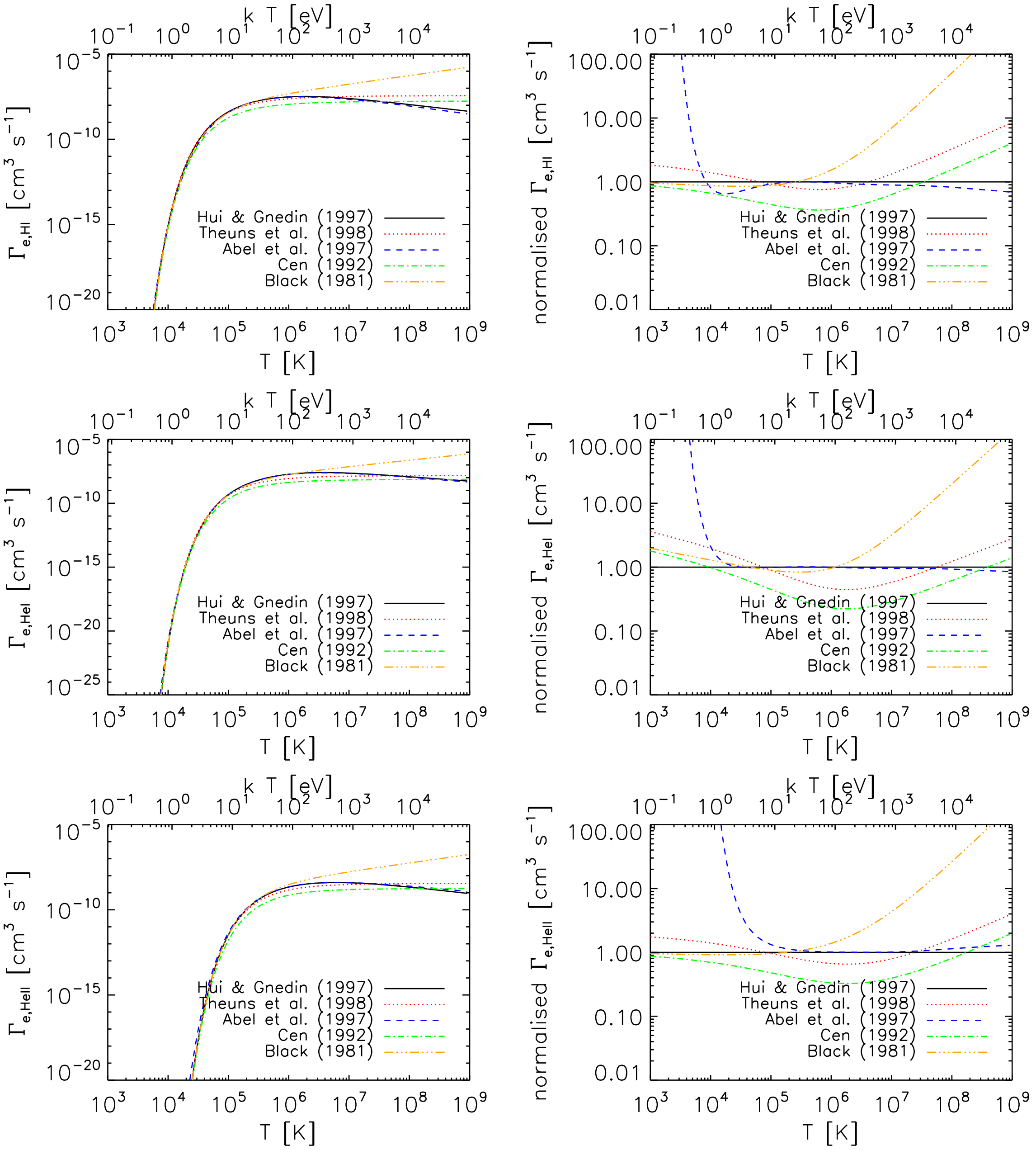

Figure 7.2: *Left-hand panels:* Rate coefficients for collisional ionisation of HI (top), HeI (middle) and HeII (bottom) by electron impact. *Right-hand panels:* Same as the left-hand panels, but all rates have been divided by the Hui & Gnedin (1997) rates to facilitate their comparison.

for radiative recombination and photo-ionisation are therefore closely connected, as expressed by the Milne (or Einstein-Milne) relations (e.g. Rybicki & Lightman 2004). It is thus clear that the accuracy of calculations of the radiative recombination coefficients depends on the accuracy with which the photo-ionisation cross-sections have been obtained.

Two recombination coefficients are of special interest and are referred to as case A and case B. The case A recombination coefficient $\alpha_{\mathrm{A}i} \equiv \sum_{l=1} \alpha_{il}$ is the sum over all the recombination coefficients α_{il}. On the other hand, the case B recombination coefficient is defined as $\alpha_{\mathrm{B}i} \equiv \sum_{l=2} \alpha_{il}$ and thus does not include the contribution from recombinations to the ground state. The introduction of the case B recombination coefficient is motivated by the observation that for pure hydrogen gas that is optically thick to ionising radiation, recombinations to the ground state are cancelled by the immediate re-absorption of the recombination photon by a neutral atom in the vicinity of the recombining ion. Radiative transfer simulations of ionising radiation in an optically thick hydrogen-only gas may therefore work around the (often expensive) explicit transfer of recombination photons by simply employing the case B (instead of the full, i.e. case A) recombination coefficient. Although this on-the-spot-approximation (e.g, Osterbrock 1989) is only strictly valid when considering the transport of ionising radiation in optically thick gas, it is for simplicity usually also employed in radiative transfer simulations to model the transport of radiation in gas that is optically thin (but see, e.g., Ritzerveld 2005).

In Fig. 7.3 we show fits to the case A and case B radiative recombination coefficients that are commonly employed in the astrophysical literature. Hummer (1994) provided tables for the total radiative recombination coefficient (both case A and B) of hydrogen over the temperature range $10\ \mathrm{K} < T < 10^7\ \mathrm{K}$. Recombination coefficients for hydrogen were also obtained by Ferland et al. (1992) over the temperature range $3\ \mathrm{K} \lesssim T < 10^{10}\ \mathrm{K}$. Accurate fits to these coefficients are presented in Hui & Gnedin (1997). As can be seen from Fig. 7.3, the coefficients from Hummer (1994) and Ferland et al. (1992) agree over the overlapping temperature interval. We also show the HII recombination coefficients presented in Spitzer (1978), which are based on calculations by Seaton (1959).

The recombination coefficients for hydrogenic ions (like HeIII) can be obtained by scaling along the iso-electronic series[2],

$$\alpha(T, Z) = Z\alpha(T/Z^2, 1), \tag{7.19}$$

where Z is the ion charge (e.g. Hummer 1994). Radiative recombination coefficients for non-hydrogenic ions are more difficult to obtain, due to their more complex atomic structure. For HeII, the only calculations of the *total* recombination coefficients we are aware of are the coefficients by Burgess & Seaton (1960) and Hummer & Storey (1998). The former tabulated the case A and B coefficients for only three temperatures (0 K, 10^4 K and 2×10^4 K), whereas the latter provided a dense grid of case A and B coefficients over the range $10\ \mathrm{K} < T < 10^{4.4}\ \mathrm{K}$. Black (1981) and Hui & Gnedin (1997) provide fits to the Burgess & Seaton (1960) coefficients. Surprisingly, they state a range of validity of $5 \times 10^3\ \mathrm{K} \lesssim T \lesssim 5 \times 10^5\ \mathrm{K}$. As can be seen in Fig. 7.3, the fit employed by Hui & Gnedin (1997) results in coefficients that differ from the coefficients tabulated by Hummer & Storey (1998) for $T \gtrsim 2 \times 10^4$ K, which is in agreement with the fact that the Hui & Gnedin (1997) fit should perhaps be considered to be valid only for $T \lesssim 2 \times 10^4$ K.

We have not yet discussed the dielectronic contribution to the HeII recombination coefficient. Dielectronic HeII recombination (e.g. Savin 2000a; Badnell 2001 for a review), like radiative HeII recombination, is the capture of a free electron along with the emission of a recombi-

---

[2] An iso-electronic series is a group of ions having the same number of bound electrons.

nation photon. In contrast to HeII radiative recombination, dielectronic HeII recombination is a two-step process that can only take place at certain free-electron energies: The free electron excites another electron in the recombining ion and in the process transfers sufficient energy that it is captured into an auto-ionising state. If an electron (either the captured one or another of the electrons in the ion) makes a spontaneous radiative transition to a non-auto-ionising state, then the recombination can be viewed as complete. Dielectronic recombination is the dominant recombination process for temperatures $T \gtrsim 10^5$ K (see Fig. 7.3). Its significance arises because it can take place via many intermediate auto-ionising states, increasing its effective statistical weight (e.g, Badnell et al. 2003). We note that the values for the dielectronic recombination rate coefficients are strongly sensitive to external electric and magnetic fields (Savin 2000b, Badnell 2001), impeding their determination. In the left-hand panel of Fig. 7.5 we show the dielectronic recombination coefficient computed and fitted by Aldrovandi & Pequignot (1973).

In this work we use the following coefficients to describe radiative recombinations. For HII and HeIII case A and case B radiative recombination, we employ the fits from Hui & Gnedin (1997), which are as accurate as the Hummer (1994) coefficients but extend over a larger temperature range. For the HeII case A and case B radiative recombination coefficient, we employ the tabulated coefficients of Hummer & Storey (1998) using linear interpolation in log-log and we add the dielectronic contribution from Aldrovandi & Pequignot (1973).

7.3 HEATING AND COOLING

Our main goal in this chapter is to thermally couple our radiative transfer code TRAPHIC, that is, to compute, in addition to the evolution of the ionisation state, the evolution of the temperature of gas parcels exposed to ionising radiation. For the discussion it is helpful to review the relevant thermodynamical relations, which is the subject of this section.

The internal energy per unit mass for gas of monoatomic species that are at the same temperature T is

$$u = \frac{3}{2}\frac{nk_{\rm B}T}{\rho} = \frac{3}{2}\frac{k_{\rm B}T}{\mu m_{\rm H}}, \tag{7.20}$$

where k_B is the Boltzmann constant and μ is the mean particle mass in units of the hydrogen mass,

$$\begin{aligned}
\mu &= \frac{\rho}{nm_H} && (7.21)\\
&= \frac{\rho}{m_{\rm H}\left(n_{\rm e} + \sum n_i\right)} && (7.22)\\
&= \frac{\rho}{m_{\rm H}\sum(1+Z_i)n_i} && (7.23)\\
&= \left(\sum \frac{X_i(1+Z_i)}{\mu_i}\right)^{-1}. && (7.24)
\end{aligned}$$

In the last equation, Z_i is the number of free electrons contributed by species i, where $i = \mathrm{H}, \mathrm{He}$. For neutral gas $\mu = 1.230$, for a singly ionised gas $\mu = 0.615$ and for a fully ionised gas $\mu = 0.593$.

From the first law of thermodynamics (which states that the energy of a closed system is conserved),

$$d(u\rho V) = -PdV + n_{\rm H}^2(\mathcal{H} - \mathcal{C})V, \tag{7.25}$$

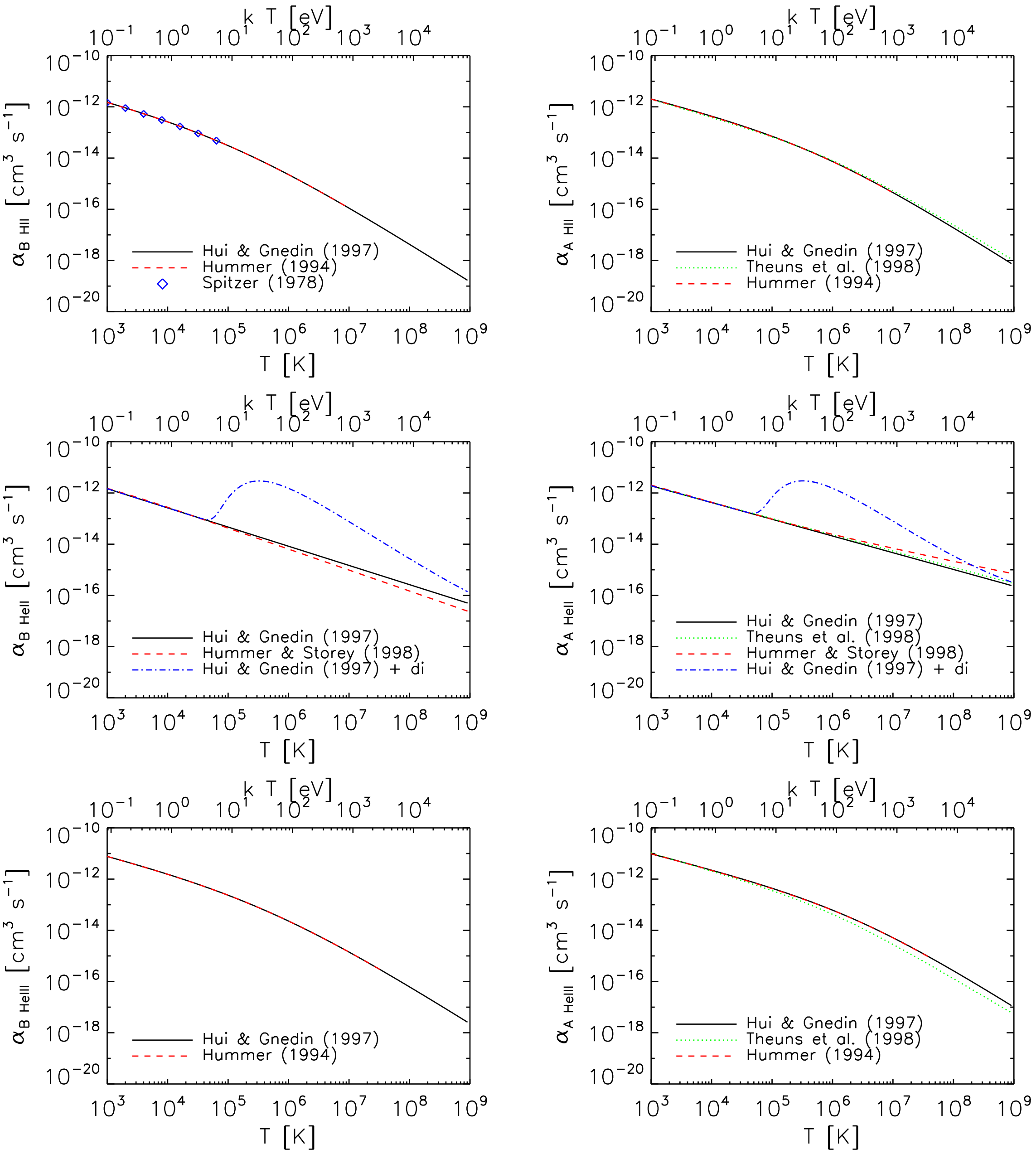

Figure 7.3: *Left-hand panels:* Case B recombination rate coefficients for HII (top), HeII (middle) and HeIII (bottom). For HeII, dielectronic recombination dominates for temperatures $T \gtrsim 10^5$ K. *Right-hand panels:* Case A recombination rate coefficients for HII (top), HeII (middle) and HeIII (bottom).

where $\mathcal{H}$ and $\mathcal{C}$ are the normalised heating and cooling rates, such that the rates of energy gain and loss per unit volume are described by $n_{\rm H}^2\mathcal{H}$ and $n_{\rm H}^2\mathcal{C}$, respectively. It follows that

$$\frac{du}{dt} = -\frac{P}{\rho V}\frac{dV}{dt} + \frac{n_{\rm H}^2}{\rho}(\mathcal{H}-\mathcal{C}), \tag{7.26}$$

where we have assumed that mass is conserved, $d(\rho V) = 0$. Using 7.20 and the ideal gas law, we find that the gas temperature evolves according to

$$\frac{dT}{dt} = \frac{2\mu m_{\rm H} n_{\rm H}^2}{3\rho k_{\rm B}}(\mathcal{H}-\mathcal{C}) + \frac{T}{\mu}\frac{d\mu}{dt} - \frac{2T}{3V}\frac{dV}{dt}. \tag{7.27}$$

For applications in cosmology it is useful to rewrite the last equation using $-dV/V = d\rho/\rho = d(\langle\rho\rangle\Delta)/\rho$, where $\langle\rho\rangle$ is the average (gas) density of the Universe and $\Delta \equiv \rho/\langle\rho\rangle$ is the (local) overdensity. Then,

$$\frac{dT}{dt} = \frac{2\mu m_{\rm H} n_{\rm H}^2}{3\rho k_{\rm B}}(\mathcal{H}-\mathcal{C}) + \frac{T}{\mu}\frac{d\mu}{dt} - 2HT + \frac{2T}{3\Delta}\frac{d\Delta}{dt}. \tag{7.28}$$

We have employed the Hubble constant $H \equiv \dot{a}/a$ at redshift $z = a^{-1} - 1$. With these substitutions the terms on the right-hand side of Eq. 7.28 can be interpreted as follows. The first term accounts for radiative heating and cooling, the second term accounts for changes in the mean particle mass (caused by changes in the electron number density), the third and fourth term account for adiabatic cooling due to cosmological expansion and structure formation, respectively.

In the following we briefly discuss the processes that contribute to the heating and cooling rate, relying in large parts on the presentations in the text books by Osterbrock (1989), Spitzer (1978) and Rybicki & Lightman (2004). As part of this discussion we compare cooling rates that are commonly employed in the literature. Based on this comparison we build our reference set of cooling rates that we will employ in this chapter and which is summarised in Tbl 7.1.

7.3.1 Cooling

The normalised cooling rate $\mathcal{C}$ is the sum over the contributions from the rates of the individual cooling processes,

$$\mathcal{C} = \sum c_i. \tag{7.29}$$

The cooling processes i that we consider are collisional ionisation by electron impact (cic), radiative + dielectronic recombination (rec), collisional excitation by electron impact (cec), bremsstrahlung (brems) and Compton scattering (compton).

Collisional ionisation cooling

We assume that for each collisional ionisation by electron impact the ionisation threshold energy $h\nu_i$ is removed from the thermal bath (e.g. Shapiro & Kang 1987). Hence, we write

$$c_{\rm cic} = \eta_{\rm e}\sum_i \eta_i \xi_{{\rm cic},i}, \tag{7.30}$$

where $\xi_{{\rm cic},i} = h_{\rm p}\nu_i\Gamma_{{\rm e}i}$ is the collisional ionisation cooling rate coefficient and $i \in \{\text{HI, HeI, HeII}\}$. We employ the collisional ionisation rate coefficients $\Gamma_{{\rm e}i} = \langle v\sigma_{{\rm e}i}\rangle$ discussed in Sec. 7.2.2.

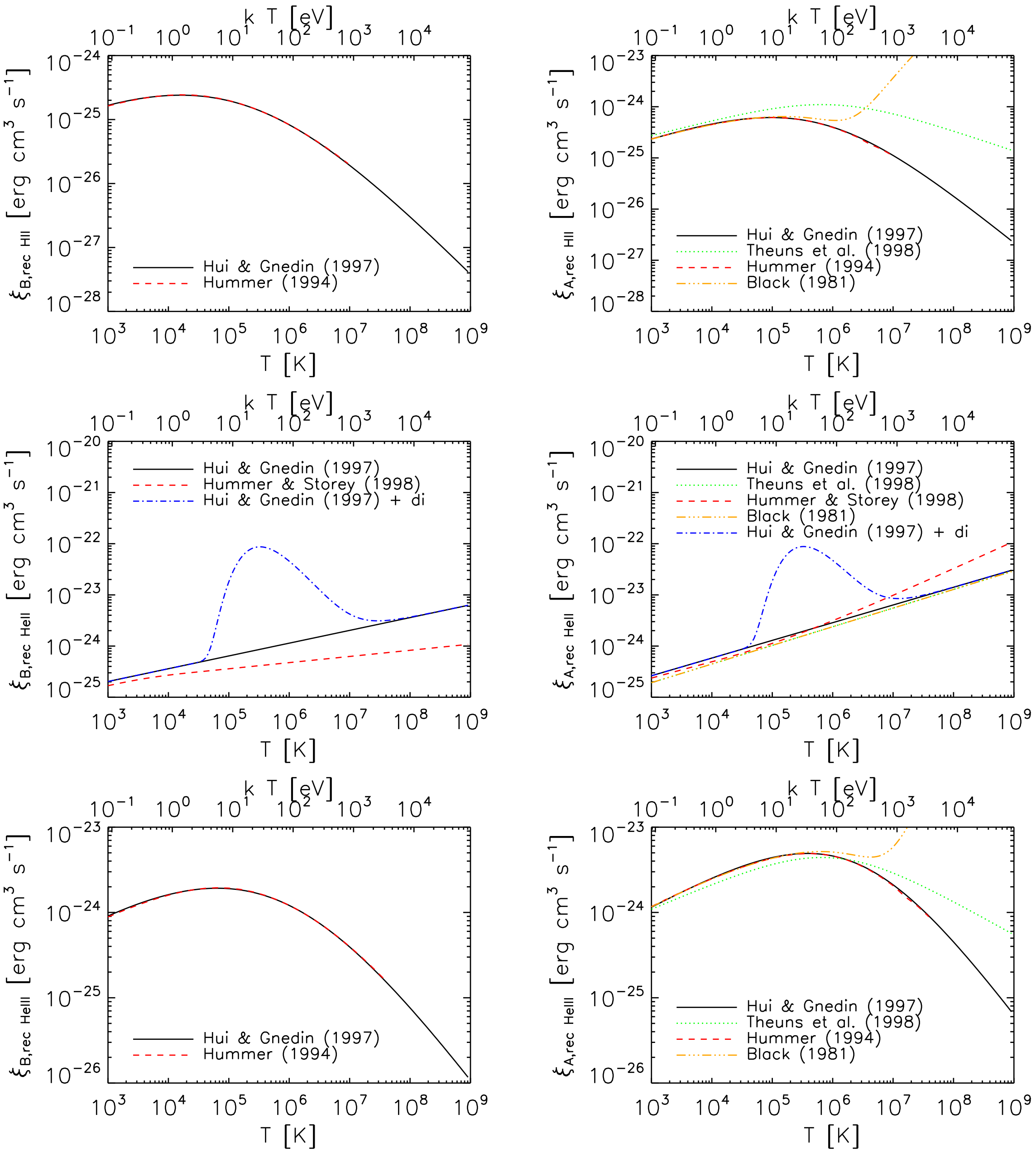

Figure 7.4: *Left-hand panels:* Case B recombination cooling rate coefficients for HII (top), HeII (middle) and HeIII (bottom). *Right-hand panels:* The same as left-hand panels, but for case A recombination cooling.

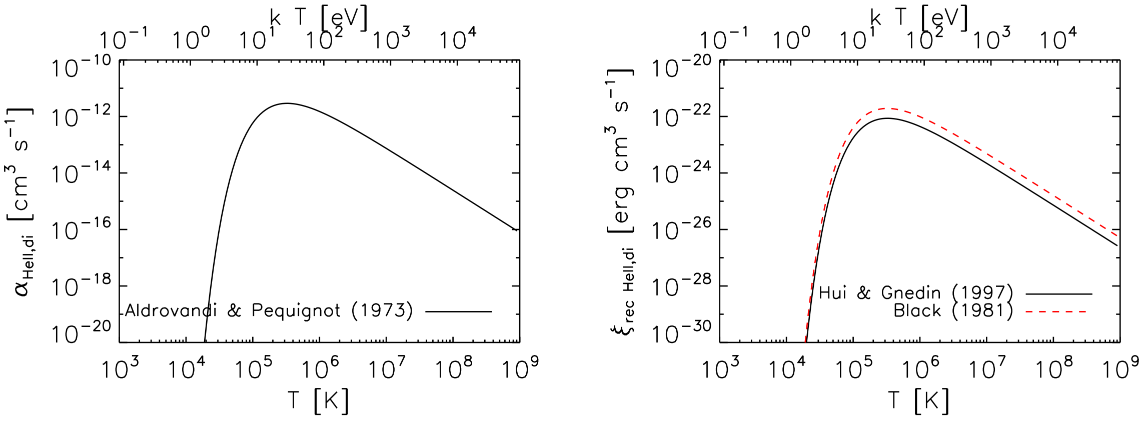

Figure 7.5: *Left-hand panel:* The dielectronic contribution to the HeII recombination coefficient. *Right-hand panel:* The dielectronic contribution to the HeII recombination cooling coefficient.

Recombination cooling

The kinetic energy released per unit volume per unit time due to radiative recombination of ion i is given by

$$n_{\rm H}^2 c_{\rm rec} = \eta_{\rm e} n_{\rm H}^2 \sum_i \eta_i \xi_{{\rm rec},i}, \tag{7.31}$$

where

$$\xi_{{\rm rec},i} = \sum_{l=l_0} \langle v\sigma_{il} m_{\rm e} v^2/2 \rangle \tag{7.32}$$

is the *kinetic-energy-averaged* recombination rate coefficient (e.g. Osterbrock 1989) and $i \in \{$HII, HeII, HeIII$\}$. In Fig. 7.4 we show fits to the recombination cooling coefficients $\xi_{{\rm rec},i}$ for case A and B recombinations that are commonly employed in cosmological simulations.

Case A and B recombination cooling coefficients $\xi_{{\rm rec},i}$ for hydrogenic ions have been presented in Hummer (1994) and Ferland et al. (1992). Accurate fits to the Ferland et al. (1992) coefficients are given in Hui & Gnedin (1997). They agree very well with the Hummer (1994) coefficients. The same is true for the case A coefficients used by Black (1981) over their range of validity 5×10^3 K $\lesssim T \lesssim 5 \times 10^5$ K. In contrast, the case A recombination cooling coefficients used in Theuns et al. (1998) (which are identical to those used in Cen 1992) show a very different behaviour. These coefficients are based on the Black (1981) coefficients, but were adapted to extend their range of validity to higher temperatures. This adaption seems to have degraded the accuracy of the coefficients for temperatures $T \lesssim 10^6$ K, without bringing them in agreement with the Hui & Gnedin (1997) or Hummer (1994) coefficients at higher temperatures.

For HeII recombination cooling, coefficients have been tabulated by Hummer & Storey (1998) (not including cooling due to dielectronic recombination). Hui & Gnedin (1997) presented HeII (and HeII dielectronic) recombination cooling rates obtained by multiplying their HeII (and HeII dielectronic) recombination rates by the ionisation threshold energy (for dielectronic recombination cooling they employ an additional factor 0.75). The reasoning behind this recipe remains somewhat unclear to us.

In this work we evaluate the recombination cooling rate using the following values for the coefficients $\xi_{{\rm rec},i}$. For HII and HeIII recombination cooling we use the fits to $\xi_{{\rm rec},i}$ by Hui & Gnedin (1997). For HeII recombination cooling we use the tabulated coefficients of Hummer

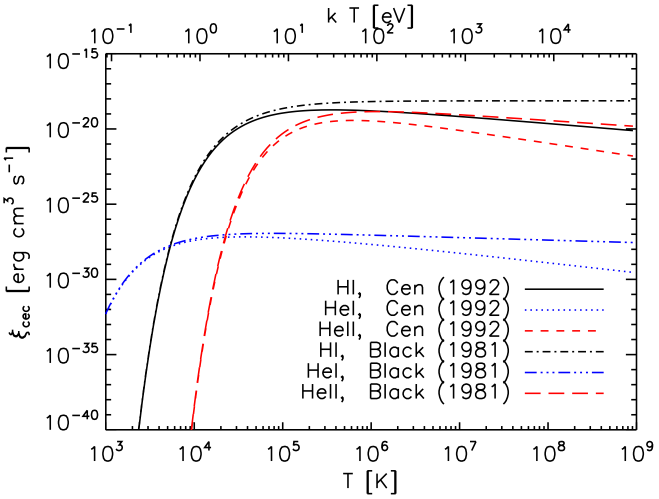

Figure 7.6: Rate coefficients for radiative cooling by electron-impact collisional excitation.

& Storey (1998), linearly interpolating in log-log. We add the dielectronic contribution to the cooling coefficient from Black (1981).

Collisional excitation cooling

Electron-atom (electron-ion) collisions may excite the atoms (ions). The excitation energy may then be radiated away in the subsequent de-excitation. We will see later, in Sec. 7.6.1, that de-excitation cooling from collisionally excited atoms and ions, i.e. collisional excitation cooling, constitutes one of the most important cooling processes that determine the evolution of the temperature in a cosmological setting.

For illustration, we consider the collisional excitation of a two-level atom by electrons[3], following Osterbrock (1989). The cross-section σ_{12} for excitation from level 1 to level 2 is a function of the electron kinetic energy. It is zero for kinetic energies below the excitation energy χ_{12}. For larger energies it approaches the asymptotic scaling $\sigma_{12} \propto v^{-2}$ (see Sec. 7.2.2). It is therefore common to introduce the (dimensionless) collision strength Ω_{12} and write

$$\sigma_{12} = \frac{\pi \hbar^2}{m_{\rm e}^2 v^2} \frac{\Omega_{12}}{\omega_1}, \text{for } m_{\rm e} v^2/2 > \chi_{12}, \tag{7.33}$$

where ω_1 is the statistical weight of the lower level. Ω_{12} generally is a function of velocity, but close to the excitation threshold χ_{12} can be well approximated by a constant.

With this definition, the collisional excitation rate per unit volume per unit time is $n_{\rm e} n_1 \langle v \sigma_{12} \rangle$, where n_1 is the density of atoms in level 1 and the average is over the velocity distribution of the electrons. In the limit of very low electron density ($n_{\rm e} \rightarrow 0$) each collisional excitation is followed by a spontaneous emission (at rate A_{12}) of a photon with frequency ν_{21}. In this case, the cooling rate is given by $n_{\rm H}^2 c_{\rm cec} = n_{\rm e} n_1 \xi_{\rm cec}$, where $\xi_{\rm cec} = \langle v \sigma_{12} \rangle h_{\rm P} \nu_{21}$ is the collisional excitation cooling rate coefficient. We note that for larger densities the cooling rate is reduced due to collisional de-excitations (e.g. Osterbrock 1989). Asymptotically, for $n_{\rm e} \rightarrow \infty$ it is given by the thermodynamic-equilibrium rate $n_{\rm H}^2 c_{\rm cec} = n_1 (w_2/w_1) \exp(-\chi_{12}/k_{\rm B} T) A_{12} h_{\rm P} \nu_{21}$.

---

[3] We note that collisional excitation by neutral atoms may become important for low ionised fractions. Collisional excitation by ions can generally be neglected because of the Coulomb repulsion between the colliding particles (e.g. Dalgarno & McCray 1972)

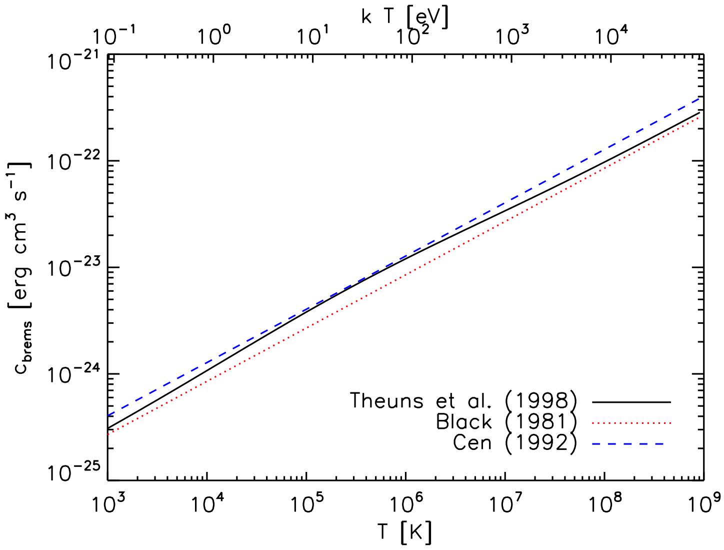

Figure 7.7: Normalised bremsstrahlung cooling rate. Different rates only differ in the employed gaunt factors.

In this work we employ collisional excitation cooling rates in the low-density limit $n_{\rm e} \rightarrow 0$, which is appropriate for the cosmological simulations of interest (e.g., Tegmark et al. 1997). Values for the collisional excitation cooling rate coefficients are highly uncertain (e.g. Chang, Avrett, & Loeser 1991). In this work we use the coefficients from Cen (1992), as shown in Fig. 7.6, which are commonly employed in the literature. They are based on Black (1981) but are corrected such as to obey the proper high-temperature scaling. It is, however, not clear whether they should be modified to cancel a possible over-correction (as was done for the collisional ionisation coefficients by Theuns et al. 1998, see Sec. 7.2.2).

Bremsstrahlung

Bremsstrahlung, or free-free emission, is radiation emitted due to the acceleration of a charge in the electric field of another charge (e.g. Rybicki & Lightman 2004). The bremsstrahlung emissivity is often computed using classical physics and quantum effects are taken into account by multiplication of the classical result with a corrective term, the so-called gaunt factor $g_{\rm f}$. We limit ourselves to non-relativistic thermal bremsstrahlung, which is valid for electrons obeying a Maxwellian velocity distribution of temperature $T < m_{\rm e}c^2/k_{\rm B} \lesssim 10^9$ K. As noted in Rybicki & Lightman (2004), bremsstrahlung due to collisions of like particles (e.g. electron-electron) is zero in the dipole approximation, because the dipole moment is simply proportional to the centre of mass, a constant of the motion. One must therefore consider two different particles.

In Fig. 7.7 we show (normalised) bremsstrahlung cooling rates employed in the literature,

$$c_{\rm brems} = 1.42 \times 10^{-27} g_{\rm f} T^{1/2} \eta_{\rm e} (\eta_{\rm HII} + \eta_{\rm HeII} + 4\eta_{\rm HeIII}). \qquad (7.34)$$

The quoted rates only differ in the gaunt factor employed, which is sometimes just taken to be constant (Black 1981; Cen 1992) and sometimes depends on the temperature (Theuns et al. 1998). In this work we employ the Theuns et al. (1998) gaunt factor.

Compton cooling

Electrons can loose energy by Compton scattering off photons. The associated Compton cooling[4] rate per unit volume is (Weymann 1965)

$$n_{\rm H}^2 c_{\rm compton} = \frac{4aT_\gamma^4 \sigma_{\rm T} n_{\rm e}}{m_{\rm e}c}(k_{\rm B}T - k_{\rm B}T_\gamma), \tag{7.35}$$

where a is the Stefan-Boltzmann constant, $\sigma_{\rm T}$ is the Thompson scattering cross-section, $m_{\rm e}$ is the electron mass and $k_{\rm B}T_\gamma$ is the photon energy. The derivation of the last expression assumes a low-energy, homogeneous, isotropic photon gas interacting with a low-density, non-relativistic electron gas with a Maxwellian distribution.

In the cosmological context, Compton cooling occurs because hot electrons scatter off cosmic microwave background photons. The photon energy of the cosmic microwave background at redshift z is $T_\gamma = 2.73(1+z)$ K (Fixsen et al. 1996). Thus, Compton cooling, which scales as T_γ^4 for $T \gg T_\gamma$, becomes important at high redshifts. We therefore include Compton cooling off the microwave background in our compilation of cooling rates, employing the numerical expression provided in Theuns et al. (1998).

7.3.2 Heating

The normalised heating rate $\mathcal{H}$ is the sum over the contributions from the rates of the individual heating processes,

$$\mathcal{H} = \sum h_i. \tag{7.36}$$

Spitzer (1948) provides a detailed discussion of the importance of various heating processes. Here we only consider the contribution from photo-ionisation heating, which will be the main contributor to the heating rate for the high-redshift radiative transfer simulations of interest. We note, however, that Compton heating by X-rays may not be negligible (Madau & Efstathiou 1999).

Photo-ionisation heating

We write the heating rate due to photo-ionisation as

$$n_{\rm H}^2 h_\gamma = (\eta_{\rm HI}\mathcal{E}_{\gamma\rm HI} + \eta_{\rm HeI}\mathcal{E}_{\gamma\rm HeI} + \eta_{\rm HeII}\mathcal{E}_{\gamma\rm HeII})n_{\rm H} \tag{7.37}$$

where

$$\mathcal{E}_{\gamma i} = \int_{\nu_i}^{\infty} d\nu \frac{4\pi J_\nu(\nu)}{h_{\rm p}\nu}\sigma_{\gamma i}(\nu)(h_{\rm p}\nu - h_{\rm p}\nu_i). \tag{7.38}$$

Using Eq. 7.14, we can write

$$\mathcal{E}_{\gamma i} = \Gamma_{\gamma i}\langle\epsilon_i\rangle, \tag{7.39}$$

where

$$\langle\epsilon_i\rangle = \left[\int_{\nu_i}^{\infty} d\nu \frac{4\pi J_\nu(\nu)}{h_{\rm p}\nu}\sigma_{\gamma i}(\nu)(h_{\rm p}\nu - h_{\rm p}\nu_i)\right]\left[\int_{\nu_i}^{\infty} d\nu \frac{4\pi J_\nu(\nu)}{h_{\rm p}\nu}\sigma_{\gamma i}(\nu)\right]^{-1} \tag{7.40}$$

is the average excess energy of ionising photons. Note that, using Eq. 7.16, $\mathcal{E}_{\gamma_i} = \langle\sigma_{\gamma i}\rangle\langle\epsilon_i\rangle\dot{\mathcal{N}}_\gamma$.

---

[4] Note that for $T_\gamma > T$, Compton scattering provides a heating mechanism.

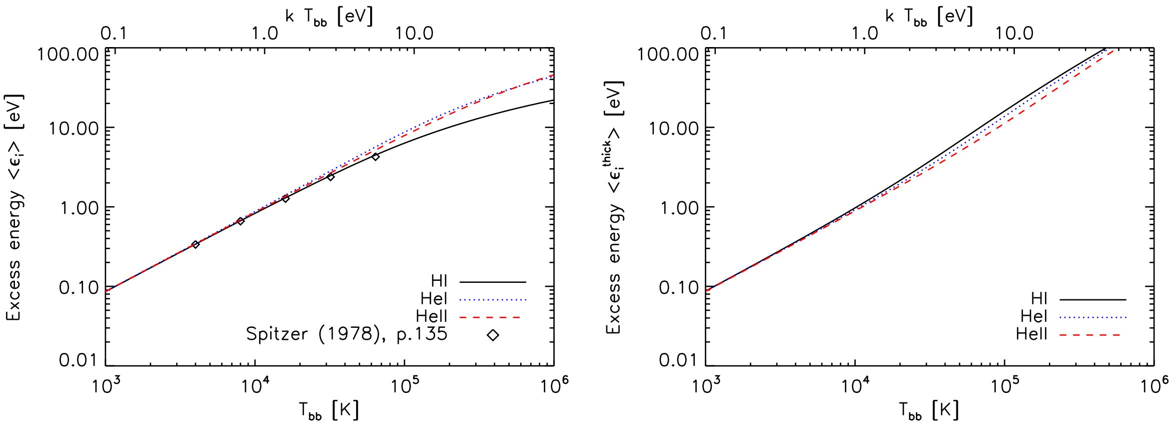

Figure 7.8: Average excess energy injected per photo-ionisation of species i for a range of temperatures of the incident black-body spectrum J_ν. *Left-hand panel:* Optically thin case (Eq. 7.40), using the fits to the photo-ionisation cross-sections reported in Verner et al. (1996). For comparison, we show the average excess energy per photo-ionisation of a hydrogen atom presented in Spitzer (1978). Note that $\langle\epsilon_i\rangle \sim k_{\mathrm{B}}T_{\mathrm{bb}}$ for black-body temperatures $T_{\mathrm{bb}} \lesssim 10^5$ K typical of stars. *Right-hand panel:* Optically thick case (Eq. 7.41), i.e. assuming photo-ionisation cross-sections $\sigma_{\gamma i} = 1$.

As for the average photo-ionisation cross-section, the average excess energy can be calculated analytically for only a few special cases. For the important case of a black-body spectrum and the functional form of the Verner et al. (1996) photo-ionisation cross-section referred to in Table 7.1, no analytic solution is available. The numerically calculated average excess energies $\langle\epsilon_i\rangle$ are shown in the left-hand panel of Fig. 7.8. For example, the values for a black-body temperature $T_{\mathrm{bb}} = 10^5$ K are $\langle\epsilon_{\mathrm{HI}}\rangle = 6.32$ eV, $\langle\epsilon_{\mathrm{HeI}}\rangle = 8.70$ eV and $\langle\epsilon_{\mathrm{HeII}}\rangle = 7.88$ eV. Note that the average excess energy is about equal to $k_{\mathrm{B}}T_{\mathrm{bb}}$ for black-body temperatures typical of stars (Spitzer 1948).

Sometimes, e.g. when considering the energy balance of entire HII-regions, one is interested in computing the total photo-heating rate integrated over a finite volume, assuming all photons entering this volume are absorbed within it. The average excess energy injected at each photo-ionisation in this optically thick limit is also obtained from Eq. 7.40, but after setting $\sigma_{\gamma i}(\nu) = 1$, since all photons are absorbed (e.g., Spitzer 1978, p.135),

$$\langle\epsilon_i^{\mathrm{thick}}\rangle = \left[\int_{\nu_i}^{\infty} d\nu \frac{4\pi J_\nu(\nu)}{h_{\mathrm{p}}\nu}(h_{\mathrm{p}}\nu - h_{\mathrm{p}}\nu_i)\right]\left[\int_{\nu_i}^{\infty} d\nu \frac{4\pi J_\nu(\nu)}{h_{\mathrm{p}}\nu}\right]^{-1}. \tag{7.41}$$

We show the numerically calculated average excess energies for the optically thick case $\langle\epsilon_i^{\mathrm{thick}}\rangle$ in the right-hand panel of Fig. 7.8, assuming a black-body spectrum. As example, the values for a black-body temperature $T_{\mathrm{bb}} = 10^5$ K are $\langle\epsilon_{\mathrm{HI}}^{\mathrm{thick}}\rangle = 16.01$ eV, $\langle\epsilon_{\mathrm{HeI}}^{\mathrm{thick}}\rangle = 13.72$ eV and $\langle\epsilon_{\mathrm{HeII}}^{\mathrm{thick}}\rangle = 11.24$ eV.

In writing Eqs. 7.40 and 7.41 we assumed that all of the photon excess energy is used to heat the gas, corresponding to a complete thermalization of the electron kinetic energy. In reality, (very energetic) photo-electrons may loose some of their energy due to the generation of secondary electrons (e.g. Shull & van Steenberg 1985).

7.4 EQUILIBRIUM SOLUTION

Most state-of-the-art cosmological simulations do not include the transport of radiation, but compute photo-ionisation rates from a uniform photo-ionising background in the optically thin limit. The employed photo-ionisation rates imply typical photo-ionisation time scales much smaller than the Hubble time. The gas in these simulations is therefore assumed to remain in ionisation equilibrium. The internal energy of the gas is then evolved using cooling rates computed based on the equilibrium ionised fractions.

For reference, and as a consistency check, we here evaluate the cooling rates discussed in the previous section that we will employ in radiative transfer simulations with TRAPHIC for ionisation equilibrium.

7.4.1 Collisional ionisation equilibrium

For the special case of $\Gamma_{\gamma i} = 0$, that is, in the absence of ionising radiation (collisional ionisation equilibrium), the equilibrium ionised fractions are given by (set $\Gamma_{\gamma i} = 0$ in Eqs. 7.7 - 7.13)

$$\begin{aligned}
\eta_{\rm HI} &= \left(1 + \frac{\Gamma_{\rm eHI}}{\alpha_{\rm HII}}\right)^{-1}, &(7.42)\\
\eta_{\rm HII} &= 1 - \eta_{\rm HI}, &(7.43)\\
\eta_{\rm HeI} &= \eta_{\rm He} \times \left[1 + \frac{\Gamma_{\rm eHeI}}{\alpha_{\rm HeII}}\left(1 + \frac{\Gamma_{\rm eHeII}}{\alpha_{\rm HeIII}}\right)\right]^{-1}, &(7.44)\\
\eta_{\rm HeII} &= \eta_{\rm HeI}\frac{\Gamma_{\rm eHeI}}{\alpha_{\rm HeII}}, &(7.45)\\
\eta_{\rm HeIII} &= \eta_{\rm HeII}\frac{\Gamma_{\rm eHeII}}{\alpha_{\rm HeIII}}, &(7.46)\\
\eta_{\rm e} &= \eta_{\rm HII} + \eta_{\rm HeII} + 2\eta_{\rm HeIII}. &(7.47)
\end{aligned}$$

They are shown in the left-hand panel of Fig. 7.9. Using the equilibrium fractions, we determine the normalised individual and total cooling rates c_i and $\mathcal{C}$ (see Sec. 7.3). They are shown, for the rates listed in Table 7.1, in the middle and right-hand panels of Fig. 7.9, respectively. For reference, the total cooling rate is compared to cooling rates commonly employed in the literature, as indicated in the legend. Note that the ionised fractions in collisional ionisation equilibrium do not depend on the density of the gas, they only depend on its temperature. If we exclude Compton cooling from our considerations, then the normalised cooling rate also becomes independent of the density.

The dependence of the collisional equilibrium cooling rate on temperature, the collisional equilibrium *cooling curve*, has been well-studied (e.g., Cox & Tucker 1969; Sutherland & Dopita 1993; Schmutzler & Tscharnuter 1993; Gnat & Sternberg 2007). The cooling curve of atomic primordial gas exhibits two prominent peaks around the temperatures $T \sim 10^4$ K and $T \sim 10^5$ K, corresponding to cooling from collisionally excited hydrogen and singly ionised helium atoms, respectively. Temperatures $T < 10^4$ K are too low for atoms to be collisionally excited and the cooling curve shows a sharp cut-off. The cut-off is so steep because the distribution of the excitation states is given by the Boltzmann distribution, which depends exponentially on the temperature (Sec. 7.3.1). In reality, the gas would also contain molecular hydrogen (H_2) and deuterated hydrogen (HD), which would extend its ability to efficiently cool down to temperatures $T \lesssim 300$ K (e.g., Tegmark et al. 1997; Lipovka, Núñez-López, & Avila-Reese 2005). For

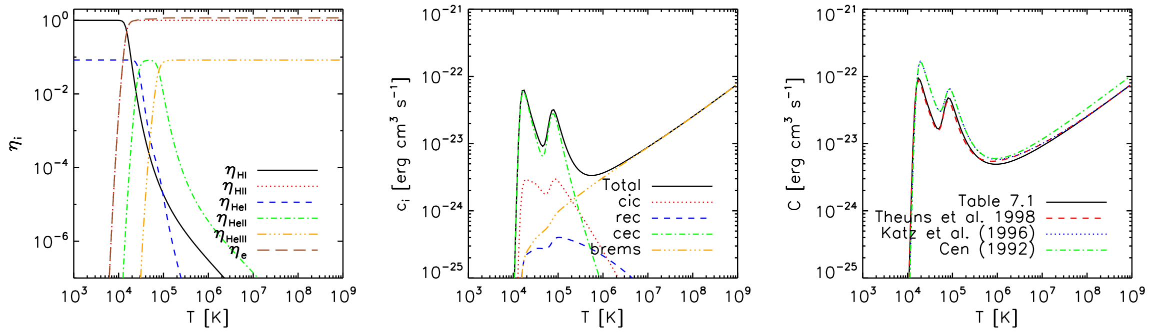

Figure 7.9: Case A collisional ionisation equilibrium. *Left-hand panel:* Equilibrium fractions. Note the small enhancement in $\eta_{\rm HeI}$ due to dielectronic recombination for $T \approx 10^5$ K. *Middle panel:* Total and individual normalised collisional equilibrium cooling rates employed in this work (Table 7.1). From top to bottom in the legend: total cooling, collisional ionisation cooling, recombination cooling, collisional excitation cooling, Bremsstrahlung. *Right-hand panel:* Comparison of the total normalised equilibrium cooling rate employed in this work (Table 7.1) with those employed in other works, as indicated in the legend. The contribution from Compton cooling to the total cooling rate has been excluded, such that the total normalised cooling rate becomes independent of the gas density and redshift.

temperatures $T \gtrsim 10^5$ K, on the other hand, both hydrogen and helium are too highly ionised (cp. the left-hand panel Fig. 7.9) to cool via collisional excitation. At these temperatures the gas cools mainly through the emission of bremsstrahlung due to the deceleration of the free electrons in the Coloumb field of the collisionally ionised hydrogen and helium atoms. We will see later (Fig. 7.10) that, for typical densities and redshifts, at these temperatures Compton cooling also becomes important.

7.4.2 Photo-ionisation equilibrium

Before we move on to discuss the general equilibrium solution, we briefly comment on the special case $\Gamma_{ei} = 0$ (pure photo-ionisation equilibrium) to point out the following interesting fact. In photo-ionisation equilibrium, each photo-ionisation of HI is offset by a recombination of HII. The hydrogen photo-ionisation rates are therefore simply related to the hydrogen recombination rates (set $\Gamma_{ei} = 0$ in Eqs. 7.7 and 7.8),

$$\eta_{\rm HI}\Gamma_{\gamma \rm HI} = \eta_{\rm HII}\alpha_{\rm HII} n_{\rm e} \tag{7.48}$$

The corresponding photo-heating rate per unit volume can thus be written as (see Sec. 7.3.2)

$$n_{\rm H}^2 h_{\gamma \rm HI} = n_{\rm HII}\alpha_{\rm HII} n_{\rm e}\langle\epsilon_{\rm HI}\rangle. \tag{7.49}$$

Hence in photo-ionisation equilibrium the heating rates associated with photo-ionisations of hydrogen are independent of the amplitude $\dot{\mathcal{N}}_\gamma$ of the ionising spectrum. They only depend on its spectral shape, through Eq. 7.40.

7.4.3 General ionisation equilibrium

In the general case, i.e. if both $\Gamma_{\gamma i} > 0$ and $\Gamma_{ei} > 0$, the equilibrium ionised fractions depend not only on the temperature, but also on the density of the gas (and on the ionising radiation field).

For illustration, we show these fractions, evaluated for three characteristic gas densities, in the top panels of Fig. 7.10. The ionised fractions shown in these panel assume a gas density equal to the cosmic mean density at redshifts $z = 9, 6$ and 3 (from left to right). We have assumed photo-ionisation rates $\Gamma_{\gamma \mathrm{HI}} = \Gamma_{\gamma \mathrm{HeI}} = 10^{-13}\ \mathrm{s}^{-1}$ and $\Gamma_{\gamma \mathrm{HeII}} = 10^{-15}\ \mathrm{s}^{-1}$ to be representative for photo-ionisation rates expected at redshifts $z = 9$ and 6, and $\Gamma_{\gamma \mathrm{HI}} = \Gamma_{\gamma \mathrm{HeI}} = 10^{-12}\ \mathrm{s}^{-1}$ and $\Gamma_{\gamma \mathrm{HeII}} = 10^{-14}\ \mathrm{s}^{-1}$ for $z = 3$ (e.g., Haardt & Madau 2001, Faucher-Giguère et al. 2008). The total (normalised) *net* (i.e. heating minus cooling) cooling rates computed using these equilibrium fractions are shown in the bottom panels of Fig. 7.10 (black solid curves). This time we have included Compton cooling. We have also indicated the contributions from the individual cooling processes and from photo-heating. For reference, the cooling rate computed using collisional ionisation equilibrium fractions is also shown (grey solid curve, with Compton cooling included).

The general ionisation equilibrium cooling curve exhibits several prominent differences with respect to the collisional ionisation equilibrium cooling curve discussed above. The net cooling curve shows a zero crossing at $T_{\mathrm{eq}} \sim 10^4$ K, where cooling is balanced by photo-heating. For temperatures $T < T_{\mathrm{eq}}$, the main contribution to the net cooling curve is from photo-heating and for temperatures $T > T_{\mathrm{eq}}$, the shape of the net cooling function is mainly determined by cooling.

The value for T_{eq} depends on both the gas density and the ionising radiation (e.g., Thoul & Weinberg 1996). A harder spectrum yields higher excess energies $\langle \epsilon_i \rangle$, raising the equilibrium temperature. Higher densities, on the other hand, increase the cooling and hence lower the equilibrium temperatures. Fig. 7.10 shows that for reasonable choices of parameters the equilibrium temperature of gas at the cosmic mean density increases from $T_{\mathrm{eq}} \approx 10^4$ K at $z = 9$ and $z = 6$ to $T_{\mathrm{eq}} \approx 2 \times 10^4$ K at $z = 3$. Note, however, that we have ignored the important contribution from adiabatic cooling of the gas due to the expansion of the Universe (Hui & Gnedin 1997).

Another important consequence of the inclusion of ionising radiation is the decrease of the amplitude of the cooling curve peaks at $T \sim 10^4$ K and $T \sim 10^5$ K. Here, the increased ionisation rate reduces the HI and HeI fractions, which lowers the efficiency of the gas to cool by emission of de-excitation radiation. Observe that the effect is stronger at $z = 6$ than at $z = 9$ and still stronger at $z = 3$, due to a decreased gas density. This reduction of the amplitude of the hydrogen and helium cooling peaks (and their slight shifts in position along the temperature axis) due to the inclusion of ionising radiation and its implications for the formation of structures in the Universe has been pointed out and thoroughly discussed in the past (e.g., Efstathiou 1992; Thoul & Weinberg 1996; Wiersma, Schaye, & Smith 2009).

For temperatures $T \gtrsim 10^5$ K, the inclusion of ionising radiation does not noticeably affect the cooling curve, because the atoms are already highly ionised due to collisional ionisation. Note that Compton scattering is the dominant cooling process for temperatures $T \gtrsim 10^7$ K for the densities and redshifts considered.

7.5 NON-EQUILIBRIUM SOLUTION

In the last section we presented cooling rates in ionisation equilibrium for known values of the gas temperature. The ionisation state and the gas temperature are, however, tightly coupled. In (cosmological) hydrodynamical simulations they are therefore not determined independently of each other. The ionised fractions depend on the gas temperature through the collisional ionisation and recombination rates. On the other hand, the temperature is determined by the

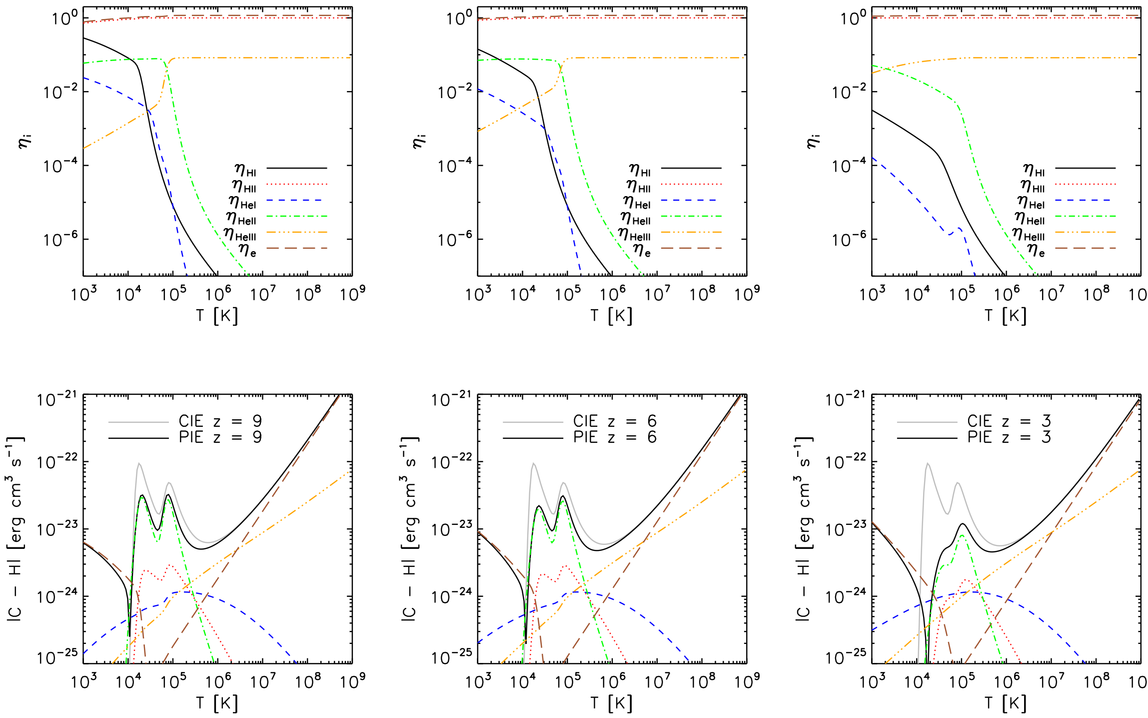

Figure 7.10: Case A ionisation equilibrium. *Top panels:* Equilibrium ionised fractions at redshift $z = 9, 6$ and 3 (from left to right) for gas at the cosmic mean density. *Bottom panels:* Total normalised (photo-) ionisation equilibrium (PIE) net cooling rates (black solid curves) computed using the equilibrium ionised fractions for gas at the cosmic mean density at redshifts $z = 9, 6$ and 3 shown in the top panels. We have assumed values for the photo-ionisation rates of $\Gamma_{\gamma\mathrm{HI}} = \Gamma_{\gamma\mathrm{HeI}} = 10^{-13}\ \mathrm{s}^{-1}$ and $\Gamma_{\gamma\mathrm{HeII}} = 10^{-15}\ \mathrm{s}^{-1}$ at both $z = 9$ and $z = 6$ and $\Gamma_{\gamma\mathrm{HI}} = \Gamma_{\gamma\mathrm{HeI}} = 10^{-12}\ \mathrm{s}^{-1}$ and $\Gamma_{\gamma\mathrm{HeII}} = 10^{-14}\ \mathrm{s}^{-1}$ at $z = 3$. We have indicated the contributions to the cooling rate from collisional excitation (green dot-dashed curve), collisional ionisation (red dotted curve), recombination (blue dashed curve), bremsstrahlung (orange triple-dot-dashed) and Compton scattering (brown long-dashed curve that converges towards the total net cooling curve at high temperatures). We have also shown the contribution from photo-heating (brown long-dashed curve that converges towards the total net cooling curve for low temperatures). For comparison, the total normalised cooling rate computed assuming collisional ionisation equilibrium (CIE) is also shown (grey solid curve, cp. Fig. 7.9), with Compton cooling included.

cooling rates, which depend on the ionised fractions.

In this section we will therefore study the combined evolution of ionised fraction and temperature. We will, moreover, drop the assumption of ionisation equilibrium and compute the evolution of the temperature of a gas parcel exposed to ionising radiation based on its non-equilibrium cooling rates. The cooling rates are determined using the non-equilibrium ionised fractions computed self-consistently along with the thermal evolution of the parcel. Our investigations will pave the way for accomplishing the main goal of this chapter, the thermal coupling of our radiative transfer code TRAPHIC.

We start by explaining our numerical method to follow the ionisation state and temperature of gas exposed to ionising radiation. We will then apply this method to solve an idealised test problem. For simplicity, we confine our considerations to gas consisting of hydrogen only, but expect that they are straight-forward to generalise.

7.5.1 Method and implementation

In Chapter 5 we presented a method to follow the ionisation state of a gas parcel exposed to (hydrogen-)ionising radiation at a fixed temperature. The method solved the (photo-)ionisation rate equation, Eq. 5.4, over radiative transfer time steps Δt_r, by integrating it using sub-cycle steps $\delta t \equiv f \times \tau_\mathrm{eq} \le \Delta t_\mathrm{r}$, where

$$\tau_\mathrm{eq} \equiv \frac{\tau_\mathrm{ion}\tau_\mathrm{rec}}{\tau_\mathrm{ion} + \tau_\mathrm{rec}} \tag{7.50}$$

is the time scale to reach ionisation equilibrium (Eq. 5.7 in Chapter 5), $\tau_\mathrm{rec} \equiv 1/(n_\mathrm{e}\alpha_\mathrm{HII})$ is the recombination time scale, $\tau_\mathrm{ion} = 1/(\Gamma_{\gamma\mathrm{HI}} + n_\mathrm{e}\Gamma_\mathrm{eHI})$ is the ionisation time scale (see footnote 1 in Chapter 5) and f is a dimensionless factor that controls the integration accuracy (see App. 5.A in Chapter 5).

The sub-cycling was introduced to allow radiative transfer time steps Δt_r to be chosen independently of the values of the ionisation and recombination time scales, which determine the local evolution of the ionised fraction of a gas parcel exposed to a constant ionising radiation field. A radiative transfer time step Δt_r limited by the ionisation and recombination time scales would prevent efficient radiative transfer simulations, since these time scales may become very small. The only assumption employed in the sub-cycling is that the ionising flux is constant over the radiative transfer time step Δt_r, consistent with the discretisation of the radiative transfer equation. We demonstrated the accuracy of the sub-cycling by comparing its results in test simulations with the corresponding exact analytical solution.

Here we are interested in the self-consistent computation of the non-equilibrium ionisation state of gas with an evolving temperature. In this case we will employ the sub-cycling technique as follows. As for the case of a non-evolving temperature, the ionisation rate equation is integrated over sub-cycle steps $\delta t = f \times \tau_\mathrm{eq}$ (see Eqs. 5.21 and 5.22). Recombination and collisional ionisation rates are determined using the temperature at the beginning of each sub-cycle step and the ionised fractions are advanced in a photon-conserving manner (assuming a constant ionising flux).

In addition, the temperature is advanced by evolving the internal energy according to Eq. 7.26 over the same sub-cycle step assuming iso-choric evolution[5], $dV = 0$. We use the mean particle mass μ derived from the current species fractions to convert between temperature and internal energy using Eq. 7.20. We also employ this equation after each update of the internal energy to compute the corresponding temperature required to determine the new cooling rates (which are functions of temperature, not internal energy). Note that the species fractions and the temperature are evolved independently of each other over a single sub-cycle step. Their evolution is coupled at the beginning of the next sub-cycle step, where the new temperature and species fractions determine new collisional ionisation, recombination and cooling rates.

We now describe our numerical implementation of the sub-cycling. Because we have already described the implementation of the sub-cycling of the ionised fraction in Chapter 5, we can here limit ourselves to the description of our method to advance the internal energy over a single sub-cycle step. The internal energy is advanced by solving a discretized version of the energy equation (i.e. Eq. 7.26 with $dV = 0$). There are several possibilities to perform this

---

[5] In radiation-hydrodynamical simulations, the sub-cycling is to be considered in operator-split (e.g., Castor 2004) with the hydrodynamical evolution of the gas (volume).

discretisation, which we will only briefly mention here. We refer the reader to Chapter 5 for a more detailed discussion.

In the explicit Euler discretisation scheme,

$$u_{t+\delta t} = u_t + \frac{n_{\mathrm{H},t}^2}{\rho_t}(\mathcal{H}_t - \mathcal{C}_t)\delta t, \tag{7.51}$$

the new value $u_{t+\delta t}$ for the internal energy at time $t + \delta t$ is determined by its present value u_t at time t. The scheme is straightforward to implement, but requires the size of the time step to be smaller than the characteristic time scales involved. For larger time steps, the scheme may become numerically unstable. The internal energy evolves on the cooling time scale

$$\tau_{\mathrm{u}} \equiv u/(du/dt) \tag{7.52}$$

which may be shorter than the time scale τ_{eq} on which the ionised fraction is evolving. Its accurate computation may therefore require an integration time step smaller than the size of the sub-cycle step employed to evolve the ionised fraction. The description given in the last paragraph assumed, however, an integration step that is identical to this sub-cycle step.

To solve this problem, we can refer to the same arguments as in Chapter 5. We could either sub-cycle the evolution of the temperature in turn (i.e. over the sub-cycle step used to advance the ionised fraction), or consider using an implicit integration scheme. Our main motivation for employing sub-cycling, rather than implicit integration, to determine the evolution of the ionised fraction was to ensure the accurate conservation of photons. This argument does, however, not apply to the temperature evolution.

For the evolution of the temperature we will therefore make use of the implicit Euler integration, since it has the advantage that it is often (but not always) computationally less expensive. That is, we advance the internal energy according to

$$u_{t+\delta t} = u_t + \frac{n_{\mathrm{H},t}^2}{\rho_t}(\mathcal{H}_{t+\delta t} - \mathcal{C}_{t+\delta t})\delta t, \tag{7.53}$$

The last equation is solved iteratively, by finding the zero of the function

$$f(u_{t+\delta t}) = u_{t+\delta t} - u_t - \frac{n_{\mathrm{H},t}^2}{\rho_t}(\mathcal{H}_{t+\delta t} - \mathcal{C}_{t+\delta t})\delta t. \tag{7.54}$$

In fact, in our implementation[6] we combine the advantages of the explicit scheme (its accuracy) with that of the implicit scheme (its stability): if the cooling time τ_{u} is large compared to the sub-cycle time step δt, the internal energy is evolved explicitly (using Eq. 7.51), and otherwise it is evolved implicitly (using Eq. 7.54).

Recall from Sec. 5.3.2 that, for the case of a constant temperature, we sped up the sub-cycling of the neutral fraction once ionisation equilibrium has been reached by keeping the species fractions fixed. We employ a similar recipe here. Thermal equilibrium is reached on the cooling time scale τ_{u}, which is often much larger than the time scale τ_{eq} to reach ionisation equilibrium. In this case the temperature continues to evolve after the species fractions attained their equilibrium values. The evolution of the temperature implies an evolution of the recombination and collisional ionisation rates, and hence an evolution of the equilibrium species fractions. Our recipe for speeding up the sub-cycling should respect this evolution.

---

[6] This implementation is a straight copy of that used to compute the gas temperature in the SPH code P-GADGET3-BG, an improved version of GADGET-2 (Springel 2005).

We therefore proceed as follows. Once ionisation equilibrium has been reached, we stop the sub-cycling of the species fractions. Over the remainder of the time step $\Delta t_{\rm r}$ only the internal energy is sub-cycled, which can be done using time steps $\delta_{\rm u} t \equiv f_{\rm u} \times \tau_{\rm u}$, where $f_{\rm u} < 1$ is a dimensionless parameter (we set $f_{\rm u} = f$). This results in a speed-up since typically $\delta_{\rm u} t \gg \delta t$. After each such sub-cycle step, we reset the species fractions to their current equilibrium value (Eqs. 7.7, 7.8,7.13)

$$\eta_{\rm HI} = \left(1 + \frac{\Gamma_{\gamma \rm HI} + \eta_{\rm e} n_{\rm H} \Gamma_{\rm eHI}}{\alpha_{\rm HII} \eta_{\rm e} n_{\rm H}}\right)^{-1}, \tag{7.55}$$

$$\eta_{\rm e} = \eta_{\rm HII} = 1 - \eta_{\rm HI}. \tag{7.56}$$

In summary, we solve the evolution of the neutral fraction and temperature using a hybrid numerical method that makes use of both explicit and implicit Euler integration schemes. The ionisation rate equation is solved explicitly using the sub-cycling procedure presented in Chapter 5. This ensures the accurate conservation of photons and allows us to choose the size of the radiative transfer time step independently of the (often very small) ionisation and recombination time scales, a pre-requisite for efficient radiative transfer simulations. The temperature is evolved along with the ionised fraction by following the evolution of the internal energy of the gas. We use an explicit discretisation scheme to advance the internal energy if the cooling time is larger than the size of the sub-cycle step. For smaller cooling times, stability considerations lead us to employ an implicit discretisation scheme to advance the internal energy. Once ionisation equilibrium has been reached, the sub-cycling computation is sped up by fixing the species fractions to their (temperature-dependent) quasi-equilibrium values. From then on, only the evolution of the internal energy needs to be sub-cycled.

7.5.2 Test 5: Sub-cycling

In this section we test the numerical approach for following the ionisation state and temperature of gas parcels exposed to ionising radiation that we have described in the last section.

The set-up of the test is as follows. We simulate the evolution of an optically thin hydrogen-only gas parcel with number density $n_{\rm H} = 1 \ {\rm cm}^{-3}$. The simulation starts at time $t = 0$ with a fully neutral particle with initial temperature $T = 10^2$ K. We then apply a photo-ionising flux of $F = 10^{12} \ {\rm s}^{-1} \ {\rm cm}^{-2}$ with a black-body spectrum of characteristic temperature $T_{\rm bb} = 10^5$ K. Consequently, the parcel becomes highly ionised and is heated to a temperature $T \sim 10^4$ K. After $t = 50$ Myr we switch off the ionising flux and the particle recombines and cools. The simulation ends at $t_{\rm end} = 1$ Gyr.

The test described here is identical to Test 0 of Chapter 5, except that this time we self-consistently follow the temperature evolution (instead of assuming it to be constant), and that collisional ionisations are now also included. We have also chosen to switch off the flux somewhat later than we have done in Test 0, because now the gas parcel evolves on a somewhat larger time scale, as we will see below. Except for the switch-off time, the test here is identical to Test 0 presented in Iliev et al. (2006).

We employ a grey photo-ionisation cross-section $\langle \sigma_{\rm HI} \rangle = 1.63 \times 10^{-18}$ (Sec. 7.2.1), yielding a photo-ionisation rate $\Gamma_{\gamma \rm HI} = 1.63 \times 10^{-6} \ {\rm s}^{-1}$ (see the description of Test 0 in Chapter 5 for its computation). We assume that each photo-ionisation adds $\langle \epsilon_{\rm HI} \rangle = 6.32$ eV to the internal energy of the gas (Sec. 7.3.2), which corresponds to the optically thin limit. The dimensionless parameter f that controls the size of the sub-cycling steps is set to $f = 10^{-2}$. When computing Compton cooling rates off the cosmic microwave background, we assume a redshift $z = 0$.

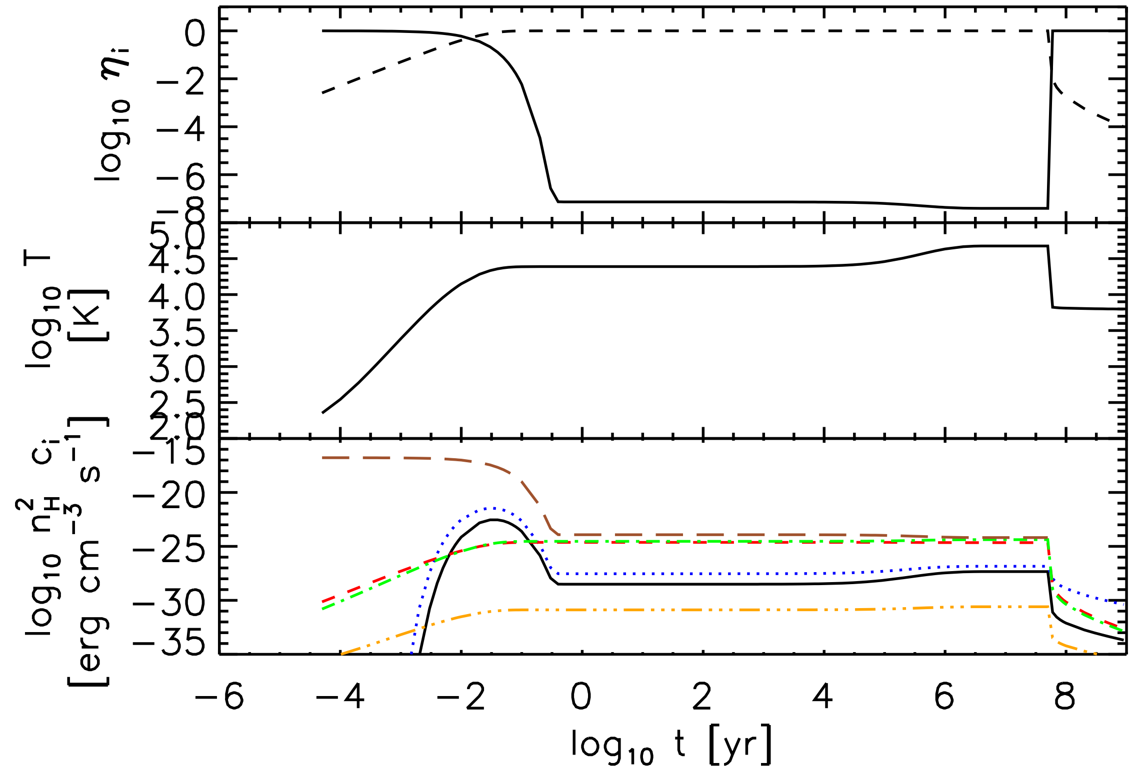

Figure 7.11: Test 5. Optically thin hydrogen-only gas parcel ionising up and recombining. The parcel has a hydrogen number density $n_{\rm H} = 1$ cm^{-3} and is initially fully neutral at temperature $T = 200$ K. It is exposed to a constant ionising photon flux $F = 10^{12}$ s^{-1} (with a black-body temperature $T_{\rm bb} = 10^5$ K), which is turned off at $t = 50$ Myr. The test is similar to Test 0 in Chapter 5, but now we also compute the gas temperature. *Top panel:* neutral (solid curve) and ionised (dashed curve) fraction. *Middle panel:* temperature. *Bottom panel:* heating and cooling rates (energy losses or gains per unit time per unit volume). Processes shown are collisional ionisation cooling (black solid curve), collisional excitation cooling (blue dotted curve), recombination cooling (red dashed curve), bremsstrahlung (green dot-dashed curve), Compton cooling off the $z = 0$ cosmic microwave background (orange triple-dot-dashed curve) and photo-heating (brown long dashed curve).

Fig. 7.11 shows the evolution of the neutral fraction $\eta_{\rm HI}$ (solid curve in the top panel), ionised fraction $\eta_{\rm HII}$ (dashed curve in the top panel) and gas temperature T (middle panel). It contains results from a set of simulations with different time steps (shown in Fig. 7.12) such as to economically cover the more than thirteen orders of magnitude in time. We also show the corresponding cooling and heating rates (bottom panel). The parcel quickly approaches photo-ionisation equilibrium, reaching its equilibrium neutral fraction after a few (photo-)ionisation time scales $\tau_{\rm ion} \equiv \Gamma_{\gamma {\rm HI}}^{-1} \approx 0.02$ yr. During this period, photo-heating raises its temperature to $T \sim 10^4$ K. Throughout most of its evolution, the cooling rate is dominated by Bremsstrahlung and recombination radiation. Collisional excitation and collisional ionisation cooling become, however, important when the temperature $T \approx 10^4$ K and the neutral fraction is sufficiently large. The contribution due to Compton cooling (off the $z = 0$ cosmic microwave background)

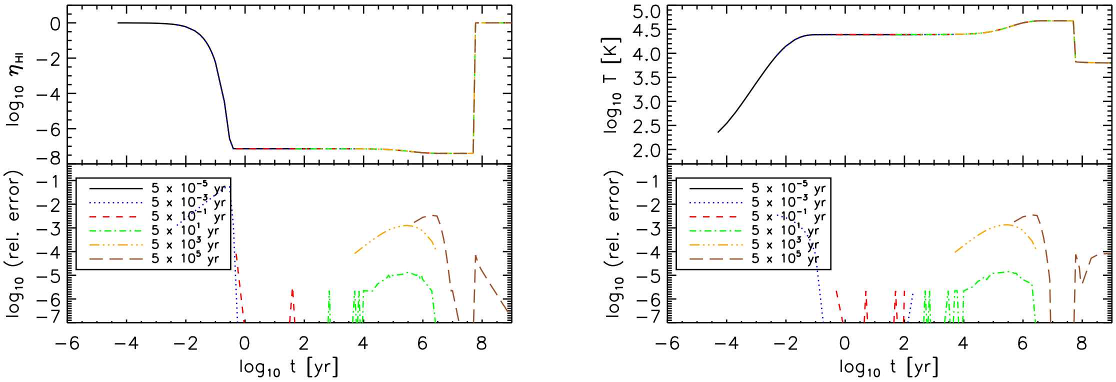

Figure 7.12: Test 5. Evolution of neutral fraction (*left-hand panel*) and temperature (*right-hand panel*), cp. Fig. 7.11. The top panels show the evolution of the neutral fraction and temperature for simulations with different radiative transfer time steps $\Delta t_{\rm r}$, as indicated in the legend. All simulations use $f = 10^{-2}$. The bottom panels show the relative error of the evolutions shown in the top panel with respect to the evolutions obtained from the simulations with the next smaller time step.

is always negligible.

Around $t \sim 10^5$ yr, the neutral fraction exhibits a slight decrease. This is caused by the decrease in the recombination rate due to the rise in temperature that can be observed at this time. The fact that the temperature still evolves after the neutral fraction reached its equilibrium value means that thermal equilibrium is reached on a larger time scale than photo-ionisation equilibrium. The observed behaviour can be understood as follows. When thermal equilibrium is approached from a temperature lower than the equilibrium temperature, the net cooling rate is approximately given by the photo-heating rate (see the bottom panel of Fig. 7.11). In photo-ionisation equilibrium, the photo-heating rate is proportional to the recombination rate (Eq. 7.49). The time scale $\tau_{\rm u} \equiv u/(du/dt)$ to reach thermal equilibrium can therefore be expressed in terms of the recombination time $\tau_{\rm rec} \equiv 1/(n_{\rm e}\alpha_{\rm HII})$,

$$\begin{aligned} \tau_{\rm u} &= \frac{(3/2)nk_{\rm B}T}{n_{\rm H}^2 h_\gamma} && (7.57)\\ &= \frac{(3/2)nk_{\rm B}T}{n_{\rm HII}n_{\rm e}\alpha_{\rm HII}\langle\epsilon_{\rm HI}\rangle} && (7.58)\\ &= \frac{(3/2)nk_{\rm B}T}{\langle\epsilon_{\rm HI}\rangle n_{\rm HII}}\tau_{\rm rec} && (7.59)\\ &\sim \tau_{\rm rec}, && (7.60) \end{aligned}$$

where in the last step we assumed that the gas is highly ionised, i.e. $n_{\rm HII} \approx n_{\rm H} \approx n/2$, and that $T \approx 10^4$ K. The recombination time (and hence the thermal time) is much larger than the time $\tau_{\rm eq} \equiv (\tau_{\rm ion}\tau_{\rm rec})/(\tau_{\rm ion} + \tau_{\rm rec})$ to reach ionisation equilibrium for $\tau_{\rm ion} \ll \tau_{\rm rec}$ (see the discussion in Sec. 5.2 in Chapter 5). Here, $\Gamma_{\gamma\rm HI}^{-1} \approx 0.02$ yr (as noted above) and $\tau_{\rm rec} \approx 10^5$ yr. Accordingly, thermal equilibrium is reached much later than photo-ionisation equilibrium.

After thermal equilibrium is reached, the ionising flux is switched off and the particle recombines and cools. Once it has cooled to a temperature $T \lesssim 10^4$ K, cooling by the processes included here becomes inefficient (see, e.g, the right-hand panel of Fig. 7.9). The temperature of the recombining particle therefore remains constant.

In Fig. 7.12 we quantify the accuracy of our sub-cycling approach. The top left-hand panel shows the evolution of the neutral fraction, while the top right-hand panel shows the evolution of the temperature for simulations with radiative transfer time steps $\Delta t_{\rm r} = 5 \times (10^{-5}, 10^{-3}, 10^{-1}, 10^{1}, 10^{3}, 10^{5})$ yr. Note that not all of the simulations have been evolved until the end of the simulation time, but have been stopped once their simulation time overlapped with that of simulations with the next larger radiative transfer time step. Clearly, the results of the sub-cycling are insensitive to the size of the time step.

The bottom panels of Fig. 7.12 show the relative error with respect to the result of the simulation with the next smaller time step. For all time steps the relative error is small, $\lesssim 10\%$. It can be further reduced by lowering the numerical factor f, which determines the size of the sub-cycle steps.

In summary, we have demonstrated that our sub-cycling recipe accurately predicts, independently of the size of the radiative transfer time step, the combined evolution of the neutral fraction and temperature of gas exposed to hydrogen-ionising radiation. In the following section we will employ the sub-cycling to compute the species fractions and temperature of gas parcels in radiative transfer simulations.

7.6 THERMAL COUPLING

In this section we extend the implementation of TRAPHIC that we presented in Chapters 5 and 6 to perform ionising radiative transfer simulations that additionally evolve the temperature of the gas. We will limit our implementation to the transport of mono-chromatic (or grey) ionising radiation on static density fields. The extension to multi-frequency transport and the thermal coupling of the radiation to the hydrodynamical evolution of the gas are left for future work.

We start by briefly recalling the parameters that control the performance of TRAPHIC and describing the changes made to incorporate the computation of the gas temperature. We then test our thermally coupled implementation. First, in test 6, we compute the evolution of the ionised fraction and the temperature around a single ionising source that is embedded in an initially cold and neutral homogeneous hydrogen-only cloud. This test is thus similar to the Test 1 that we have presented in Chapter 5. We compare our results to reference solutions obtained with TT1D, a one-dimensional (multi-frequency) radiative transfer code that we have developed for this purpose (see Chapter 5). We briefly comment on the importance of a detailed multi-frequency treatment of this problem and compare the performance of TRAPHIC with that of other radiative transfer codes whose performance in this test has been published in Iliev et al. (2006). Second, similar to what we have done in Test 4 in Chapter 5, we apply our implementation to solve the radiative transfer equation in a scaled-down version of a typical reionisation simulation. Again, we compare the results obtained in this test to results obtained with other radiative transfer codes for the same test problem (Iliev et al. 2006).

As mentioned in the introduction, TRAPHIC is a radiative transfer scheme for use with SPH simulations. It solves the radiative transfer equation in a spatially adaptive way by tracing photons from radiation sources directly on the unstructured grid comprised by the SPH particles. The linear scaling of the computation time with the number of light sources that is exhibited by conventional radiative transfer schemes is avoided by employing a source merging procedure that strictly respects the chosen angular resolution. Photons are traced by propagating photon packets from particles to their $\tilde{N}_{\rm ngb}$ neighbours (residing in the surrounding sphere of radius $\tilde{h}$) inside cones. The introduction of cones is necessary to accomplish the transport of radiation in a directed manner on the generally highly irregular distribution of the SPH particles. The opening angle Ω of the cones determines the formal angular resolution of the radiative transfer. It is conveniently expressed in terms of a cone number, $N_{\rm c} \equiv 4\pi/\Omega$. In practice the angular resolution is, however, much higher than the formal one because the photon transport with TRAPHIC is adaptive in angle.

The photon transport can be decomposed into two main parts. First, source particles emit photon packets to their $\tilde{N}_{\rm ngb}$ neighbouring SPH particles (at a rate determined by their luminosity), by means of a set of $N_{\rm c}$ tessellating emission cones. The number of neighbours $\tilde{N}_{\rm ngb}$ is a parameter that is usually matched to the number of neighbours $N_{\rm ngb}$ (residing in the sphere of radius h) used in the computation of the particle's SPH properties, $\tilde{N}_{\rm ngb} \lesssim N_{\rm ngb}$. Second, the photon packets received by the neighbouring SPH particles are propagated further downstream. They are confined to the emission cones into which they were originally emitted through the use of transmission cones of solid angle $4\pi/N_{\rm c}$. The transport is performed using radiative transfer time steps of size $\Delta t_{\rm r}$. After each such time step, the properties of the SPH particles are updated according to their interactions (absorptions, scatterings) with the photon packets. We refer the reader to Chapter 4 for a more detailed and complete description of TRAPHIC.

In Chapters 5 and 6 we have presented, respectively, implementations of TRAPHIC into the SPH codes GADGET-2 and P-GADGET3-BG. These implementations aimed to solve the transfer of ionising radiation and the evolution of the non-equilibrium ionisation state of gas in cosmological simulations for prescribed gas temperatures. Compared with the preparatory work presented earlier in this chapter, the modifications to these implementations that are required to compute the temperature in addition to the ionisation state of the gas are small. We only need to replace the sub-cycling routine presented in Chapter 5 by that presented in Sec. 7.5. In addition, we replace the expressions for the recombination rate and the photo-ionisation cross-section used in Chapters 5 and 6 by those listed in Table 7.1 and we also include collisional ionisations.

7.6.1 Test 6: HII region expansion in the grey approximation

Here we apply our thermally coupled implementation of TRAPHIC to compute the evolution of the ionisation state and temperature around an ionising source surrounded by gas of constant density. This is an idealised test problem designed to facilitate the verification of our implementation through the direct comparison to results obtained with our one-dimensional code TT1D as well as to published results obtained with other radiative transfer codes for the same test problem (Iliev et al. 2006). It captures the main characteristics of a thermally coupled radiative transfer simulation that we wish to verify: conservation of the number of ionising photons, which ensures that the final ionised region attains the correct size, and conservation of their associated energy, which, together with an accurate implementation of the relevant cooling processes, ensures that the ionised region settles into the correct thermal structure.

Despite its simplicity, an analytical solution to the present problem cannot be obtained. This is because the coupling between the ionisation and temperature state through the dependence of the collisional ionisation, recombination and cooling rates on the temperature and species fractions impedes the evaluation of the governing differential equations (Eq. 7.1 and 7.26). To provide an approximate point of reference, the evolution of the ionised region in this problem can be compared to the evolution of the ionised region in an equivalent problem that employs a fixed gas temperature and for which an analytical solution is known (assuming that the ionised region is fully ionised and ignoring collisional ionisations). We have reviewed this solution in

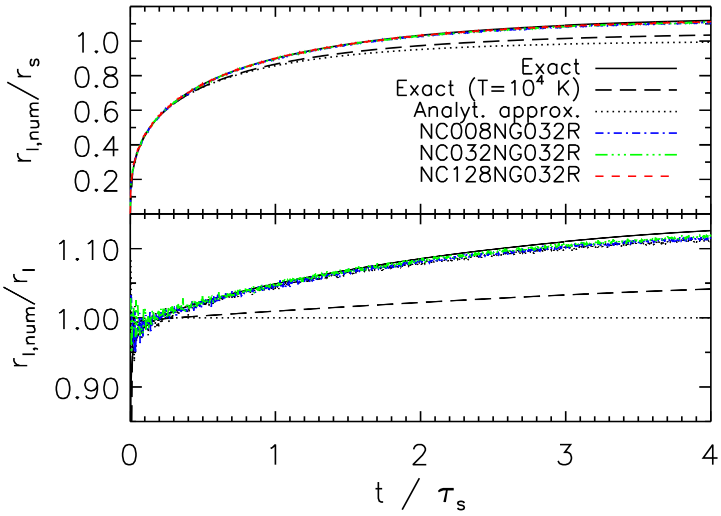

Figure 7.13: Test 6. Evolution of the ionisation front radius. *Top panel:* Ionisation front radius divided by the Strömgren radius r_{S}. For comparison, the evolution of the ionisation front radius obtained from the analytical approximation (which assumes a constant temperature) is indicated with the black dotted curve. *Bottom panel:* Ionisation front radius divided by the analytical approximation r_{I}. All simulations show very good agreement with the exact solution (black solid curve). The predicted ionisation front radius is larger than that found in Test 1, Chapter 5 (black long-dashed curve), which assumed a different value for the photo-ionisation cross-section (and a constant temperature of $T = 10^4$ K throughout the ionised region).

Chapter 5, where we showed that the radius of the ionised sphere around a source of ionising luminosity $\dot{\mathcal{N}}_\gamma$ that is located in a homogeneous hydrogen-only medium of density n_{H} is given by

$$r_{\mathrm{I}}(t) = r_{\mathrm{s}}(1 - e^{-t/\tau_{\mathrm{s}}})^{1/3}, \tag{7.61}$$

where $r_{\mathrm{s}} = [3\dot{\mathcal{N}}_\gamma/(\alpha_{\mathrm{B,HII}} n_{\mathrm{H}}^2)]^{1/3}$ is the Strömgren radius and $\tau_{\mathrm{s}} = 1/(\alpha_{\mathrm{B,HII}} n_{\mathrm{H}})$ is the Strömgren time scale, which equals the recombination time for fully ionised gas. In some of our comparisons we will employ this approximate point of reference, using a recombination coefficient $\alpha_{\mathrm{B,HII}} = 2.59 \times 10^{-13}$ cm^3 s^{-1} appropriate for ionised gas of temperature $T \approx 10^4$ K (see Fig. 7.3). We will refer to it as an analytical approximation.

The parameters for the test are taken from Iliev et al. (2006). We consider an ionising source embedded in a homogeneous hydrogen-only density field with number density $n_{\mathrm{H}} = 10^{-3}$ cm^{-3}. The source has a black-body spectrum with temperature 10^5 K and emits radiation with an ionising luminosity $\dot{N}_\gamma = 5 \times 10^{48}$ photons s^{-1}. The test described here is identical to Test 1 in Chapter 5, except that now the gas temperature is allowed to vary due to heating and cooling processes as described in Sec. 7.3 (with Compton cooling off the redshift $z = 0$ cosmic microwave background included) and that collisional ionisation is included.

The hydrogen is assumed to have an initial ionised fraction $\eta_{\mathrm{HII}} = 1.2 \times 10^{-3}$ (approximately corresponding to the ionised fraction implied by collisional ionisation equilibrium at temperature $T = 10^4$ K, Fig. 7.9). Its initial temperature is set to 100 K. For reference, the recombination time is $\tau_{\mathrm{S}} = 122.4$ Myr and the Strömgren radius is $r_{\mathrm{S}} = 5.4$ kpc (assuming a temperature of $T = 10^4$ K, appropriate for the ionised gas). Radiation is transported using a single frequency bin in the grey approximation (see Sec. 5.3.5 in Chapter 5). For the assumed spectrum this implies a cross-section for absorption of ionising photons $\langle\sigma_{\rm HI}\rangle = 1.63\times10^{-18}$ cm^2 (Sec. 7.2). Each photo-ionisation results in a free electron with kinetic energy $\langle\epsilon_{\rm HI}\rangle = 6.32$ eV (Sec. 7.3, optically thin limit). Below, in Sec. 7.6.2, we will discuss the effects of this approximate treatment of the present multi-frequency problem.

The numerical realization of the initial conditions is similar to that used for Test 1 in Chapter 5. The ionising source is located at the centre of a simulation box with side length $L_{\rm box} = 13.2$ kpc. The box boundary is photon-transmissive. We assign each SPH particle a mass $m = n_{\rm H}m_{\rm H}L_{\rm box}^3/N_{\rm SPH}$, where $N_{\rm SPH}$ is the total number of SPH particles. The positions of the SPH particles are chosen to be glass-like, which yields initial conditions that are more regular when compared to those obtained from a Monte Carlo sampling of the density field. The SPH smoothing kernel is computed and the SPH densities are found using the SPH formalism implemented in GADGET-2, with $N_{\rm ngb} = 48$.

The radiative transfer time step is set to $\Delta t_{\rm r} = 10^{-2}$ Myr to facilitate a comparison to Test 1 in Chapter 5. For the same reason, we limit ourselves to solving the time-independent radiative transfer equation and propagate photons during each time step only from a given particle to its direct neighbours (see the discussion in Sec. 5.3.3, Chapter 5). All simulations presented in this section employ $N_{\rm SPH} = 64^3$ SPH particles, which are evolved for a total of 500 Myr. Some of our simulations employ the resampling technique introduced in Chapter 5 to reduce artefacts due to the particular setup of the initial conditions. Briefly, each SPH particle is, within its spatial resolution element whose size is determined by the diameter of the SPH kernel $2h$, regularly (here: every 10th radiative transfer time step) offset randomly from its initial position. For comparison, we repeat all simulations without employing this technique. We perform simulations of increasing angular resolution, from $N_{\rm c} = 8$ and $N_{\rm c} = 32$ to $N_{\rm c} = 128$, with fixed $\tilde{N}_{\rm ngb} = 32$. Figs. 7.13 - 7.16 show our results.

In Fig. 7.13 we show the evolution of the ionisation fronts for the simulations with resampling. The black dotted curve indicates the analytical approximation, Eq. 7.61. The black solid curve shows the ionisation front obtained with our one-dimensional radiative transfer code TT1D. It is referred to as the exact solution. All simulations accurately predict the evolution of the ionisation front. We also show the exact solution for the ionisation front evolution employed in Test 1 (Chapter 5), which assumed a fixed temperature $T = 10^4$ K (and a slightly different value for the photo-ionisation cross-section). The final ionisation front radius obtained in the present test is slightly larger that that obtained in Test 1, which is mostly due to the differences in the employed photo-ionisation cross-sections, as we demonstrate below (Fig. 7.17). Some of the differences in the final radii may also be attributed to the fact that the typical temperatures found here are slightly larger than the temperature $T = 10^4$ K that was assumed in Test 1, implying a smaller recombination rate. Our results are in excellent agreement with those shown in Fig. 15 of Iliev et al. (2006).

We now discuss the internal structure of the ionised and photo-heated sphere. In Fig. 7.14 we present slices through the centre of the simulation box showing the neutral fraction (top two rows) and temperature (bottom two rows) at time[7] $t = 100$ Myr. From left to right in each row, the panels show simulations with angular resolution $N_{\rm c} = 8, 32$ and 128. Counting from the top, the second and fourth row show the results of the simulations which included resampling, while the first and third row show the results of identical simulations but for which the resampling was turned off. In each panel we indicate, as a point of reference, the analytical

---

[7] The reason why we do not show the slices at the end of the simulations, i.e. at time $t = 500$ Myr, as we did in the corresponding Test 1 in Chapter 5, is that the simulation box is slightly too small to contain the whole ionised sphere at this time (because of the smaller photo-ionisation cross-section that is employed here).

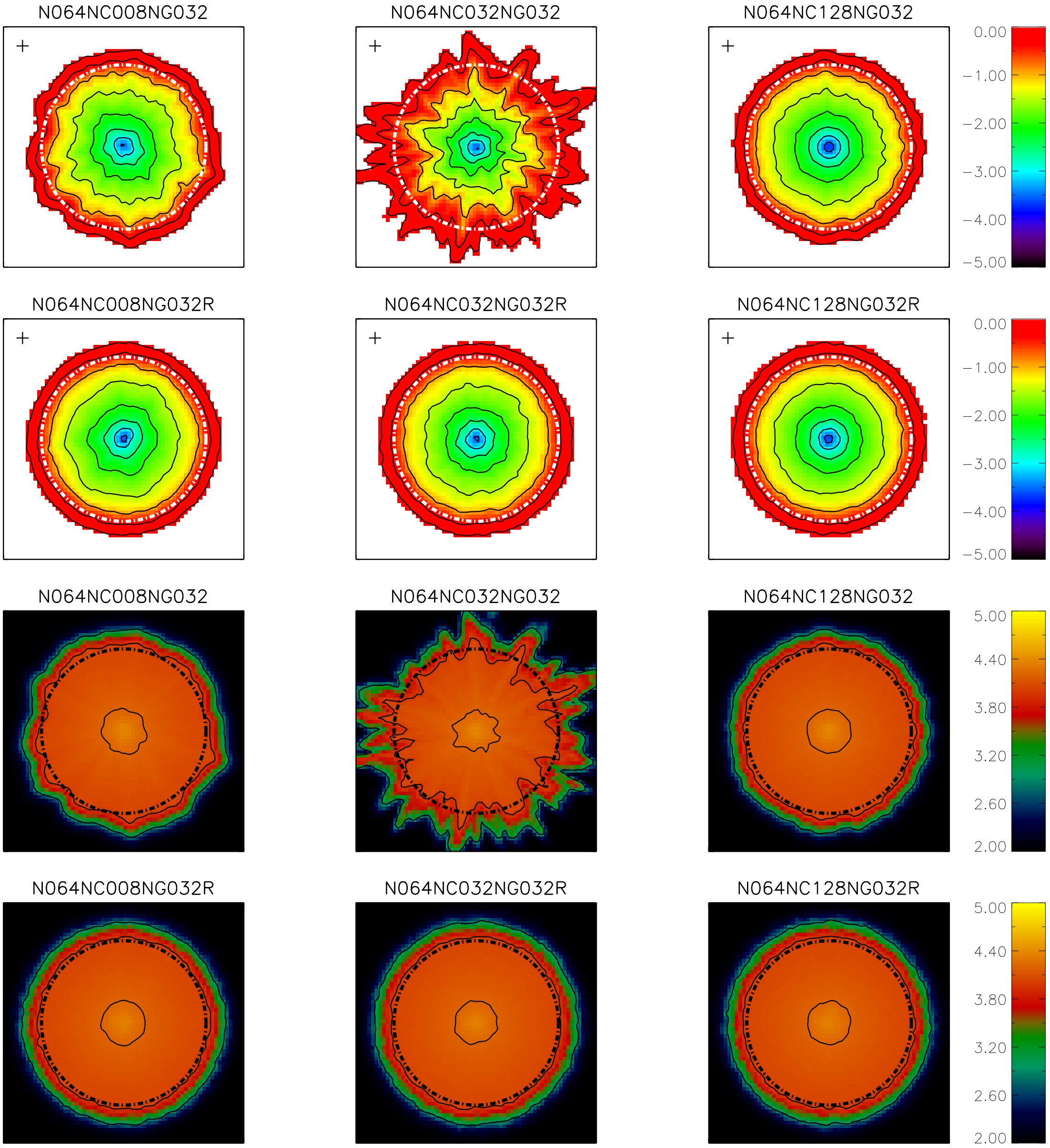

Figure 7.14: Test 6. Neutral fraction (*top two rows*) and temperature (*bottom two rows*) at time $t = 100$ Myr in a slice through the centre of the simulation box. *From left to right:* angular resolution $N_\mathrm{c} = 8, 32$ and 128. *First and third row:* No resampling. *Second and fourth row:* Resampling of the particle positions after every 10th radiative transfer time step. The dot-dashed circle indicates the position of the ionisation front, calculated using the analytical approximation discussed in the text. Contours show neutral fractions of $\eta_\mathrm{HI} = 0.9, 0.5$, $\log_{10} \eta_\mathrm{HI} = -1, -1.5, -2, -2.5, -3, -3.5$ and temperatures $\log_{10} T = (3, 4, 4.2) \times 10^4$ K (from the outside in). The colour scale employed for the neutral fraction is identical to that used in the corresponding Fig. 5.4 of Test 1 (Chapter 5). The crosses in the top two rows indicate the spatial resolution $\langle 2\tilde{h} \rangle$.

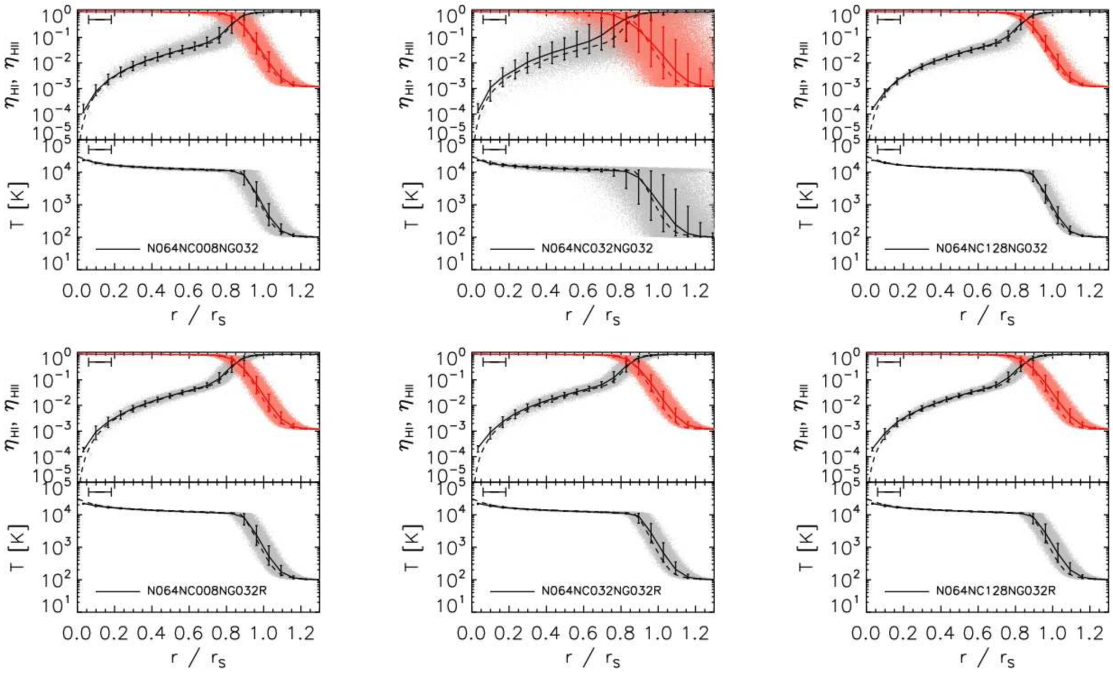

Figure 7.15: Test 6. Scatter plots and profiles of the neutral (ionised) fraction and temperature at time $t = 100$ Myr for simulations with angular resolution $N_c = 8$ (left), 32 (middle) and 128 (right). *Top row:* No resampling. *Bottom row:* Resampling of the particle positions after every 10th radiative transfer time step. Each dot represents the neutral fraction (ionised fraction, temperature) of a single particle. Solid curves show the median neutral fraction (ionised fraction, temperature) in spherical bins around the ionising source. The vertical error bars show the 68.3% confidence interval in each bin. Dashed curves indicate the reference solution obtained with our one-dimensional radiative transfer code TT1D. The horizontal error bars in the upper left corners indicate the spatial resolution. The results of all simulations in excellent agreement with the reference solution. Without the resampling, the results are slightly noisier if $N_c \approx \tilde{N}_{ngb}$ (top middle panel).

approximation for the position of the ionisation front by a dash-dotted circle.

Interior to the ionisation front the gas is highly ionised and photo-heated to typical temperatures $T \approx 1.5 \times 10^4$ K (with maximum temperatures $T \approx 2 \times 10^4$ K). The results obtained in the simulations that employed the resampling of the density field are independent of the angular resolution, an observation that is in agreement with expectations based on the spherical symmetry of the problem. The runs that did not employ the resampling, however, show slight deviations from the expected spherical shape which depend on the angular resolution. As discussed for Test 1 in Chapter 5, the deviations are caused by the particular arrangement of the SPH particles. Reducing this particle noise, which is strongest when $N_c \approx \tilde{N}_{ngb}$, was the motivation for introducing the resampling technique.

In Fig. 7.15 we compare the median profiles of the neutral fraction and the temperature at time $t = 100$ Myr obtained from the three-dimensional simulations with TRAPHIC (solid curves with error bars, which indicate the 68.3 confidence interval in the corresponding bin) to the reference simulation obtained with our one-dimensional radiative transfer code TT1D (dashed curves). From left to right in each row, the panels show simulations with angular resolution $N_c = 8, 32$ and 128, respectively. We show profiles obtained from both the simulations that employed the resampling of the particle positions (bottom row) and from the simulations that

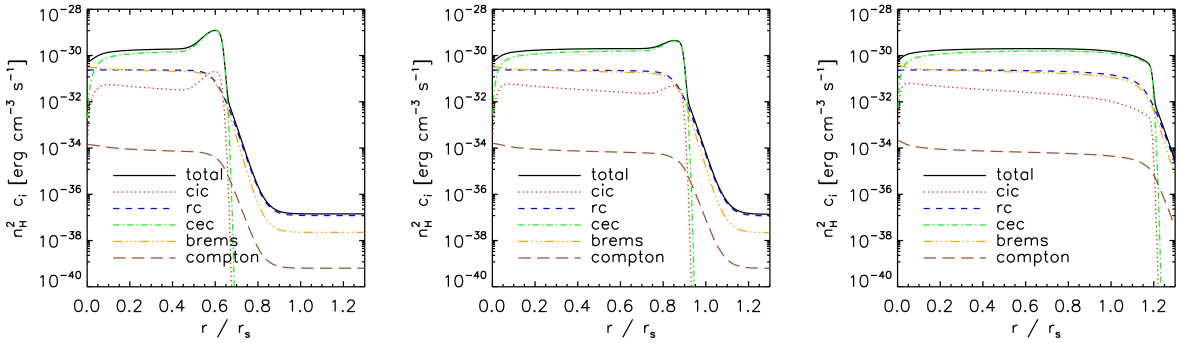

Figure 7.16: Test 6. Radial dependence of individual cooling rates at 30 Myr (*left-hand panel*), 100 Myr (*middle panel*) and 500 Myr (*right-hand panel*): From top to bottom in the legend: total cooling rate, collisional ionisation cooling, recombination cooling, collisional excitation cooling, bremsstrahlung, Compton cooling (off the $z = 0$ cosmic microwave background).

did not employ it (top row).

The results of all simulations are in excellent agreement with the reference result. The small deviations that are present very close to the ionising source and in regions where the profile gradients are steep are due to the finite spatial resolution (indicated with horizontal error bars). The effect of resampling in reducing noise can most clearly be seen when comparing the simulations with angular resolution $N_{\rm c} = \tilde{N}_{\rm ngb} = 32$ with each other (middle panels). Note, however, that for the simulation with the highest angular resolution that we have considered here ($N_{\rm c} = 128$), the resampling slightly reduces the agreement with the reference simulation because it introduces additional scatter. This scatter is, however, consistent with the spatial resolution employed.

Finally, it is interesting to take a closer look at the cooling rates that determine the evolution of the gas temperature in the current problem. Fig. 7.16 shows the cooling rates (per unit volume) employed in our reference simulation with TT1D at times $t = 30, 100$, and 500 Myr. For most of the ionised region collisional excitation is the dominant cooling process. Outside the ionised region recombination cooling and bremsstrahlung dominate. The latter two cooling processes become, however, also important very close to the ionising source, where the neutral fraction becomes too low for collisional excitation to contribute significantly to the cooling rate.

7.6.2 HII-region expansion: multi-frequency simulation

We now briefly comment on the grey treatment of the multi-frequency problem presented in the last section by comparing it to a full multi-frequency simulation. Because the current implementation of TRAPHIC only uses a single frequency bin, we will employ our one-dimensional mesh-code TT1D for the numerical investigations in this section.

We start by verifying our multi-frequency treatment in TT1D by comparing its performance in a simple test problem, similar to the one presented in the previous section, to the corresponding equilibrium solution that can be analytically derived (except for a numerical evaluation of the integrals involved). The test consists of simulating the spherically symmetric growth of the ionised region around a single ionising source in a homogeneous hydrogen-only medium. The source emits $\dot{N}_\gamma = 5 \times 10^{48}$ photons s^{-1} with a black-body spectrum of $T_{\rm bb} = 10^5$ K. The gas

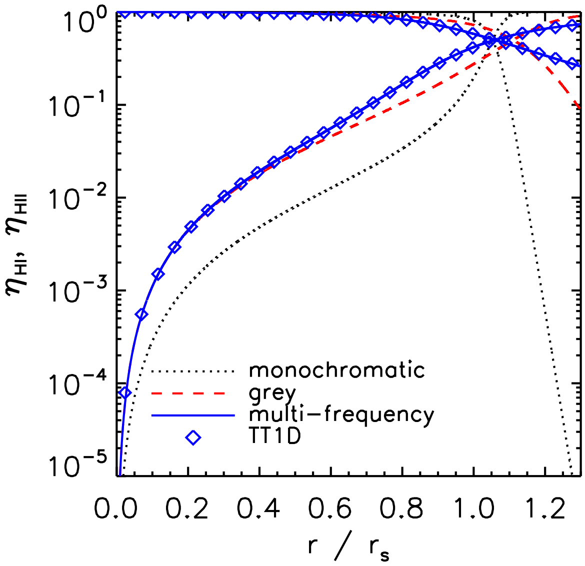

Figure 7.17: Photo-ionisation equilibrium profiles of the neutral and ionised fraction around a single black-body source in a homogeneous hydrogen-only medium. The numerical result obtained with TT1D (diamonds) shows excellent agreement with the analytically computed exact results (blue solid curve). For comparison, we also show the analytically computed exact solutions assuming the grey approximation used in Sec. 7.6.1 (red dashed curve) and the mono-chromatic treatment used in Test 1 of Chapter 5 (black dotted curve). The grey approximation agrees with the exact solution in the optically thin limit (i.e. in the absence of spectral hardening), while the monochromatic treatment always fails.

density is $n_{\rm H} = 10^{-3}$ cm^{-3}. In contrast to the test in the previous section, the initial ionised fraction is $\eta_{\rm HII} = 0$, the gas temperature is assumed to be constant and we use a recombination coefficient $\alpha_{\rm B,HII} = 2.59 \times 10^{-13}$ cm^3 s^{-1}, appropriate for photo-ionised gas with temperature $T \approx 10^4$ K. Collisional ionisation is not included. The test is therefore identical to Test 1 in Chapter 5. The spatial resolution, the time step and the number of frequency bins used in the simulation with TT1D are chosen such as to achieve numerical convergence.

In Fig. 7.17 we show the neutral (ionised) fraction profile in photo-ionisation equilibrium. Diamonds show the result of the simulation with TT1D (at $t = 2000$ Myr). The blue solid curve indicates the exact equilibrium solution that we have already employed in Chapter 5, obtained by solving (e.g., Osterbrock 1989)

$$\frac{\eta_{\rm HI,eq}(r) n_{\rm H}}{4\pi r^2} \int d\nu \, \dot{\mathcal{N}}_\gamma(\nu) e^{-\tau_\nu} \sigma_\nu = \eta^2_{\rm HII,eq}(r) n^2_{\rm H} \alpha_{\rm B,HII}, \tag{7.62}$$

where the frequency-dependent optical depth $\tau_\nu(r)$ is given by

$$\tau_\nu(r) = n_{\rm H} \sigma_\nu \int_0^r dr' \, \eta_{\rm HI,eq}(r'). \tag{7.63}$$

The simulation result is in excellent agreement with the exact equilibrium solution, verifying our multi-frequency implementation of TT1D. For comparison, we also show the exact equilibrium solutions assuming that the radiation is monochromatic (dotted black curve), assuming a photo-ionisation cross-section evaluated at the ionisation threshold, i.e. $\sigma_{\rm HI} = 6.3 \times 10^{-18}$ cm^2 , and grey, i.e. using the average cross-section $\langle \sigma_{\rm HI} \rangle = 1.63 \times 10^{-18}$ cm^2 that we have already employed in the last section (dashed red curve). Observe that the grey treatment provides an excellent description of the multi-frequency problem at small distances. The monochromatic solution, on the other hand, shows large deviations with respect to the multi-frequency solution at all distances from the source.

The reason for the differences between the results of the multi-frequency computation and the results of the grey and monochromatic computation can be readily understood. The absorption cross-section for ionising photons is a strongly decreasing function of the photon energy. The ionising photons with the lowest energy are therefore preferentially absorbed, which leads to an increase in the typical photon energy with distance. This is referred to as spectral hardening. Because the photon mean free path is inversely proportional to the absorption cross-section, spectral hardening increases the width of the ionisation front with respect to that obtained in the absence of spectral hardening. Note that spectral hardening only becomes important for large optical depths, which explains why the grey approximation reproduces the multi-frequency solution at small distances where the neutral fraction is low. The monochromatic approximation, on the other hand, always fails to describe the multi-frequency problem, since it implies an inappropriate value for the photo-ionisation rate[8]. For completeness we note that the use of the photo-ionisation cross-section from Osterbrock (1989) instead of that from Verner et al. (1996) leads to nearly indistinguishable results.

Having demonstrated the validity of our multi-frequency treatment with TT1D, we now use it to repeat the test problem analysed in the previous section. The resulting neutral (ionised) fraction and temperature profiles at times $t = 30, 100$ and 500 Myr are shown in Fig. 7.18 (black solid curves). They are compared to the results of the grey treatment that we have discussed in the previous section (red dotted curves). We recall that there we employed photo-heating rates computed in the optically thin limit (Eq. 7.40), according to which each photo-ionisation adds $\langle \epsilon_{\rm HI} \rangle = 6.32$ eV (Sec. 7.3.2) to the internal energy of the gas. We henceforth employ the label *grey thin* to distinguish this simulation from a simulation that was identical except for the fact that we employed photo-heating rates computed in the optically thick limit (Eq. 7.41), i.e. adding $\langle \epsilon_{\rm HI}^{\rm thick} \rangle = 16.01$ eV (Sec. 7.3.2) per photo-ionisation to the internal energy of the gas. This simulation is labelled *grey thick* in Fig. 7.18 (blue dashed curves). We also show the results obtained with the other radiative transfer codes C^2-RAY (Mellema et al. 2006), CRASH (Ciardi et al. 2001; Maselli, Ferrara, & Ciardi 2003) and FTTE (Razoumov & Cardall 2005) for the same test problem, as published in Iliev et al. (2006).

The differences in the neutral fractions between the grey and the multi-frequency simulations that we have discussed above for Fig. 7.17 are again clearly visible (top panels of Fig. 7.18). The grey simulation that employed photo-heating in the optically thin limit yields results that asymptote to those obtained in the multi-frequency simulation at small distances from the ionising source. At large distances, i.e. near the ionisation front and beyond, on the other hand, the multi-frequency simulation predicts significantly larger ionised fractions than those predicted by this grey simulation. This is because the photon mean free path is larger in the multi-frequency simulation than in the grey simulations due to spectral hardening, leading to a smoother transition between the highly ionised gas interior to and the neutral gas far ahead of the ionisation front.

The grey simulation that employed photo-heating rates computed in the optically thick limit (*grey thick*) yields neutral fractions that are very similar to those found in the grey simulation that computed photo-heating in the optically thin limit (*grey thin*). The *grey thick* simulation predicts, however, slightly lower neutral fractions than the *grey thin* simulation, since it yields slightly larger temperatures, and thus smaller recombination rates, throughout the ionised region (bottom panels of Fig. 7.18). In contrast to the *grey thin* simulation, the neutral fractions obtained in the *grey thick* simulation therefore do not asymptote to those obtained in

---

[8] As discussed in Sec. 5.3.5 of Chapter 5, the photo-ionisation rate implied by the grey approximation, on the other hand, is by construction identical to the true photo-ionisation rate computed in the multi-frequency simulation.

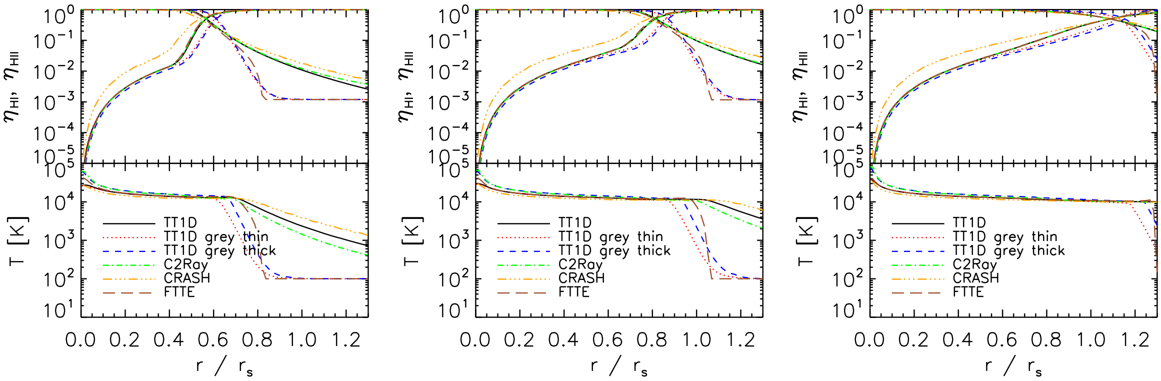

Figure 7.18: Comparison of the grey approximations with the full multi-frequency solution, both obtained with TT1D. Panels show spherically averaged profiles of neutral (ionised) fraction (top) and temperature (bottom) at times $t = 30$ (left), 100 (middle) and 500 Myr (right). The black solid curve shows the multi-frequency solution. The red dotted (blue dashed) curve shows its grey approximation assuming photo-heating rates computed in the optically thin (thick) limit. The grey and multi-frequency simulations show clear differences close to and beyond the ionisation front, where the large optical depth causes a spectral hardening of the emitted black-body radiation spectrum. For reference, we also show results obtained with other radiative transfer codes as published in Iliev et al. (2006). The large differences between these results at large distances mainly reflect the large differences in the numerical treatment of multi-frequency radiation in these codes. Most of the differences close to the ionising source have their origin in the use of different assumptions for computing photo-heating rates, as a comparison to the results obtained with TT1D reveals.

the multi-frequency simulation at small distances to the ionising source. Instead, they remain systematically too small.

The differences between the grey and multi-frequency simulations (and between the *grey thin* and *grey thick* simulations) become particularly apparent when inspecting the corresponding temperature profiles. The multi-frequency simulation predicts substantially higher gas temperatures ahead of the ionisation front. This *pre-heating* is a simple consequence of the increase in the photon mean free path above the one predicted by the grey simulations. As already noted, at fixed radii the *grey thick* simulation predicts systematically higher gas temperatures than the *grey thin* simulation. The reason is that in the optically thin limit the contribution of high-energy photons to the photo-heating rate is reduced due to the weighting by the absorption cross-section $\sigma_{\rm HI}(\nu)$, which is a strongly decreasing function of the photon energy. Observe that the temperatures (like the neutral fractions) obtained in the *grey thin* simulation asymptote to those obtained in the multi-frequency simulation at small distances to the ionising source, while the temperatures predicted by the *grey thick* simulation are too high even in this limiting case.

We summarise our discussion of the differences between the grey and multi-frequency simulations for the present problem by noting that the use of the grey approximation leads to neutral fractions and temperatures that generally are very different from those obtained in detailed multi-frequency simulations. At large optical depths, i.e. generally close to and beyond the ionisation front, the neutral fractions are systematically too high and the temperatures are systematically too low, due to the lack of spectral hardening. The grey treatment yields neutral fractions and temperatures that asymptote to those obtained in the corresponding multi-frequency simulation at small distances to the ionising source when photo-heating rates are computed in the optically thin limit, i.e. using Eq. 7.40. When computing photo-heating rates in the optically thick limit, i.e. using Eq. 7.41, the neutral fractions and temperatures do not asymptote to the correct values at small distances to the ionising source , i.e. the values predicted by the multi-frequency simulation. Consequently, when one invokes the grey approximation to compute the thermal structure of ionised regions, one should compute photo-heating rates in the optically thin limit. Photo-heating rates in the optically thick limit should only be employed when considering the thermal balance of an ionised region as a whole. Ideally, one would perform detailed multi-frequency simulations and simply dispense with the grey approximation.

Finally, we compare the results of our simulations with TT1D to those obtained with C^2-RAY, CRASH and FTTE for the same test problem (Iliev et al. 2006). We note that the simulation with CRASH employed multiple frequency bins, while the one with FTTE was done using a single frequency bin and computing photo-ionisation and optically thick photo-heating in the grey approximation (Alexei Razoumov, private communication). Finally, C^2-RAY used a hybrid method (Garrelt Mellema, private communication): the absorption of ionising radiation was computed as a function of frequency, but each photo-ionisation injected the same amount of energy, regardless of the frequency of the absorbed photon. This method thus accounts fully for the spectral hardening of the radiation but ignores it when computing photo-heating rates.

There are large differences in the results obtained with these three codes. At large distances from the ionising source, i.e. close to and beyond the ionisation front, most of these differences may certainly be attributed to differences in the multi-frequency implementation, leading to differences in the spectral hardening of the emitted black-body spectrum. At these distances, the neutral fractions obtained in our grey simulations agree closely with those obtained with FTTE, while the neutral fractions obtained in our multi-frequency simulations closely agree with those obtained with C^2-RAY, as expected from our discussion above.

The results exhibit, however, also large differences in the neutral fractions and temperatures close to the ionising source, where the gas is optically thin and the emitted black-body radiation spectrum is not deformed due to spectral hardening. Some of these differences can be attributed to the fact that the different codes employ different expressions for cross-sections, recombination and cooling rates. As demonstrated in Iliev et al. (2006) (their Fig. 4), different recombination and cooling rates may, however, only account for differences in the neutral fraction and temperature of at most $\lesssim 10\%$. We have verified this observation by employing the rates used with the different codes (Table 2 in Iliev et al. 2006) in simulations with TT1D.

Most of the differences close to the ionising source may instead be traced back to the use of different assumptions underlying the computation of the photo-heating rates. In fact, the temperatures predicted with CRASH are in excellent agreement with the temperatures predicted in our multi-frequency and grey thin simulations, while the temperatures predicted by FTTE and C^2-RAY are in excellent agreement with the temperatures predicted in our grey thick simulation. We note that the fact that the neutral fractions obtained with CRASH are systematically too large may indicate that the radiation field was too poorly sampled (see Maselli, Ciardi, & Kanekar 2009; Iliev et al. 2006 for discussions).

7.6.3 Test 7: Expansion of multiple HII regions in a cosmological density field

In this section we use our thermally coupled implementation of TRAPHIC to repeat the Test 4 that we have discussed in Chapter 5. Recall that this test involved the simulation of the evolution of ionised regions around multiple sources in a static cosmological density field at redshift $z \approx 8.85$ and that it was designed to resemble important aspects of state-of-the-art simulations of the epoch of reionisation. In contrast to our Test 4 simulations in Chapter 5, where the gas temperature was assumed to be constant at $T = 10^4$ K, here we will compute the evolution of

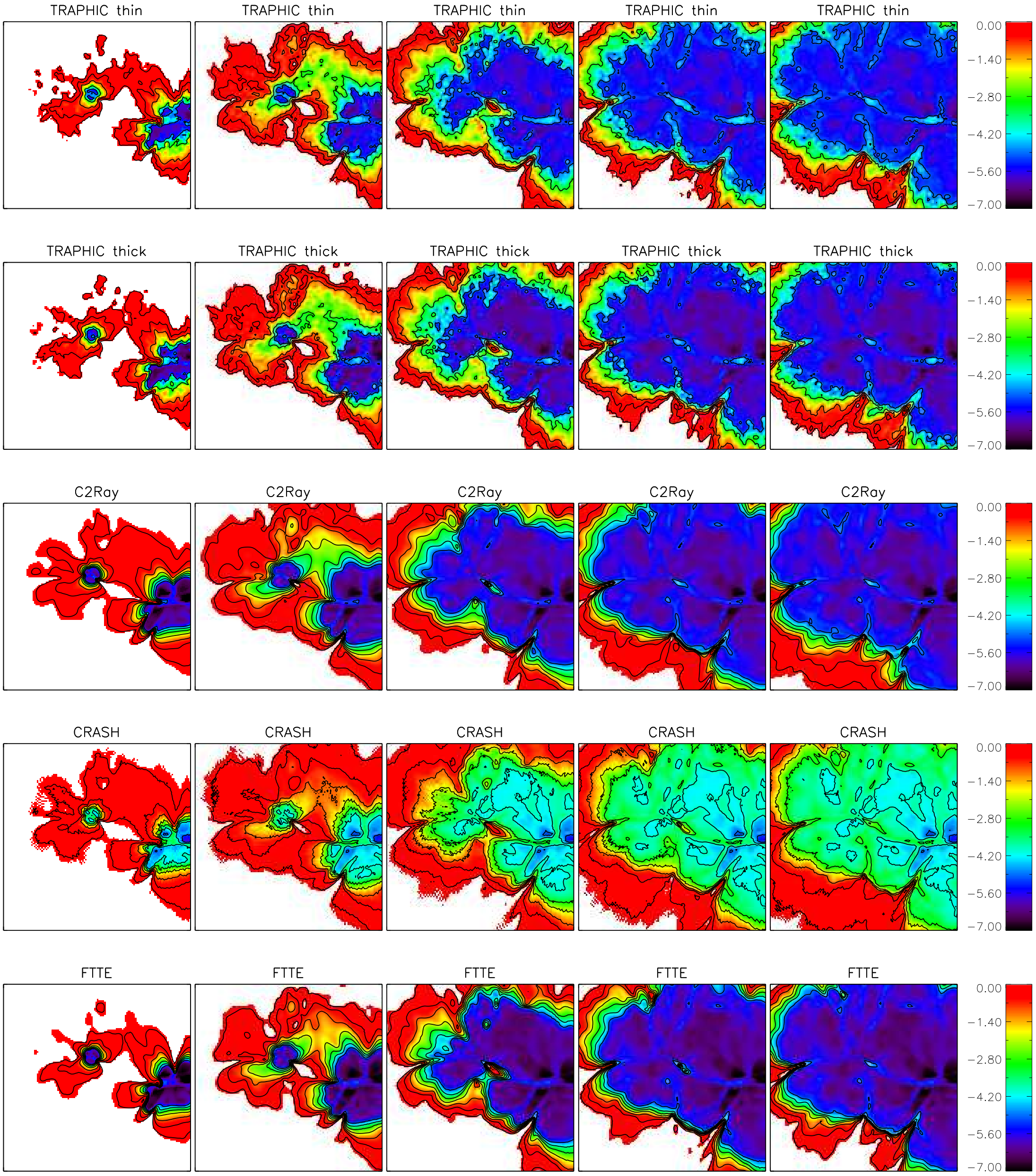

Figure 7.19: Test 7. Neutral fraction in a slice through $z = L_{\rm box}/2$. *From left to right:* $t = 0.05, 0.1, 0.2, 0.3$ and 0.4 Myr. *From top to bottom:* TRAPHIC *thin* (assuming grey optically thin photo-heating rates), TRAPHIC *thick* (assuming grey optically thick photo-heating rates), C^2-RAY, CRASH, FTTE. Contours show neutral fractions $\eta = 0.9, 0.5, \log \eta = -1, -3$ and -5, from the outside in. The colour scale is logarithmic and has a lower cut-off of $\eta = 10^{-7}$ (and hence is identical to that used in the top row panels of Fig. 5.15 in Chapter 5). The results obtained with TRAPHIC *thick* are in excellent agreement with those obtained with FTTE. They are also in excellent agreement with the results obtained with C^2-RAY in highly ionised regions, where the neutral fraction is unaffected by spectral hardening. The small differences in the neutral fractions obtained with TRAPHIC *thick* and TRAPHIC *thin* are mostly due to differences in the recombination rate, caused by differences in the gas temperatures (see Fig. 7.21). *See Fig. 4 in the appendix at the end of this thesis for a coloured version.*

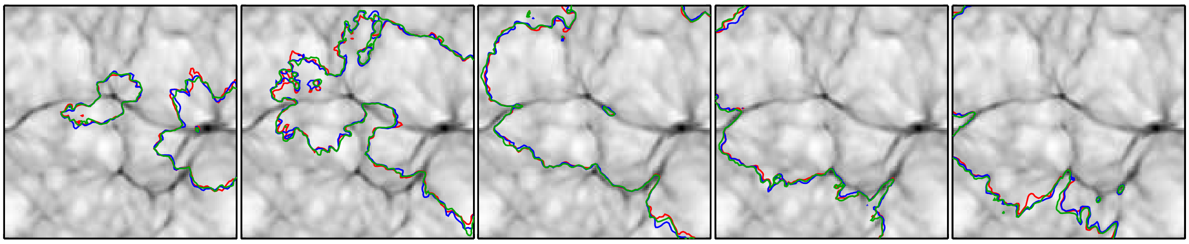

Figure 7.20: Test 7. Ionisation front evolution in a slice through $z = L_{\rm box}/2$. *From left to right:* $t = 0.05, 0.1, 0.2, 0.3$ and 0.4 Myr. Blue contours show ionisation fronts (neutral fraction of $\eta_{\rm HI} = 0.5$) obtained with TRAPHIC *thin*, i.e. computing photo-heating rates in the optically thin limit (cp. the top row panels in Fig. 7.19) and green contours show ionisation fronts obtained with TRAPHIC *thick*, i.e. computing photo-heating rates in the optically thick limit (cp. the second to top row panels in Fig. 7.19). For comparison, red contours show the ionisation front evolution in the fiducial ($N_{\rm c} = 32, \tilde{N}_{\rm ngb} = 32$) simulation presented in Sec. 5.4.5 in Chapter 5, which assumed a fixed temperature $T = 10^4$ K. The background grey-scale image shows the density field. Because all simulations employ similar photo-ionisation cross-sections and because of the weak dependence of the ionisation front position on temperature, the ionisation fronts are at nearly the same location.

the temperature along with that of the ionisation state of the gas.

The setup of this test is identical to that of Test 4 in Chapter 5, to which we refer the reader for a detailed description. Briefly, the initial conditions are provided by a snapshot (at redshift $z \approx 8.85$) from a cosmological N-body and gas-dynamical uniform-mesh simulation. The simulation box is $L_{\rm box} = 0.5\ h^{-1}$ comoving Mpc on a side, uniformly divided into $N_{\rm cell} = 128^3$ cells. We Monte Carlo sample this input density field to replace the mesh cells with $N_{\rm SPH} = N_{\rm cell} = 128^3$ SPH particles. The gas is assumed to be initially fully neutral and to have an initial temperature $T = 100$ K. The ionising sources are chosen to correspond to the 16 most massive halos in the box. They are assumed to have black-body spectra $B_\nu(\nu, T_{\rm bb})$ with temperature $T_{\rm bb} = 10^5$ K. The ionising photon production rate is taken to be constant and all sources are switched on at the same time. The boundary conditions are photon-transmissive, i.e. photons leaving the box are lost from the computational domain.

In this section we will perform two radiative transfer simulations to solve the time-independent radiative transfer equation, both with an angular resolution of $N_{\rm c} = 32$ (and setting $\tilde{N}_{\rm ngb} = 32$). We have demonstrated in Test 4 (Chapter 5) that for the current problem this angular resolution is sufficiently high to obtain converged results. To facilitate the direct comparison with the corresponding simulation performed in Test 4, we employ the same time step $\Delta t_{\rm r} = 10^{-4}$ Myr (and transport photons only over a single inter-particle distance per time step). We note that the current simulations do not employ the resampling technique that we have introduced in Chapter 4 to suppress noise in the neutral fraction caused by the particular realisation of the SPH density field. As discussed in Test 4, in the present test this noise is small.

For both our simulations we transport radiation using a single frequency bin, employing the grey photo-ionisation cross-section $\langle\sigma_{\rm HI}\rangle = 1.63 \times 10^{-18}$ cm^2 (Sec. 7.2). The difference between the two simulations is in the computation of the photo-heating rates used to evolve the gas temperatures. For one simulation we compute photo-heating in the optically thin limit (using Eq. 7.40), assuming that each photo-ionisation adds $\langle\epsilon_{\rm HI}\rangle = 6.32$ eV to the thermal energy of the gas (Sec. 7.3). In the other simulation we compute photo-heating in the optically thick limit (using Eq. 7.40), assuming that each photo-ionisation on average adds $\langle\epsilon_{\rm HI}^{\rm thick}\rangle = 16.01$ eV

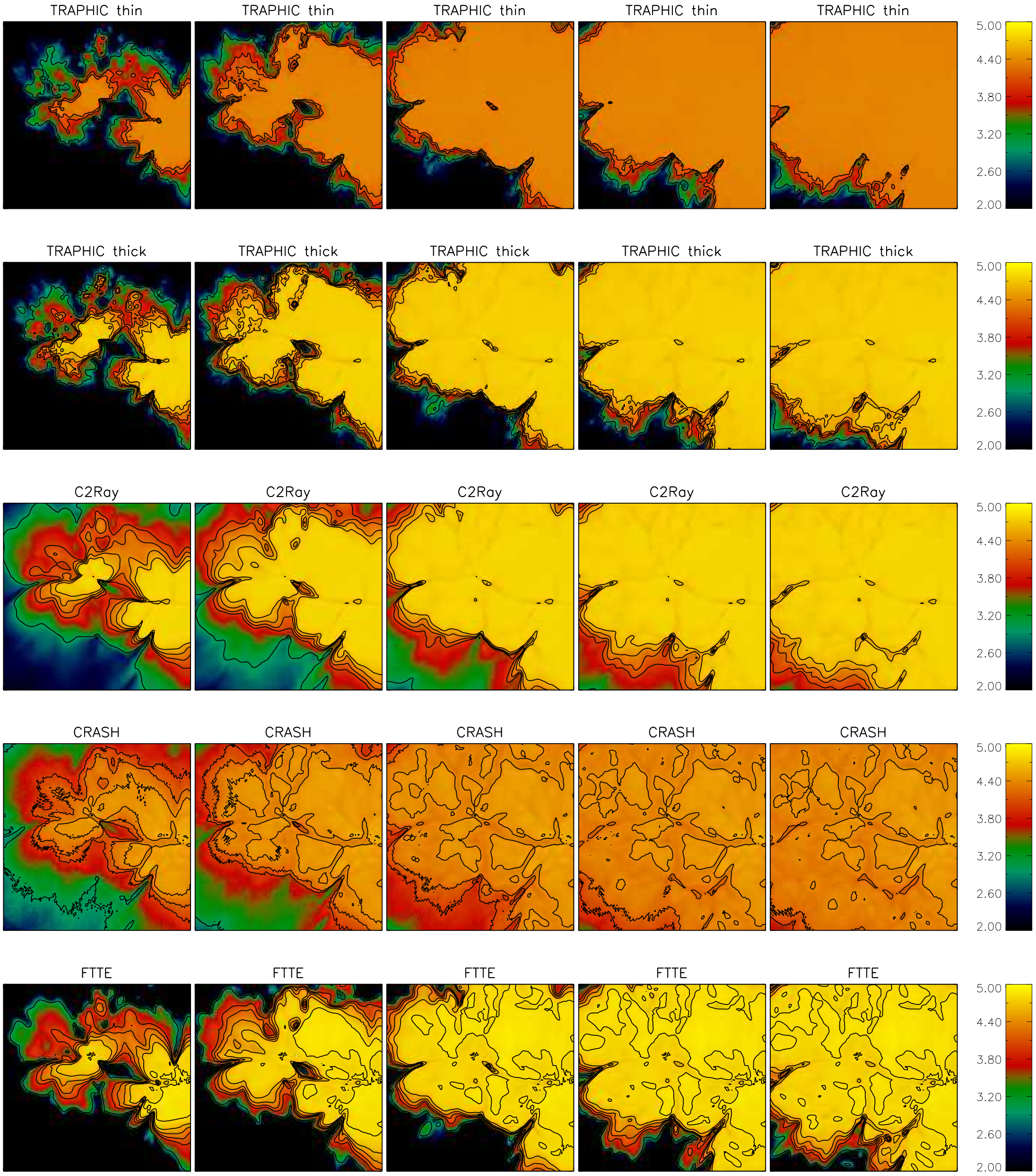

Figure 7.21: Test 7. Temperature in a slice through $z = L_{\rm box}/2$. *From left to right:* $t = 0.05, 0.1, 0.2, 0.3$ and 0.4 Myr. *From top to bottom:* TRAPHIC *thin* (assuming optically thin photo-heating rates), TRAPHIC *thick* (assuming optically thick photo-heating rates), C^2-RAY, CRASH and FTTE. Contours show temperatures $\log_{10}(T\ [\mathrm{K}]) = 3, 4, 4.2, 4.4$ and 4.6, from the outside in. Most of the morphological differences may be attributed to differences in the spectral hardening of the ionising radiation (with the multi-frequency codes C^2-RAY and CRASH predicting a substantial amount of pre-heating and the monochromatic (grey) codes TRAPHIC and FTTE predicting sharp transitions between the hot ionised and the cold neutral phase), while the differences in the maximum gas temperatures are mainly due to photo-heating being computed in the optically thick limit (TRAPHIC thick, C^2-RAY, FTTE), the optically thin limit (TRAPHIC thin) or using multiple frequency bins (CRASH). *See Fig. 5 in the appendix at the end of this thesis for a coloured version.*

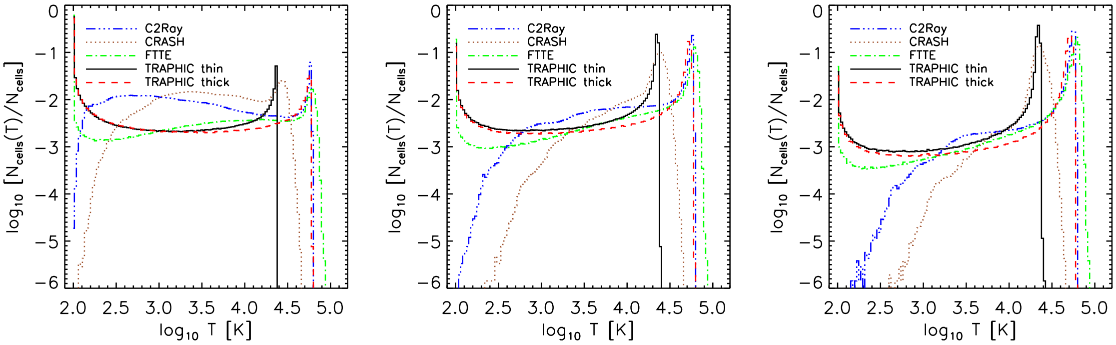

Figure 7.22: Test 7. Histograms of the temperature at times $t = 0.05, 0.2$ and 0.4 Myr (*from left to right*). At low temperatures the differences in the shape of the histograms are mainly due to differences in spectral hardening. The differences exhibited at high temperatures are mainly due photo-heating being computed in the optically thick limit (TRAPHIC *thick*, C^2-RAY, FTTE), the optically thin limit (TRAPHIC *thin*) or using multiple frequency bins (CRASH).

to the thermal energy of the gas (Sec. 7.3). For definiteness we mention that in both simulations we include collisional ionisations and all relevant cooling processes (including Compton cooling off the $z = 8.85$ cosmic microwave background), employing the rates listed in Table 7.1. Figs. 7.19-7.22 show our results.

Fig. 7.19 shows images of the neutral fraction in slices through the centre of the simulation box at times $t = 0.05, 0.1, 0.2, 0.3$ and 0.4 Myr (from left to right). The panels in the top two rows show the results obtained with TRAPHIC, with photo-heating computed in the optically thin (top row) and optically thick (second to top row) limit. They can be compared directly to the panels in the top row of Fig. 5.15 (Chapter 5), which show images of the neutral fraction in identical slices and at identical times obtained using identical (except for the temperature, recombination rate and photo-ionisation-cross-section) parameters. Neutral fraction contours are shown to facilitate this comparison. For reference, we also show the results obtained with other radiative transfer codes for the same test problem as published in Iliev et al. (2006). We have already employed the results obtained with C^2-RAY (Mellema et al. 2006) and CRASH (Ciardi et al. 2001; Maselli, Ferrara, & Ciardi 2003) in our comparisons of Test 4. For completeness, here we additionally compare our results with those obtained with FTTE (Razoumov & Cardall 2005). We recall that while the simulation with CRASH treated the present problem by performing a multi-frequency computation, the simulation with FTTE, as our simulations, solved it in the grey approximation, using optically thick photo-heating rates. Finally, C^2-RAY employed a hybrid method that treats the transport of radiation with multiple frequency bins but computes photo-heating rates in the grey (optically thick) approximation (for more details see our discussion in Sec. 7.6.2).

The differences in the neutral fractions between the results obtained in the thermally coupled simulation shown in the top row of Fig. 7.19 and those obtained assuming a fixed (but appropriately chosen) temperature shown in the top row of Fig. 5.15 (Chapter 5) are small. The simulation that employs photo-heating rates in the optically thick limit produces a smaller minimum neutral fraction as a result of lower recombination rates due to the higher temperatures it predicts (see Fig. 7.21). The ionisation fronts are, however, essentially at the same positions. This is explicitly demonstrated in Fig. 7.20, where we compare the ionisation fronts in these two simulations on top of images of the density field in the same slices through the centre of the simulation box and at the same times as we have used for the images of the neutral fraction shown in Figs. 7.19 and 5.15. This close matching was expected, given the agreement in the employed photo-ionisation cross-sections and the weak dependence of the ionisation front position on the gas temperature (cp. our discussion of the evolution of the ionisation front in Test 6, Fig. 7.13).

The panels in the top two rows of Fig. 7.21 show images of the gas temperature in slices through the centre of the simulation box at times $t = 0.05, 0.1, 0.2, 0.3$ and 0.4 Myr (from left to right) that correspond to the images of the neutral fraction shown in the top two rows of Fig. 7.19. That is, the panels in the top row show the predicted temperatures using photo-heating rates computed in the optically thin limit, while the panels in the second to top row show the temperatures obtained by computing photo-heating rates in the optically thick limit. We also show again the corresponding results obtained with C^2-RAY, CRASHand FTTE, as published in Iliev et al. (2006). To facilitate the comparison, we show contours of constant temperature on top of each of the images.

The results obtained with different codes exhibit large differences both in the morphologies of the photo-heated regions and the typical temperatures attained by the photo-ionised gas. Outside the ionisation fronts, differences in morphologies and gas temperatures can mostly be attributed to differences in the spectral hardening of the ionising radiation. Both C^2-RAY and CRASH predict a substantial pre-heating of the gas ahead of the ionisation fronts. This pre-heating is not seen in the simulations with TRAPHIC and FTTE since both treat the current problem in the grey approximation. In Sec. 7.6.2 we have already discussed, for the same set of codes, the differences between a multi-frequency treatment and its grey approximations in idealised simulations of the evolution of a single, spherically symmetric, ionised region. The results here are in close qualitative agreement with that discussion.

The results obtained with the different codes also exhibit large variations in the gas temperature in regions well inside the ionisation fronts. While CRASH and TRAPHIC *thin* predict typical temperatures of $T \approx 2 \times 10^4$ K, the typical temperatures predicted by C^2-RAY FTTE and TRAPHIC *thick* are, with $T \approx 6 \times 10^4$ K, substantially higher. Note that there is also disagreement between the results obtained with codes which incorporate the detailed treatment of multi-frequency radiation (C^2-RAY, CRASH) and between those obtained with codes in which the radiation is treated in the grey approximation (FTTE, TRAPHIC *thin*, TRAPHIC *thick*). Differences in spectral hardening are therefore unlikely to explain the observed temperature differences. Effects due to spectral hardening would also be expected to be small in the low-density, highly ionised and hence optically thin regions under consideration.

We recall that in Sec. 7.6.2, where we simulated the evolution of a single, spherically symmetric, photo-ionised region, we found qualitatively similar differences between the results obtained with C^2-RAY, CRASH and FTTE. In the optically thin region close to the ionising source, the simulations that employed C^2-RAY and FTTE predicted gas temperatures that were substantially larger than those predicted by the simulation that employed CRASH. By comparing with results obtained with our one-dimensional radiative transfer code TT1D, we were able to explain most of these temperature differences in terms of differences in the assumptions underlying the computation of photo-heating rates. The results presented in Fig. 7.21 are another manifestation of this explanation. We remind the reader that the temperatures obtained from CRASH and TRAPHIC *thin* (near ionising sources, where the neutral fractions are low) will be more accurate than those obtained from the codes that employ the optically thick limit for computing photo-heating rates (see Fig. 7.18).

In Fig. 7.22 we compare histograms of the temperature at times $t = 0.05, 0.2$ and 0.4 Myr (from left to right). For the simulations with C^2-RAY, CRASH and FTTE we have computed these histograms directly from the $N_{\rm cell} = 128^3$ values of temperatures published in Iliev et al. (2006). For the simulation with TRAPHIC we assigned the temperatures to a corresponding uniform mesh with $N_{\rm cell} = 128^3$ cells using (mass-conserving) SPH interpolation (see Sec. 5.4 in Chapter 5) before we computed the histograms.

The histograms provide a quantitative confirmation of our qualitative discussion above. The simulations with TRAPHIC *thin* predict, in close agreement with the simulations performed with CRASH, typical temperatures of $T \approx 2 \times 10^4$ K. On the other hand, the simulations performed with C^2-RAY, FTTE and TRAPHIC *thick* closely agree on typical temperatures of $T \approx 6 \times 10^4$ K. The differences between the histograms at low values of the temperature are mostly caused by the differences in spectral hardening. Due to the pre-heating of gas ahead of the ionisation fronts predicted by the multi-frequency codes C^2-RAY and CRASH, the number of cells that are still at their initial temperature $T = 100$ K is much smaller than found by FTTE and TRAPHIC, which only employ a single frequency bin.

Note that TRAPHIC predicts transitions between the photo-ionised hot and the neutral cold gas that are slightly more extended than those predicted by FTTE, as can be concluded from the small enhancement in the fraction of cells with temperatures 10^2 K $\lesssim T \lesssim 10^3$ K. This may be the result of the Monte Carlo sampling of the input density field that we employed to initialise the particle densities. As noted in our description of Test 4 in Chapter 5, in low-density regions Monte Carlo sampling may lead to a smaller effective resolution than that inherent to the input density field. The reduced spatial resolution would then imply an effective smoothing. Such a smoothing may also be caused by the interpolation of the particle properties to the uniform mesh that we performed for the computation of the histograms.

In summary, in this section we have repeated the simulation of the expansion of multiple ionised regions in a cosmological density field that we discussed in Test 4 (Chapter 5), but this time we explicitly computed, in addition to the evolution of the ionised fraction, the evolution of the temperature of the photo-ionised gas. We performed two simulations that were identical except for the photo-heating rates employed: one simulation computed photo-heating in the grey, optically thin limit (TRAPHIC *thin*), while the other computed photo-heating in the gry, optically thick limit (TRAPHIC *thick*).

Both simulations showed only small differences in the neutral fractions when compared with each other and with the corresponding simulation presented as part of Test 4 in Chapter 5 (which assumed a fixed temperature of $T = 10^4$ K), which was expected due to the similarity in the photo-ionisation cross-sections employed. We also compared the results of our thermally coupled simulations with results obtained with other radiative transfer codes for the same test problem (Iliev et al. 2006). We found excellent agreement between these and our results when comparing simulations that employed similar assumptions for computing photo-ionisation and photo-heating rates.

7.7 CONCLUSION

The thermal evolution of the (intergalactic) gas in the Universe is an important observable. It is determined by the (photo-) ionisation, heating and cooling rates that it experiences. For the applications of interest, the most important radiative cooling and heating processes are collisional excitation cooling, collisional ionisation cooling, recombination cooling, cooling by Bremsstrahlung, Compton cooling of the cosmic microwave background and photo-heating by ultra-violet radiation. The accurate incorporation of the effects of photo-heating into cosmological simulations poses a particularly difficult problem, because it requires the use of accurate and efficient, thermally coupled radiative transfer schemes. The main aim of this chapter was to provide an implementation of such a scheme, based on the radiative transfer scheme TRAPHIC that we have described in Chapter 4.

This implementation required some preparatory work. We started by briefly discussing the physics of the main ionisation, recombination, cooling and heating processes that determine the gas temperature. Their numerical evaluation requires atomic data, i.e. cross-sections and rate coefficients, which often are not very well constrained. This is partly due to the fact that the dependence of these cross-sections and rate coefficients on temperature and density is difficult to probe experimentally for the extremely low densities and high temperatures that are of interest in astrophysical applications.

Different works reported in the literature employ different extrapolations into these regimes which causes, sometimes significant, differences in the employed heating and cooling rates. We have illustrated and discussed these differences for each individual process and have also compared total (equilibrium) cooling rates that are commonly employed. Heating and cooling are amongst the main processes that determine the evolution of gas in hydrodynamical cosmological simulations. The lack of strong efforts to establish an accurate standard of atomic data for the evaluation of heating and cooling rates is therefore somewhat worrying.

From the set of atomic data and their fits that we have discussed we chose reference expressions for the photo-ionisation cross-sections, ionisation, recombination and cooling rates for use with the simulations presented in this chapter. Based on these rates we discussed, for reference, the properties of primordial gas subject to (photo-)ionisation, heating and cooling in ionisation equilibrium. Amongst other things, we illustrated the well-known fact that cooling in primordial atomic gas becomes highly inefficient for gas temperatures lower than $T \approx 10^4$ K. We also showed that ionising radiation reduces the cooling efficiency of primordial gas, which is also well-known.

We then described a method to compute the non-equilibrium evolution of the ionised fraction of gas exposed to (hydrogen-) ionising radiation together with its thermal evolution. A self-consistent method is required, since the ionisation state and the gas temperature are coupled through the dependence of the collisional ionisation, recombination and cooling rate coefficients on the temperature and ionisation state of the gas. Our method extends the sub-cycling technique that we have described in Chapter 5 to compute the evolution of the ionised fraction of gas at a fixed temperature indepedently of the size of the radiative transfer time step. We demonstrated in test simulations of the evolution of an optically thin gas particle subject to photo-ionisation that the sub-cycling can be successfully employed, independently of the size of the radiative transfer time step, also in the case of a self-consistently evolving temperature.

With these preparations in hand we were able to describe an extension of TRAPHIC, the radiative transfer scheme for use with smoothed particle hydrodynamics simulations that we described in Chapters 4 and 5, to include the computation of the gas temperature subject to photo-heating by the UV field computed by the radiative transfer simulation itself. This thermal coupling was the main aim of this chapter. We have applied TRAPHIC to compute the evolution of the ionised fraction and the temperature around a single ionising source with a black-body spectrum in a homogeneous, hydrogen-only medium. The set-up of this test calculation was chosen to facilitate the comparison with both analytical and numerical reference solutions. We performed such a comparison and found excellent agreement.

Since our implementation of TRAPHIC currently employs only a single frequency bin, we treated this multi-frequency problem in the grey approximation. We discussed this approximation by comparing our results to results obtained in a full multi-frequency simulation with our one-dimensional radiative transfer code TT1D that we developed for this purpose. We performed grey simulations, computing photo-heating both in the optically thin limit, which is the relevant limit when considering the thermal structure of highly-ionised regions, and in the optically thick limit, which is the relevant limit when considering the energy balance of the ionised region as a whole.

We found significant differences in the results obtained from the grey and the multi-frequency simulations. Close to and ahead of the ionisation front these differences were mostly due to the spectral hardening of the radiation field caused by the dependence of the absorption cross-section on the photon energy. We also found significant differences between the grey simulations that employed the optically thin and the optically thick limits to compute photo-heating rates. Close to the ionsing source, the simulation using optically thick photo-heating rates predicted temperatures that are substantially larger than those predicted by the simulation using optically thin photo-heating rates. Only the latter asymptotes to the multi-frequency simulation in the limit of small optical depths.

Finally, we simulated the evolution of ionised regions around multiple sources in a cosmological density field. The simulation was similar to those presented in Test 4 (Chapter 5), but now we also followed the evolution of the gas temperature. A comparison to results obtained with other codes showed excellent agreement in the predicted morphologies and gas temperatures of the photo-ionised and photo-heated regions, when comparing simulations that employed similar assumptions for computing photo-ionisation and photo-heating rates.

We have limited our consideration in this chapter to radiative transfer simulations on pre-computed static density fields. Our goal for the future will be to drop this simplification and perform hydrodynamically coupled radiative transfer simulations.

ACKNOWLEDGEMENTS

We thank Alexei Razoumov and Dominique Aubert for very useful exchanges on the computation of photo-heating rates. We thank Garrelt Mellema and Antonella Maselli for valuable discussions.

REFERENCES

Abel T., Anninos P., Zhang Y., Norman M. L., 1997, NewA, 2, 181

Abel T., Haehnelt M. G., 1999, ApJ, 520, L13

Aldrovandi S. M. V., Pequignot D., 1973, A&A, 25, 137

Anninos P., Zhang Y., Abel T., Norman M. L., 1997, NewA, 2, 209

Badnell N. R., 2001, ASPC, 247, 37

Badnell N. R., et al., 2003, A&A, 406, 1151

Barkana R., Loeb A., 2001, PhR, 349, 125

Bernardi M., et al., 2003, AJ, 125, 32

Bethe H. A., Salpeter E. E., 1957, Quantum Mechanics of One and Two Electron Atoms (Springer)

Black J. H., 1981, MNRAS, 197, 553

Bolton J., Meiksin A., White M., 2004, MNRAS, 348, L43

Bromm V., Yoshida N., Hernquist L., 2003, ApJ, 596, L135

Burgess A., Seaton M. J., 1960, MNRAS, 121, 471

Castor J., 2004, Radiation Hydrodynamics, Cambridge University Press

Cen R., 1992, ApJS, 78, 341

Chang E. S., Avrett E. H., Loeser R., 1991, A&A, 247, 580

Choi J.-H., Nagamine K., 2009, MNRAS, 395, 1776

Ciardi B., Ferrara A., Marri S., Raimondo G., 2001, MNRAS, 324, 381

Cox D. P., Tucker W. H., 1969, ApJ, 157, 1157

Dalgarno A., McCray R. A., 1972, ARA&A, 10, 375

Dijkstra M., Haiman Z., Rees M. J., Weinberg D. H., 2004, ApJ, 601, 666

Efstathiou G., 1992, MNRAS, 256, 43P

Faucher-Giguère C.-A., Lidz A., Hernquist L., Zaldarriaga M., 2008, ApJ, 688, 85

Ferland G. J., Peterson B. M., Horne K., Welsh W. F., Nahar S. N., 1992, ApJ, 387, 95

Ferland G. J., Korista K. T., Verner D. A., Ferguson J. W., Kingdon J. B., Verner E. M., 1998, PASP, 110, 761

Fixsen D. J., Cheng E. S., Gales J. M., Mather J. C., Shafer R. A., Wright E. L., 1996, ApJ, 473, 576

Furlanetto S. R., Oh S. P., Briggs F. H., 2006, PhR, 433, 181

Gnat O., Sternberg A., 2007, ApJS, 168, 213

Haardt F., Madau P., 2001, in the proceedings of XXXVI Rencontres de Moriond, preprint (astroph/0106018)

Haiman Z., Thoul A. A., Loeb A., 1996, ApJ, 464, 523

Hui L., Gnedin N. Y., 1997, MNRAS, 292, 27

Hui L., Haiman Z., 2003, ApJ, 596, 9

Hummer D. G., 1994, MNRAS, 268, 109

Hummer D. G., Storey P. J., 1998, MNRAS, 297, 1073

Iliev I. T., Shapiro P. R., Raga A. C., 2005b, MNRAS, 361, 405

Iliev I. T., et al., 2006, MNRAS, 371, 1057

Kitayama T., Ikeuchi S., 2000, ApJ, 529, 615

Komatsu E., et al., 2008, preprint (arXiv:0803.0547)

Lipovka A., Núñez-López R., Avila-Reese V., 2005, MNRAS, 361, 850

Lotz W., 1967, ApJS, 14, 207

Madau P., Efstathiou G., 1999, ApJ, 517, L9

Maselli A., Ferrara A., Ciardi B., 2003, MNRAS, 345, 379

Maselli A., Ciardi B., Kanekar A., 2009, MNRAS, 393, 171

Mellema G., Iliev I. T., Alvarez M. A., Shapiro P. R., 2006, NewA, 11, 374

McQuinn M., Lidz A., Zaldarriaga M., Hernquist L., Hopkins P. F., Dutta S., Faucher-Giguère C.-A., 2009, ApJ, 694, 842

Miralda-Escudé J., Rees M. J., 1994, MNRAS, 266, 343

Osterbrock D. E., 1989, agna.book,

Petkova M., Springel V., 2008, arXiv, arXiv:0812.1801

Press W. H., Teukolsky S. A., Vetterling W. T., Flannery B. P., 1992, nrca.book,

Razoumov A. O., Cardall C. Y., 2005, MNRAS, 362, 1413

Ricotti M., Gnedin N. Y., Shull J. M., 2000, ApJ, 534, 41

Ritzerveld J., 2005, A&A, 439, L23

Ritzerveld J., Icke V., 2006, PhRvE, 74, 026704

Rybicki G. B., Lightman A. P., 2004, rpa..book,

Savin D. W., 2000, ApJ, 533, 106
Savin D. W., 2000, RMxAC, 9, 115
Schaye J., Theuns T., Rauch M., Efstathiou G., Sargent W. L. W., 2000, MNRAS, 318, 817
Schmutzler T., Tscharnuter W. M., 1993, A&A, 273, 318
Seaton M. J., 1959, MNRAS, 119, 81
Shapiro P. R., Kang H., 1987, ApJ, 318, 32
Shapiro P. R., Iliev I. T., Raga A. C., 2004, MNRAS, 348, 753
Shull J. M., van Steenberg M. E., 1985, ApJ, 298, 268
Smith B., Sigurdsson S., Abel T., 2008, MNRAS, 385, 1443
Spitzer L., 1978, ppim.book,
Spitzer L. J., 1948, ApJ, 107, 6
Springel V., 2005, MNRAS, 364, 1105
Susa H., Umemura M., 2004, ApJ, 600, 1
Sutherland R. S., Dopita M. A., 1993, ApJS, 88, 253
Tegmark M., Silk J., Rees M. J., Blanchard A., Abel T., Palla F., 1997, ApJ, 474, 1
Theuns T., Leonard A., Efstathiou G., Pearce F. R., Thomas P. A., 1998, MNRAS, 301, 478
Theuns T., Schaye J., Zaroubi S., Kim T.-S., Tzanavaris P., Carswell B., 2002, ApJ, 567, L103
Thoul A. A., Weinberg D. H., 1996, ApJ, 465, 608
Tittley E. R., Meiksin A., 2007, MNRAS, 380, 1369
Trac H., Cen R., 2007, ApJ, 671, 1
Verner D. A., Ferland G. J., Korista K. T., Yakovlev D. G., 1996, ApJ, 465, 487
Weymann, 1965, Phys. Fluids, 8, 2112
Whalen D., Norman M. L., 2008, ApJ, 673, 664
Wiersma R. P. C., Schaye J., Smith B. D., 2009, MNRAS, 393, 99

> Misschien is niets geheel waar, en zelfs dat niet.
>
> Multatuli, Ideeën

Nederlandse samenvatting

HET TIJDPERK VAN REIONISATIE

De eerste sterren en sterrenstelsels vormden een paar honderd miljoen jaar na de oerknal, toen het heelal nog maar een fractie van zijn huidige leeftijd had. Er wordt gedacht dat hun straling het koude en neutrale waterstof in de ruimte veranderde in het hete en geïoniseerde kosmische plasma dat wij nu waarnemen. Deze mijlpaal in de geschiedenis van het heelal wordt het tijdperk van reïonisatie genoemd (Fig. 1).

Veel van dit tijdperk is nog onbekend. Precies kennis van reïonisatie is echter belangrijk om de huidige toestand van het universum te begrijpen. Het effect van reïonisatie op de vorming en evolutie van sterrenstelsels zou misschien de helderheidsverdeling van satellieten rond de Melkweg, ons eigen sterrenstelsel, kunnen verklaren. Wanneer vond reïonisatie plaats? Was het een eenvoudige gebeurtenis of was het een ingewikkelde, langdurige overgang? Waren de eerste sterren in de eerste sterrenstelsels krachtig genoeg om het heelal te ioniseren? Of waren er nog andere lichtbronnen van ioniserende straling?

Nog nooit zijn wij zo dichtbij het ontrafelen van de geheimen van dit kosmische proces geweest. Theoretische studies van reïonisatie zijn nu bijzonder nodig, omdat er binnenkort veel waarnemingen met nieuwe telescopen gedaan worden. Radio telescopen, zoals LOFAR[1], MWA[2] en SKA[3], zullen het mogelijk maken om een onontdekt deel van het heelal te bekijken, met lagere frequenties en hogere resolutie dan tot nu toe kon. De infrarood-ruimtetelescoop JWST[4] en de veertig meter optische telescoop ELT[5] zullen de bronnen verantwoordelijk voor het reïonisatie proces direct kunnen zien.

Hoeveel straling is er nodig om het universum te ioniseren? Deze vraag klinkt simpeler dan hij is. Sterker nog, deze vraag is waarschijnlijk een van de ingewikkeldste vragen die je kan stellen over reïonisatie. Pogingen om antwoord hierop te geven hebben al geleid tot belangrijke inzichten in de productie en de vernietiging van de straling, die het heelal geïoniseerd heeft. Hun werkelijke verdienste ligt in het besef dat een dieper begrijp van de thermische interactie tussen het gas en de ioniserende straling noodzakelijk is.

Ionisaties produceren vrije elektronen wiens bewegingsenergie bijdraagt aan de thermische energie van het geïoniseerde gas. Omdat een toename in de temperatuur van het gas een toename in de druk met zich meebrengt, dijt het gas uit. De uitdijing vermindert de dichtheidsfluctuaties en 'kookt' het gas uit de lage massa sterrenstelsels. Deze verdamping onderdrukt de kosmische stervormingssnelheid en de hoeveelheid straling. Dit noemen wij negatieve feed-

---

[1] http://www.lofar.org

[2] http://www.haystack.mit.edu/ast/arrays/mwa/

[3] http://www.skatelescope.org

[4] http://www.jwst.nasa.gov/

[5] http://www.eso.org/sci/facilities/eelt/

back. Maar deze verhitting zorgt ook voor positieve feedback, omdat het aantal recombinaties vermindert ten gevolge van het uitsmeren van de dichtheidsfluctuaties. Daardoor zijn er minder ioniserende fotonen nodig om het heelal geïoniseerd te houden. De combinatie van deze twee effecten bepaalt hoeveel ioniserende fotonen er nodig zijn om het heelal te reïoniseren.

Een van de meest veelbelovende technieken om de aard van thermische feedback te bestuderen zijn hoge resolutie, hydrodynamische simulaties met stralingstransport. Het simuleren van reïonisatie is echter een uitdagende taak, omdat wij de stralingsvergelijking moeten oplossen in een groot, representatief volume van het universum waar typisch een groot aantal bronnen van ioniserende straling in zitten. De bestaande methoden voor stralingstransport waren ontwikkeld voor hele andere doeleinden, zoals het uitrekenen van de ionisatiestructuur rond een enkele stralingsbron in een heel klein volume. Deze bereiken snel hun grenzen wanneer ze toegepast worden op moderne simulaties van reïonisatie.

De belangrijkste wetenschappelijke bijdrage van dit proefschrift is de ontwikkeling van een nieuwe methode om het stralingstransport-probleem in grote simulaties van reïonisatie op te lossen. Deze methode - TRAPHIC (TRAnsport of PHotons In Cones) - is ontworpen om de obstakels van de simulatie van reïonisatie in grote volumes en met veel bronnen te overwinnen. Het is een van de eerste van zijn soort.

DIT PROEFSCHRIFT

In deze sectie geven wij korte samenvattingen van de inhoud van hoofdstukken 2-7 van dit proefschrift.

Hoofdstuk 2. De kritische dichtheid van stervormingssnelheid die nodig is om het intergalactische waterstof geïoniseerd te houden, hangt af van de gemiddelde recombinatiesnelheid in het intergalactische medium (IGM). Deze snelheid is evenredig met de *clumping factor* $C \equiv \langle \rho_{\mathrm{b}}^2 \rangle_{\mathrm{IGM}} / \langle \rho_{\mathrm{b}} \rangle^2$, waar ρ_{b} en $\langle \rho_{\mathrm{b}} \rangle$ de locale en kosmische gemiddelde dichtheid van baryonen zijn en de haakjes $\langle \rangle_{\mathrm{IGM}}$ geven het middelen over de ruimte aan. Wij hebben een reeks kosmologische simulaties (*smoothed particle hydrodynamics* simulaties) inclusief afkoeling door straling om de clumping factor van het IGM op roodverschuiving $z \geq 6$ uit te rekenen. Wij focussen op het effect van verhitting door foto-ionisatie door een uniforme ultraviolette achtergrond en vinden dat verhitting de clumping factor sterk reduceert omdat de toegenome druk de dichtheidsfluctuaties op kleine schaal uitsmeert. Er wordt vaak gezegd dat verhitting door foto-ionisatie een negatief feedback-effect heeft op de reïonisatie van het IGM omdat het de stervormingssnelheid verminderd door gas uit lage massa sterrenstelsels te koken. Echter, door de reductie van de clumping factor is het juist ook makelijker om het IGM geïoniseerd te houden. Verhitting zorgt daardoor ook voor een positief feedback-effect, die hoewel bekend, veel minder aandacht heeft gekregen. Wij demonstreren dat dit positieve feedback-effect erg sterk is. Met conservatieve aannames tonen wij aan dat, als het IGM op $z \gtrsim 9$ was verhit, de waargenomen populatie stervormende sterrenstelsels op $z \approx 6$ genoeg kan zijn om het IGM geïoniseerd te houden mits de fractie van ontsnappende ioniserende fotonen groter is dan ~ 0.2

Hoofdstuk 3. Het is eerder aangetoond dat verhitting ten gevolge van reïonsatie en kinetische feedback van supernovae de kosmische stervormingssnelheid op hoge roodverschuiving kan onderdrukken. Hier onderzoeken wij het samenspel van verhitting en supernova feedback, gebruikmakend van een set van kosmologische *smoothed particle hydrodynamics* simulaties. We laten zien dat verhitting en supernova feedback elkaar versterken in het onderdrukken van de stervormingssnelheid. Onze resultaten demonstreren het belang van het simultaan, niet onafhankelijk toevoegen van deze twee processen in modellen van de vorming van ster-

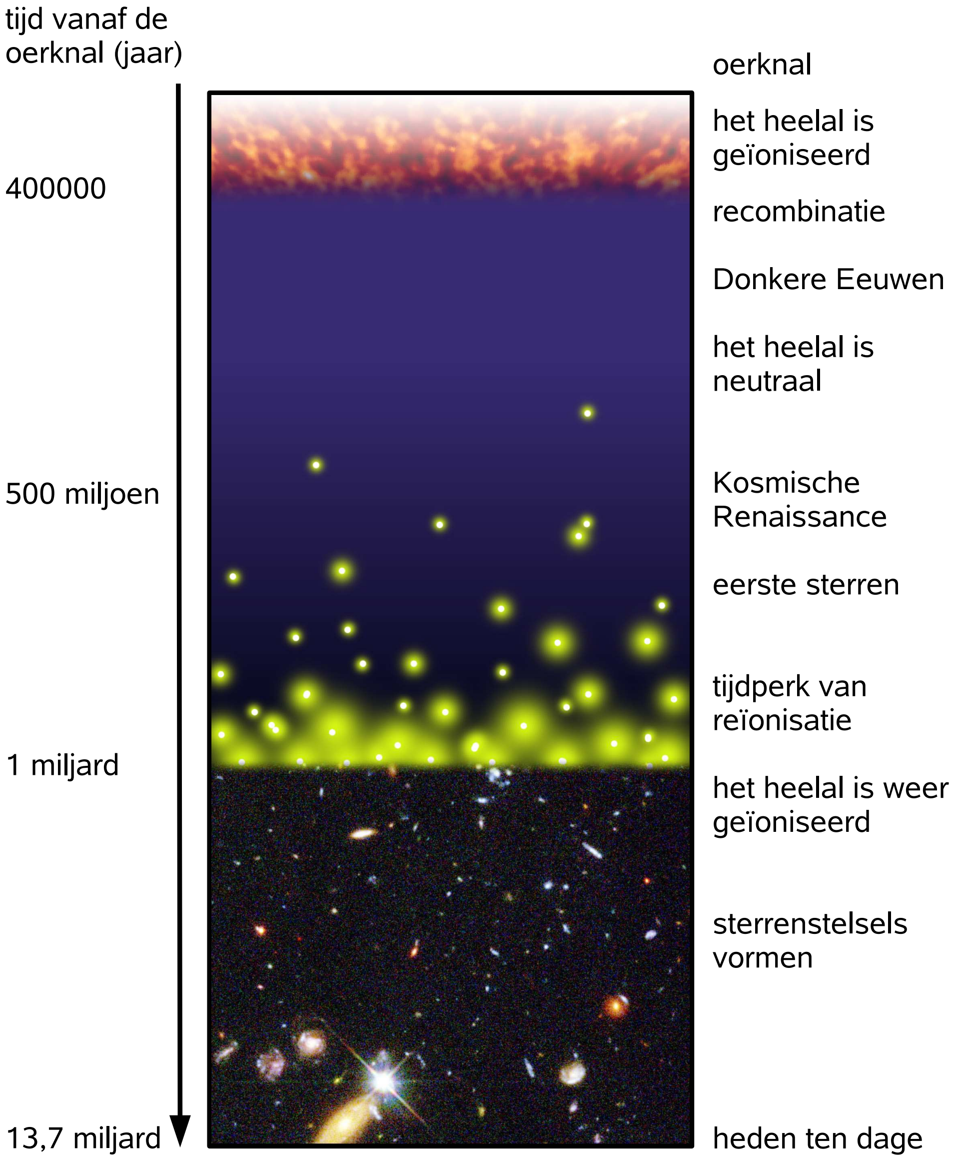

Djorgovski et al. & Digital Media Center, Caltech

Figuur 1: De geschiedenis van het uitdijende universum begint met zijn geboorte in de oerknal (Big Bang) ongeveer 13,7 miljard jaar geleden. Maar het duurde tot ongeveer 400.000 jaar na de oerknal voordat het heelal genoeg was afgekoeld zodat de vorming van atomen mogelijk was. Na deze gebeurtenis, bekend als recombinatie, bestond het heelal voornamelijk uit atomair waterstof. Na recombinatie kwam het heelal terecht in de Donkere Eeuwen, een periode waarin het ondoorlatend was voor ioniserende straling. De eerste sterren vormden honderd miljoen jaar na de oerknal, het begin van de Kosmische Renaissance. Hun straling reïoniseerde het neutrale waterstof gedurende het tijdperk van reïonisatie, waarna het universum transparant werd voor ioniserende straling. Heden ten dage bestuderen astronomen de geboorte van de eerste sterrenstelsels door de observatie van deze straling. Image credits: S. G. Djorgovski et al. & the Caltech Digital Media Center.

renstelsels, om het totale effect van negatieve feedback te schatten. Zij zullen daardoor vooral relevant zijn voor semi-analytische modellen waarin de effecten van verhitting en supernova feedback onafhankelijk van elkaar worden behandeld.

Hoofdstuk 4. Wij presenteren TRAPHIC, een nieuwe methode voor het transporteren van straling in *Smoothed Particle Hydrodynamics* (SPH) simulaties. TRAPHIC (TRAnsport of PHotons In Cones) is ontworpen voor gebruik in simulaties met een groot dynamische bereik en een hoog aantal lichtbronnen. Het is adaptief zowel in ruimte als in hoek en kan toegepast worden op computers met gedistribueerd geheugen. De (tijd-afhankelijke) stralingstransport-vergelijking wordt opgelost door individuele fotonpakketjes te volgen op een expliciet foton behoudende manier direct op het ongestructueerde rooster gemarkeerd door de set van SPH deeltjes. Om het directe transport van straling te verwezenlijken ondanks de onregelmatige ruimtelijke verdeling van de SPH deeltjes, worden fotonen binnen kegels geleid. De dure schaling van rekentijd met het aantal lichtbronnen waar in conventionele transportmethoden tegen aangelopen wordt, wordt ontweken door de samenvoeging van bronnen.

Hoofdstuk 5. Wij presenteren en testen een parallelle numerieke implementatie van onze stralingstransportmethode TRAPHIC voor het transport van monochromatische waterstof ioniserende straling in de *smoothed particle hydrodynamics* code GADGET-2. De tests bestaan uit meerdere stralingstransport-problemen van toenemende complexiteit. Sommige van deze tests zijn specifieke ontworpen om TRAPHIC's vermogen om het stralingstransportprobleem in grote kosmologische reïonisatie simulaties op te lossen, waar het voor was ontwikkeld. Andere tests zijn ontworpen om te demonstreren dat TRAPHIC ook in meer algemene context gebruikt kan worden. De resultaten van alle tests komen uitstekend overeen met zowel analytische oplossingen als numerieke referentie-resultaten.

Hoofdstuk 6. Simulaties van stralingstransport (ST) gekoppeld aan kosmologische hydrodynamische simulaties zijn een van de meest veelbelovende technieken om reïonisatie, een belangrijk tijdperk in het hoge roodverschuiving universum, te bestuderen. Huidige generaties van ST methodes zijn echter vaak beperkt in het gebruik met uniforme en relatief grove roosters, die een veel lagere resolutie hebben dan huidige hydrodynamische simulaties. Kleine schaal structuur in het kosmische gas kan dan niet of slechts statistisch bestudeerd worden. Hier gebruiken wij de ruimtelijke adaptieve ST methode TRAPHIC (Hoofdstuk 4) om de implicaties van deze benadering te onderzoeken. Wij vergelijken ST simulaties uitgevoerd op een ruimtelijk adaptief *smoothed particle hydrodynamics* dichtheidsveld met ST simulaties uitgevoerd op een dichtheidsveld gedefinieerd op een uniform rooster. Vergelijkingen van de evolutie van de gemiddelde geïoniseerde fractie, de afhankelijkheid van de geïoniseerde fractie op de locale gasdichtheid en de *power spectra* van het 21 cm signaal van neutraal waterstof onthullen significante verschillen veroorzaakt door het verschil in het dynamische bereik toegepast door de twee types ST simulaties. Onze resultaten bevestigen eerdere suggesties dat het negeren van de inhomogene distributie van gas op kleine schaal, zoals gebruikelijk is in huidige ST simulaties van reïonisatie, kunnen leiden tot misleidende conclusies over de ruimtelijke verdeling van het geïoniseerde gas en dus over de interpretatie van huidige en de voorspellingen van toekomstige observaties van reïonisatie.

Hoofdstuk 7. De temperatuur van het kosmische gas is een belangrijke astrofysische grootheid. Het gedetailleerd modelleren van zijn ontwikkeling met kosmologische hydrodynamische simulaties vergt het gebruik van stralingstransport methoden om nauwkeurig de effecten van foto-ionisatie en verhitting op de desbetreffende koeling en verwarming te kunnen berekenen. We breiden onze implementatie van TRAPHIC (Hoofdstuk 4 en 5) uit om de niet-evenwicht evolutie van de temperatuur van het gas blootgesteld aan waterstof-ioniserende straling te kunnen berekenen. Wij controleren deze uitbreiding door vergelijking van TRAPHIC's resultaten in thermisch gekoppelde stralingstransport tests met referentieresultaten verkregen met andere stralingstransport codes.

Colour figures

This appendix contains a selection of figures from this thesis in full colour. A full colour version of the complete thesis is available electronically at http://proefschrift.leidenuniv.nl.

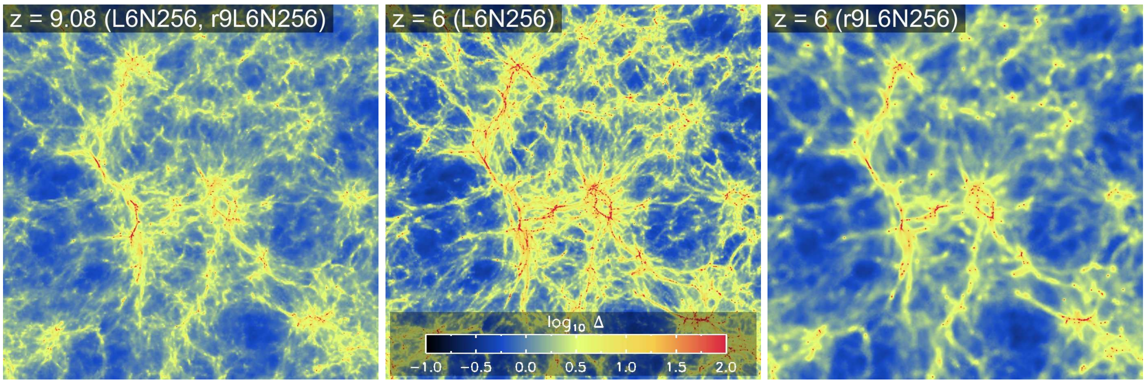

Figure 2: Identical to Fig. 2.2. Slices (of thickness $1.25\ h^{-1}$ comoving Mpc) through the centre of the simulation box, showing the SPH overdensity field in the simulations *L6N256* and *r9L6N256* at redshifts $z = 9.08$ (left-hand panel; where they are identical) and $z = 6$ (middle panel: *L6N256*, right-hand panel: *r9L6N256*). The inclusion of photo-heating in *r9L6N256* leads to a strong smoothing of the density field (right-hand panel).

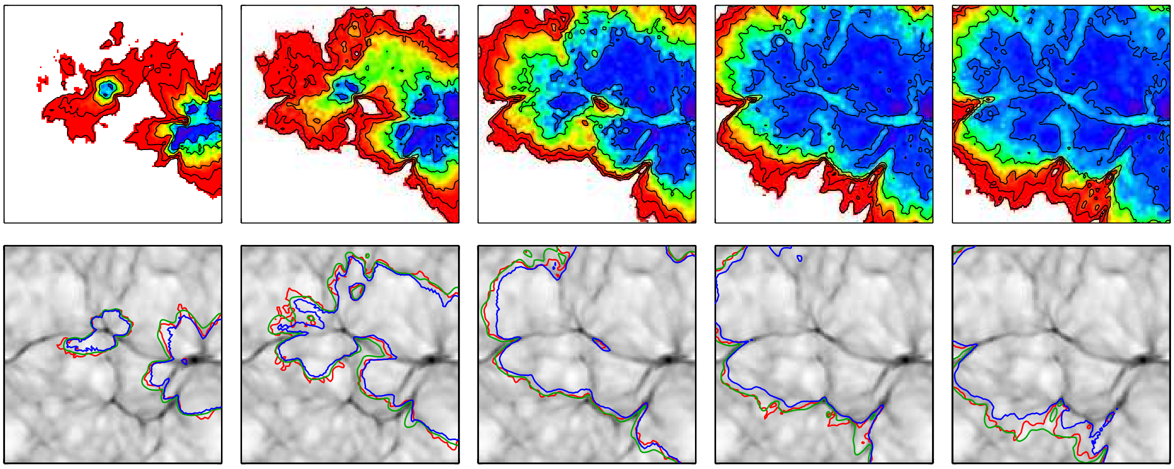

Figure 3: Identical to Fig. 5.15. Test 4: *Top row:* neutral fraction in a slice through $z = L_{\rm box}/2$ at times $t = 0.05, 0.1, 0.2, 0.3, 0.4$ Myr (from left to right). Contours show neutral fractions $\eta = 0.9, 0.5$, $\log \eta = -1, -3$ and -5, from the outside in. The colour scale is logarithmic and has a lower cut-off of $\eta = 10^{-7}$. It is identical to the colour scale used and shown in Fig. 7.19 of the corresponding test 7 in Chapter 7 (see Fig. 4 for a colour version). *Bottom row:* Density field in the slices shown in the top panels. Contours show ionisation fronts (neutral fraction of $\eta = 0.5$). Red contours show the results of our fiducial ($N_{\rm c} = 32, \tilde{N}_{\rm ngb} = 32$) simulation. For comparison, we show the results of C^2-RAY (green) and CRASH (blue). The agreement is excellent.

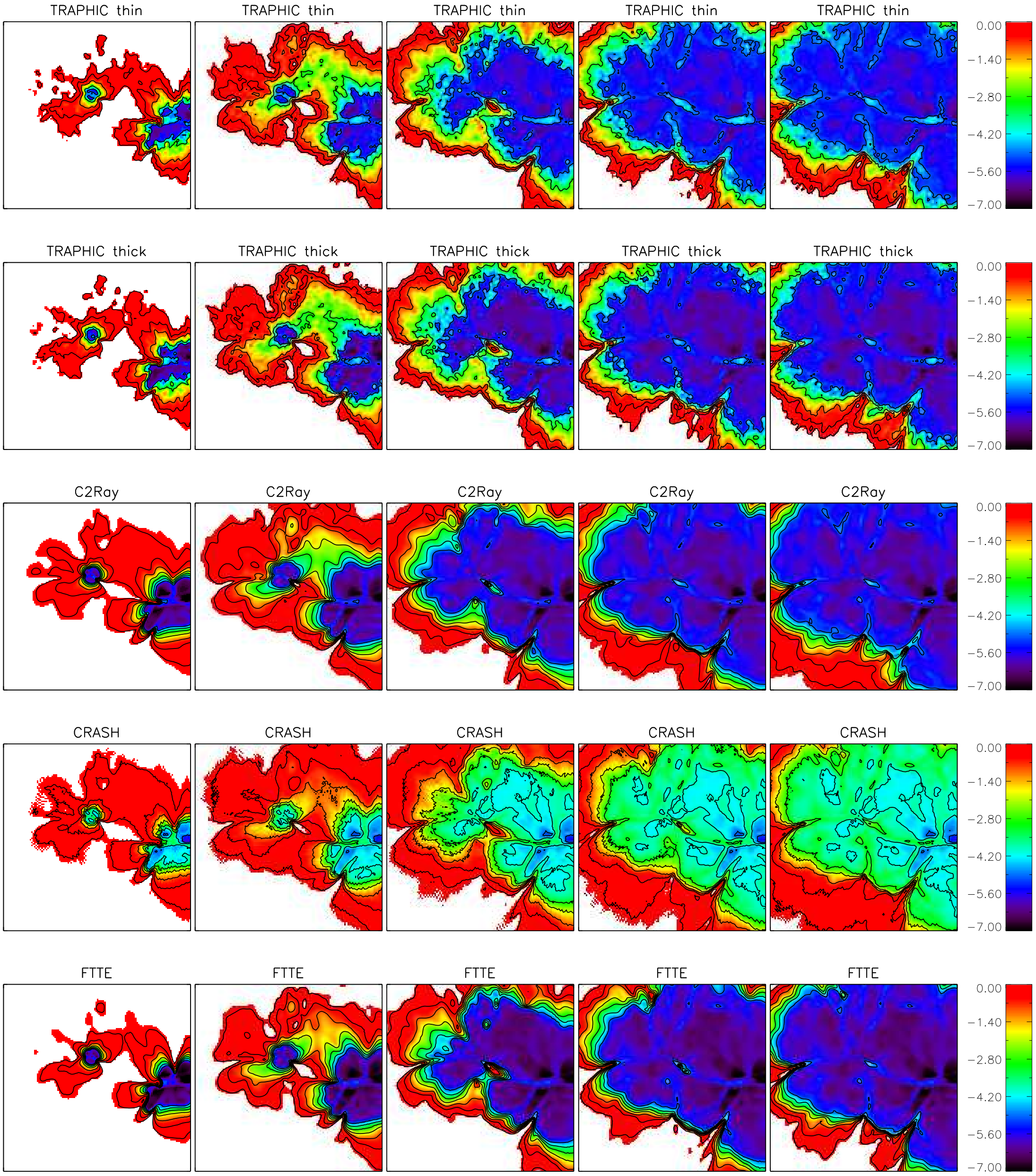

Figure 4: Identical to Fig. 7.19. Test 7: Neutral fraction in a slice through $z = L_{\rm box}/2$. *From left to right:* $t = 0.05, 0.1, 0.2, 0.3$ and 0.4 Myr. *From top to bottom:* TRAPHIC *thin* (assuming grey optically thin photo-heating rates), TRAPHIC *thick* (assuming grey optically thick photo-heating rates), C^2-RAY, CRASH, FTTE. Contours show neutral fractions $\eta = 0.9, 0.5$, $\log \eta = -1, -3$ and -5, from the outside in. The colour scale is logarithmic and has a lower cut-off of $\eta = 10^{-7}$ (and hence is identical to that used in the top row panels of Fig. 5.15 in Chapter 5). The results obtained with TRAPHIC *thick* are in excellent agreement with those obtained with FTTE. They are also in excellent agreement with the results obtained with C^2-RAY in highly ionised regions, where the neutral fraction is unaffected by spectral hardening. The small differences in the neutral fractions obtained with TRAPHIC *thick* and TRAPHIC *thin* are mostly due to differences in the recombination rate, caused by differences in the gas temperatures (see Fig. 7.21; see Fig. 5 for a colour version).

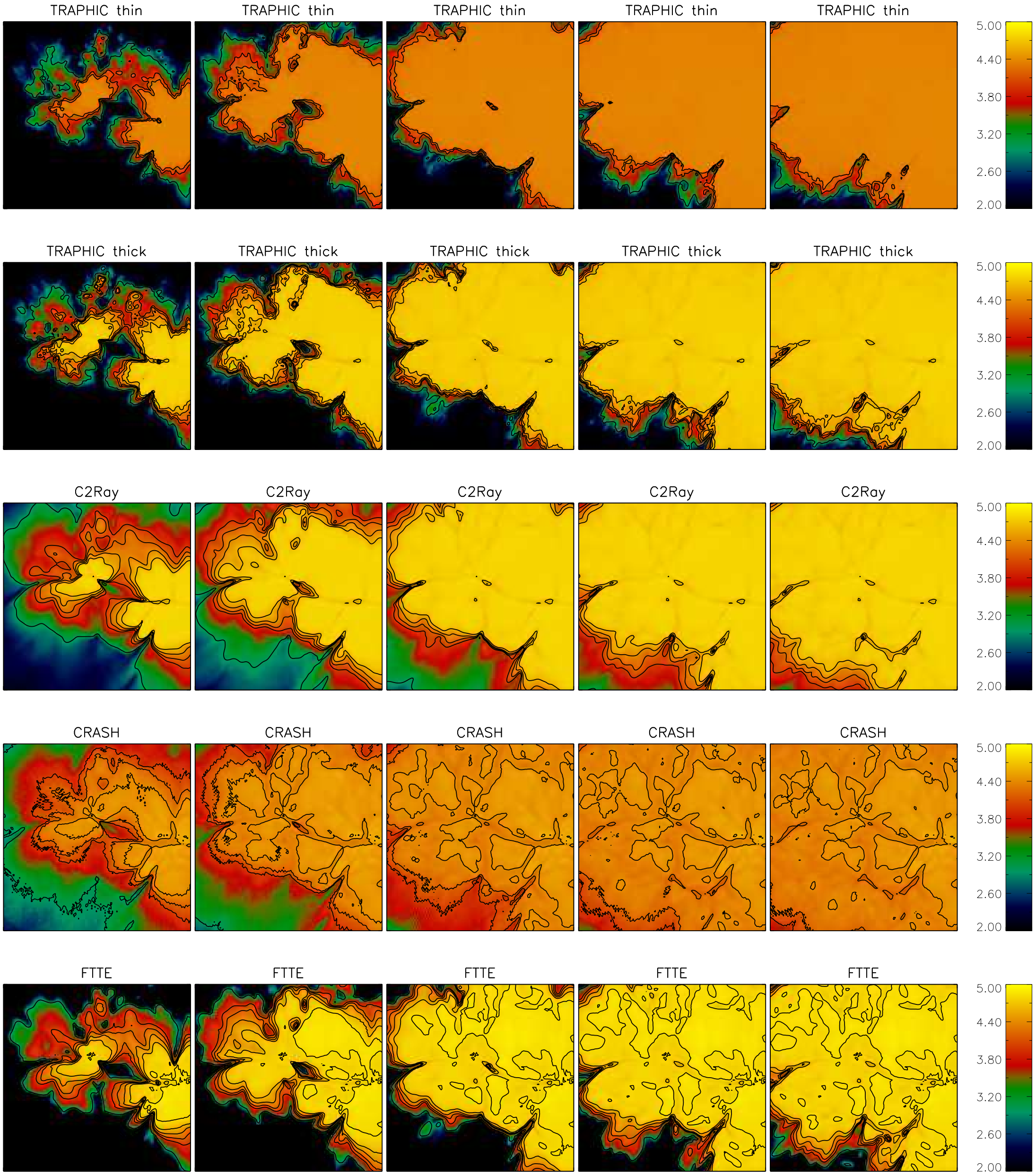

Figure 5: Identical to Fig. 7.21. Test 7: Temperature in a slice through $z = L_{\mathrm{box}}/2$. *From left to right:* $t = 0.05, 0.1, 0.2, 0.3$ and 0.4 Myr. *From top to bottom:* TRAPHIC *thin* (assuming optically thin photo-heating rates), TRAPHIC *thick* (assuming optically thick photo-heating rates), C^2-RAY, CRASH and FTTE. Contours show temperatures $\log_{10}(T\ [\mathrm{K}]) = 3, 4, 4.2, 4.4$ and 4.6, from the outside in. Most of the morphological differences may be attributed to differences in the spectral hardening of the ionising radiation (with the multi-frequency codes C^2-RAY and CRASH predicting a substantial amount of pre-heating and the monochromatic (grey) codes TRAPHIC and FTTE predicting sharp transitions between the hot ionised and the cold neutral phase), while the differences in the maximum gas temperatures are mainly due to photo-heating being computed in the optically thick limit (TRAPHIC thick, C^2-RAY, FTTE), the optically thin limit (TRAPHIC thin) or using multiple frequency bins (CRASH).

Curriculum vitae

I WAS born on June 6, 1978, in Finsterwalde, a small town not far south of Berlin. In 1998, after thirteen years of school education, I received my diploma (Abitur) at the Sängerstadt-Gymnasium in Finsterwalde and joined the German Air Force to take up a career as an officer. I quickly realised, however, that my childhood dream of exploring the sky was more likely to become true by studying astrophysics rather than survival guides and quit the army in 1999.

I subsequently enrolled at the University of Potsdam to study physics. In 2003, after four years of study, I abandoned my original plans of specialising in astrophysics and became a member of the research group Statistical Physics/Theory of Chaos. My decision was mostly triggered by my interest in the lectures on statistical physics held by Prof. Arkardy Pikovsky. Under his supervision I investigated the dynamics of self-sustained oscillators as forced by a delayed feedback and an external noise. I received my diploma in 2005, after finishing my thesis with title Effects of Noise and Delay on Nonlinear Oscillators, and was awarded the Wilhelm und Else Heraeus excellence prize.

By then I had accepted a PhD position at the astronomy department of the University of Leiden, The Netherlands. For the next four years, i.e. from 2005 to 2009, I thus had the opportunity to follow upon my interests in astrophysics and study the origin and evolution of the Universe. The times were exciting. LOFAR, a novel-technique radio telescope being built in the Netherlands, was soon to open a new observational window on a previously largely unexplored epoch in the history of the Universe: the epoch of reionisation. I followed the invitation of my supervisors Dr. Joop Schaye and Prof. Huub Röttgering to focus on the investigation of this interesting epoch using numerical simulations. The development of a novel radiative transfer method for application in epoch-of-reionisation simulations may be considered my main scientific achievement during my PhD.

PhD time is travel time. I participated in several schools on topics such as radio interferometry (Manchester, UK, 2005) and cosmology/astroparticle physics (Trieste, Italy, 2006). I visited the research group of Dr. Volker Springel at MPA (Garching, Germany, Jan-April 2008) as part of an EARA traineeship. I presented my work during conferences, workshops and seminars at institutes across the world, including IAP (Paris, France, 2005), Nordita (Stockholm, Sweden, 2007), ICC (Durham, UK, 2007), MPA (Garching, Germany, 2008, 2009), ETH conference center (Ascona, Switzerland, 2008), CITA (Toronto, Canada, 2008), CfA (Cambridge, USA, 2008), Caltech (Pasadena, USA, 2008) and others.

I will continue research in astrophysics at the University of Texas in Austin, USA. Being employed as a postdoctoral researcher from 2009-2012, I will use numerical simulations to investigate the physics of the first generation of stars and black holes in the first galaxies that formed in our Universe and assess their observability with future telescopes.

Publication list

Photoheating and supernova feedback amplify each other's effect on the cosmic star formation rate
Pawlik, A. H., Schaye, J.
2009, Monthly Notices of the Royal Astronomical Society, 396, L64

Keeping the Universe ionized: photoheating and the clumping factor of the high-redshift intergalactic medium
Pawlik, A. H., Schaye, J., van Scherpenzeel, E.
2009, Monthly Notices of the Royal Astronomical Society, 394, 1812

Detection and extraction of signals from the epoch of reionization using higher-order one-point statistics
Harker, G. J. A., Zaroubi, S., Thomas, R. M., Jelic, M., Labropoulos, P., Mellema, G., Iliev, I. T., Bernardi, G., Brentjens, M. A., de Bruyn, A. G., Ciardi, B., Koopmans, L. V. E., Pandey, V. N., **Pawlik, A. H.**, Schaye, J., Yatawatta, S.
2009, Monthly Notices of the Royal Astronomical Society, 393, 1449

Fast large-scale reionization simulations
Thomas, R. M., Zaroubi, S., Ciardi, B., **Pawlik, A. H.**, Labropoulos, P., Jelic, V., Bernardi, G., Brentjens, M. A., de Bruyn, A. G., Harker, G. J. A.; Koopmans, L. V. E., Mellema, G., Pandey, V. N., Schaye, J., Yatawatta, S.
2009, Monthly Notices of the Royal Astronomical Society, 393, 32

TRAPHIC - radiative transfer for smoothed particle hydrodynamics simulations
Pawlik, A. H., Schaye, J.
2008, Monthly Notices of the Royal Astronomical Society, 389, 651

Control of oscillators coherence by multiple delayed feedback
Pawlik, A. H., Pikovsky, A.
2006, Physics Letters A, 358 (3), 181

> Ich bin nicht um ein Haar breit höher,
> Bin dem Unendlichen nicht näher.
>
> Goethe, Faust I

Nawoord

THIS is my thesis. Without Joop, I would not have started it. Without Claudio, I would not have finished it. It was a pleasure to work under your supervision. Joop, I am grateful that you gave me both the opportunity to succeed and the freedom to fail. Claudio, I admire the selflessness with which you provided help and the patience with which you listened to my problems. Much must remain unsaid. Huub, I thank you for your valuable, often comfortably practical, advice. Rob, we went through it together. Olivera, I could not imagine the time without you. Marcel, I appreciate your refreshingly normal appearance; days without you are definitely less fun. Duffy, I will miss your comments in the group calendar. Freeke, I enjoyed your cheerful company; thank you for your help with the Dutch summary. Eveline, it was a great experience to work with you. Akila, Craig and David, I benefited from your interesting contributions to the group meetings and other scientific discussions.

I experienced the astronomy department at Leiden University, the *Sterrewacht*, as an exceptional environment for pursuing my research interests. Exciting colloquia and lunch seminars, the possibility to attend presentations at the nearby Lorentz conference center and the scientific exchange with the theoretical physics department all contributed to an atmosphere that enabled me to look beyond my own nose and to place my research into the larger context. The financial support was excellent, and I particularly thank Jan, Christine and Peter that I never had to worry about where all the money that I needed came from. I thank the secretaries Anita, Elise, Jeanne, Kirsten and Liesbeth and the computer administrators David, Tycho, Erik and Aart for their competent support. I appreciate that David and Erik were also reachable outside office hours, which was helpful at weekends before many a conference.

Simon, I will remember your readiness to help. Remco, I enjoyed being your office mate. Chocolate Easter eggs, t-shirt contests, the transformation of our office into a spaceship: I am looking forward to meeting you in Austin. Tracey, our after-work squash sessions were great fun. Niruj and Dharam, your disputes on radio astronomy were as passionate as your cookery. Cyril, thank you for helping me to produce my first (and last!) radio image. Maria, thank you for surprising me with the original version of War and Peace. Nina, Rik, Ann-Marie, Esther, Richard, Brent, Sarah, Cat, Kalle, Maaike, Rafael, Raymond, Ryan, Sergio, Christian, Mariska, Dominic, Edith, Jeanette and all who remain unmentioned, it was fun to meet you at vrijdag borrels, dinners, parties and for beers in the sun. Carolina, thank you for infecting me with your enthusiasm. Nadine, I enjoyed your company at theatres. David, your strong opinions turned every discussion into an event. Hendrik, I thank you for providing me with the German drug Tatort. Ernst and Karoliina, I am happy to see you reviving the vrijdags borrel.

I spent a wonderful time at MPA and I thank Volker for his hospitality and Maria and Kate for organising my stay. I enjoyed discussions, dinners and parties with Margarita, Margherita, Jens, Tom, Miro, Simone, Matthias, Mona, Umberto, Silvia, Ewald, Cecilia, Andre, Antonella, Benedetta and many more. Jens, thank you for your warm reception at CITA.

Whenever I came back to Potsdam/Berlin I felt very comfortable. I thank Prof. Arkady Pikovsky for his cordiality during my stays at the University of Potsdam. I enjoyed discussions with Arthur, Markus and Herr Hachenberger. Arthur, your advice was crucial for my decision to stay. Eric, Christian and Christoph, I am happy to have friends whom I can blindly trust.

Thomas, thank you for designing a great cover. Mathias, Franziska und René, bis hier und noch viel weiter. Ich danke meiner Familie. Ich danke meiner Mutter für ihre unbedingte und aufopferungsvolle Unterstützung.

In Erinnerung an meinen Vater.